

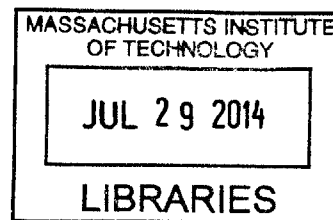
# An Improved Method for Measuring the Absolute DD Neutron Yield and Calibrating Neutron Time-of-Flight Detectors in Inertial Confinement Fusion Experiments

by

Caleb J. Waugh

M.S. Technology and Policy  
Massachusetts Institute of Technology, 2012

B.S. Electrical Engineering, B.A. Philosophy  
Brigham Young University, 2009



ARCHIVES

Submitted to the Department of Nuclear Science and Engineering in  
Partial Fulfillment of the Requirements for the Degree of

Master of Science in Nuclear Science and Engineering at the  
Massachusetts Institute of Technology  
June 2014

© 2014 Massachusetts Institute of Technology  
All rights reserved.

Signature redacted

Signature of Author.....

Department of Nuclear Science and Engineering  
May 9th, 2013

Signature redacted

Certified by..

Dr. Richard Petrasso  
Senior Research Scientist  
Division Head, High-Energy-Density Physics  
Thesis Supervisor

Signature redacted

Certified by.....

Dr. Dennis G. Whyte  
Professor of Nuclear Science and Engineering  
Thesis Reader

Signature redacted

Accepted by.....

Dr. Mujid S. Kazimi  
TEPCO Professor of Nuclear Engineering  
Chair, Department Committee on Graduate Students



## Abstract

Improved Methods for Measuring the Absolute DD Neutron Yield and Calibrating Neutron Time-of-Flight Detectors in Inertial Confinement Fusion Experiments

By  
Caleb J. Waugh

Submitted to the Department of Nuclear Science and Engineering on  
October 25, 2014 in partial fulfillment of the requirements for the degree of  
Master of Nuclear Science and Engineering

Since the establishment of nuclear physics in the early 1900's and the development of the hydrogen bomb in the 1950's, inertial confinement fusion (ICF) has been an important field in physics. Funded largely through the U.S. National Nuclear Security Agency (NNSA), the Laboratory for Laser Energetics (LLE), Sandia National Laboratories (SNL) and Lawrence Livermore National Laboratory (LLNL) have advanced ICF as a platform for stockpile stewardship and weapons physics, but also have contributed to basic science in high energy density regimes and for pursuing fusion an energy source.

One of the primary goals of the ICF research program is to produce a thermonuclear burn in an ICF capsule where the power balance of the reaction is net positive. This criterion is often referred to as ignition. One of the most common metrics for gauging progress towards ignition in an ICF implosion is the ITFX parameter (similar to the Lawson Criterion) and is primarily a function of the implosion areal density ( $\rho R$ ) and fusion yield. An ITFX value greater than one indicates net energy production. In deuterium/tritium fuel mixtures the yield is determined by measuring the reactant 14.0 MeV neutrons. Subsequently, the ability to obtain highly accurate absolute neutron yield measurements is vital to determining the ITFX and hence progress toward ignition. Although ignition implosions all use deuterium/tritium fuel mixes, other capsule fuel mixes such as pure deuterium and deuterium/helium 3 are also used to improve understanding of capsule performance.

At the LLE and LLNL, neutron time-of-flight (nTOF) detectors routinely measure the absolute neutron yield from laser-driven ICF implosions. Although originally calibrated through a series of cross-calibrations with indium and copper neutron activation systems, an alternative method has been developed for measuring the DDn yield that provides a more accurate calibration by directly calibrating nTOF *in situ* to CR-39 range filter (RF) proton detectors. A neutron yield can be inferred from the CR-39 RF proton measurement since the DD proton and DD neutron branching ratio is well characterized and close to unity. By obtaining highly accurate DDp yields from a series of exploding pusher campaigns on OMEGA, an excellent absolute DDn yield measurement was obtained and used to calibrate the 3m nTOF detector. Data obtained suggest the existing OMEGA nTOF

calibration coefficient to be low by  $9.0 \pm 1.5$  % based on the inferred CR-39 DD neutron yield.

In addition, comparison across multiple exploding pusher campaigns indicate that significant reduction in charged particle flux anisotropies can be achieved on shots where capsule bang time occurs significantly (on the order of 500ps) after the end of the laser pulse. This is important since the main source of error in the RF DDp yield measurement is due to particle flux anisotropies. Results indicate that the CR-39 RF/nTOF *in situ* calibration method can serve as a valuable platform for measuring the DDn yield from ICF implosions and for calibrating and reducing the uncertainty of calibration coefficients of nTOF detector systems on OMEGA and other larger facilities such as the National Ignition Facility (NIF).

Thesis Supervisor: Dr. Richard Petrasso  
Title: Division Head, High-Energy-Density Physics

## Acknowledgements

In Nichomachean Ethics, Aristotle states that “intellectual excellence owes its birth and growth mainly to instruction...” Throughout my education at MIT I have been impressed that there is very little we can truly call our own, especially when it comes to academic achievement and success. If there is any “intellectual excellence” I may have achieved in my attempt to improve existing methodologies for measuring the absolute DD neutron yield in inertial confinement fusion experiments I owe it largely to the instruction and guidance of my advisor and colleagues at the Division for High-Energy-Density Physics at the MIT Plasma Science and Fusion Center.

Specifically, I would like to thank my advisor Rich Petrasso for giving me the opportunity to work in high-energy-density physics, for granting me the opportunity to be involved in a wide variety of projects in conjunction with our colleagues at the national laboratories, and for instilling an excitement, passion, and drive for physics and research in general in a way that only people who have had the pleasure to know him can understand. I would also like to thank Frederick Seguin, Johan Frenje and Chikang Li for their unmatched expertise and for personally assisting me in understanding the mysteries of inertial confinement fusion, nuclear diagnostics, and above all, the “magical” properties of CR-39. Many thanks go to Maria Gatu-Johnson, Daniel Casey, Mario Manuel, Nareg Sinenian, Hans Rinderknecht, Alex Zylstra, Mike Rosenberg and Hong Sio for assisting me with countless questions and problems over the last two years, for offering of their time and expertise on numerous occasions in the MIT Linear Electrostatic Ion Accelerator (LEIA) laboratory, and for always providing thoughtful feedback and suggestions, always in the spirit of improvement and commitment to doing the absolute best science possible. Special thanks go to the Laboratory for Laser Energetics, the National Ignition Facility, the U.S. Department of Energy, the U.S. National Nuclear Security Administration, Los Alamos National Laboratories, Sandia National Laboratories and the National Laser Users Facility, for their never-ending commitment to supporting and engaging students in HEDP and ICF research in a meaningful and collaborative way.

Finally, to Ece for her love, support, inspiration and patience while working on this thesis and to my parents, Jody and Marsha Waugh, for instilling in me a passion for the outdoors, an appreciation of hard work, and the knowhow to live each day to its fullest.

This work was supported in part by the U.S. Department of Energy (DOE) (DE-FG52-09NA-29553), the National Laser User's Facility (DOE Award No. DE-NA0000877), the Fusion Science Center at the University of Rochester (Rochester Sub Award PO No. 415023-G), and the Laboratory for Laser Energetics (LLE) (No. 412160-001G).

# Table of Contents

Abstract .....	3
Acknowledgements.....	5
List of Figures.....	9
List of Tables.....	15
1 Introduction .....	17
1.1 Nuclear Fusion and Nucleosynthesis.....	20
1.2 High Energy Density Physics .....	29
1.3 Thesis Outline .....	30
2 Inertial Confinement Fusion .....	33
2.1 Contemporary Motivation for Inertial Confinement Fusion Research.....	33
2.2 The Physics of Inertial Confinement Fusion.....	37
3 Previous DDn Yield Measurements and nTOF Calibration Methods.....	43
3.1 The Indium Activation Method .....	46
3.2 NOVA In/nTOF Cross-calibration .....	49
3.3 OMEGA In/NOVA nTOF Cross-calibration.....	49
3.4 OMEGA nTOF/CR-39 Neutron Verification.....	50
3.5 OMEGA In/nTOF Cross-calibration .....	51
4 Measuring the Absolute DDn Yield on OMEGA.....	53
4.1 High Accuracy $Y_{DDp}$ Measurements on OMEGA using CR-39 Range Filters.....	54
4.2 Relation Between Particle Flux Anisotropies and Bang Time .....	63
4.3 CR-39/nTOF Yield Comparison and Calibration Coefficient Verification .....	66
5 Conclusion.....	73
6 Bibliography.....	75

<b>Appendix 1: Derivation of the Fusion Reaction Rate .....</b>	<b>79</b>
<b>Appendix 2: MIT Linear Electrostatic Ion Accelerator (LEIA) Ion Beam Current Measurements (Faraday Cup) .....</b>	<b>93</b>
<b>Appendix 3: Radiochromic Film Slit Width Verification on OMEGA Charged Particle Spectrometers.....</b>	<b>97</b>
<b>A4.1 Introduction .....</b>	<b>97</b>
<b>A4.2 Overview .....</b>	<b>97</b>
<b>A4.3 Results.....</b>	<b>106</b>
<b>A4.4 Radiochromic Film Setup.....</b>	<b>112</b>
<b>A4.5 Data .....</b>	<b>113</b>
<b>Appendix 4: Stage Etching of High Fluence Range Filter CR-39 Modules On Omega.....</b>	<b>123</b>
<b>Appendix 5: Absolute DDp Measurements taken on Exploding Pushers on OMEGA (Febuary 7<sup>th</sup> and 9<sup>th</sup>, 2012).....</b>	<b>127</b>
<b>Shot 64958.....</b>	<b>128</b>
<b>Shot 64961.....</b>	<b>138</b>
<b>Shot 64963.....</b>	<b>147</b>
<b>Shot 64965.....</b>	<b>157</b>
<b>Shot 64967.....</b>	<b>167</b>
<b>Shot 64993.....</b>	<b>177</b>
<b>Shot 64995.....</b>	<b>187</b>
<b>Shot 64997.....</b>	<b>197</b>
<b>Shot 64999.....</b>	<b>207</b>
<b>Shot 65001.....</b>	<b>217</b>



## List of Figures

Figure 1. First ionization energies of the elements (energy required to free one electron). 18

Figure 2. Fractional ionization for light elements hydrogen, helium, and lithium as a function of ion temperature. The corresponding ionization energies are: 13.60 eV (H), 24.59 eV (He), and 5.39 eV (Li). .....19

Figure 3. The Cat's Eye nebula as seen from the Hubble telescope. ....20

Figure 4. Binding energy per nucleon for all known nuclides (both stable and unstable). Fusion reactions resulting in heavier nuclides and fission reactions creating lighter nuclides release energy while moving toward more heavily bond states. Deuterium (D), tritium (T), helium, iron ( $^{56}\text{Fe}$ ) and uranium ( $^{235}\text{U}$ ) are noted. ....22

Figure 5. Image depicting the standard fusion problem [3]. A nuclei with energy  $\epsilon$  is incident on a second nuclei. As the two nuclei approach the Coulomb repulsive force acts to push the two particles apart. Under classical mechanics, if the relative energy (center of mass energy) of the two particles is less than  $V_b$  the two particles will not fuse. However, under quantum mechanics there is a finite probability of the particles tunneling through the Coulomb barrier even though  $\epsilon$  is lower than the  $V_b$ . ....24

Figure 6. (a) fusion cross sections and (b) fusion reactivities for primary light isotope fusion reactions. The fusion reactivities assume a Maxwellian velocity distribution characterized by temperature T. ....26

Figure 7. The first three steps in the proton-proton (pp) fusion chain resulting in  $^4\text{He}$ . ....28

Figure 8. Natural and man-made regimes in high-energy-density physics. ....29

Figure 9. Aerial views taken of the Nevada test site. Both images depict craters left from underground tests. ....34

Figure 10. The Titan supercomputer at Oak Ridge National Laboratory. ....36

Figure 11. Major research facilities that are part of the National Nuclear Security Administration's Stockpile Stewardship program: (a) the Z-Machine pulsed power facility at Sandia National Laboratories, (b) the OMEGA laser at the Laboratory for Laser Energetics, (c) the National Ignition Facility at Lawrence Livermore National Laboratory. ....37

Figure 12. Basic principles of inertial confinement fusion: (a) a driver beam heats the capsule surrounding a small pellet of fuel, (b) the fuel is compressed and a hot spot forms in the center, (c) the fuel stagnates and temperatures and densities are sufficient for thermonuclear burn, (d) alpha particles emitted from the hot spot heat the remaining fuel and the nuclear burn propagates through the fuel.....38

Figure 13. Progress towards ignition during the National Ignition Campaign measured using the ITXF ratio which is a function of yield and areal density. An ITXF of 1 corresponds to ignition.....42

Figure 14. A sample nTOF response with the raw single passed through an inverting amplifier and fit using the method outlined in [27, 28]. An absolute neutron yield for DD and DT neutrons is obtained by time integrating the signal ( $S_{nTOF}$ ) and then multiplying by a detector-specific calibration coefficient ( $C_{nTOF}$ ). (Figure as given in [29]).....44

Figure 15. LLNL linear electrostatic ion accelerator setup for In-activation gamma spectrometer calibration. D+ ions incident on a deuterium doped titanium target generate DDn and DDp. The DDn yield ( $Y_{DDn}$ ) is inferred from the  $Y_{DDn}/Y_{DDp}$  branching ratio where  $Y_{DDp}$  is obtained using a charged particle detector. The gamma ray spectrometer calibration coefficient is obtained from  $Y_{DDn}$  and the total gamma count of the In slug ( $N_{\gamma,Tot}$ ) using Equation 3.5.....47

Figure 16. Flowchart outlining the series of cross-calibrations leading to the current OMEGA nTOF calibration coefficient. Values in  $\diamond$  represent fundamental diagnostic measurements, values in  $\square$  represent calculations, and values in  $\circ$  represent fundamental calculated quantities. (a) The gamma spectrometer calibration coefficient ( $C_{\gamma:NOVA}$ ) was obtained from the observed gamma count ( $N_{\gamma,Cnt}$ ) and DD proton yield ( $Y_{DDp}$ ) on a Cockcroft-Walton accelerator. (b) The NOVA 2m nTOF calibration coefficient ( $C_{nTOF:NOVA}$ ) was obtained from the NOVA In-activation system over a series of shots on NOVA. NOVA 10m nTOF was then cross calibrated to NOVA 2m nTOF. (c) The OMEGA gamma spectrometer calibration coefficient ( $C_{\gamma:NOVA}$ ) was obtained through cross-calibration to the NOVA 10m nTOF. Finally, (d) OMEGA nTOF calibration coefficients  $C_{nTOF:OMEGA}$  were obtained through cross calibration to the OMEGA In-activation system.....52

Figure 17. Flowchart outlining the steps for a method to obtain detector-specific nTOF calibration coefficients *in situ* during ICF implosions using CR-39 nuclear track detector range filter (RF) modules. The values in  $\diamond$  represent fundamental diagnostic measurements, values in  $\square$  represent calculations, and values in  $\circ$  represent fundamental calculated quantities.....53

Figure 18. (a) Campaign A, (b) and Campaign B exploding pusher shot campaigns on OMEGA used to obtain an absolute yield calibration coefficient for 3m nTOF.....54

Figure 19. Aitoff projection of the OMEGA target chamber showing the diagnostic ports (given in yellow) and laser drive ports (given in green red and blue). CR-39 range filter (RF) modules for nTOF calibration shots were fielded in ten inch manipulators (TIMs) 1,2,3, and 5 to provide broad angular coverage over the target chamber solid angle and account for particle flux anisotropies.....55

Figure 20. The range filter (RF) DDp and nTOF DDn yield results from (a) Campaign A and (b) Campaign B shots on OMEGA. The DDp yields from the Campaign A shots on average show a significant amount of spread in the RF measurement whereas the Campaign B shots show very little spread and are in good agreement with 3m nTOF.....56

Figure 21. The simulated capsule radius and areal density are given for shot 64999 as a function of time (where  $t = 0$  corresponds to the beginning of the laser pulse).....59

Figure 22. Measured and modeled values of proton track diameter in CR-39 as a function of incident proton energy (MeV). As given in Seguin et al. [31]......60

Figure 23. CPS2 measured energy spectrums for (a) shot 64967 (Campaign A—D<sup>3</sup>He) and (b) shot 64961 (Campaign B—DD). .....61

Figure 24. The effect of the occurrence of bang time relative to the end of the laser pulse on yield variation measured by CR-39 RF modules. The results from three exploding pusher campaigns on OMEGA are presented: (1) January 13, 2012, (3) Campaign A (February 7 & 9, 2012), and (3) Campaign B (February 7 & 9, 2012). The yield variation reduces significantly when bang time occurs significantly (at least 500ps) after the end of the laser pulse.....64

Figure 25. The  $Y_{DDn}/Y_{DDp}$  branching ratio is given by the ratio of the parameterized reaction rates obtained from Bosch and Hale for DDn and DDp. This ratio as a function of ion

temperature is given by the black line. The inferred branching ratios for the OMEGA Campaign A and Campaign B shots are obtained using the fuel burn-averaged ion temperatures from nTOF and plotted on the black line. The error bars given for each shot in Campaign A and Campaign B indicate the measured error in the nTOF ion temperature measurement (x-axis) and the inferred error in the branching ratio (y-axis). .....68

Figure 26. The expected value of the average of the  $R_{Fn}/n_{TOF}$  DDn yield ratio ( $E[\langle Y_{RFn}/Y_{nTOF} \rangle]$ ) with the associated 95% confidence interval obtained from the error analysis for the OMEGA Campaign A and Campaign B shots.....72

Figure 27. The "fusion problem" where  $V_{Tot}(r)$  is the potential energy barrier particle  $X_2$  experiences as it approaches particle  $X_1$  and  $r$  is the distance between particles. ....81

Figure 28. The wave-function solution to the Schrodinger equation for the fusion problem. ....88

Figure 29. Impact parameter  $b$ , and cross section of nuclear collision. ....90

Figure 30. Fusion collisions with a density of target particles.....91

Figure 31. Linear Electrostatic Ion Accelerator (LEIA).....93

Figure 32. LEIA faraday cup beam current measurements with a negatively biased electron suppression voltages.....95

Figure 33. Magnet used for both CPS1 and CPS2 with particles entering from the "target" end and being deflected based on particle energy (Figure courtesy of LLE standard operating procedure D-ES-P-092). ....98

Figure 34. (a) CPS data cartridge assembly showing the baseplate, slit finger, CR-39 nuclear track detector fingers, and slit-width x-ray finger. (b) Data cartridge assembly being mounted over the magnet in CPS1 (Both figures courtesy of LLE standard operating procedure D-ES-P-092). ....99

Figure 35. (a) CR-39 slit image from CPS1 (OMEGA shot 59484), slit is discernible. (b) CR-39 slit width image for CPS2 (OMEGA shot 59489), slit is not discernible..... 100

Figure 36. (a) BIOMAX x-ray film fielded on OMEGA shot 62412 on CPS1. (b) Radiochromic film fielded on OMEGA shot 62407 on CPS2..... 101

Figure 37. Inventory of CPS1 slits include nominal widths of 0.09mm, 0.2mm, 0.5mm, 1.0mm, 2.0mm, 3.0mm, 4.0mm, 5.0mm, and 10.0mm. .... 103

Figure 38. Slit images obtained for the CPS1 slit inventory on June 29th, 2011 using RCF. .....	103
Figure 39. Slit images obtained for CPS2 on June 29th, 2011 using RCF along with CPS2 collimator slit inventory (all slit images included except for 7.0mm, and all slit inventory included except 5.0mm).....	104
Figure 40. (a) Double feature appearing in CR-39 slit image for CPS1 (OMEGA shot 61082). (b) Double Feature appearing in RCF slit image for CPS1 (OMEGA shot 62754). (c) Overlapping target and backlighter images from 2.0mm slit on CPS1. ....	105
Figure 41. View of target capsule and backlighter foil from (a) CPS 2, and (b) CPS 1. In (a) both the front of the back lighter foil and the target are in the field of view providing to point X-ray sources. In (b) the target is in the field of view but the back of the backlighter foil seen which may limit X-ray emissions.....	106
Figure 42. Experimental configuration for CPS1 and CPS2 with corresponding magnification factors.....	107
Figure 43. Target slit image for 0.1mm slit on CPS1 with lineout showing slit thickness (microscope magnification set to 100x). ....	108
Figure 44. Overlapping target and backlighter image for 3mm slit on CPS1 with lineout showing slit thickness (microscope set to 100x in scanning mode).....	108
Figure 45. Effect of rotational perturbation on slit image width: (a) no rotation, (b) rotation of angle $\theta_S$ .....	109
Figure 46. Preparation specifications for RCF used for imaging collimator slit width on CPS1 and CPS2. ....	112
Figure 47. Average track diameter vs. etch time for CR-39 etched in a sodium hydroxide solution. ....	124
Figure 48. (a) CR-39 Normal Fluence (standard 5 hour etch) with a track density of $\sim 1 \times 10^4$ tracks/cm <sup>2</sup> , (b) CR-39 high fluence (standard 5 hour etch) track density $2.4 \times 10^5$ tracks/cm <sup>2</sup> . ....	124
Figure 49. The qualitative detection efficiency of CR-39 as a function of etch time. The track undercount, optimal etch range, and track overlap regime for CR-39 are also identified..	125

**Figure 50. The actual etch time vs. track detection rate for OMEGA Shot 62409 which had a D3he-p fluence of  $3.69 \times 10^5$  tracks/cm<sup>2</sup>. ..... 125**

## List of Tables

Table 1. Table of primary fusion reactions in the p-p and CNO.....28

Table 2. U.S. Department of Energy supercomputers as of June 2013. ....35

Table 3. nTOFs comprising the NOVA nTOF system in the 1990s along with their corresponding distance to target chamber center (TCC), the method used for cross-calibration, and the resulting detector-specific calibration coefficient ( $C_{nTOF}$ ).....49

Table 4. Primary fusion product charged particles incident on CR-39 RF modules in Campaigns A and B. Given are the source fusion reactions, the particle birth energy, the range of the particle in aluminum corresponding to the birth energy, and the energy of the particle after passing through the 25  $\mu\text{m}$  range filter. ....58

Table 5. Calculation of DD protons lost to lower energy tail of distribution.....62

Table 6. The errors associated with the averaged expected value of the  $RFn/nTOF$   $DDn$  yield ratios for the Campaign A, Campaign B, and both campaigns are given.  $\sigma_E$  is the accompanied instrumentation error,  $\sigma_C$  is the error from yield variation (due to particle flux anisotropies), and  $\sigma_T$  is the total error in the expected value. The 95% confidence interval is also given. ....71

Table 7. Inventory of slits for CPS1 and CPS2..... 102

Table 8. Benchmarked measured and calculated widths of slits in CPS1 and CPS2 inventory. For CPS1, both widths from the target and backlighter (BL) images are given separately. .... 110

Table 9. Measured slit width and slit depths, calculated and measured RCF slit images and the angle of rotational perturbation needed to reduce the yield measurement by 20%.... 111





# 1 Introduction

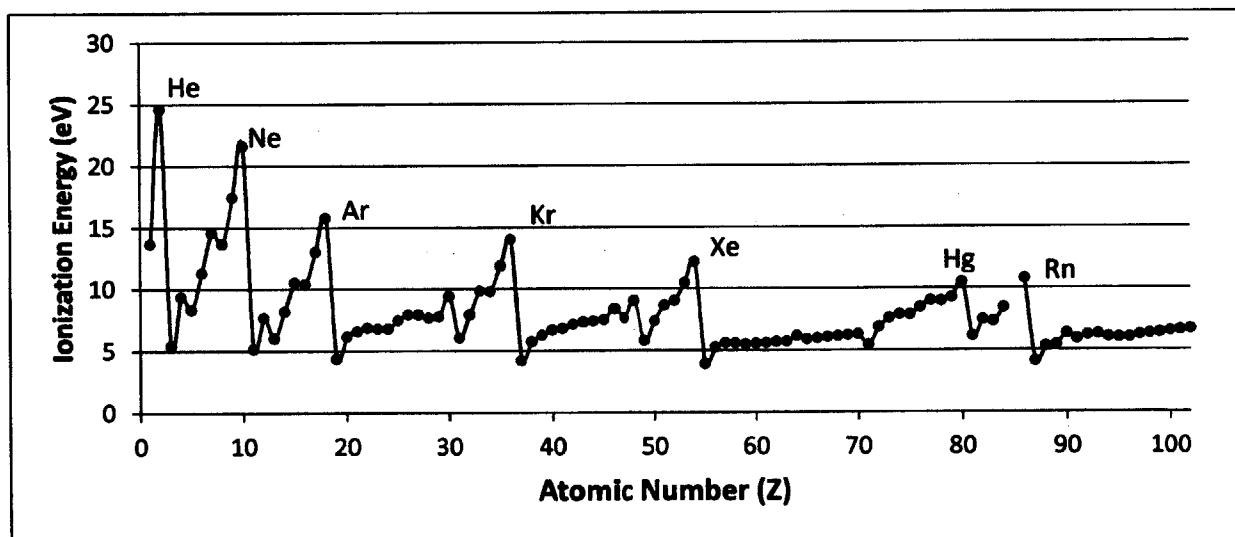
*“...if both observation and conceptualization,  
fact and assimilation to theory, are inseparably linked in discovery,  
then discover is a process and must take time...”*

*—Thomas Kuhn [1]—*

Understanding of the cosmos and the nature of terrestrial substance has a long tradition dating back to the very first of the natural philosophers who sought to apply the tools of reason to overthrow the confines of mythological explanations of the universe and establish complete and consistent arguments for the nature of the phenomena they observed. Of the first in the tradition, Thales of Miletus circa 600 B.C. claimed all substance was made of water. Anaximenes circa 550 B.C. claimed all substance was air. Later, Heraclitus circa 500 B.C. claimed all was fire, while Empedocles synthesizing all preceding views, and adding a fourth, claimed all substance was air, fire, water, or earth. In 350 B.C. Aristotle accepted Empedocles categorization of the earthly substances and added a fifth, aether, the perfect and unchanging material of the celestial regions and heavenly bodies that was otherworldly compared to the terrestrial elements which are subject to change, rot and decay. This view of the heavens as a place of unchanging perfection lasted for 2000 years until Galileo, while staring through the lens of his telescope in Padua in the 16<sup>th</sup> century, observed mountains, craters, and other imperfections on the surface of the moon, suggesting that what was once regarded in reverence as perfect, unchanging, and divine, was strikingly more similar to the terrestrial elements than had ever previously been thought.

In our day the Aristotelian paradigm for terrestrial substance has long been replaced, but at the same time this ancient categorization of substance is strikingly similar to what we now view as the four states of matter: solids, liquids, gases, and plasma. Solids are characterized by strong binding between particles with low kinetic energy. As the kinetic energy of the particles increases, the solid experiences a phase transition to liquid where the particles are still bound together although the bonds are much weaker. In water at

atmospheric pressure this occurs at 273K. As additional energy is added, the inter-particle bonds start to break apart and the liquid goes through a second phase transition to a gas which has virtually no bonding between particles. In water at atmospheric pressure, this occurs at 373K. Finally, if enough energy is added, the Coulomb forces holding the electrons to the nuclei themselves are overcome and the electrons disassociate with the nuclei altogether. In this stage the particles are ionized and the matter is said to be in the plasma state. For hydrogen, this occurs at  $1.58 \times 10^5$  K or 13.59 eV (where 1 eV is equal to 11604.5 K). Elements are often characterized by their atomic number  $Z$  which corresponds to the number of protons. Heavier elements with high  $Z$  have  $Z$  electrons and there is a distinct energy required to ionize each electron. The energy required to ionize the first electron is the 1<sup>st</sup> ionization energy, the energy required to ionize the 2<sup>nd</sup> electron is the second ionization energy, and so on. The ionization energies differ for each element based on the filling of orbitals in the electron shell structure. The 1<sup>st</sup> ionization energies for all known elements are given in **Figure 1** as a function of  $Z$ .



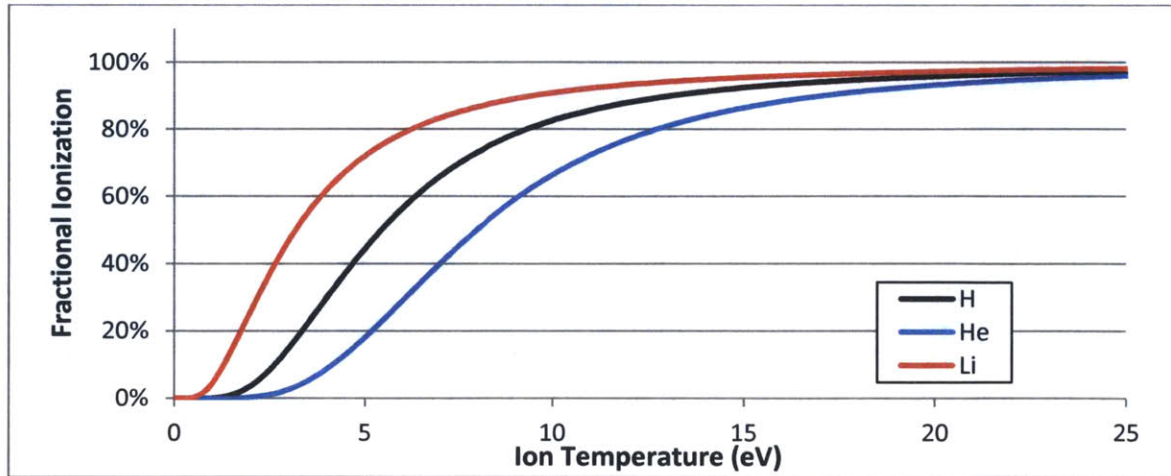
**Figure 1. First ionization energies of the elements (energy required to free one electron).**

For a given volume of gas, some atoms may be ionized while others remain neutral. Within an ionized gas, the extent to which the gas is ionized is a function of the particle

density ( $n_0$ ) and temperature ( $T$ ) and is given by the Saha Equation as the ratio of the density of singly ionized ions ( $n_i$ ) to neutrals ( $n_n$ ):

$$\frac{n_i}{n_n} = \frac{2}{\Lambda^3} \frac{g_1}{g_0} \frac{1}{n_i} \exp\left[-\frac{\varepsilon}{k_B T}\right], \quad \Lambda \equiv \sqrt{\frac{h^2}{2\pi m_e k_B T}} \quad (1.1)$$

where  $n_i$  is the density of singly ionized ions,  $n_n$  is the density of neutral ions,  $g_0$  is the quantum mechanical degeneracy of the ground state,  $g_1$  is the degeneracy of the states of singly ionized ions,  $\varepsilon$  is the 1<sup>st</sup> ionization energy (these values were shown in Figure 1.1),  $k_B$  is Boltzmann's constant,  $\Lambda$  is the thermal de Broglie wavelength of an electron,  $h$  is Planck's constant, and  $m_e$  is the electron mass. At temperatures much less than the ionization energy, the exponential term dominates and the fractional ionization is  $\approx 0$ . As the thermal temperature approaches and then exceeds the ionization temperature ( $\varepsilon$ ), the exponential term becomes of order unity and the temperature dependence in the thermal de Broglie wavelength term ( $\Lambda$ ) begins to dominate. To illustrate the effect of temperature on ionization, the fractional ionization as a function of temperature for H, He and Li at a constant density of  $10^{13} \text{ m}^{-3}$  is given in **Figure 2**.



**Figure 2. Fractional ionization for light elements hydrogen, helium, and lithium as a function of ion temperature. The corresponding ionization energies are: 13.60 eV (H), 24.59 eV (He), and 5.39 eV (Li).**

If we solve the Saha equation for air (density  $\sim 10^{25} \text{ m}^{-3}$ ) at room temperature ( $T \sim 300\text{K}$ ) and using the ionization energy of nitrogen we calculate a fractional ionization of  $\sim 10^{-122}$

which is essentially zero! The fractional ionization for other gases at these temperatures and densities on earth is comparable. This result indicates that it is virtually impossible to find ionized gases naturally on earth (although there are some exceptions such as lightning and the aurora borealis). By contrast, in interstellar medium consisting of hydrogen, we find extremely low densities on the order of  $10^3 \text{ m}^{-3}$ , and particles are fully ionized at temperatures less than 1 eV. In addition, temperatures in stars, gas-giant cores, supernovae, and neutron stars often greatly exceed the ionization energy resulting in complete ionization. From the Saha equation one can estimate that as much as 99% of all matter in the non-terrestrial universe—the matter making up Aristotle’s unchanging and divine aether—is nothing more than the same material found on earth except existing in a plasma state. As we gaze into the heavens we observe plasmas everywhere in stars, galaxies, and nebula such as the Cat’s Eye nebula pictured in **Figure 3**.



**Figure 3. The Cat's Eye nebula as seen from the Hubble telescope.**

### 1.1 Nuclear Fusion and Nucleosynthesis

Of all the theories of the original natural philosophers (i.e. Thales, Anaximenes, Empedocles, Aristotle, etc.) the hypothesis most closely resembling our contemporary theory of substance was given by Democritus who claimed that everything was composed of “atoms” that were physically indivisible and constituted the smallest building blocks of

the universe. Atoms, as Democritus claimed, were infinite in number, could be different in kind, size, and shape, and were separated by empty space or void. The processes responsible for creating daughter atoms of different kind, size, and shape, from parent atoms of smaller Z only occur when matter is in the plasma state through nuclear fusion reactions. Additionally, nuclear fission and radioactive decay (e.g. alpha, beta, and gamma decay) produce daughter atoms from parent atoms of higher Z. The process responsible for creating new atomic nuclei from pre-existing nucleons with smaller Z through nuclear fusion is called nucleosynthesis. We now turn the problem of how atoms are formed and the nuclear reactions that lead to their formation.

In Albert Einstein's paradigm-shattering paper "On the Electrodynamics of Moving Bodies" we learn that the rest mass of a particle can be expressed as an energy equivalence that is given by the famous equation  $E=mc^2$  [2]. One result of this relationship is that any change in the rest mass of an atom leads to a change in its kinetic energy as given in **Equation 1.2:**

$$\Delta E = \Delta m \cdot c^2 \quad (1.2)$$

where  $\Delta E$  is in joules,  $\Delta m$  is in kilograms, and  $c$  is in meters per second. In nuclei, this mass differential contributes to the binding energy,  $E_B$ , that is responsible for binding the nuclear protons and neutrons together. The binding energy is expressed in terms of the mass differential between the total mass of the individual protons, neutrons and electrons, and the actual mass of the atom as a whole. The binding energy relationship is given in **Equation 1.3:**

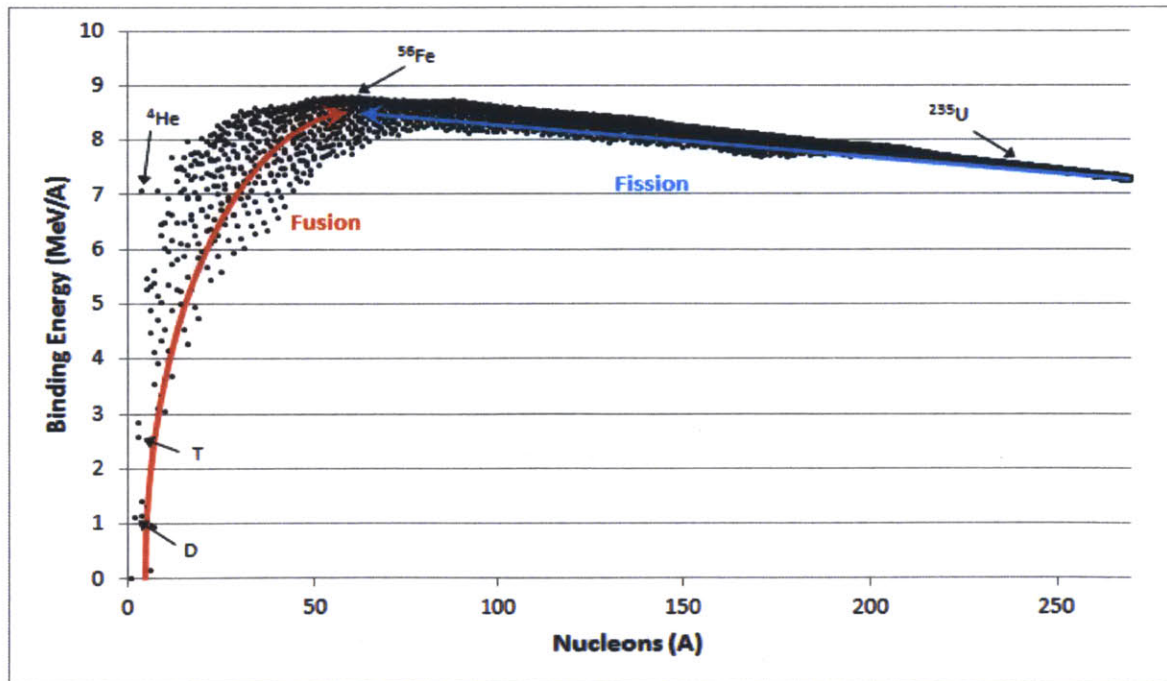
$$E_B = \left\{ Z \cdot m_p + N \cdot m_n - \left[ m(^A X) - Z \cdot m_e \right] \right\} \cdot c^2 \quad (1.3)$$

where  $Z$  is the number of protons and electrons,  $N$  is the number of neutrons,  $m_p$  is the proton mass,  $m_n$  is the neutron mass,  $m_e$  is the electron mass, and  $m(^A X)$  is the mass of atom  $X$  with atomic mass number  $A$ . Nuclear reactions are often represented similarly to chemical reactions with the reactants on the left side and the products on the right side of a reaction chain. An example of this is given by **Equation 1.4**



where  $X_1$  and  $X_2$  are the reacting nuclei,  $X_3$  and  $X_4$  are the fusion product(s)—depending on the reaction there may be more than one—and  $Q_F$  is the change in energy which is based on the mass differential between the reactant nuclei and the fusion products. For positive  $Q_F$  the reaction is exothermic, for negative  $Q_F$  the reaction is endothermic. An equivalent alternative notation that is commonly used for the fusion reaction is:  $X_1(X_2, X_3)X_4$ .

When a nuclear reaction occurs such that the mass of the reacting nuclei is greater than the mass of its products, the binding energy is converted to kinetic energy and released with the reaction products as  $Q_F$ . Despite the change of mass, the number of nucleons in a nuclear reaction remains constant. Since the total number of nucleons is conserved, it is customary to express the binding energy of an atom in terms of its binding energy per nucleon (MeV/A). A graph depicting the binding energy per nucleon for all known nuclides (both stable and unstable) for  $A$  (ranging from  $A=1$  to  $A=270$ ) is given in **Figure 4**.



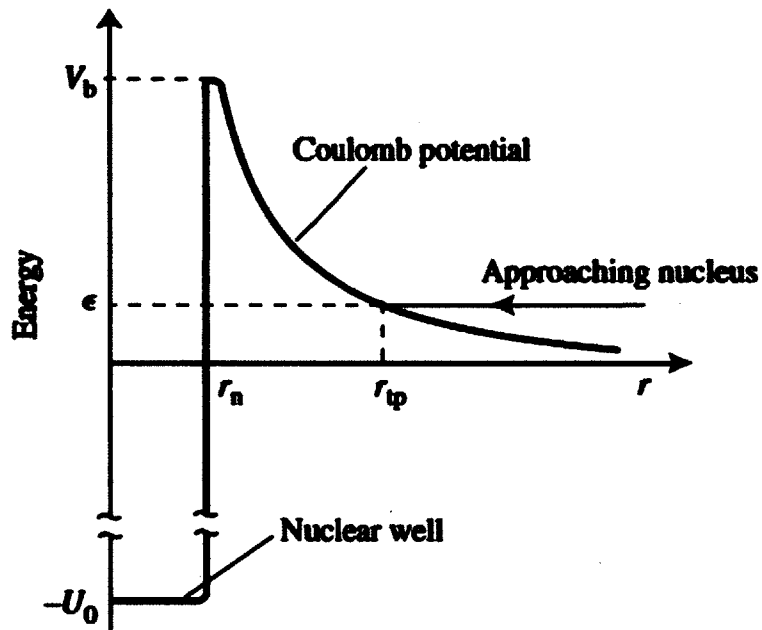
**Figure 4. Binding energy per nucleon for all known nuclides (both stable and unstable). Fusion reactions resulting in heavier nuclides and fission reactions creating lighter nuclides release energy while moving toward more heavily bond states. Deuterium (D), tritium (T), helium, iron ( $^{56}\text{Fe}$ ) and uranium ( $^{235}\text{U}$ ) are noted.**

As can be seen, initially the binding energy per nucleon increases from  $A=1$ —where by definition it is 0—until it reaches a maximum at 8.79 MeV/A around  $^{56}\text{Fe}$ . From there the binding energy per nucleon gradually decreases arriving at 7.87 MeV/A for  $^{235}\text{U}$ . From the graph we gain a clear understanding of the kinds of nuclear reactions that have the potential of releasing energy. Any reactions among nuclei that go from lower to higher binding energies convert mass energy to kinetic energy and are therefore exothermic. For nuclei with  $A$  less than 56 this happens for nuclear fusion reactions whereas for nuclei with  $A$  greater than 56 this only happens through fission. The amount of energy released is referred to as the  $Q$ -value and is equal to the energy mass differential of the reaction products and reactants as expressed earlier in Equation 1.2.

Having established the kinds of nuclear reactions and the source of energy released in these reactions, we now look at the physics behind the reactions themselves. Fusion reactions are the result of particle collisions and the attractive and repulsive forces that act on particles when they collide. The two primary forces of interest include (1) the Coulomb repulsive force which is due to each nuclei having a positive charge, and (2) the strong nuclear force which is attractive between nucleons. Due to the long range nature of the Coulomb force relative to the short range nature of the strong nuclear force, as two positive nuclei first begin to approach each other the initial force experienced by the particles is the Coulomb force. However, when the distance between the two nuclei reaches the order of a nuclear radius (a few femtometers) the strong nuclear force begins to take over and eventually pulls the two nuclei together. An image of the standard fusion problem is given in **Figure 5**. Nuclear fusion occurs when particles collide in such a way so that the Coulomb repulsion force is overcome and the strong nuclear force pulls the two nuclei together to form a single new nucleus.

The ability of two particles to fuse depends on the energy and relative velocities (i.e. center of mass velocities) of the two particles colliding. Under classical mechanics the relative velocity between the two particles must be greater than the Coulomb energy (given by  $V_b$  in Figure 5) in order for fusion to occur. If this were the actual energy threshold required for fusion reactions in reality, fusion reactions would be very rare. As an example, consider the center of the sun which has an average particle temperature of approximately

1.4keV and an energy distribution that is roughly Maxwellian. Based on Figure 5, the Coulomb barrier is estimated as being on the order of 500keV (for proton/proton and deuterium/proton collisions). If only classical mechanics were at play only particles with energies substantially higher than the average 1.4keV particle energy in a Maxwellian energy distribution would be able to overcome the 500keV barrier energy. If only classical mechanics were considered fusion reactions on the sun would be very rare.



**Figure 5. Image depicting the standard fusion problem [3]. A nuclei with energy  $\epsilon$  is incident on a second nuclei. As the two nuclei approach the Coulomb repulsive force acts to push the two particles apart. Under classical mechanics, if the relative energy (center of mass energy) of the two particles is less than  $V_b$  the two particles will not fuse. However, under quantum mechanics there is a finite probability of the particles tunneling through the Coulomb barrier even though  $\epsilon$  is lower than the  $V_b$ .**

However, classical mechanics are not the only phenomena when it comes to fusion reactions. Due to quantum effects where particles exhibit wave-like properties and are represented mathematically as waves, there exists a finite probability that one particle colliding with another particle will “tunnel” through the potential barrier ( $V_b$ ) even if the relative energy between the particles ( $\epsilon$ ) is less than  $V_b$ . The derivation of this probability is somewhat involved and is provided in detail in Appendix A. The resulting probability of



one particle tunneling through the potential barrier to a second particle was originally derived by Gamow [4] and is given here as:

$$P_{Tun}(E) = \exp\left(-\sqrt{\frac{E_G}{E}}\right), \text{ where } E_G = \frac{Z_1^2 Z_2^2 q^4 m_r}{8\epsilon_0 \hbar^2} \quad (1.5)$$

where  $E$  is the center of mass energy of the particles,  $E_G$  is the Gamow energy,  $m_r$  is the reduced mass of the two particles ( $m_r = (m_1 + m_2) / (m_1 * m_2)$ ),  $m_1$  is the mass of particle 1,  $m_2$  is the mass of particle 2,  $\hbar$  is the reduced Planck's constant,  $Z_1$  is the atomic number of particle 1,  $Z_2$  is the atomic number of particle 2,  $q$  is the charge of an electron, and  $\epsilon_0$  is the permittivity of free space.

When looking at the tunneling probability given by **Equation 1.5** a few things stand out. The threshold energy required to achieve a high probability of tunneling is highly affected by the Gamow energy ( $E_G$ ). The higher the Gamow energy, the higher the center of mass energy between the particles must be for tunneling to occur. The Gamow energy itself is mainly dependent on the charge and mass of the colliding particles. The larger the atomic number, the greater the nuclear charge, the greater the Coulomb repulsion force between the particles, and the lower the probability the particles will tunnel. Even for the smallest of Coulomb repulsion force between particles, the center of mass energy required for even a small probability of tunneling can be large when compared to the ionization energy. As an example, evaluating Equation 1.4 for a collision between deuterium and tritium and for a tunneling probability of 10%, the energy required is on the order of 220keV. Since the ionization energy for hydrogen is only 13.59eV we see that fusion reactions can only occur when matter is very hot and in an ionized state.

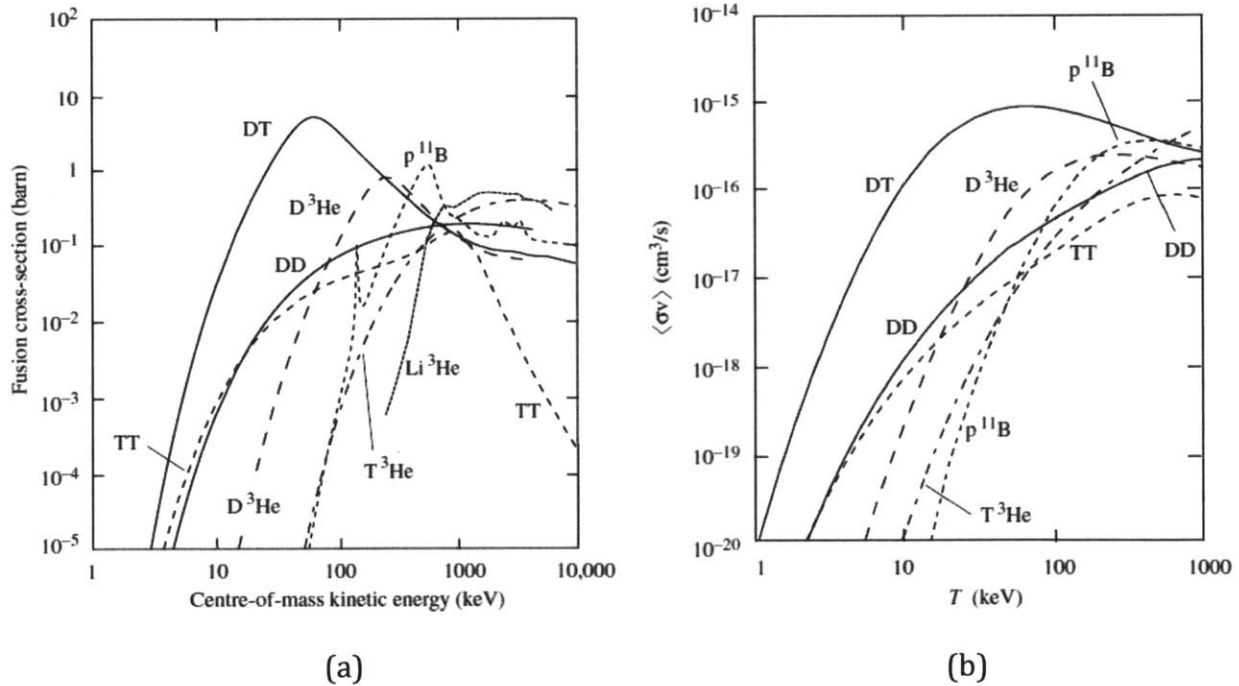
We have now looked at the problem of fusion reactions for individual colliding particles. In most applications of interest, instead of looking at single particle interactions we are dealing with systems consisting of many particle collisions. For these situations we can express the fusion reactions in terms of a fusion reaction rate that gives the number of fusion collisions in a set volume over a given period of time. The reaction rate for particles colliding at a set energy is derived in Appendix A and is given as:

$$R = n_1 n_2 \sigma v \quad (1.6)$$

where  $R$  is the fusion reaction rate ( $\text{m}^{-3}\cdot\text{s}^{-1}$ ),  $n_1$  is the density of particle species 1,  $n_2$  is the density of particle species 2,  $\sigma$  is the fusion reaction cross-section, and  $v$  is the relative velocity between particles. The fusion reaction cross-section represents an area defining where a fusion collision reaction is likely to occur and is a function of the particle's center of mass energy. The fusion cross section is derived in its entirety in Appendix A but is given below in **Equation 1.7**:

$$\sigma(E) = \frac{\pi \hbar^2}{2m_r} \cdot \frac{1}{E} \cdot \exp\left(-\sqrt{\frac{E_G}{E}}\right), \quad \text{where} \quad E_G = \frac{Z_1^2 Z_2^2 q^4 m_r}{8\epsilon_0 \hbar^2} \quad (1.7)$$

A plot of the fusion cross-sections for a variety of primary fusion reactions of interest is given in **Figure 6(a)**.



**Figure 6. (a) fusion cross sections and (b) fusion reactivities for primary light isotope fusion reactions. The fusion reactivities assume a Maxwellian velocity distribution characterized by temperature T.**

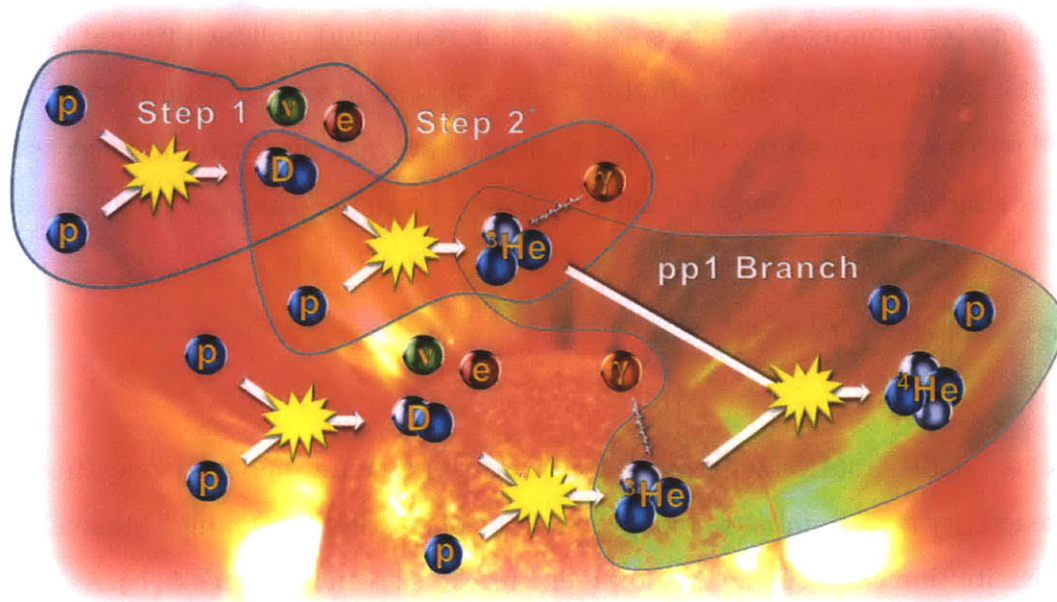
In most situations, the relative velocity between particles is not homogenous but rather is spread across a distribution of velocities. Since, as shown in Equation 1.7, the fusion reaction cross section ( $\sigma$ ) is also function of the center of mass energy (or also the velocity), the value of  $\sigma v$  (commonly referred to as the fusion reactivity) will be different for each particle velocity in the distribution. In this case, a convenient way to obtain a set reaction rate for all particles in a volume is by determining an average reactivity rate across the velocity distribution. The average fusion reactivity is given in **Equation 1.8** as:

$$\langle \sigma v \rangle = \int_0^{\infty} \sigma(v) v f(v) dv \quad (1.7)$$

where  $f(v)$  is the distribution function of the relative (i.e. center of mass) velocities . The average reactivity for a number of fusion reactions of interest, assuming a Maxwellian velocity distribution characterized by temperature  $T$ , is given in **Figure 6(b)**. As can be seen, the reaction with the highest reactivity is the D-T reaction which reaches a maximum with an average reactivity of around  $10^{-15} \text{ cm}^3\text{s}^{-1}$ . Because D-T fusion has the highest reaction rate and also produces among the highest amounts of energy per reaction (17.6 MeV) it is the primary reaction of interest for purposes of energy production.

With an understanding of the fundamentals of fusion reactions we return to the discussion on the formation of atoms and the original atomic hypothesis presented by Democritus. It is now widely accepted that the first atomic nuclei were formed shortly after the Big Bang through a chain of fusion reactions known as nucleosynthesis. In general, nucleosynthesis is the process by which new atomic nuclei are formed from preexisting nuclei and/or protons and neutrons. The first nucleosynthesis chain is known as the proton-proton or pp chain and results in the formation of  $^2\text{H}$ ,  $^3\text{He}$ , and  $^4\text{He}$  from individual protons. An illustration of the first few steps of the pp chain is given in **Figure 7**. From this chain, many other fusion reaction chains can be traced and if followed out in their entirety would eventually lead to the formation of all atomic nuclei. One of the more important chains in addition to the pp chain is the CNO chain which gives the formation of carbon (C), nitrogen (N), and oxygen (O), the most important elements for biological

organisms. A summary of the primary controlled fusion reactions of interest, the first p-p fusion cycle chain and the CNO cycle reactions are given in **Table 1**.



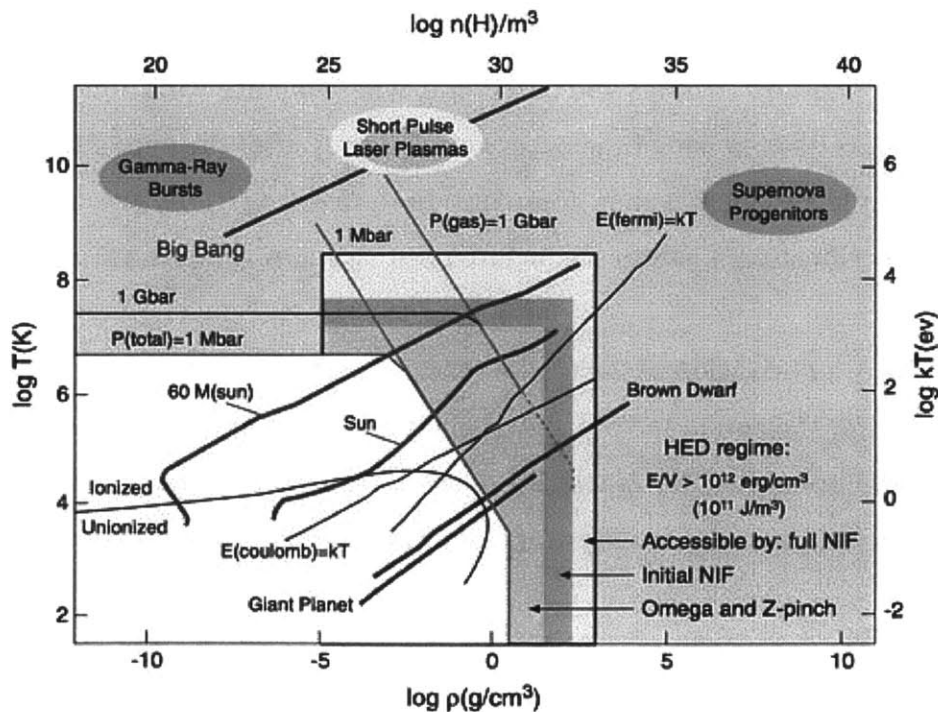
**Figure 7.** The first three steps in the proton-proton (pp) fusion chain resulting in  ${}^4\text{He}$ .

**Table 1.** Table of primary fusion reactions in the p-p and CNO.

	Q (MeV)
<i>Primary controlled fusion reactions</i>	
$\text{D} + \text{T} \rightarrow \alpha + \text{n}$	17.59
$\text{D} + \text{D} \rightarrow \text{T} + \text{p}$	4.04
$\text{D} + \text{D} \rightarrow {}^3\text{He} + \text{n}$	3.27
$\text{D} + \text{D} \rightarrow \alpha + \gamma$	23.85
$\text{T} + \text{T} \rightarrow \alpha + 2\text{n}$	11.33
<i>The p-p cycle</i>	
$\text{p} + \text{p} \rightarrow \text{D} + \text{e}^+ + \nu$	1.44
$\text{D} + \text{p} \rightarrow {}^3\text{He} + \gamma$	5.49
${}^3\text{He} + {}^3\text{He} \rightarrow \alpha + 2\text{p}$	12.86
<i>The CNO Cycle</i>	
$\text{p} + {}^{12}\text{C} \rightarrow {}^{13}\text{N} + \gamma$	1.94
${}^{13}\text{N} \rightarrow {}^{13}\text{C} + \text{e}^+ + \nu + \gamma$	2.22
$\text{p} + {}^{13}\text{C} \rightarrow {}^{14}\text{N} + \gamma$	7.55
$\text{p} + {}^{14}\text{N} \rightarrow {}^{15}\text{O} + \gamma$	7.29
${}^{15}\text{O} \rightarrow {}^{15}\text{N} + \text{e}^+ + \nu + \gamma$	2.76
$\text{p} + {}^{15}\text{N} \rightarrow {}^{12}\text{C} + \alpha$	4.97

## 1.2 High Energy Density Physics

The interstellar environments in which many natural nuclear reactions and nucleosynthesis occur are characterized by very high particle energies at high densities. Physical systems in this regime with an energy density (product of density and temperature) greater than around  $10^5 \text{ J/cm}^3$  are in the regime of high energy density physics (HEDP). Many HEDP regimes of interest occur naturally in solar and gas-giant cores, supernovae, neutron stars, and black holes. It was not, however, until the mid-1900s that experimental facilities existed to probe environments in HEDP in a laboratory setting. Many of the first experiments to cross into this regime used particle accelerators, similar to the first one developed by Cockcroft and Walton, to focus and collimate particle beams on stationary targets [5]. The advent of the laser in the 1960's opened the possibility of using high powered lasers to create HEDP environments in the lab[6]. Since being introduced, high powered lasers in the terawatt and petawatt range have been developed as an additional platform for creating HEDP environments in the lab. One of the primary platforms for conducting HEDP research that has emerged since the 1950s is inertial confinement fusion [7]. Many HEDP regimes of interest are given in **Figure 8**.



**Figure 8. Natural and man-made regimes in high-energy-density physics.**

### 1.3 Thesis Outline

The primary focus of this thesis is to present work conducted aimed at reducing the uncertainty in DDp and DDn yield measurements in inertial confinement fusion (ICF) experiments on the OMEGA laser. In addition, some additional work in support of nuclear diagnostic development conducted on behalf of the High Energy Density Physics group at the MIT Plasma Science and Fusion Center is also given in the appendices.

In Chapter 2 a brief history and overview of the contemporary inertial confinement fusion program with primary motivations for the research as well as a brief overview of inertial confinement fusion physics is given. For a complete treatment on ICF physics see Atzeni *et al.* [3]. Chapter 3 presents the background and history behind the DDn yield measurement on the OMEGA laser and the many interconnected efforts that went into establishing the current absolute yield calibration factor for the OMEGA nTOF detector system. These efforts include a series of cross calibrations between accelerator DDp measurements, indium activation systems on the NOVA<sup>1</sup> laser and OMEGA, and cross calibration between NOVA and OMEGA nTOF systems. In Chapter 4 an improved method for measuring the DDp yield on OMEGA using CR-39 range filter (RF) modules is presented from which the DDn yield can be inferred. The data obtained suggest a relationship between particle flux anisotropies and bang time, where fluence variation is observed to be significantly reduced when bang time occurs significantly after the end of the laser pulse. The CR-39 DDn inferred yield is then compared to the existing nTOF DDn absolute yield calibration for verification. Chapter 5 concludes with a summary of the findings and ideas for next steps.

In Appendix A, a derivation of the fusion reaction rate from first principles is presented as a supplement for the equations presented in Chapter 1. In Appendix B, work done to install a Faraday Cup on the MIT Linear Electrostatic Ion Accelerator (LEIA) is presented as well as beam current readings to determine optimal electron suppression bias source

---

<sup>1</sup> A high power laser for ICF at Lawrence Livermore National Laboratory that was decommissioned in 1999.

settings. In Appendix C, a project is presented that was conducted to establish a way to unequivocally and consistently verify the slit width on Charged Particle Spectrometers (CPS) on OMEGA. Appendix D presents work that was used to increase the dynamic range of CR-39 detectors by stage etching high-fluence range filter detectors fielded on OMEGA. Finally, in Appendix E the raw data from the OMEGA campaigns used for low uncertainty DDn absolute yield measurements for nTOF calibration is presented in its entirety.





## 2 Inertial Confinement Fusion

Inertial confinement fusion (ICF) is an approach by which fusion occurs in a laboratory setting by using the inertia of a hot dense plasma to confine the plasma long enough for a significant amount of fuel to undergo nuclear fusion and release energy. The concept was first envisioned in the late 1950's after the successful development of the hydrogen bomb. At that time Edward Teller, the "father of the hydrogen bomb" and co-founder of Lawrence Livermore National Laboratory, called for the exploration of nuclear fusion for peaceful purposes. Some of the original ideas included the use of hydrogen bombs for excavation and mining, constructing dams and canals, and energy. Early ideas for the use of fusion for energy included detonating hydrogen bombs in water-filled underground caverns deep in the earth to generate steam from which electricity would be generated, and using small non-nuclear micro-implosions to drive a shock wave into the fusion fuel. The idea of micro-implosion induced shock waves compressing and igniting the fusion fuel led to the concept of a tiny droplet of fuel being heated and burned using an external driver as a heating source.

### 2.1 Contemporary Motivation for Inertial Confinement Fusion Research

After the initial success of the Manhattan Project in producing the first fission bombs, and the subsequent success of the first fusion bombs, the U.S. continued an extensive nuclear weapons testing program for the purposes of: (1) gaining a better understanding of weapon physics, (2) testing the effectiveness of different weapon designs, (3) understanding the effects of weapons and nuclear fallout on organisms and the environment, and (4) exploring the peaceful use of nuclear explosions. From the first nuclear test at the Trinity site at Alamogordo, New Mexico in 1945 to the last U.S. nuclear test at the Nevada Test Site in 1992, the United States conducted 1054 nuclear tests including both underground and atmospheric testing. Most of these tests were conducted at the Nevada Test Site (pictured below in **Figure 9**) and the Pacific Proving Grounds in the Marshall Islands.

Throughout the period of weapons testing, multiple attempts had been made to limit or ban nuclear tests. The first step toward a comprehensive ban on nuclear weapons testing occurred in 1963 through the Partial Test Ban Treaty that banned nuclear tests underwater and in the atmosphere but not underground. In 1968, the Nuclear Non-proliferation Treaty was passed that prohibited previously non-nuclear states from acquiring nuclear weapons capabilities. Little additional progress in banning nuclear testing was made until the end of the Cold War. In 1993, negotiations for a comprehensive nuclear test ban treaty began in the United Nations General Assembly. In 1996 the Comprehensive Test Ban Treaty was adopted by the United Nations and has now been signed and ratified by 159 states. Despite ratification of the treaty by peer nuclear powers such as Russia, France, and the United Kingdom, the U.S. has yet to ratify the treaty although a moratorium on all nuclear weapons testing has essentially been in effect since 1992.



**Figure 9. Aerial views taken of the Nevada test site. Both images depict craters left from underground tests.**

Many arguments have been made in opposition to the U.S. ratifying the Comprehensive Test Ban Treaty. One argument holds that by ratifying the treaty, the U.S. would lose its ability to make continued advancements in weapons science and to gain fundamental understanding of material properties under nuclear detonations. Another argument is that in order to ensure the continued reliability of the nuclear stockpile, periodic testing of weapons is needed to verify that weapons in the nuclear arsenal are still functional and will remain a strong deterrent. This is important since no new weapons are currently being

developed and aging weapons have the potential to fail or prove unreliable in a number of ways.

To the end of providing an alternative to weapons testing and to continue advanced weapons science and maintain the reliability of the nation’s nuclear deterrent, inertial confinement fusion has been promoted and funded as a platform for continuing weapons research without the need of detonating weapons. The goal is that eventually the underlying physics will be well enough understood and benchmarked to experimental data gained from ICF experiments so that “virtual” testing using advanced codes run on supercomputers will be able to eliminate the need for physical nuclear tests altogether. This goal of obtaining virtual testing and simulations as a perfect substitute for physical testing has motivated the U.S. government through the National Nuclear Security Administration of the U.S. Department of Energy under the Stockpile Stewardship program to invest significantly in both supercomputers capable of running advanced plasma codes as well as facilities used to experimentally benchmark key code parameters. As part of this effort, four of the top ten supercomputers in the world are owned and operated by the U.S. Department of Energy including the Titan Supercomputer at Oak Ridge National Laboratory (given in **Figure 10**), which as of June 2013, was the second fastest super computer in the world. A list of the top U.S. Department of Energy supercomputers is given in **Table 2** along with the number of cores and fastest recorded floating point operations (Flops) per second.

**Table 2. U.S. Department of Energy supercomputers as of June 2013.**

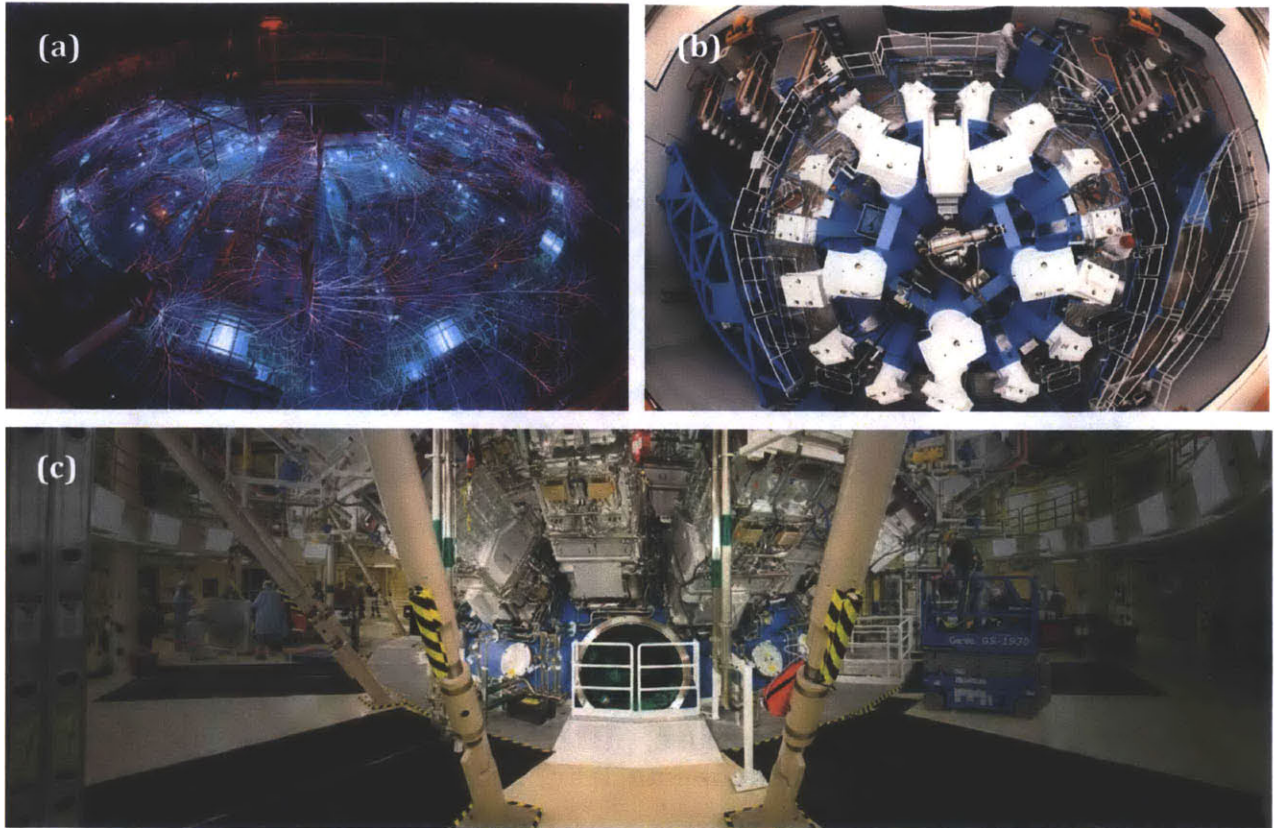
<b>Rank</b>	<b>Site</b>	<b>System</b>	<b>Cores</b>	<b>TFlops/s</b>
2	Oak Ridge National Laboratory	Titan—Cray	560640	17590
3	Lawrence Livermore National Laboratory	Sequoia	1572864	17173.2
5	Argonne National Laboratory	Mira—BlueGene	786432	8586.6
8	Lawrence Livermore National Laboratory	Vulcan—BlueGene	393216	4293.3
22	Los Alamos National Laboratory	Cielo—Cray	142272	1110.0
34	Lawrence Livermore National Laboratory	Zin	46208	773.7
61	Sandia National Laboratories	Red Sky	42440	433.5



**Figure 10. The Titan supercomputer at Oak Ridge National Laboratory.**

In addition to the impressive supercomputing infrastructure that has been built in support of the DOE NNSA Stockpile Stewardship's program to create the capabilities to perform "virtual" nuclear tests, major experimental facilities have been built with the goal of using experimental data from ICF, equation of state, and materials tests, to benchmark computer codes. The primary DOE laboratories supporting this effort are Los Alamos National Laboratory, Lawrence Livermore National Laboratory, and Sandia National Laboratories. Major experiments at these labs include the Z-Machine at Sandia National Laboratory which is used for z-pinch driven inertial confinement fusion and material equation of state experiments [8], the National Ignition Facility at Lawrence Livermore National Laboratory which aims at achieving a thermonuclear burn using laser indirectly-driven ICF [9], and the OMEGA laser at the Laboratory for Laser Energetics (LLE) at the University of Rochester which acts as a small laser ICF test-bed [10]. Images of these research facilities are given in **Figure 10**.

In addition to stockpile stewardship, other contemporary interests and motivations for ICF research include energy and basic research in HEDP such as atomic physics, nuclear physics, plasma physics, astrophysics, material science, and laser science. Many of these additional interests are addressed through user programs at the major research facilities where academic and government collaborators work to further understanding of basic science. That said, stockpile stewardship remains the primary policy goal of the program, has a dominant share of shot time at experimental facilities, and remains the justification for the significant amount of federal funding ICF receives [11].

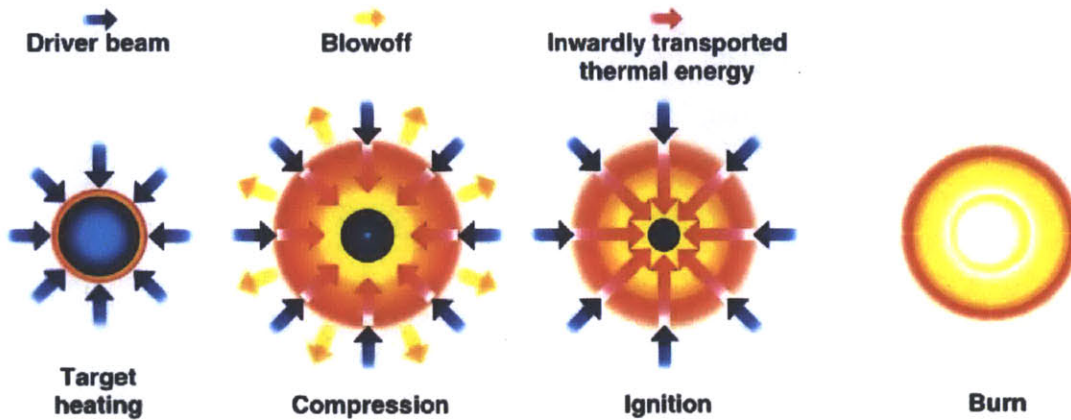


**Figure 11. Major research facilities that are part of the National Nuclear Security Administration's Stockpile Stewardship program: (a) the Z-Machine pulsed power facility at Sandia National Laboratories, (b) the OMEGA laser at the Laboratory for Laser Energetics, (c) the National Ignition Facility at Lawrence Livermore National Laboratory.**

## 2.2 The Physics of Inertial Confinement Fusion

Laser driven inertial confinement fusion is the process of creating a fusion burn by imploding a small capsule of fuel and then confining fuel particles by their own inertia long enough for a significant portion of the fuel to burn. The process for directly driven ICF can be summarized in four steps as given in **Figure 12**. First, a driver beam (either directly driven by the laser or indirectly driven with laser generated x-rays) incident on the capsule shell heats the capsule. After sufficient heating, the capsule ablates with half the shell material blowing off while the other half drives the fuel toward the center of the capsule compressing and heating the fuel in the process. Eventually the imploding material stagnates in the center and the kinetic energy of the fuel drive is converted into internal

energy. In the center of the compressed fuel, a hot spot develops that ignites the fuel and initializes a thermonuclear burn that then propagates outward through the rest of the fuel.



**Figure 12. Basic principles of inertial confinement fusion: (a) a driver beam heats the capsule surrounding a small pellet of fuel, (b) the fuel is compressed and a hot spot forms in the center, (c) the fuel stagnates and temperatures and densities are sufficient for thermonuclear burn, (d) alpha particles emitted from the hot spot heat the remaining fuel and the nuclear burn propagates through the fuel.**

The thermonuclear burn in an ICF implosion occurs when the internal heating of the fusion products exceeds all energy losses so that no additional external energy from the laser drive is needed to keep the plasma in a burning state. The primary irreducible energy loss in a fusion plasma is due to Bremsstrahlung radiation where electromagnetic radiation is produced by the deflection and change of momentum of fuel particles. The power loss due to Bremsstrahlung expressed as a power density loss ( $\text{W}\cdot\text{cm}^{-3}$ ) is given by **Equation 2.1**.

$$W_b = C_b Z_{\text{eff}} n_e^2 T^{1/2} \quad (2.1)$$

where  $W_b$  is the power density loss due to Bremsstrahlung,  $C_b$  is a constant equal to  $5.35 \times 10^{-37}$ ,  $Z_{\text{eff}}$  is the average atomic number of particles in the plasma,  $n_e$  is the electron density of the plasma, and  $T$  is the plasma temperature given in keV (assuming electrons and ion temperatures are the same). Internal heating of the plasma comes from particle collisions resulting in fusion reactions as was developed previously in Section 1.1. The power density due to fusion reactions is given by multiplying the volumetric reaction rate times the energy released per reaction. This gives a fusion power density (in  $\text{W}\cdot\text{m}^{-3}$ ) of:

$$W_{12} = n_1 n_2 \langle \sigma v \rangle Q_{12} \quad (2.2)$$

where  $W_{12}$  is the power density due to the fusion reactions between particle species 1 and particle species 2,  $n_1$  is the density of species 1,  $n_2$  is the density of species 2,  $\langle \sigma v \rangle$  is the velocity averaged fusion reactivity between particles 1 and 2, and  $Q_{12}$  is the energy released for the charged particle fusion reactions. The governing power density equation for the plasma is then given by:

$$\frac{dW}{dt} = W_{12} - W_b - \frac{W}{\tau_E} \quad (2.3)$$

where  $W$  is the energy density of the plasma and  $\tau_E$  is energy loss rate.

Under the plasma power density equation (**Equation 2.3**), power breakeven occurs when  $dW/dt=0$ . Assuming a 50/50 deuterium-tritium fuel mix where the electrons and ions have the same temperature and substituting 2.1 and 2.2 into 2.3, the energy breakeven or ignition condition (also commonly known as the Lawson criteria) for a DT plasma is given as:

$$n_e \tau_E = \left[ \frac{\langle \sigma v \rangle Q_c}{12T} - \frac{C_b Z_{eff}}{3T^{1/2}} \right]^{-1} \quad (2.4)$$

Recall that DT fusion reactions are of particular interest since the DT fusion cross section is the highest for all fusion reactions. For magnetically confined plasmas,  $\tau_E$  is the average loss time for heat to be transported out of the plasma by diffusion or other mechanisms. For inertial confinement fusion the duration of the fusion reaction is often interpreted as the time that the plasma stays confined by the particle's mass inertial before flying apart. This is different than the energy loss rate  $\tau_E$ . To distinguish between the two we introduce  $\tau_c$  as the ICF plasma confinement time.

After the fusion fuel stagnates at the center of the implosion it begins to expand sonically traveling at the isothermal sound velocity given by Equation 2.5:

$$c_s = \sqrt{\frac{T_e + 3T_i}{m_f}} \quad (2.5)$$

where  $T_e$  is the electron temperature,  $T_i$  is the ion temperature, and  $m_f$  is the average mass of the ions (for a DT plasma this is  $2.5 m_p$ , where  $m_p$  is the mass of a proton). A reasonable estimate of the plasma confinement time is determined by the ratio of the implosion radius ( $R_f$ ) to the ion sound speed. This relation is given in **Equation 2.6**.

$$\tau_c = \frac{R_f}{c_s} \quad (2.6)$$

Multiplying Equation 2.6 by the electron density and then recognizing the mass density as  $\rho = n \cdot m$  gives the following expression.

$$n_e \tau_c = \frac{\rho}{m} \frac{R}{c_s} = \frac{1}{m c_s} \rho R \quad (2.7)$$

Additionally, it can be shown that the fraction of the fuel that undergoes nuclear reactions (or burn fraction) is related to the plasma confinement time ( $\tau_c$ ) and the energy loss rate ( $\tau_E$ ) by **Equation 2.8**:

$$f_r = \frac{\tau_c}{\tau_c + \tau_E} \quad (2.8)$$

where  $f_r$  is the burn fraction. Solving Equation 2.8 for  $\tau_c$  and then substituting the result back into Equation 2.7 results in:

$$n_e \tau_E = \frac{1}{m c_s} \left( \frac{1 - f_r}{f_r} \right) \rho R \quad (2.9)$$

For ICF researchers, the result of **Equation 2.9** is very useful. When the burn fraction and areal density of an ICF capsule implosion are known, Equation 2.7 can be interpreted



as a Lawson-type criteria of the ignition requirement for ICF. In addition, the expression of the ignition requirement in terms of the quantity  $\rho R$  is particularly useful since  $\rho R$  can be physically interpreted as the plasma mass density integrated over the capsule radius or areal density.

$$\rho R = \int_0^R \rho(r) dr \quad (2.10)$$

The areal density can be interpreted as the amount of material that an energetic particle passes through while escaping the plasma sphere. Many diagnostics (such as neutron time-of-flight detectors [12] and the Magnetic Recoil Spectrometer [13]) have been developed to probe  $\rho R$  by measuring the energy downshift of fusion particles (neutrons and alpha's) that occurs when the particles pass through the plasma. In addition, the burn fraction can be determined by measuring the absolute fusion yield of the implosion. From measurements of the areal density ( $\rho R$ ), ion temperatures, and the overall fusion yield, progress towards ignition criteria can be determined.

An alternative and more rigorous ignition criteria for ICF implosions that is currently used to gauge progress toward thermonuclear ignition on the National Ignition Facility is the Ignition Threshold Factor (ITFX). This Lawson-type ignition criteria is much more rigorous than the simple derivation given above and is benchmarked to simulations to account for implosion velocities, hot spot shape, entropy of the compressed fuel, and the adiabat of the compressed fuel [14]. A plot depicting progress towards thermonuclear ignition for a number of cryogenic shots as part of the National Ignition Campaign on the National Ignition Facility is given in **Figure 13**. Here the layered target ITFX (curved lines on the graph) is given as a function of the measured down scattered neutron ratio (which is proportional to the areal density), and the DT yield. As can be seen, progress towards ignition on the NIF has been significant during the Ignition Campaign going from an ITFX of 0.001 in September 2010 to 0.10 in March 2012.

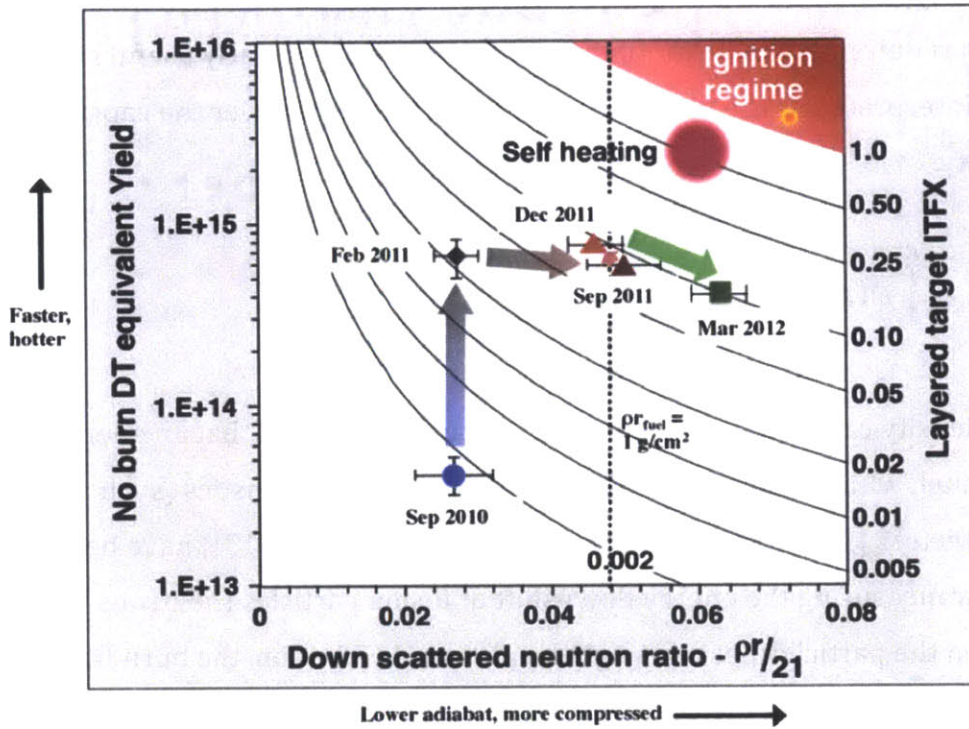
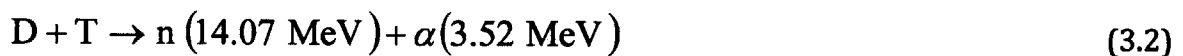


Figure 13. Progress towards ignition during the National Ignition Campaign measured using the ITXF ratio which is a function of yield and areal density. An ITXF of 1 corresponds to ignition.

### 3 Previous DDn Yield Measurements and nTOF Calibration Methods

As mentioned above, in addition to areal density, the fuel burn fraction is also a key measurement in determining the performance of an ICF implosion and this is determined from measurements of the absolute fusion yield. Accurate absolute yield measurements are therefore vital to determining ICF capsule performance and overall progress toward the ignition criteria. As can be seen from Table 1, many fusion reactions of interest from controlled fusion experiments result in charged particles such as protons, tritons,  $^3\text{He}$  and alphas but also produce neutrons. Neutron time-of-flight (nTOF) current-mode detectors fielded on large inertial confinement fusion (ICF) facilities, such as OMEGA [10], the National Ignition Facility [9], and which will be fielded on Laser Megajoule (LMJ) upon completion [15, 16], are principle diagnostics that regularly measure key properties of neutrons produced from ICF implosions. Time-of flight refers to the time it takes neutrons to travel from the target chamber center to the nTOF detector and is can be used to infer particle energies and the overall neutron energy spectrum. On ICF facilities implosion neutrons are generally generated from the primary fusion reactions of deuterium (DD), or a deuterium/tritium fuel mix (DT) as given in **Equation 3.1** and **Equation 3.2**.



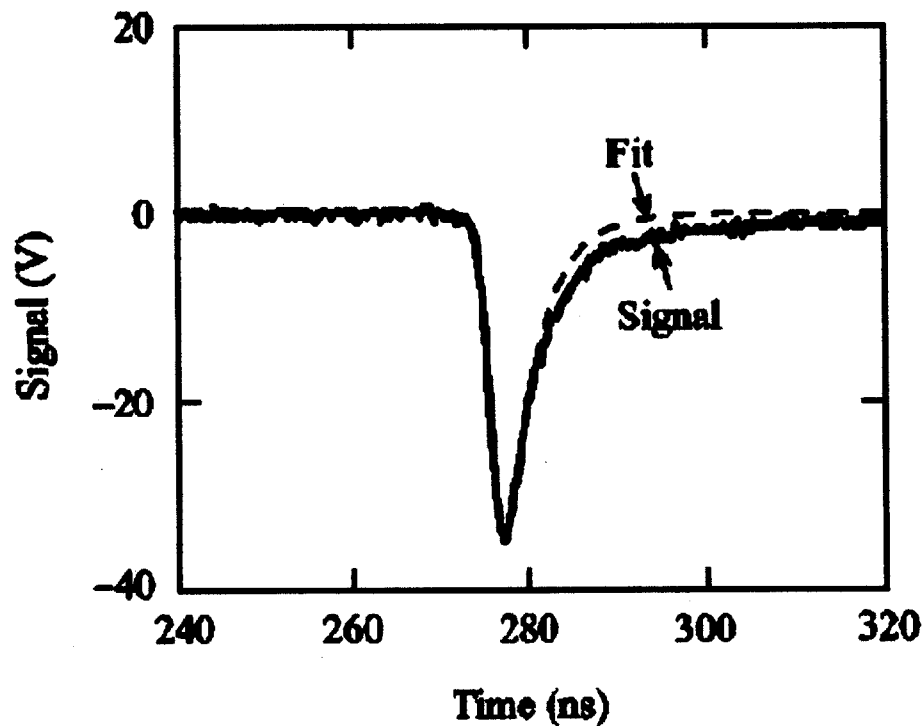
The principles of nTOF operation are straightforward. Neutrons incident on a scintillator generate photons which are then optically coupled to a photomultiplier tube (PMT) or photo diode (PD). More recently, nTOF detectors using chemical vapor deposition (CVD) diamonds have been developed that directly measure the neutron response without use of a scintillator [17].

nTOF detectors are used to diagnose: (1) the absolute neutron yield by time integrating the neutron response [18], (2) fuel burn-average ion temperatures by fitting the signal to a response function and then using the Brysk formula [19-24], (3) the peak neutron emission time relative to the start of the laser pulse—also commonly referred to as shot bang-time

[25], and more recently (4) the areal density ( $\rho R$ ) in cryogenic DT implosions on OMEGA and the NIF [26]. Because the neutron response is a linear function of the number of incident neutrons as long as the detector does not saturate, measurement of the absolute neutron yield only requires a detector-specific calibration coefficient ( $C_{nTOF}$  [ $n \cdot mV^{-1} \cdot ns^{-1}$ ]) to relate the integrated nTOF signal ( $S_{nTOF}$  [ $mV \cdot ns$ ]) to the neutron response as given in **Equation 3.3**.

$$Y_n = S_{nTOF} \cdot C_{nTOF} \quad (3.3)$$

A sample of a typical nTOF pulse is given in **Figure 14**. Since the detector neutron response varies with the neutron energy, separate calibration coefficients must be obtained to characterize the different responses for DT (14.07 MeV) and DD (0.82 MeV) neutrons.



**Figure 14.** A sample nTOF response with the raw single passed through an inverting amplifier and fit using the method outlined in [27, 28]. An absolute neutron yield for DD and DT neutrons is obtained by time integrating the signal ( $S_{nTOF}$ ) and then multiplying by a detector-specific calibration coefficient ( $C_{nTOF}$ ). (Figure as given in [29]).

Historically, detector-specific nTOF calibration coefficients were obtained by either (1) cross-calibration to a previously calibrated nTOF, or (2) cross-calibration to Copper (Cu) or indium (In) activation samples for DT and DD neutrons respectively [30]. In the second approach, Cu and In slugs were activated by incident neutrons from DT and DD neutrons. After activation the resulting Cu and In radioisotopes would decay back to stable isotopes emitting gamma rays in the process. The calibration coefficients for the gamma ray spectrometers used to measure gammas emitted from Cu and In-activation were obtained separately from accelerator produced DD and DT fusion products by measuring the charged particle counts associated with those reactions. For Cu-activation, this was done by measuring the 3.52 MeV alpha yield from the reaction given in Equation 3.2. For In-activation, this was done by measuring the proton yield from the other DD reaction branch, given in **Equation 3.4**, and then using the corresponding branching ratio to infer an equivalent neutron yield [30].



In the next two chapters, a method for obtaining detector-specific DD neutron (DDn) nTOF calibration coefficients through an *in situ* measurement of DD protons (DDp) produced during OMEGA ICF implosions is presented. The method involves calibrating the integrated nTOF neutron response ( $S_{nTOF}$ ) to DDp measurements obtained using CR-39 nuclear track range filter (RF) modules [31]. An advantage of using CR-39 is that it has 100% particle detection when operating in optimal detection regimes and does not need to be calibrated. An equivalent DDn yield ( $Y_{DDn}$ ) is inferred from the DDp RF yield ( $Y_{DDp}$ ) using the  $Y_{DDn}/Y_{DDp}$  branching ratio which at ion temperatures common in laser driven ICF experiments is close to unity. This approach for obtaining an nTOF absolute yield calibration has the advantage over previous calibration methods in that: (1) it reduces the dependence on what had been a series of multiple cross-calibrations between accelerators, In-activation systems, and other nTOF detectors, and (2) it takes advantage of the fact that CR-39 has 100% detection efficiency. By directly calibrating the nTOF response to a DDn inferred yield from DDp using CR-39 RF modules, the uncertainty in the calibration coefficient can be well quantified.

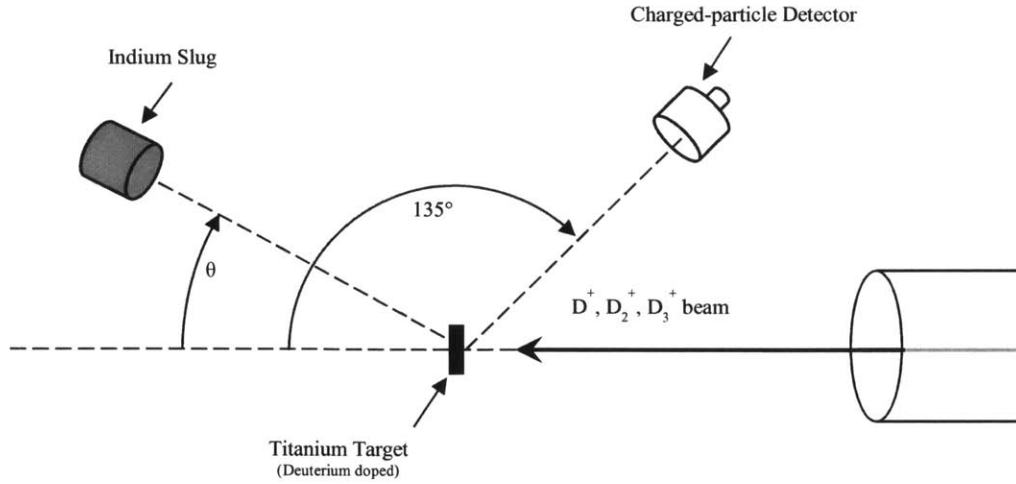
As has been mentioned, the history of the DDn absolute yield calibration of the OMEGA nTOF system follows a series of cross-calibrations between accelerators, In-activation systems, and other nTOF detectors. In 1988, 1990, and 1993, an In-activation system at Lawrence Livermore National Laboratory (LLNL) was calibrated using DDn and DDp fusion products generated from an ion accelerator. At the time, In-activation was the primary neutron yield diagnostic on NOVA<sup>2</sup>. nTOF detectors developed for NOVA were then cross-calibrated to the LLNL In-activation system. In 1997, the OMEGA In-activation system was cross-calibrated to the NOVA 10m nTOF detector that had been ported to LLE from LLNL. OMEGA nTOF detectors were then cross-calibrated to the OMEGA In-activation system over a series of calibration shots. Each of the developments in the series of cross-calibrations leading to the current OMEGA nTOF absolute yield calibration are now discussed individually.

### 3.1 The Indium Activation Method

The In-activation method is based on the  $^{115}\text{In}(n,n')^{115}\text{In}^*$  reaction where an inelastic collision between an energetic neutron and  $^{115}\text{In}$  produces  $^{115}\text{In}^*$  in an isomeric state ( $T_{1/2}=4.48\text{h}$ ) which then emits a 336.2 keV gamma ray while decaying back to  $^{115}\text{In}$ . On the NOVA laser at LLNL, In-activation calibration coefficients were obtained in 1988, 1990, and 1993 by activating ~4cm long by ~1cm diameter 30g In slugs on a Cockcroft-Walton linear electrostatic ion accelerator. DDn and DDp fusion products from the reactions given in Equation. 3.1 and Equation. 3.4 respectively were generated by running a deuterium beam into a deuterium doped titanium target as shown in **Figure 15**. After activation, the In slugs were placed in gamma ray spectrometers—a sodium iodide (NaI) spectrometer was used for the 1993 calibration and a high-purity germanium spectrometer (HPGe) was used for the 1988 and 1990 calibrations—where the gamma ray spectrum and gamma count ( $N_{\gamma,\text{Cnt}}$ ) were obtained over a fixed time interval ( $\tau_c$ ).

---

<sup>2</sup> ICF facility at Lawrence Livermore National Laboratory that was decommissioned in 1999.



**Figure 15. LLNL linear electrostatic ion accelerator setup for In-activation gamma spectrometer calibration. D+ ions incident on a deuterium doped titanium target generate DDn and DDp. The DDn yield ( $Y_{DDn}$ ) is inferred from the  $Y_{DDn}/Y_{DDp}$  branching ratio where  $Y_{DDp}$  is obtained using a charged particle detector. The gamma ray spectrometer calibration coefficient is obtained from  $Y_{DDn}$  and the total gamma count of the In slug ( $N_{\gamma,Tot}$ ) using Equation 3.5.**

The inferred total gamma activation ( $N_{\gamma,Tot}$ ) of an In slug sample using the gamma spectrometer is determined by **Equation 3.5**.

$$N_{\gamma,Tot} = \frac{N_{\gamma,Cnt}}{e^{-\tau_d/T_{1/2}} (1 - e^{-\tau_c/T_{1/2}})} \quad (3.5)$$

where  $\tau_d$  is the delay time between when the In slug is extracted from the accelerator and placed in the gamma spectrometer, and  $T_{1/2}$  is the  $^{115}\text{In}^*$  half-life (4.48h).  $N_{\gamma,Tot}$  is then related to the  $Y_{DDn}$  by the relation given in **Equation 3.6**.

$$Y_{DDn} = \frac{4\pi r^2 N_{\gamma,Tot} A_{In}}{\sigma f \epsilon N_a a_{115} m} \quad (3.6)$$

where  $r$  is the distance from the target to the In slug,  $\sigma$  is the  $^{115}\text{In}(n,n')^{115}\text{In}^*$  cross-section,  $f$  is the  $^{115}\text{In}(n,n')^{115}\text{In}^*$  branching ratio,  $\epsilon$  is the efficiency of the gamma ray detector,  $N_A$  is

Avogadro's number,  $A_{In}$  is the atomic weight of indium,  $a_{115}$  is the isotopic abundance of  $^{115}In$  in the slug, and  $m$  is the mass of the slug. The calibration coefficient ( $C_{In}$ ) for the gamma spectrometer response to the  $^{115}In^*$  gammas is then given by **Equation 3.7**.

$$C_{In} = \frac{4\pi A_{In}}{\sigma f \epsilon N_a a_{115}} = \frac{Y_{DDn}}{N_{\gamma, Tot}} \frac{m}{r^2} \quad (3.7)$$

In the LLNL accelerator calibration,  $Y_{DDn}$  was then inferred from the  $Y_{DDp}$  measurement obtained from a charged particle detector by multiplying  $Y_{DDp}$  by the  $DDn/DDp$  branching ratio ( $\beta_{np}$ ). In determining the branching ratio, the kinematics of the experimental setup (such as the angle of the detector and the angle of the In slug relative to the deuterium beam) were taken into account. In sum, by inferring a  $Y_{DDn}$  yield on the accelerator from the  $Y_{DDp}$  measurement, the gamma spectrometer calibration coefficient was obtained so that future  $Y_{DDn}$  yields could be inferred from the  $^{115}In^*$  gamma count.

For the NOVA In-activation calibrations,  $C_{In}$  was determined by averaging calibration coefficients obtained from measured values of  $Y_{DDn}$  and  $N_{\gamma, Tot}$  over multiple accelerator runs which varied the In slug distances from the titanium target ( $r$ ), and the angle of the In slug with respect to the beam line ( $\theta$ ). The angle of the charged particle detector was set at  $135^\circ$  while the angle of the In slug ( $\theta$ ) was fielded at multiple angles between  $-135^\circ$  and  $45^\circ$  (see Figure 15). By averaging over multiple accelerator runs and accounting for the kinematics of scattered  $DDp$  in the target chamber, a 1993 In-activation gamma spectrometer calibration coefficient ( $C_{In}$ ) of 39,200 was obtained for the LLNL NaI gamma spectrometer, while a 1988 calibration coefficient of 104,400 was obtained for the high-purity germanium (HPGe) spectrometer. Since  $C_{In}$  is inversely proportional to the gamma ray detector efficiency ( $\epsilon$ ) as given by Equation 3.7, one can see that gamma spectrometer calibration coefficients are spectrometer specific and will vary among individual gamma spectrometers as the efficiency of each spectrometer varies. Because of this the calibration coefficient of the gamma spectrometers must be determined experimentally.



### 3.2 NOVA In/nTOF Cross-calibration

With calibration coefficients determined for the NaI and HPGe gamma spectrometers, the NOVA  $Y_{DDn}$  nTOF response was later cross-calibrated to In-activation samples fielded on a series of NOVA ICF implosions. At the time, the NOVA nTOF system consisted of four nTOF detectors—50cm nTOF, 2m nTOF, 10m nTOF, and 20m nTOF—located at 62cm, 1.9m, 8.36m, and 18.33m from the NOVA target chamber center respectively. For the cross-calibrations, only the 2m nTOF was directly calibrated against neutron yields obtained from In-activation. With a time-integrated signal ( $S_{nTOF}$ ) for 10m nTOF, and  $Y_{DDn}$  determined using In-activation, the 10m nTOF calibration coefficient  $C_{nTOF}$  was found using Equation 3.3. 50 cm nTOF and 10m nTOF were then cross-calibrated against 2m nTOF, and in subsequent shots, 20m nTOF was calibrated against 10m nTOF. A summary of the NOVA nTOF specifications and calibration information is given in **Table 3**.

**Table 3. nTOFs comprising the NOVA nTOF system in the 1990s along with their corresponding distance to target chamber center (TCC), the method used for cross-calibration, and the resulting detector-specific calibration coefficient ( $C_{nTOF}$ ).**

nTOF Detector	Distance to TCC	Cross-calibrated to	$C_{nTOF}$ [ $n \cdot mV^{-1} \cdot ns^{-1}$ ]
50cm	0.62m	2m nTOF	$1.92 \times 10^3$
2m	1.92m	In-activation	$3.92 \times 10^4$
10m	8.36m	2m nTOF	$6.94 \times 10^5$
20m	18.33m	10m nTOF	$3.24 \times 10^6$

### 3.3 OMEGA In/NOVA nTOF Cross-calibration

In 1996, methods were explored to calibrate an In-activation system using a HPGe gamma ray spectrometer for the OMEGA 60 laser that at that time had recently been upgraded from OMEGA 24. The initial calibration approach was similar to that used to calibrate the

In-activation system on NOVA previously. A 2MeV Van DeGraff accelerator at SUNY Geneseo<sup>3</sup> resulted in a calibration coefficient for the OMEGA HPGe gamma spectrometer of  $7.35 \times 10^6$ . However, additional accelerator runs at SUNY Geneseo performed early in 1997 resulted in a calibration coefficient of  $5.92 \times 10^5$ , over an order of magnitude lower than the coefficient previously obtained. To address the discrepancy, other calibration techniques were utilized including direct calculation of the gamma spectrometer calibration coefficient from first principles (which resulted in a coefficient of  $1.7 \times 10^7$ ), and using a multi-line gamma source to characterize the HPGe efficiency (which resulted in a coefficient of  $8.93 \times 10^5$ ). Overall these early attempts at calibrating the OMEGA In-activation gamma spectrometer resulted in large discrepancies in the calibration coefficients obtained and the associated uncertainty regarding what the actual value of the coefficient should be.

In a final attempt to resolve the calibration discrepancy, the 10m nTOF from NOVA was ported to and fielded on OMEGA where a calibration coefficient of  $2.20 \times 10^6$  was obtained (3.3 times smaller than the first calibration coefficient obtained at SUNY Geneseo). As the NOVA 10m nTOF had originally been calibrated to an In-activation system where consistent results had been obtained over a wide range of accelerator runs and with two different kinds of gamma spectrometers (both the In and HPGe), the final OMEGA In-activation system In-activation gamma spectrometer calibration coefficient used was the one obtained through the cross-calibration to the ported NOVA 10m nTOF.

### 3.4 OMEGA nTOF/CR-39 Neutron Verification

In 2000, CR-39 nuclear track detectors were characterized to directly measure absolute neutron yields in DD and DT implosions on OMEGA [32]. CR-39 is regularly used to measure charged particle yields in the low energy range ( $\sim$ MeV) as charged particles leave a trail of damage in the plastic in the form of broke molecular chins and free radicals. Through post-shot etching of CR-39 in a sodium hydroxide solution (NaOH), damage trails are enlarged to become conical pits or tracks that are readily identified under

---

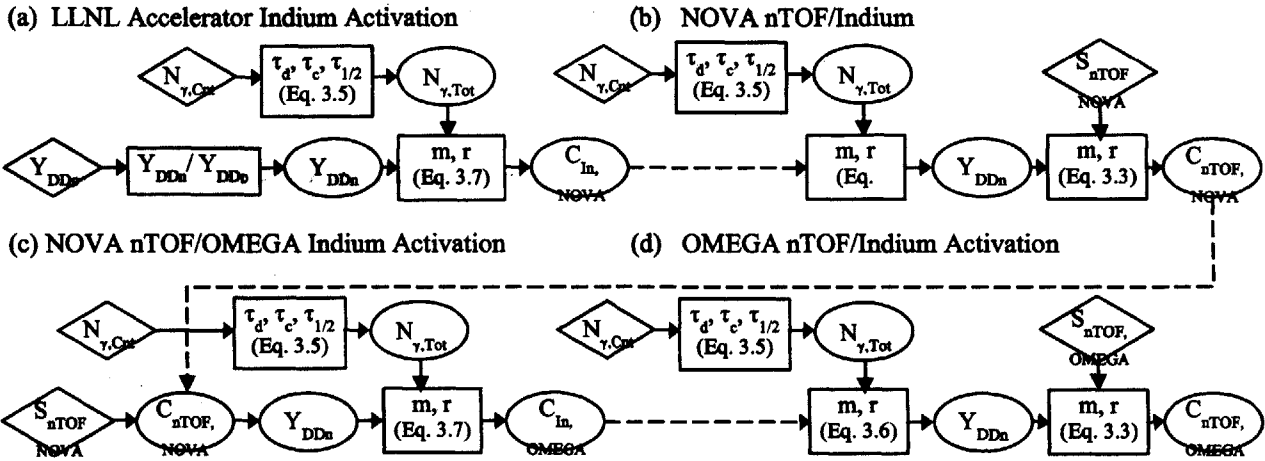
<sup>3</sup> Geneseo State University of New York, 1 College Circle, Geneseo, NY 14454.

magnification [31]. Elastic scattering of DD neutrons within the CR-39 produce recoil protons, or oxygen or carbon nuclei that also leave identifiable damage trails on both the front and back sides of the CR-39 detectors. If the CR-39 neutron detection efficiency—probability that an incident neutron produces a recoil charged particle that leaves a visible track—is known, a neutron yield can be inferred from the recoil particle count.

The CR-39 neutron detection efficiency was determined by cross-calibration to the OMEGA In-activation system (shot 19556). Efficiencies of  $(1.1 \pm 0.2) \times 10^{-4}$  and  $(3.3 \pm 0.3) \times 10^{-4}$  were determined for the front and back sides respectively, and were in good agreement with Monte Carlo simulations of the neutron response. Subsequent DD shots on OMEGA showed good agreement between the In-activation DD yield and the inferred CR-39 neutron yield, however, since the CR-39 detection efficiency was benchmarked to the OMEGA In-activation system, these experiments do not constitute an absolute calibration but rather only provide a CR-39 neutron detection efficiency.

### 3.5 OMEGA In/nTOF Cross-calibration

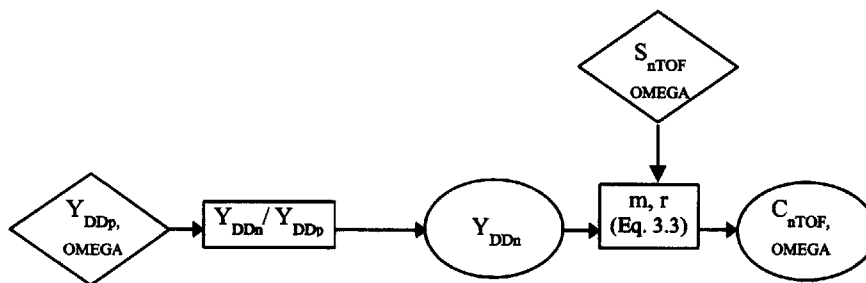
With the HPGe gamma ray spectrometer at OMEGA calibrated to the ported NOVA 10m nTOF, the OMEGA nTOF system was then cross-calibrated to the OMEGA In-activation system over a series of OMEGA ICF implosions similar to the way that the NOVA nTOF system was calibrated to the NOVA In-activation system. On OMEGA, however, the In-activation system continued to be used as the primary  $Y_{DDn}$  diagnostic from 1996-2000 with the nTOF system being run as a backup. As has now been shown in detail, the current OMEGA nTOF calibration coefficients are the results of extensive cross calibrations that took place across multiple diagnostic platforms and facilities. To aid in visualizing all the cross-calibrations that were conducted leading to the current OMEGA nTOF calibration coefficient, a flow chart of the cross-calibrations along with references to the equations needed to infer fundamental calculated quantities is given in **Figure 16**.



**Figure 16. Flowchart outlining the series of cross-calibrations leading to the current OMEGA nTOF calibration coefficient. Values in  $\diamond$  represent fundamental diagnostic measurements, values in  $\square$  represent calculations, and values in  $\circ$  represent fundamental calculated quantities. (a) The gamma spectrometer calibration coefficient ( $C_{\gamma, \text{NOVA}}$ ) was obtained from the observed gamma count ( $N_{\gamma, \text{Cnt}}$ ) and DD proton yield ( $Y_{\text{DDp}}$ ) on a Cockcroft-Walton accelerator. (b) The NOVA 2m nTOF calibration coefficient ( $C_{\text{nTOF, NOVA}}$ ) was obtained from the NOVA In-activation system over a series of shots on NOVA. NOVA 10m nTOF was then cross calibrated to NOVA 2m nTOF. (c) The OMEGA gamma spectrometer calibration coefficient ( $C_{\gamma, \text{NOVA}}$ ) was obtained through cross-calibration to the NOVA 10m nTOF. Finally, (d) OMEGA nTOF calibration coefficients  $C_{\text{nTOF, OMEGA}}$  were obtained through cross calibration to the OMEGA In-activation system.**

## 4 Measuring the Absolute DDn Yield on OMEGA

As has now been shown, the existing OMEGA nTOF absolute DD neutron yield calibration has a long history consisting of a series of cross-calibrations spanning multiple facilities and calibration methods. Following Figure 16, one notes that if all the various cross-calibrations leading to the current nTOF absolute yield calibration coefficient are traced back far enough, they eventually lead to an original calibration to DDp on the Cockcroft-Walton linear electrostatic ion accelerator at the NOVA facility at LLNL using the DDn/DDp branching ratio. An alternative calibration approach for the OMEGA nTOF calibration coefficient ( $C_{nTOF}$ ), then, that eliminates the potential for calibration errors to propagate through the cross-calibration chains given in Figure 16, and allows for improved quantitative analysis of the calibration coefficient uncertainty, is to apply the branching ratio method directly and *in situ* during ICF implosions. This is accomplished by directly comparing the integrated nTOF signal ( $S_{nTOF}$ ) to  $Y_{DDp}$  taking into account the  $Y_{DDn}/Y_{DDp}$  branching ratio. In contrast to the cross-calibration chain that led to the current OMEGA nTOF calibration coefficient given in Figure 16, the flow diagram for the steps involved for the *in situ* calibration method are given in Figure 17.

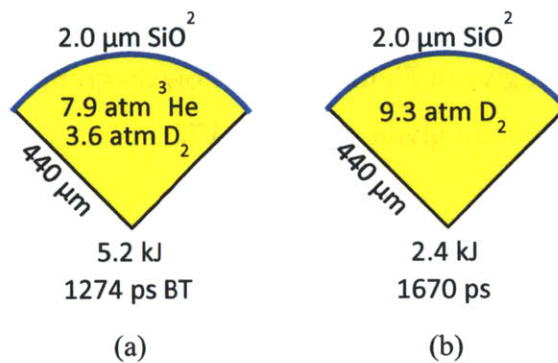


**Figure 17. Flowchart outlining the steps for a method to obtain detector-specific nTOF calibration coefficients *in situ* during ICF implosions using CR-39 nuclear track detector range filter (RF) modules. The values in  $\diamond$  represent fundamental diagnostic measurements, values in  $\square$  represent calculations, and values in  $\circ$  represent fundamental calculated quantities.**

## 4.1 High Accuracy $Y_{DDp}$ Measurements on OMEGA using CR-39 Range Filters

As has been previously mentioned, CR-39 nuclear track detectors are widely used for charged particle detection. As such they serve as the primary detection mechanism in a wide array of ICF diagnostics on OMEGA and the NIF [33-44]. The CR-39 response to protons in particular has been studied extensively and is well documented [31, 45-49].

To test the CR-39/nTOF *in situ* calibration method, a series of directly-driven exploding pusher shots on OMEGA were taken where DDn yields obtained from nTOF using the existing absolute yield calibration coefficient ( $C_{nTOF}$ ) were compared to DDn yields inferred from DDp yields obtained from CR-39 RF modules. Exploding pushers are thin shell capsules made of glass or plastic in which a high-density shell is heated rapidly to temperatures on the order of a few keV and then explodes. For the experiments comprising the study, two shot campaigns were designed to optimize both the CR-39 RF DDp and nTOF DDn responses and reduce measurement uncertainty.



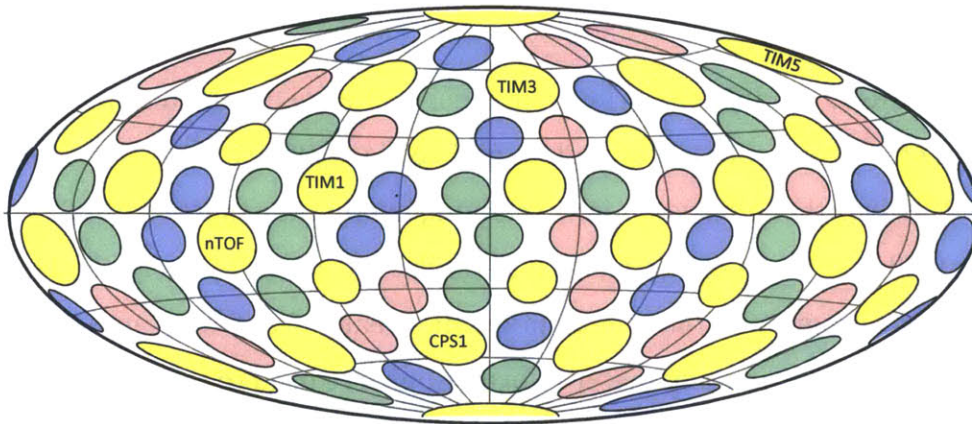
**Figure 18. (a) Campaign A, (b) and Campaign B exploding pusher shot campaigns on OMEGA used to obtain an absolute yield calibration coefficient for 3m nTOF.**

For what we will henceforth refer to as Campaign A, the targets were nominally 880 $\mu\text{m}$  in diameter 2.0  $\mu\text{m}$  thick silicon dioxide ( $\text{SiO}_2$ ) and were filled with 3.6 atm  $\text{D}_2$  and 7.9 atm  $^3\text{He}$ . Laser conditions included 60 beams providing a total nominal energy of 5.3 kJ. For the second campaign, which we will refer to as Campaign B, the capsules were also nominally 880 $\mu\text{m}$  in diameter 2.0 $\mu\text{m}$  thick silicon dioxide ( $\text{SiO}_2$ ) filled with 9.3 atm of  $\text{D}_2$ . Laser conditions included 60 beams providing a total nominal energy of 2.5kJ. Both shot campaigns used a 1ns square laser pulse, smoothing by spectral dispersion (SSD), SG4

phase plates, and a distributed polarization rotator (DPR). Campaign A consisted of six shots while Campaign B consisted of four. A standard capsule pie cutout indicating the capsule and laser conditions for the two campaigns is given in **Figure 18**. In addition to DDp, the Campaign A shots also produced D<sup>3</sup>He fusion products as given in **Equation 4.1**.

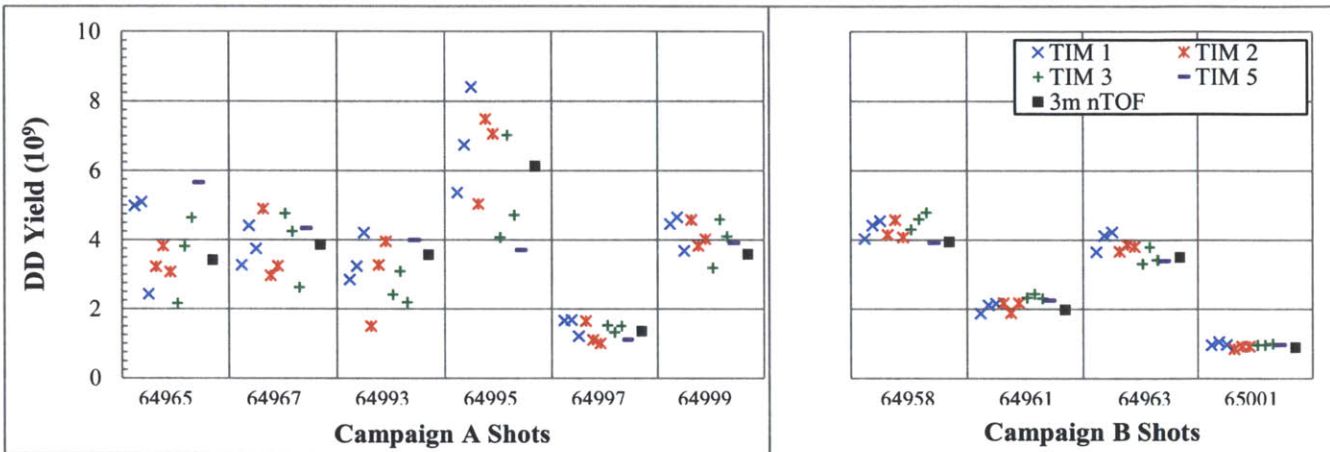


Nominally the flux of DDp being emitted from the implosion would be isotropic so that only one detector should be needed to gain an accurate measurement of the DDp fluence. In practice, particle fluxes around the capsule exhibit some degree of anisotropy. In order to account for these anisotropies 10 CR-39 RF modules were fielded to provide multiple fluence samples over the target chamber solid angle. The modules were fielded in standard OMEGA ten inch manipulators (TIMs) using “trident” allowing three RF modules to be fielded per TIM. The final RF module configuration for the campaigns included tridents in TIMs 1, 2, and 3, and a single RF module in TIM 5 for a total of 10 RFs fielded per shot. All RF modules were fielded 150cm from the OMEGA target chamber center (TCC). The location of the TIMs and other diagnostic ports on OMEGA are shown in **Figure 19**.



**Figure 19. Aitoff projection of the OMEGA target chamber showing the diagnostic ports (given in yellow) and laser drive ports (given in green red and blue). CR-39 range filter (RF) modules for nTOF calibration shots were fielded in ten inch manipulators (TIMs) 1,2,3, and 5 to provide broad angular coverage over the target chamber solid angle and account for particle flux anisotropies.**

The DDp yields from the 10 individual RF modules from Campaign A and Campaign B are given in **Figure 20** along with the OMEGA 3m nTOF DDn yields. Yields from Campaign A shots averaged over all RF modules were in close agreement with 3m nTOF although significant yield variation was observed among individual modules. Yields from Campaign B shots were also in close agreement with 3m nTOF, however, the yield variation between individual RF modules within a given shot was significantly less.



**Figure 20. The range filter (RF) DDp and nTOF DDn yield results from (a) Campaign A and (b) Campaign B shots on OMEGA. The DDp yields from the Campaign A shots on average show a significant amount of spread in the RF measurement whereas the Campaign B shots show very little spread and are in good agreement with 3m nTOF.**

The individual CR-39 module yields given in Figure 20 were obtained as follows. Each piece of CR-39 was etched in a solution of sodium hydroxide to expose the pits created by the DDp. The CR-39 was then placed under a scanning microscope that recorded every track on the piece as well as track information such as track contrast, eccentricity, and diameter. Using an analysis program to read the scanned file created from the scanning microscope, the contrast, eccentricity, and diameter information were used to separate the DDp tracks from noise. In CR-39, tracks left by charged particles are characterized by high contrast and very low eccentricity whereas noise typically has high eccentricity and low contrast. After the signal was separated from the noise, the analysis software provided a charged particle fluence given in tracks/cm<sup>2</sup>. An overall DDp yield was then obtained by multiplying the track fluence by the area of the solid angle enclosed at the distance from the detector to TCC (which was 150cm). Although not given here, full details regarding the processing and



signal to noise separation in CR-39 detectors is given in Sequin *et al.* [31]. A full overview of the raw data and analysis used to obtain the individual RF yield measurements is given Figure 20 are provided in Appendix E.

Upon observing the measured yields from the shot campaigns in Figure 20—and in particular the shots from Campaign A—ones notes the significant variation in individual RF yield measurements within a given shot. This variation exists between the RF modules fielded in different TIMs, but also within the RF modules fielded in a trident within a single TIM. We now look at the source of this variation in more detail and consider whether this is caused by: (1) instrumentation and measurement uncertainty in the individual measurements from CR-39 RF modules, or (2) capsule implosion effects leading to an asymmetric distribution to charged particles. What we would like to know is whether the fluences observed really do exhibit a large degree of variance or whether the variance is due to measurement uncertainty.

As has already been mentioned, one primary advantage of CR-39 is that when certain criteria are met the detector exhibits 100% detection efficiency of the charged particles of interest. To obtain 100% detection efficiency there must be 1) clear separation of charged particle species to isolate the given particle of interest, 2) the individual particles must have an energy that lies within the optimal CR-39 detection range, and 3) there must be clear signal to noise separation to keep intrinsic noise in the CR-39 from being counted as tracks.

When using CR-39 detectors to observe and isolate a single charged particle species, range filters are commonly used to range out species not of interest and to range species of interest into the CR-39 optimal detection energy range. For the shots comprising Campaign A, the primary charged particles incident on the CR-39 were from the primary DD and D<sup>3</sup>He fusion reactions and include: <sup>3</sup>He (from the DD reaction in Equation 3.1), T (from the DD reaction in Equation 3.4), protons (from the DD reaction in Equation 3.4), alphas (from the D<sup>3</sup>He reaction given in Equation 4.1), and protons (also from the D<sup>3</sup>He reaction in Equation 4.1). Other lower energy ions (on the order of less than 10keV for both Campaign A and Campaign B shots) from the SiO<sup>2</sup> capsule and fuel were also present. For campaign B the primary ions were the same except for the fusion products from the D<sup>3</sup>He reaction. For

both campaigns a 25 $\mu$ m Al filter was placed in front of the CR-39. The thickness was chosen so as to range out all the low energy ions from the capsule and fuel as well as all charge particles except for the DD and D<sup>3</sup>He protons. An overview of the charged particles generated from the primary fusion reactions from DD and D<sup>3</sup>He along with the particle birth energy, particle range in aluminum corresponding to the birth energy, and the ranged energy of the particle after passing through 25 $\mu$ m of aluminum, is given in **Table 4**. The values in Table 4 assume that no ranging other than the 25 $\mu$ m Al range filter occurs. In practice there is often additional ranging of particles through the fuel and capsule.

**Table 4. Primary fusion product charged particles incident on CR-39 RF modules in Campaigns A and B. Given are the source fusion reactions, the particle birth energy, the range of the particle in aluminum corresponding to the birth energy, and the energy of the particle after passing through the 25  $\mu$ m range filter.**

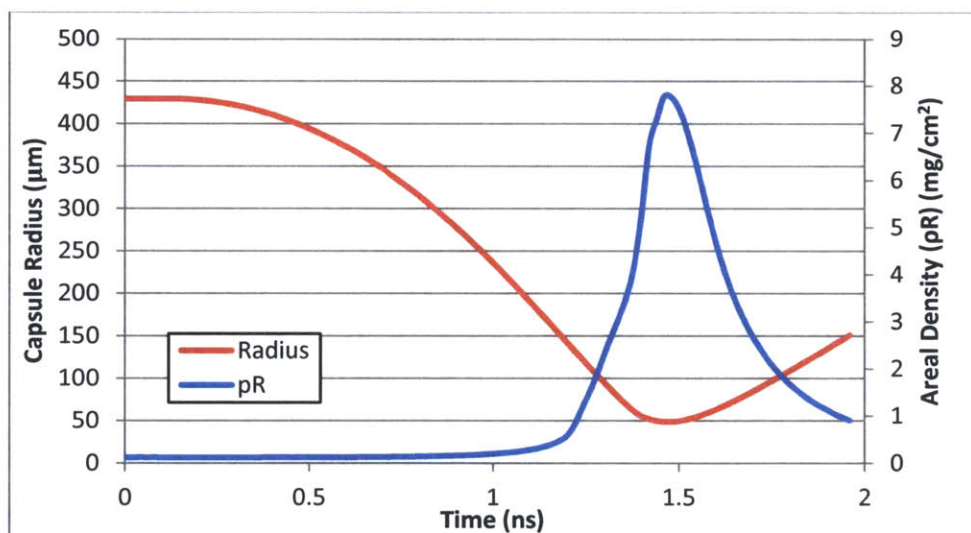
Ion	Reaction	Birth Energy (MeV)	Range ( $\mu$ m)	Ranged Energy (MeV)
<sup>3</sup> He	D(D, <sup>3</sup> He)n	0.82	2.70	0
Triton	D(D,T)p	1.01	9.82	0
Alpha	D( <sup>3</sup> He, $\alpha$ )p	3.67	14.10	0
Proton	D(D,T)p	3.02	81.47	2.42
Proton	D( <sup>3</sup> He, $\alpha$ )p	14.68	1222	14.50

From Table 4 we see that only DD and D<sup>3</sup>He protons are able to pass through the aluminum range filter and all other charged particle species are stopped. energy range and are the only charged particle species that leave observable pits in the detector.

Although only DDp are detected in the CR-39, to ensure 100% counting the entire DDp spectrum must fall within the detectable energy range of the CR-39. In addition to range filters which cause an energy downshift, the areal density ( $\rho R$ ) of the capsule and fuel in ICF implosions can also potentially have a significant effect of ranging down the proton energy from the original birth energy. In some studies the measured energy downshift of primary fusion reaction protons (DDp and D<sup>3</sup>He-p) has been used to estimate the fuel  $\rho R$  [39]. If the  $\rho R$  energy downshift is large enough there is a risk that the combined 25 $\mu$ m Al filter and  $\rho R$  energy downshift could shift the energy of the DDp incident on the CR-39 to

below the optimal energy range, will make the particle undetectable by the scanning microscope, and result in undercounting of particles. To rule out the possibility of a significant  $\rho R$  energy downshift on the DDp yield we look at simulations of the shots from Campaigns A and B given by the 1D hydrodynamic code LILAC (which is routinely used to model ICF implosions on OMEGA), as well as the DDp energy spectrum that was measured on shots from Campaign A and Campaign B.

From LILAC we obtain plots of the predicted capsule radius and  $\rho R$  as a function of time elapsed after the beginning of the 1ns laser pulse. In **Figure 21** we give these plots for shot 64999 which, after observing all the shot simulations, exhibited the highest simulated  $\rho R$  from Campaigns A and B.

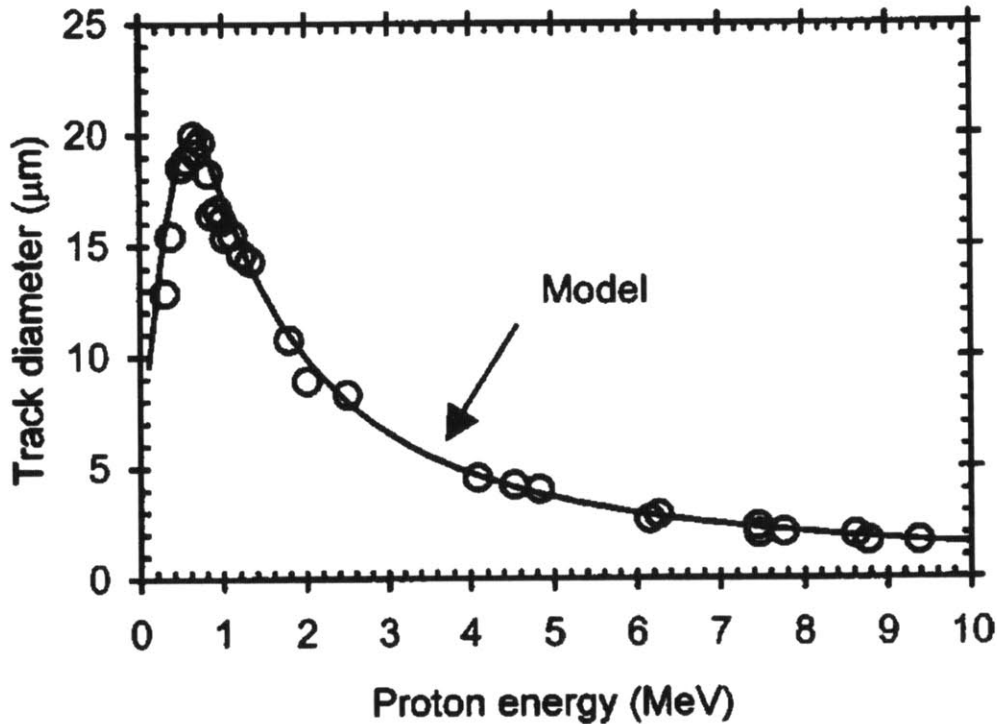


**Figure 21. The simulated capsule radius and areal density are given for shot 64999 as a function of time (where  $t = 0$  corresponds to the beginning of the laser pulse).**

As can be seen, the maximum  $\rho R$  is  $\sim 8 \text{ mg/cm}^2$  where the capsule is compressed from  $440 \mu\text{m}$  to a minimum of  $50 \mu\text{m}$  at  $1.5 \text{ ns}$ . Using SRIM (Stopping and Range of Ions in Matter code), the average stopping power of a  $3.02 \text{ MeV}$  proton for the Campaign A shots with a  $\text{D}^3\text{He}$  fuel mix is calculated to be  $0.14 \text{ MeV}/(\text{mg/cm}^2)$ . Similarly for Campaign B shots with a deuterium fuel mix, the average stopping power is calculated to be  $0.16 \text{ MeV}/(\text{mg/cm}^2)$ . For a  $\rho R$  of  $\sim 8 \text{ mg/cm}^2$  this would lead to an energy downshift of  $\sim 1.3 \text{ MeV}$  and would result in protons of energy  $1.7 \text{ MeV}$  incident on the range filter. Calculating the additional

ranging through the 25 $\mu\text{m}$  of Al using SRIM, the energy incident on the CR-39 is calculated to be  $\sim 0.7\text{MeV}$ .

In order for a track to be detectable on CR-39 it must fall within a detectable energy range. The range of detectable protons can be understood by observing a plot of the proton diameter as a function of energy as given by Seguin et al. and provided below in **Figure 22**.

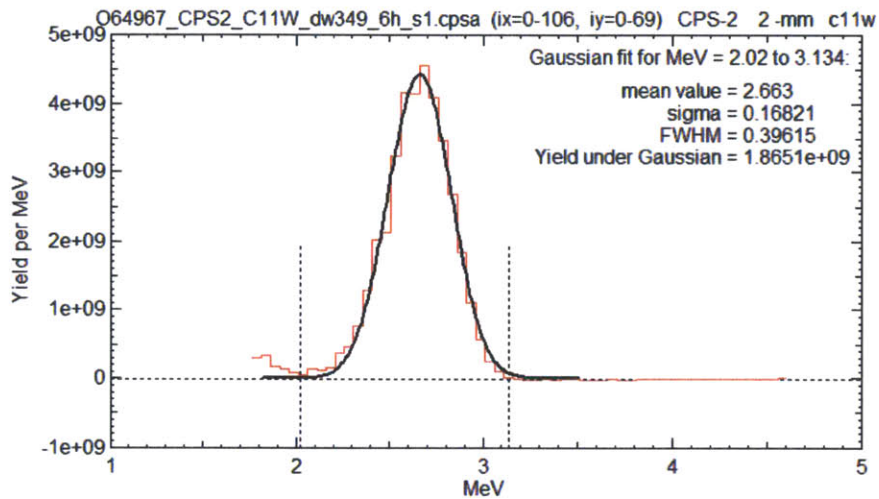


**Figure 22. Measured and modeled values of proton track diameter in CR-39 as a function of incident proton energy (MeV). As given in Seguin et al. [31].**

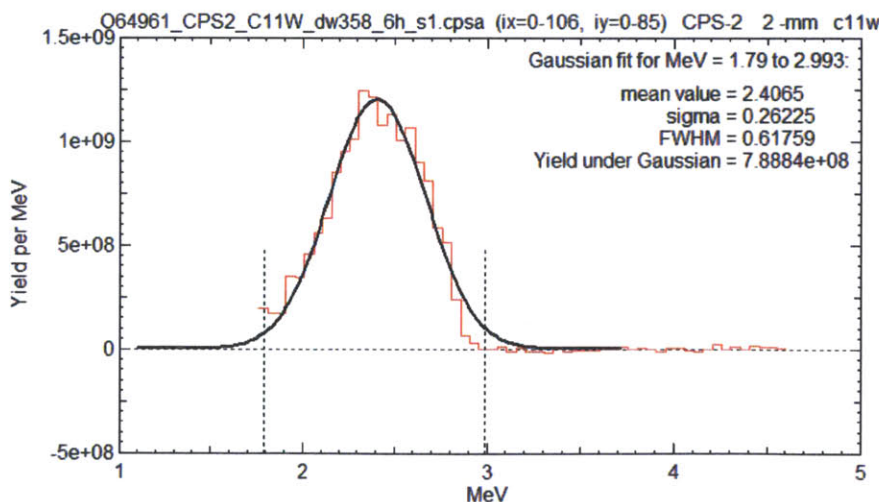
As can be seen, high energy protons leave small tracks on the order of 2-4 $\mu\text{m}$ . As the energy reaches around 4 MeV the track diameter starts to increase significantly until it peaks around 0.7MeV. For energies less than 0.7 MeV, the track diameter starts to get smaller as the proton energy is reduced and approaches 0. In addition to getting smaller, the contrast of the tracks becomes increasingly faint until they are unable to be detected by the scanning microscope. The conclusions this figure is that for protons we should expect good contrast of tracks and therefore full detection under the scanning microscope up to the peak energy of 0.7MeV, after which we would gradually start losing tracks as the proton energy goes to 0. That said, some tracks are still detectable at the lower energy levels (as

can be seen in the plot where Seguin et al. do have data on the diameter of protons with energies as low as  $\sim 0.3$  MeV).

With the estimated mean energy of the protons incident on CR-39 being  $\sim 0.7$  MeV from the LILAC and SRIM calculations there is risk that much of the lower tail of the energy distribution may be cut off. To rule this out, we look at the measured energy spectrum from two of the calibration shots (one from Campaign A and one from Campaign B). The energy spectrum from shot 64967 (Campaign B) and 64961 (Campaign B) are given in **Figure 23** below:



(a)



(b)

**Figure 23. CPS2 measured energy spectrums for (a) shot 64967 (Campaign A— $D^3He$ ) and (b) shot 64961 (Campaign B—DD).**

From Figure 23 we see that the  $\rho R$  energy downshift is only  $\sim 0.4$  MeV for the Campaign A shot and  $\sim 0.6$  for the Campaign B shot. This is significantly less than the  $\sim 1.3$  MeV predicted from the LILAC and SRIM calculations.

Using the CPS measured energy distributions from the Campaign A and B shots and a lower CR-39 detection cut off of 0.7 MeV, we estimated an upper bound for the % of tracks we would expect to lose from low energy cutoff. We consider this an upper bound since we know we do count a significant number of particles that have fallen below the cutoff even though we start losing some. Using SRIM we estimate a proton with incident energy of 1.75 MeV when filtered through 25um Al will be ranged down to 0.7 MeV (the CR-39 lower detection cut-off). From this we place a lower cutoff for the CPS distributions of 1.75 MeV. We assume conclude any particles with energies less than 1.75 MeV will not be detected since they would filter down to 0.7 MeV through the 25um Al filter and be at the threshold. Using a lower unfiltered cutoff of 1.75 MeV and the DDp energy distributions given from the CPS data we estimate by integrating over the lower tail of the distribution the % tracks lost. The results are given in **Table 5**.

**Table 5. Calculation of DD protons lost to lower energy tail of distribution.**

Shot	Species	Energy (MeV)	Spread (MeV)	Cutoff (MeV)	% DDp Lost
64961	DD	2.4065	0.262	1.75	0.6%
64967	D3He	2.663	0.168	1.75	$\sim 0$

From this we estimate that virtually no particles are lost and we can infer 100% particle detection.

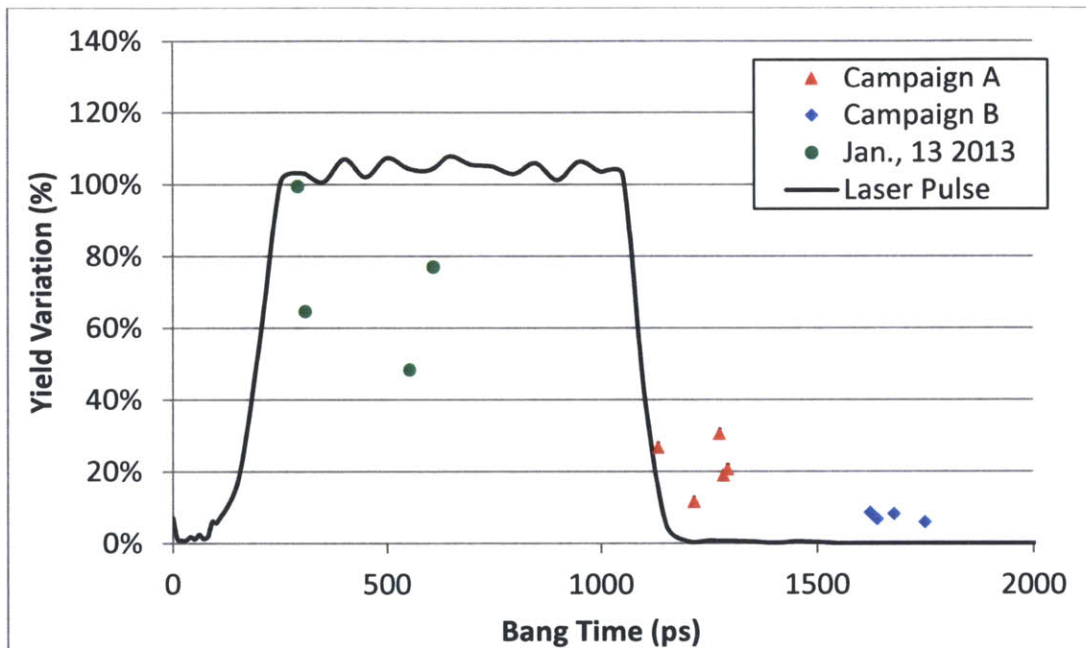
With 100% charged particle detection expected, the variation in yields shown in Figure 20 cannot be attributed to uncertainty in the CR-39 fluence measurement. We therefore accept the measurements as accurate and attribute the variation to other effects that result in an anisotropic particle distribution. Two possible affects that could explain the anisotropic distribution of charged particles are 1) areal density asymmetries and 2) electromagnetic field effects that are present during capsule implosions.

In many ICF implosions, Rayleigh-Taylor instabilities created on the capsule surface during compression result in areal density asymmetries. For charged particles passing through, we would expect greater angular particle deflection in the higher density areas than the lower density area. If the mode of these asymmetries were high enough it could lead to the kind of anisotropic particle flux distribution observed in the data in Figure 20. Another effect that has been observed is the presence of large electromagnetic fields that are generated around the target as the laser ablates the capsule. These fields have been observed in proton radiographs published by Rygg et al. in Science [33]. While the fields have no effect on neutrons, the electromagnetic fields generated are strong enough to deflect charged particles and could lead to an anisotropic flux of particles over the target chamber solid angle.

## 4.2 Relation Between Particle Flux Anisotropies and Bang Time

As can be seen in Figure 22, individual Campaign A shots exhibit significantly more yield variation between individual RF modules than the shots in Campaign B. As has been shown, the variation between the individual RF module fluence measurements is not due to measurement error: CR-39 has 100% detection efficiency and on all shots the number of tracks counted per area analyzed varied between 25,000 and 85,000 tracks so that counting errors were less than 1%. Consequently the variation is essentially entirely contributed to particle flux anisotropies which currently we attribute to either  $\rho R$  asymmetries or electromagnetic fields generated around the capsule during implosion. For the electromagnetic field explanation, these fields have been found to be strongest during the laser pulse while the laser is incident on the capsule. In addition a circuit model of the capsule from which electromagnetic fields can be inferred was recently presented in N. Sinenian's PhD thesis that also predicts significant reduction in fields shortly after the laser has turned off [50]. Shots that are designed so that the laser is not incident on the capsule when bang time occurs will have weaker electromagnetic fields during bang time and will result in less yield variation. The most significant parameter that affects when bang time occurs within the laser pulse is the laser drive energy and subsequently the capsule laser intensity. On OMEGA, laser energies of a few kilo-joules will result in late bang times while

laser energies approaching the OMEGA maximum of 60 kJ will result in much earlier bang times. In **Figure 24** we present the yield variation as a function of when bang time occurs relative to the laser pulse for three exploding pusher campaigns. As can be seen, for the January 13, 2012 campaign, bang time occurred early to mid-pulse and demonstrated significant yield variation. In contrast, Campaign B shots with bang times approximately 500 ps after the laser has turned off demonstrate little yield variation. This affect could also be explained using the  $\rho R$  asymmetry explanation since a stronger laser drive would, in addition to giving an earlier bang time, lead to greater Rayleigh-Taylor instabilities, greater  $\rho R$  asymmetries, and consequently greater fluence variation.



**Figure 24. The effect of the occurrence of bang time relative to the end of the laser pulse on yield variation measured by CR-39 RF modules. The results from three exploding pusher campaigns on OMEGA are presented: (1) January 13, 2012, (3) Campaign A (February 7 & 9, 2012), and (3) Campaign B (February 7 & 9, 2012). The yield variation reduces significantly when bang time occurs significantly (at least 500ps) after the end of the laser pulse.**

By comparing these shot campaigns we conclude that exploding pusher shots that are designed with lower energy laser drives (and consequently lower capsule intensities) will experience bang times after the laser shuts off and will result in less variation in the



individual CR-39 RF module yield measurements, hence reducing the uncertainty in the overall yield measurement.

The trend in yield variation as a function of bang time depicted in Figure 24 can also be used to evaluate the two explanations presented earlier regarding the cause of the observed particle flux anisotropies. The two explanations given were that the yield variation could be explained by 1) areal density asymmetries and 2) electromagnetic field effects that are present during capsule implosions. For the January 13 shots that exhibited high yield variation and early bang time the capsules were driven with a 30 kJ 1ns square pulse. As shown before, Campaign A shots were driven with a 5.2 kJ 1ns square pulse and Campaign B shots were driven with a 2.4 kJ 1 ns square pulse. The trend we see in Figure 24 then shows an increase in yield variation with higher laser intensity and a decrease in yield variation with lower laser intensity. However, in Lindl et al. [51] equation 46 an increase in laser intensity is shown to cause an increase in ablation velocity (i.e. the velocity with which the ablation front moves through the shell), and an increase in ablation velocity is shown to reduce the growth of Rayleigh-Taylor instabilities which would result in less  $\rho R$  asymmetries. Based on the theory presented by Lindl we would then expect lesser Rayleigh-Taylor instabilities, less  $\rho R$  asymmetries and less yield variation for the January 13 shots and greater Rayleigh-Taylor instabilities, greater  $\rho R$  asymmetries and greater yield variation in the Campaign B shots. Since Figure 24 shows the exact opposite of this the hypothesis of particle flux anisotropies being caused by  $\rho R$  asymmetries is inconsistent with the theory presented by Lindl and the observations given in Figure 24.

In addition, we consider whether the areal density of the fuel is enough to create significant angular deflection of DDp. From the measured mean energy of 2.663 MeV obtained in Figure 23(a) for shot 64967 we modeled the implosion using SRIM adjusting the plasma density until the corresponding ion energy in the simulation matched the measured mean ion energy. This resulted in a fuel density of 0.4 g/cm<sup>3</sup> compared to the 1.2 g/cm<sup>3</sup> predicted by the LILAC code. Using the Monte Carlo simulation in SRIM the mean angular deflection associated with the 0.4 g/cm<sup>3</sup> fuel density is calculated to be  $0.41^\circ \pm 0.27^\circ$ . This also matches closely to the parameterized analytical form of the angular scattering given by:

$$\theta = 0.55^\circ \left( \frac{30 \text{ MeV}}{E_p} \right)^{1.15} \sqrt{\left( \frac{2Z}{A} \right) \left( \frac{Z}{13} \right)} \sqrt{\frac{\rho R}{0.2 \text{ g} \cdot \text{cm}^2}} \quad (4.2)$$

where  $\theta$  is the deflection angle,  $E_p$  is the proton energy,  $Z$  is the effective atomic number of the plasma,  $A$  is the average mass number of the plasma, and  $\rho R$  is the areal density. Using the analytical formula we calculate the average angular deflection to be  $0.33^\circ$  which is in good agreement with the  $0.41^\circ$  calculated with the Monte Carlo code. Where the CR-39 RF modules were fielded at 150 cm from TCC, this would result in an average lateral deflection of  $3.4 \text{ mm} \pm 2.25 \text{ mm}$ . This suggests that we would expect very little angular deflection due to areal density effects.

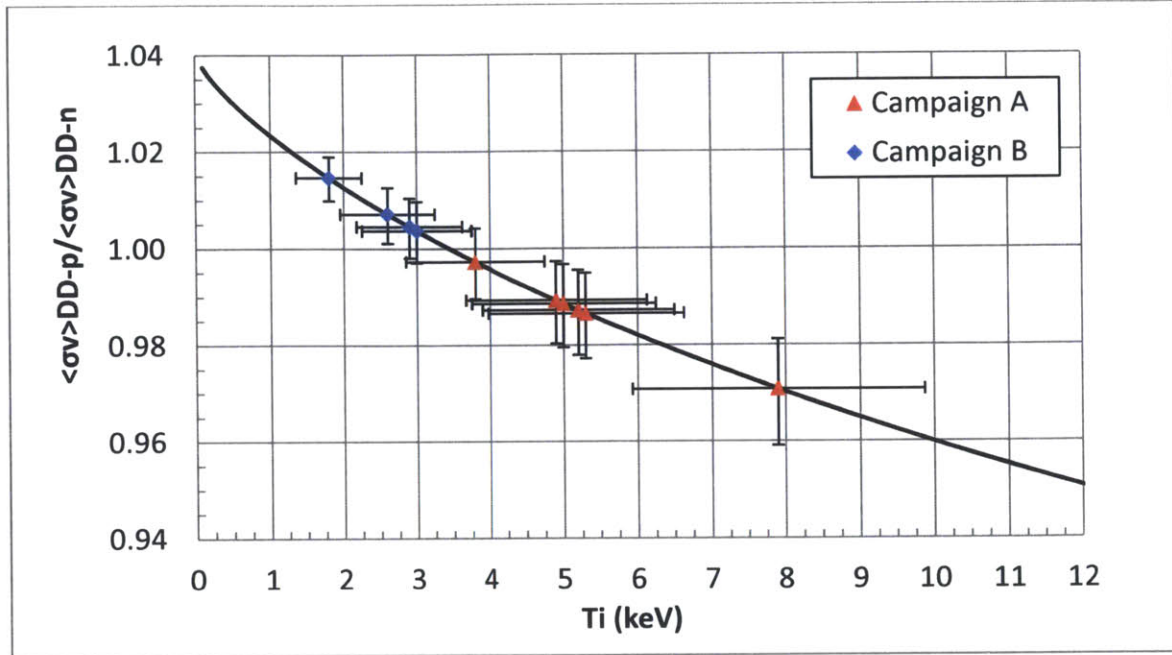
### 4.3 CR-39/nTOF Yield Comparison and Calibration Coefficient Verification

To verify the existing OMEGA 3m nTOF calibration coefficient and to more accurately quantify the calibration coefficient uncertainty, uncertainties associated with the CR-39 range filter yield measurement, the nTOF yield measurement, and the DDn/DDp branching ratio are taken into account. Uncertainties associated with the CR-39 proton response consist of three kinds: (1) the statistical uncertainty associated with the particle counts, (2) uncertainty in signal to noise track separation, and (3) uncertainty in the individual RF yield measurements due to particle flux anisotropies. As the number of tracks recorded per RF module for both shot campaigns were between 25,000 and 85,000, counting statistics result in uncertainties less than 1% can therefore be neglected since these are much less than the systematic calibration errors. As mentioned previously, in the analysis software used to analyze the CR-39 tracks, noise is separated from signal by filtering tracks based on size, eccentricity, and contrast. Using track filtering techniques, signal and noise separation usually results in only a few percent uncertainty in the track count. With counting and signal to noise separation uncertainties being small the uncertainties stemming from the particle flux anisotropies dominate. Particle flux anisotropies can be reduced by increasing the number of CR-39 RF modules fielded to obtain a greater sample size and reduce the variance in the average yield of the detectors, or by designing shots so that bang time

occurs significantly after the end of the laser pulse so that the yield variation is small and fewer CR-39 RF modules are needed to average out flux anisotropy affects.

Uncertainty of the nTOF measurements consists of (1) the instrumentation uncertainty of the nTOF neutron response, cable reflections, and intrinsic noise, and (2) the uncertainty in the calibration coefficient. Instrumentation uncertainty of nTOF is quoted as being on the order of 5%.

The  $Y_{DDn}/Y_{DDp}$  branching ratio is a function of the plasma ion energy and is near unity for low energy ions (between 1-10 keV) [52-54]. For completeness in this uncertainty analysis, instead of assuming the ratio to be unity, we include calculated values of the branching ratio using the DDn and DDp reaction rate parameterizations found in Bosch and Hale [53]. Fuel burn-average ion temperatures obtained from nTOF were used in the Bosch and Hale parameterization to obtain the branching ratio uncertainty for each shot individually. The nTOF signal can be used in this case without methodological circularity since the parameterization of the functional fit to the raw nTOF signal that is used to determine the fuel burn-average ion temperature is independent of the absolute yield calibration [19]. The nominal branching ratio along with the uncertainty in the branching ratio due to the uncertainty in the nTOF ion temperature measurement is given in **Figure 25**. The uncertainty in the Bosch and Hale parameterization reaction rate itself is quoted as being 0.3% in the 0-100 keV range and is therefore neglected.



**Figure 25. The  $Y_{DDn}/Y_{DDp}$  branching ratio is given by the ratio of the parameterized reaction rates obtained from Bosch and Hale for DDn and DDp. This ratio as a function of ion temperature is given by the black line. The inferred branching ratios for the OMEGA Campaign A and Campaign B shots are obtained using the fuel burn-averaged ion temperatures from nTOF and plotted on the black line. The error bars given for each shot in Campaign A and Campaign B indicate the measured error in the nTOF ion temperature measurement (x-axis) and the inferred error in the branching ratio (y-axis).**

Using the DDn/DDp branching ratio ( $\beta_{np}$ ) and the CR-39 RF DDp yield ( $Y_{DDp}$ ), a RF equivalent DDn yield ( $Y_{RFn}$ ) is obtained for every RF module DDp measurement. The ratio of the RF equivalent DDn yield to the nTOF DDn yield is then taken to allow for a direct yield measurement comparison among RF modules and across all shots. In the absence of particle flux anisotropies and assuming the nTOF calibration coefficient ( $C_{nTOF}$ ) is perfectly calibrated, the expected value of the ratio of the inferred RF module DDn yield to the nTOF DDn yield is unity ( $E[\langle Y_{RFn}/Y_{nTOF} \rangle] = 1$ ). Any shot specific phenomena that would affect the DDp yield should also affect the DDn yield such that the expected values would be equal provided the correct branching ratio is used to determine the RF inferred DDn yield. In practice, particle flux anisotropies are present so that the ratio is rarely unity. However, by taking an average of all the RF inferred DDn to nTOF DDn yield ratios over all shots, flux anisotropies can be averaged out so that the expected value of the average yield ratio is

unity. Using multiple detector measurements to average out flux anisotropies, therefore, isolates the effects of the calibration coefficient. Any average RF inferred DDn to nTOF DDn yield ratio other than unity that is statistically significant would suggest an anomaly in the current nTOF calibration coefficient ( $C_{nTOF}$ ). The expected value of the average of the RF inferred DDn and nTOF DDn ratios can be expressed in **Equation 4.3**.

$$E \left[ \left\langle \frac{Y_{RFn}}{Y_{nTOF}} \right\rangle \right] = \frac{1}{n} \sum_{Shot,i} \sum_{RFs,j} \frac{Y_{DDp}(i,j) \cdot \beta_{np}(i)}{Y_{DDn}(i)} \quad (4.3)$$

where E is the expectation value of the average of the inferred CR-39 DDn yield to the nTOF yield, n is the total number of RF modules being considered ( $n = i*j$ ),  $Y_{RFn}$  is the DDn yield inferred from the DDP RF measurement,  $Y_{nTOF}$  is the measured DDn yield from nTOF,  $Y_{DDp}(i,j)$  is the DDP RF measurement for shot i and RF module j,  $\beta_{np}(i)$  is the DDn/DDp branching ratio for shot i, and  $Y_{DDn}(i)$  is the DDn nTOF measurement for shot i. For Campaign A  $n = 60$  (10 RF modules per shot times 6 shots), and for Campaign B  $n = 40$  (10 RF modules per shot times 4 shots).

While the effect of the nTOF calibration coefficient on the RF inferred DDn to nTOF DDn ratio can be isolated using Equation 4.3, the uncertainties associated with the CR-39 DDP measurement, DDn/DDp branching ratio, and the nTOF DDn measurement must be taken into account to determine whether any deviation in the expected value of Equation 4.3 from unity is statistically significant. The error of the expected value is obtained by propagating the errors associated with each measurement to obtain a single instrumentation error. This error is achieved over a series of steps as follows.

First, we obtain the error associated with the RF inferred DDn yield ( $Y_{RFn}$ ) from the RF DDP measurement and DDn/DDp branching ratio ( $\beta_{np}$ ) by **Equation 4.4**.

$$\sigma_{Y_{RFn}} \approx Y_{RFp} \beta_{np} \times \sqrt{\left( \frac{\sigma_{Y_{RFp}}}{Y_{RFp}} \right)^2 + \left( \frac{\sigma_{\beta_{np}}}{\beta_{np}} \right)^2} \quad (4.4)$$

where  $\sigma_{Y_{RFp}}$  is the uncertainty in the signal to noise separation of CR-39 DDp tracks,  $Y_{RFp}$  is the RF proton yield,  $\sigma_{\beta_{np}}$  is the uncertainty in the DDn/DDP branching ratio ( $\beta_{np}$ ), and  $\sigma_{RFn}$  is the uncertainty in the RF DDp inferred DDn yield.

Next, the error of the ratio of YRFn and YnTOF is obtained similarly for an individual RF module on a specific shot by **Equation 4.5**.

$$\sigma_R \approx \frac{Y_{RFn}}{Y_{nTOF}} \times \sqrt{\left(\frac{\sigma_{Y_{RFn}}}{Y_{RFn}}\right)^2 + \left(\frac{\sigma_{Y_{nTOF}}}{Y_{nTOF}}\right)^2} \quad (4.5)$$

Where  $\sigma_{Y_{nTOF}}$  is the instrumentation uncertainty of nTOF and  $Y_{nTOF}$  is the measured nTOF DDn yield. In this we assume  $Y_{RFn}$  and  $Y_{nTOF}$  to be perfectly correlated as an increase in the yield of protons should track the neutron yield and vice versa.

With errors propagated for the individual RF/nTOF neutron yield ratios, the error associated with the average of the ratios ( $\sigma_E$ ), or in other words the error associated with Equation 4.3 can be expressed as:

$$\sigma_E \approx \frac{1}{n^2} \times \sum_i^n \sum_j^n \sigma_R(i) \cdot \sigma_R(j) \quad (4.6)$$

where  $n$  is the total number of ratios (i.e. the total number of RF modules fielded per shot times the total number of shots being considered). For Campaign A  $n = 60$  (10 RF modules per shot times 6 shots), and for Campaign B  $n = 40$  (10 RF modules per shot times 4 shots).

The total error is then obtained by adding the overall measurement error ( $\sigma_E$ ) to the standard error of the RF/nTOF DDn ratios in quadrature as given in **Equation 4.7**.

$$\sigma_{Tot}^2 = \sigma_C^2 + \sigma_E^2 \quad (4.7)$$

The standard error of the ratios is determined in the usual way as  $\sigma_C/\sqrt{n}$ , where  $\sigma_C$  is the standard deviation of the RF/nTOF DDn yield ratios. As the propagated uncertainty of all measured quantities ( $\sigma_C$ ) increases, so does the total uncertainty in the expected value ( $\sigma_{Tot}$ ). However, if there is little uncertainty in the measured quantities and  $\sigma_C \gg \sigma_E$ , then

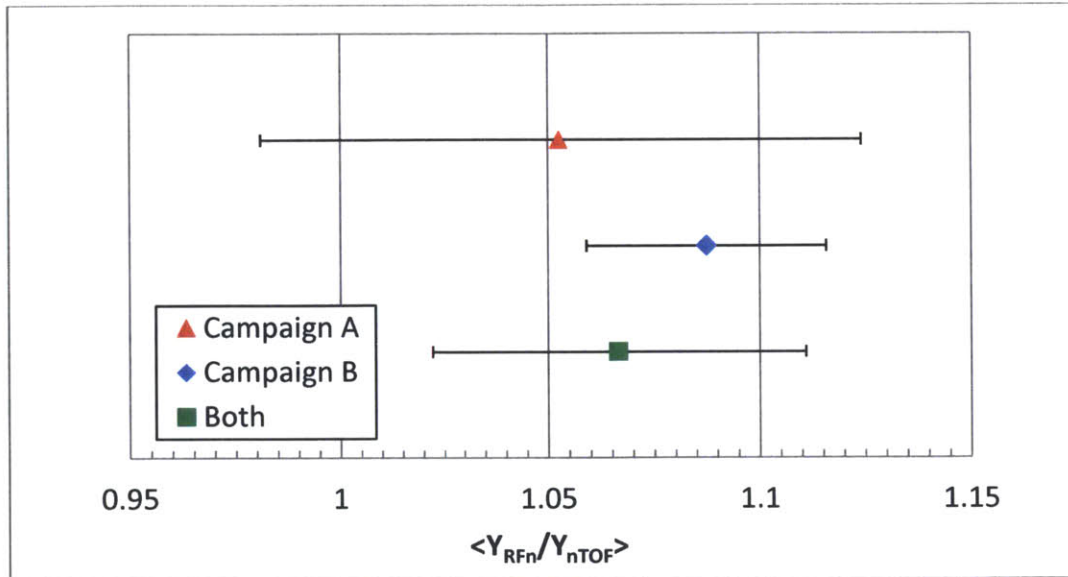
the overall uncertainty is just the uncertainty associated with the spread of the RF/nTOF DDn ratio. An overview of the instrumentation, particle flux anisotropy, and total error is given in **Table 6**. As can be seen, the uncertainty in the DDp measurement that arises from particle flux anisotropies dominates the instrumentation error.

**Table 6. The errors associated with the averaged expected value of the RFn/nTOF DDn yield ratios for the Campaign A, Campaign B, and both campaigns are given.  $\sigma_E$  is the accompanied instrumentation error,  $\sigma_C$  is the error from yield variation (due to particle flux anisotropies), and  $\sigma_T$  is the total error in the expected value. The 95% confidence interval is also given.**

Shots	$\sigma_E$	$\sigma_C$	$\sigma_{Tot}$	95% Conf. Int.
Campaign A	0.011	0.037	0.038	0.074
Campaign B	0.012	0.014	0.019	0.036
Both	0.012	0.023	0.025	0.049

From  $\sigma_{Tot}$  a 95% confidence interval for the expected value of the average RF inferred DDn to nTOF DDn yield ratio (Equation 4.3) is obtained in the usual way by multiplying the standard error by the number of standard deviations covering 95% of the distribution (which for a Gaussian distribution is 1.96). The calculated expected values for  $E[\langle Y_{RFn}/Y_{nTOF} \rangle]$  and the 95% confidence intervals are given separately in **Figure 26** for the early bang time (Campaign A) and late bang time (Campaign B) shots.

In Figure 26, the expected values and 95% confidence interval as defined by Equations 4.3 and 4.7 are given for Campaign A shots, Campaign B shots, and both shot campaigns combined. From this one sees that the greater variation in the individual RF measurements from Campaign A (as shown in Figure 22(a) ), compared to the yield variation in the measurements from Campaign B (as shown in Figure 19(b) ), has a significant effect on the standard error and associated confidence interval. Since the total error is dominated by the error due to particle flux anisotropies, and since the RF DDp measurements on the Campaign B shots have less yield variation, the 95% confidence interval obtained from the Campaign B shots provides a tighter band on the expected value of the yield ratio. From the Campaign B shots we estimate that the current 3m nTOF DDn calibration coefficient to be well calibrated, but low by  $9 \pm 1.5\%$ .



**Figure 26. The expected value of the average of the RFn/nTOF DDn yield ratio ( $E[\langle Y_{RfN}/Y_{nTOF} \rangle]$ ) with the associated 95% confidence interval obtained from the error analysis for the OMEGA Campaign A and Campaign B shots.**



## 5 Conclusion

In conclusion, in the last 50 years inertial confinement fusion has grown to be an important platform for conducting research in high energy density regimes. Although primarily funded and motivated by the goals of the Stockpile Stewardship program under the U.S. National Nuclear Security Administration, ICF has also made important advances in energy and basic research in HEDP such as atomic physics, nuclear physics, plasma physics, astrophysics, material science, and laser science.

In order to obtain more accurate measurements of DDn yields in ICF implosions, this work has presented a method for obtaining detector-specific DDn nTOF calibration coefficients through *in situ* measurements of DDp generated during ICF implosions. This method has successfully been implemented on OMEGA. The method involves calibrating the integrated nTOF neutron response to DDp measurements obtained using CR-39 nuclear track RF modules after which the DDn yield is inferred using the  $Y_{DDn}/Y_{DDp}$  branching ratio. Two advantages of this approach are that (1) it reduces the dependence on multiple layers of cross-calibration between accelerators, In-activation systems, and other nTOF detectors as was conducted previously to obtain the current nTOF absolute yield calibration coefficient, and (2) it reduces the uncertainty of propagated errors introduced through all the multiple cross-calibrations. Results from exploding pusher shot campaigns on OMEGA confirm the existing calibration coefficient of 3m nTOF to be well calibrated although slightly high by  $9 \pm 1.5\%$ . As most of the uncertainty in the calibration coefficient obtained from OMEGA using the method has been shown to be the result of charged particle flux anisotropies, highly accurate calibration coefficients can be obtained from only a few RF modules fielded per shot if calibration shots are designed in such a way as to reduce anisotropies. As was shown, this can be done by designing shots with reduced laser drive so that bang time occurs significantly after the end of the laser pulse. In sum, the CR-39 RF/nTOF *in situ* calibration method is a simple yet powerful tool for determining calibration coefficients for individual nTOF detectors on OMEGA, but may also be used to improve the absolute yield calibration of nTOF systems on other large ICF facilities such as the NIF and LMJ.



## 6 Bibliography

1. Kuhn, T.S., *The structure of scientific revolutions*. Vol. 2. 1996: University of Chicago press.
2. Einstein, A., *Zur Elektrodynamik bewegter Körper*. *Annalen der Physik*, 1905. **322**(10): p. 891-921.
3. Atzeni, S.J.M.-T.-V., *The Physics of Inertial Confinement Fusion*. International Series of Monographs on Physics, ed. O.S. Publications. 2004, Oxford, UK: Oxford University Press.
4. Gamow, G., *Zur Quantentheorie des Atomkernes*. *Zeitschrift für Physik*, 1928. **51**(3-4): p. 204-212.
5. Cockcroft, J. and E. Walton, *Experiments with high velocity positive ions. II. The disintegration of elements by high velocity protons*. *Proceedings of the Royal Society of London. Series A*, 1932. **137**(831): p. 229-242.
6. Schawlow, A.L. and C.H. Townes, *Infrared and Optical Masers*. *Physical Review*, 1958. **112**(6): p. 1940-1949.
7. Nuckolls, J. and L. Wood, *Laser Compression of Matter to Super-High Densities: Thermonuclear (CTR)*. *Nature*, 1972. **239**: p. 139.
8. Matzen, M.K., et al., *Pulsed-power-driven high energy density physics and inertial confinement fusion research*. *Physics of Plasmas*, 2005. **12**(5): p. 055503-16.
9. George, H.M., I.M. Edward, and R.W. Craig, *The National Ignition Facility: enabling fusion ignition for the 21st century*. *Nuclear Fusion*, 2004. **44**(12): p. S228.
10. Boehly, T.R., et al., *Initial performance results of the OMEGA laser system*. *Optics Communications*, 1997. **133**(1-6): p. 495-506.
11. Keane, C., D. Kovar, and Y. Thio, *Report of the Interagency Task Force on High Energy Density Physics*. National Science and Technology Council, Committee on Science, OSTP, Washington, DC, 2007.
12. Forrest, C.J., et al., *High-resolution spectroscopy used to measure inertial confinement fusion neutron spectra on Omega (invited)*. *Review of Scientific Instruments*, 2012. **83**(10): p. 10D919-6.
13. Frenje, J.A., et al., *Probing high areal-density cryogenic deuterium-tritium implosions using downscattered neutron spectra measured by the magnetic recoil spectrometer*. *Physics of Plasmas*, 2010. **17**(5): p. 056311.
14. Betti, R., et al., *Progress in hydrodynamics theory and experiments for direct-drive and fast ignition inertial confinement fusion*. *Plasma Physics and Controlled Fusion*, 2006. **48**(12B): p. B153.
15. Besnard, D., *The megajoule laser program — ignition at hand*. *The European Physical Journal D - Atomic, Molecular, Optical and Plasma Physics*, 2007. **44**(2): p. 207-213.
16. Charles, L., *The LMJ program: An overview*. *Journal of Physics: Conference Series*, 2010. **244**(1): p. 012003.
17. Schmid, G.J., et al., *CVD diamond as a high bandwidth neutron detector for inertial confinement fusion diagnostics*. *Review of Scientific Instruments*, 2003. **74**(3): p. 1828-1831.

18. Cable, M.D. and M.B. Nelson, *Neutron yield measurements with current-mode neutron time-of-flight detectors (abstract)*. Review of Scientific Instruments, 1988. **59**(8): p. 1738-1738.
19. Lerche, R.A., et al., *Laser fusion ion temperatures determined by neutron time-of-flight techniques*. Applied Physics Letters, 1977. **31**(10): p. 645-647.
20. Lerche, R.A. and B.A. Remington, *Detector distance selection for neutron time-of-flight temperature measurements*. Review of Scientific Instruments, 1990. **61**(10): p. 3131-3133.
21. Russotto, M.A. and R.L. Kremens, *Measurement of fuel ion temperatures in ICF implosions using current-mode neutron time-of-flight detectors*. Review of Scientific Instruments, 1990. **61**(10): p. 3125-3127.
22. Murphy, T.J. and R.A. Lerche, *Development of a geometry-compensated neutron time-of-flight detector for ICF applications with approximately 200 ps time response*. Review of Scientific Instruments, 1992. **63**(10): p. 4883-4885.
23. Murphy, T.J., et al., *Ion-temperature measurement of indirectly driven implosions using a geometry-compensated neutron time-of-flight detector*. Review of Scientific Instruments, 1995. **66**(1): p. 930-932.
24. Brysk, H., *Fusion neutron energies and spectra*. Plasma Physics, 1973. **15**(7): p. 611.
25. Lerche, R.A., et al., *Neutron emission time measurements for ICF targets*. Review of Scientific Instruments, 1988. **59**(8): p. 1697-1699.
26. Forrest, C., et al., *Measuring Areal Density Using nT Elastic Scattering*. Bulletin of the American Physical Society, 2011. **56**.
27. Murphy, T.J., R.E. Chrien, and K.A. Klare, *Neutron time-of-flight signals from expanding or contracting spherical sources*. Review of scientific instruments, 1997. **68**(1): p. 614-617.
28. Murphy, T.J., R.E. Chrien, and K.A. Klare, *Interpretation of neutron time-of-flight signals from current-mode detectors*. Review of scientific instruments, 1997. **68**(1): p. 610-613.
29. Ali, Z., et al., *Tests and calibration of NIF neutron time of flight detectors*. Review of scientific instruments, 2008. **79**: p. 10E527.
30. Ruiz, C.L., et al., *Absolute calibration of a total yield indium activation detector for DD and DT neutrons*. Review of scientific instruments, 1992. **63**(10): p. 4889-4891.
31. Seguin, F.H., et al., *Spectrometry of charged particles from inertial-confinement-fusion plasmas*. Review of scientific instruments, 2003. **74**(2): p. 975-995.
32. Frenje, J.A., et al., *Absolute measurements of neutron yields from DD and DT implosions at the OMEGA laser facility using CR-39 track detectors*. Review of scientific instruments, 2002. **73**(7): p. 2597-2605.
33. Rygg, J.R., et al., *Proton Radiography of Inertial Fusion Implosions*. Science, 2008. **319**(5867): p. 1223-1225.
34. Casey, D.T., et al., *Evidence for Stratification of Deuterium-Tritium Fuel in Inertial Confinement Fusion Implosions*. Physical Review Letters, 2012. **108**(7): p. 075002.
35. Casey, D.T., et al., *Measurements of the  $T(t,2n)^4\text{He}$  Neutron Spectrum at Low Reactant Energies from Inertial Confinement Implosions*. Physical Review Letters, 2012. **109**(2): p. 025003.

36. Casey, D.T., et al., *Measuring the absolute deuterium--tritium neutron yield using the magnetic recoil spectrometer at OMEGA and the NIF*. Review of Scientific Instruments, 2012. **83**(10): p. 10D912-3.
37. Seguin, F.H., et al., *Advances in compact proton spectrometers for inertial-confinement fusion and plasma nuclear science*. Review of Scientific Instruments, 2012. **83**(10): p. 10D908-3.
38. Manuel, M.J.E., et al., *Source characterization and modeling development for monoenergetic-proton radiography experiments on OMEGA*. Review of scientific instruments, 2012. **83**(6): p. 063506-9.
39. Zylstra, A.B., et al., *Charged-particle spectroscopy for diagnosing shock rho R and strength in NIF implosions*. Review of scientific instruments, 2012. **83**(10): p. 10D901-3.
40. Zylstra, A.B., et al., *Using high-intensity laser-generated energetic protons to radiograph directly driven implosions*. Review of scientific instruments, 2012. **83**(1): p. 013511-9.
41. Zylstra, A.B., et al., *Measurements of hohlraum-produced fast ions*. Physics of Plasmas, 2012. **19**(4): p. 042707.
42. Frenje, J.A., et al., *First measurements of the absolute neutron spectrum using the magnetic recoil spectrometer at OMEGA (invited)*. Review of scientific instruments, 2008. **79**(10): p. 10E502-6.
43. Li, C.K. and R.D. Petrasso, *Stopping, straggling, and blooming of directed energetic electrons in hydrogenic and arbitrary-Z plasmas*. Physical Review E, 2006. **73**(1): p. 016402.
44. Frenje, J.A., et al., *A neutron spectrometer for precise measurements of DT neutrons from 10 to 18 MeV at OMEGA and the National Ignition Facility*. Review of scientific instruments, 2001. **72**(1): p. 854-858.
45. Sinenian, N., et al., *The response of CR-39 nuclear track detector to 1--9 MeV protons*. Review of scientific instruments, 2011. **82**(10): p. 103303-7.
46. Manuel, M.J.E., et al., *Changes in CR-39 proton sensitivity due to prolonged exposure to high vacuums relevant to the National Ignition Facility and OMEGA*. Review of scientific instruments, 2011. **82**(9): p. 095110-8.
47. Casey, D.T., et al., *The coincidence counting technique for orders of magnitude background reduction in data obtained with the magnetic recoil spectrometer at OMEGA and the NIF*. Review of scientific instruments, 2011. **82**(7): p. 073502-8.
48. Zylstra, A.B., et al., *A new model to account for track overlap in CR-39 data*. Nuclear Instruments and Methods in Physics Research Section A: Accelerators, Spectrometers, Detectors and Associated Equipment, 2012. **681**(0): p. 84-90.
49. Zylstra, A.B., et al., *Increasing the energy dynamic range of solid-state nuclear track detectors using multiple surfaces*. Review of scientific instruments, 2011. **82**(8): p. 083301-7.
50. Sinenian, N., *Fast-Ion Spectrometry of ICF Implosions and Laser-Foil Experiments at the OMEGA and MTW Laser Facilities*, in *Nuclear Science and Engineering*. 2013, Massachusetts Institute of Technology: Cambridge. p. 225.

51. Lindl, J., *Development of the indirect-drive approach to inertial confinement fusion and the target physics basis for ignition and gain*. *Physics of Plasmas*, 1995. **2**(11): p. 3933-4024.
52. Boughrara, A., H. Beaumevielle, and S. Ouichaoui, *Branching ratios and screening effect in the  $d + d$  nuclear interaction*. *EPL (Europhysics Letters)*, 1999. **48**(3): p. 264.
53. Bosch, H.-S. and G.M. Hale, *Improved formulas for fusion cross-sections and thermal reactivities*. *Nuclear Fusion*, 1992. **32**(4): p. 611.
54. Erba, M., *New parametrizations of  $dd$  fusion cross sections*. *Journal of Physics D: Applied Physics*, 1994. **27**(9): p. 1874.
55. Liboff, R.L., *Introductory Quantum Mechanics*. 2003: Addison-Wesley.
56. Sinenian, N., et al., *Upgrade of the MIT Linear Electrostatic Ion Accelerator (LEIA) for nuclear diagnostics development for Omega, Z and the NIF*. *Review of scientific instruments*, 2012. **83**(4): p. 043502-11.
57. Hicks, D., *Charged-Particle Spectroscopy: A New Window on Inertial Confinement Fusion*, in *Nuclear Science and Engineering*. 1999, Massachusetts Institute of Technology: Massachusetts Institute of Technology.

## Appendix 1: Derivation of the Fusion Reaction Rate

This section contains a derivation of the fusion reaction rate from first principles.

*"...everything should be as simple as possible, but not simpler..."*

*—Albert Einstein—*

Fusion reactions occur when two atomic nuclei of low atomic numbers (low  $Z$ ) combine to create a new nucleus with higher  $Z$ . The reaction is also accompanied by the production of light fusion products such as alpha particles, neutrons, protons, and gammas. The reaction is often written as:



where  $X_1$  and  $X_2$  are the reacting nuclei,  $X_3$  is the new nucleus,  $X_4$  is the light fusion product(s)—depending on the reaction there may be more than one—and  $Q_F$  is the fusion energy released which is based on the rest mass differential between the reactant nuclei and the fusion products (this energy can also be thought of as the difference between the binding energy of the fusion products and reacting nuclei). An alternative notation for the fusion reaction is written as:  $X_1(X_2, X_3)X_4$ .

Due to their positive charge, nucleons experience a Coulomb repulsion force at distances greater than the sum of the radii of the two reacting nuclei ( $r_n$ ), which pushes the nuclei apart. However, at distances on the order of  $r_n$ , a strong nuclear force begins to exert itself that acts to bind the nucleons together and competes with the Coulomb repulsion force at distances slightly less than  $r_n$ . The binding energy of the strong force per nucleon (MeV/A) was given previously in Figure 4. The “fusion problem” then, is for the two nuclei to approach one another at distances on the order of an atomic radius (usually a few femtometers) so that the Coulomb repulsion force is overcome and the strong nuclear binding force dominates. When this occurs the two nuclei are attracted by the strong nuclear force and bind together to create a new nucleus. For two nuclei  $X_1$ , and  $X_2$ , the

potential of the Coulomb force between the two particles is given by Coulomb's law and the potential can be readily derived from Maxwell's equations and is given as:

$$V_{Coul}(r) = \frac{Z_1 Z_2 q^2}{4\pi\epsilon_0 r} \quad (\text{A1.2})$$

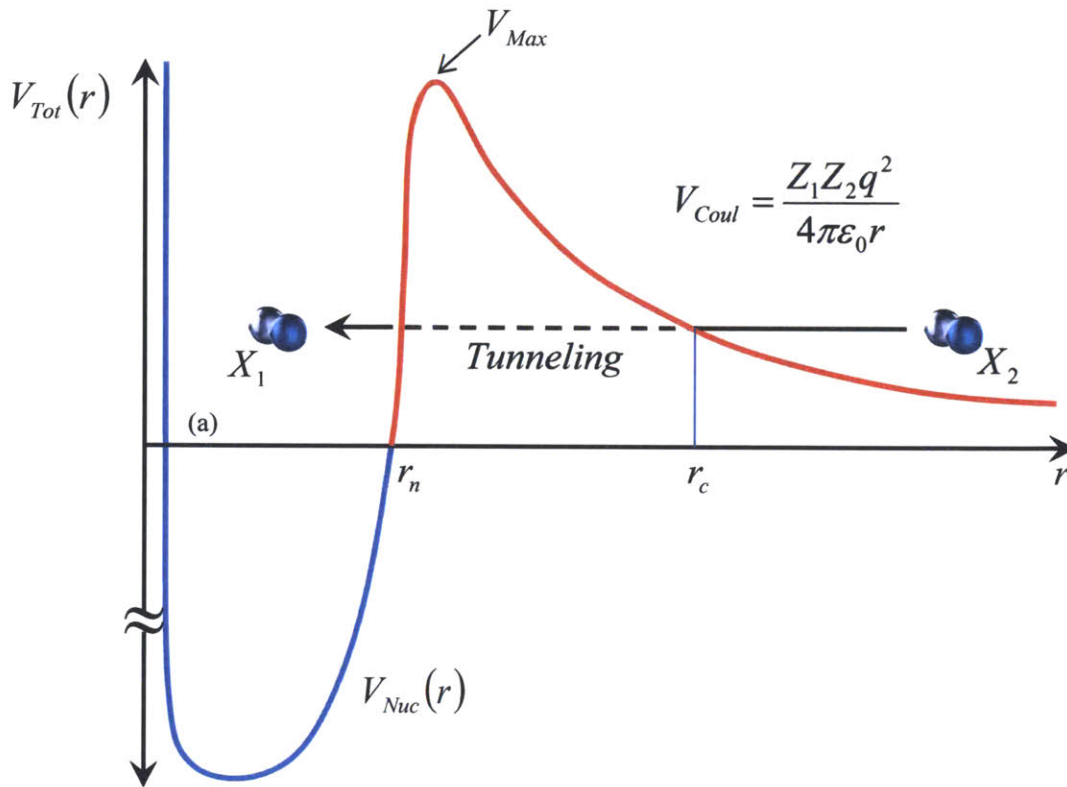
where  $q$  is the charge of an electron ( $1.602 \times 10^{-19}$  C),  $\epsilon_0$  is the permittivity of free space, and  $r$  (measured in meters) is the separation distance between nuclei  $X_1$  and  $X_2$ . In contrast to the Coulomb potential, the potential due to the strong nuclear force is much more complicated and does not have an analogous derivation from first principles in the same way that the Coulomb potential and Lorentz force is derived from Maxwell's equations. Rather, the strong nuclear force is often characterized empirically through scattering experiments where a functional form for the force is fitted to the data. Notwithstanding, the qualitative behavior of the nuclear force is straightforward. At extremely short distances ( $r \ll r_n$ ) the nuclear force is highly repulsive. Were it not so nucleons would continue to collapse into one another and there would be no separation between them. At slightly greater distances ( $r < r_n$ ) the nuclear force becomes highly attractive so as to bind the nucleons together. At these short ranges the nuclear force dominates the Coulomb repulsion force so that multiple protons (and neutrons) are held together within close proximity despite the protons having positive charge. At a range approximately equal to the nuclear radius, the nuclear binding force drops off significantly and the Coulomb repulsive force begins to dominate. At a short distance greater than the nuclear radius, the Coulomb potential peaks and then falls off as  $1/r$ . A typical potential profile of the fusion problem is given in **Figure 27**.

For the fusion problem, we take the nuclear radius ( $r_n$ ) to be the sum of the radii of the two reacting nuclei  $X_1$  and  $X_2$ . This distance is typically measured in femtometers ( $10^{-15}$  m) which is equivalent to 1 Fermi (F). The sum of the two radii is given as:

$$r_n \cong R_0 \times (A_{X_1}^{1/3} + A_{X_2}^{1/3}) \quad (\text{A1.3})$$



where  $R_0$  is determined experimentally and is equal to  $\sim 1.4 F$ ,  $A_{X_1}$  is the atomic mass number of  $X_1$ , and  $A_{X_2}$  is the atomic mass number of  $X_2$ .



**Figure 27. The "fusion problem" where  $V_{Tot}(r)$  is the potential energy barrier particle  $X_2$  experiences as it approaches particle  $X_1$  and  $r$  is the distance between particles.**

Upon looking at Figure 27, we see that under classical mechanics the incident particle ( $X_2$ ) would need to have kinetic energy greater than the peak Coulomb potential energy ( $V_{Max}$ ) to overcome the potential barrier and fuse to  $X_1$ . If only classical effects were in play, fusion reactions would be very rare. For example, for p-p fusion—one of the primary fusion process in the Sun—the sum of the nuclear radii is:  $r_n \approx 3 F$ . This leads to a Coulomb barrier potential energy of  $\sim 500\text{keV}$ . However, even in the very center of our Sun, particle energy distributions have an average energy of only  $\sim 1.4 \text{ keV}$ , significantly less than the Coulomb barrier. If only classical mechanics were at play, only particles on the tail end of the distribution with energies substantially higher than the average  $1.4\text{keV}$  particle energy would be able to overcome the  $500\text{keV}$  barrier energy. If classical mechanics were the physical affects going on fusion reactions on the sun would be very rare.

With quantum mechanics, however, nuclei exhibit a wave/particle duality so that the position of a particle has a probability of existing over a range of locations. Because of this wave nature, the incident particle ( $X_2$ ) will have a finite probability of passing through the Coulomb barrier even if its kinetic energy is much lower than the potential barrier. In quantum mechanics, the behavior of a particle passing through a potential barrier where the potential energy is greater than the kinetic energy is known as “tunneling.”

The tunneling probability for two nuclei was first derived by George Gamow in 1928 and his original approach is followed closely here[4]. The fusion problem can be represented in quantum mechanics with the multi-particle Hamiltonian operator as a three dimensional system comprised of particles  $X_1$  and  $X_2$  and the potential forces acting between them. The system described by Figure 27 is represented in terms of the Schrödinger equation as:

$$\left( \frac{-\hbar^2}{2m_1} \nabla_{r_1}^2 + \frac{-\hbar^2}{2m_2} \nabla_{r_2}^2 \right) \Psi(r_1, r_2) + V(r_1, r_2) \Psi(r_1, r_2) = E \Psi(r_1, r_2) \quad (\text{A1.4})$$

where  $m_1$  is the mass of  $X_1$ ,  $m_2$  is the mass of  $X_2$ ,  $\psi(r_1, r_2)$  is the wave-function of the system,  $V(r_1, r_2)$  is the total potential acting on the two particles (the sum of both the nuclear and Coulomb potentials), and  $E$  is the kinetic energy of the system. The solution to the Schrödinger equation that we seek is a wave-function,  $\psi(r_1, r_2)$ , which contains all information concerning the wave/particle nature of the interaction between the two particles. The probability of  $X_2$  tunneling through the barrier and fusing with  $X_1$  can be determined from the wave-function as will be shown later in the derivation.

The problem can be simplified significantly by representing equation A1.4 in the center of mass frame of reference. In this reference it can be shown that the center of mass of the system moves at a constant velocity. Because of this we can perform a Galilean coordinate transformation from the original lab frame to a frame of reference on the center of mass system where the origin of the new coordinate system is at the center of mass. In the center of mass frame, the two particle system is represented as a single particle with mass  $m_r$  that is acted on by a central force whose origin is at the center of mass. Under the center of mass representation, the Schrödinger equation in A1.4 becomes:

$$\left( \frac{-\hbar^2}{2M} \nabla_{\mathbf{R}_{CM}}^2 + \frac{-\hbar^2}{2m_r} \nabla_{\mathbf{r}}^2 \right) \Psi(\mathbf{r}, \mathbf{R}_{CM}) + V(\mathbf{r}) \Psi(\mathbf{r}, \mathbf{R}_{CM}) = E \Psi(\mathbf{r}, \mathbf{R}_{CM}) \quad (\text{A1.5})$$

where  $\mathbf{R}_{CM}$  is the center of mass coordinate,  $\mathbf{r}$  is still the relative distance between particles  $X_1$  and  $X_2$  ( $\mathbf{r} = \mathbf{r}_2 - \mathbf{r}_1$ ),  $M$  is the total mass ( $M = m_1 + m_2$ ), and  $m_r$  is the reduced mass ( $m_r = m_1 m_2 / (m_1 + m_2)$ ). Note that both the Coulomb potential and strong nuclear potential are functions of the distance between particles and therefore only functions of  $\mathbf{r}$ . For fusion reactions we are only interested in the inter-particle affects and can separate out the relative behavior from the center of mass components given in Equation A1.5 using separation of variables. For this we express the wave function as the product of two wave functions, one for the relative particle and the other for the center of mass particle. This is given by Equation A1.6:

$$\Psi(\mathbf{r}, \mathbf{R}_{CM}) = \psi(\mathbf{r}) \cdot \phi(\mathbf{R}_{CM}) \quad (\text{A1.6})$$

In addition, we can express the total kinetic energy of the system in terms of the energy attributed to the center of mass particle ( $E_{CM}$ ) and the relative particle ( $E_r$ ) where  $E = E_{CM} + E_r$ . By substituting A1.6 into A1.5 and substituting in the separate energy components we separate A1.5 into two equations as given in Equation 1.7a and 1.7b.

$$\left( \frac{-\hbar^2}{2m_r} \nabla_{\mathbf{r}}^2 \right) \psi(\mathbf{r}) + V(\mathbf{r}) \psi(\mathbf{r}) = E_r \psi(\mathbf{r}) \quad (\text{A1.7a})$$

$$\left( \frac{-\hbar^2}{2M} \nabla_{\mathbf{R}_{CM}}^2 \right) \phi(\mathbf{R}_{CM}) = E_{CM} \phi(\mathbf{R}_{CM}) \quad (\text{A1.7b})$$

With an expression for the relative particle motion between  $X_1$  and  $X_2$  we now express A1.7a in spherical coordinates observing that  $V(\mathbf{r})$  is angularly independent (e.g. the Coulomb force and strong nuclear force are angularly symmetric). Doing so allows us to express A1.7a as:

$$\frac{-\hbar^2}{2m_r} \nabla^2 \psi(r, \theta, \phi) + V(r) \psi(r, \theta, \phi) = E \psi(r, \theta, \phi) \quad (\text{A1.8})$$

where we have dropped the subscript for  $E_r$  which from here on will simply be given as  $E$ . In spherical coordinates, the Laplacian of the wave-function is given as:

$$\nabla^2 \psi(r, \theta, \phi) = \frac{1}{r^2} \frac{\partial}{\partial r} \left( r^2 \frac{\partial \psi}{\partial r} \right) + \frac{1}{r^2 \sin \theta} \frac{\partial}{\partial \theta} \left( \sin \theta \frac{\partial \psi}{\partial \theta} \right) + \frac{1}{r^2 \sin^2 \theta} \frac{\partial^2 \psi}{\partial \phi^2} \quad (\text{A1.9})$$

For three dimensional Schrödinger equations of this kind, it can be shown that if the potential is spherically symmetric (i.e. is angularly invariant), then the wave function can be expressed as the product of three separable functions of  $r$ ,  $\theta$ , and  $\phi$ . In our case both the strong nuclear potential and Coulomb potential are spherically symmetric so the wave function is expressed in terms of the separable functions as given by:

$$\psi(r, \theta, \phi) = R(r) \Theta(\theta) \Phi(\phi) \quad (\text{A1.10})$$

By using the separable form of the wave function along with A1.8, and A1.9, the Schrödinger equation in terms of the separable components can be expressed as:

$$\frac{-\hbar^2}{2m_r} \left[ \frac{1}{R(r)} \frac{\partial}{\partial r} \left( r^2 \frac{\partial R(r)}{\partial r} \right) + \frac{1}{\sin(\theta) \Theta(\theta)} \frac{\partial}{\partial \theta} \left( \sin \theta \frac{\partial \Theta(\theta)}{\partial \theta} \right) + \frac{1}{\sin^2(\theta) \Phi(\phi)} \frac{\partial^2 \Phi(\phi)}{\partial \phi^2} \right] + r^2 [V(r) - E] = 0 \quad (\text{A1.11})$$

This form of the Schrödinger equation is particularly useful since the radial and angular components appear as independent terms and are completely separated. The radial component is given as:

$$\frac{1}{R(r)} \frac{\partial}{\partial r} \left( r^2 \frac{\partial R(r)}{\partial r} \right) + \frac{2m_r r^2}{\hbar^2} [V(r) - E] = 0 \quad (\text{A1.12})$$

While the angular component can be expressed in terms of an eigenvalue problem as:

$$L^2 = \frac{\hbar^2}{\sin^2 \theta} \frac{\partial}{\partial \theta} \left( \sin \theta \frac{\partial \Theta(\theta)}{\partial \theta} \right) + \frac{1}{\sin^2 \theta} \frac{\partial^2 \Phi(\phi)}{\partial \phi^2} \quad (\text{A1.13})$$

The eigenfunctions to the eigenvalue problem of equation A1.13 are given in the form of spherical harmonics and can be represented using Legendre polynomials. The derivation of the eigenfunctions is beyond the scope of the present derivation, but a complete derivation can be found in standard introductory texts on quantum mechanics such as Liboff [55]. The eigenvalue solutions to the eigenvalue problem give the allowed values of the angular momentum,  $L$ , of the system. The angular momentum can be expressed in terms of the angular quantum number  $l$  and  $m$ , where the square of the angular momentum expressed solely in terms of  $l$  is given as:

$$L^2 = \hbar^2 l(l+1) \quad (\text{A1.14})$$

Using A1.14 as the solution to the angular component, the complete Schrödinger equation can be expressed in terms of the angular eigenvalue solution and radial eigenvalue problem by combining A1.11, A1.13 and A1.14:

$$\frac{-\hbar^2}{2m_r} \left[ \frac{1}{R(r)} \frac{\partial}{\partial r} \left( r^2 \frac{\partial R(r)}{\partial r} \right) + l(l+1) \right] + r^2 [V(r) - E] = 0 \quad (\text{A1.15})$$

Finally, we can represent the radial component of the wave function by substituting  $u(r) = R(r) \cdot r$  into equation A1.15. Doing this we obtain:

$$\left[ \frac{-\hbar^2}{2m_r} \frac{\partial^2}{\partial r^2} + \frac{\hbar^2 l(l+1)}{2m_r r^2} + V(r) - E_{(n,l)} \right] \cdot u_{(n,l)} = 0 \quad (\text{A1.16})$$

This result is much more straight forward and easier to work with. By recognizing the angular invariance of the nuclear and Coulomb potentials, and representing the problem in the center of mass frame, the whole system is reduced to a one dimensional problem with an effective particle in the center of mass frame.

Also, from A1.16 we see an additional potential term that is introduced from the solution to the angular component of the Schrödinger equation. This potential is related to the angular momentum of the system and is characterized by the quantum number  $l$ . At higher values of  $l$ , the angular momentum increases and adds an additional repulsive force to the existing Coulomb and nuclear force. The overall effective potential is the sum of all these potentials and is given as:

$$V_{\text{eff}}(r) = \frac{\hbar^2 l(l+1)}{2m_r r^2} + \frac{Z_1 Z_2 q^2}{4\pi\epsilon_0 r} + V_{\text{Nuc}}(r) \quad (\text{A1.17})$$

From this the Schrödinger equation can be expressed as:

$$\left[ \frac{-\hbar^2}{2m_r} \frac{\partial^2}{\partial r^2} + V_{\text{eff}}(r) - E_{(n,l)} \right] u_{(n,l)} = 0 \quad (\text{A1.18})$$

As can be seen by equation A1.17 and Figure 14, the effective potential is not constant and varies as a function of  $r$ . Looking back to Figure 14 we can identify three distinct regions where the potential varies. The first region is where  $r < r_n$  and the strong nuclear potential dominates. In this region the kinetic energy is greater than the potential energy. Solving the Schrödinger expressed in equation A1.18 for  $r < r_n$ , where  $E > V(r)$  we obtain the following radial wave equation:

$$u_1(r) = A \exp^{ikr} + B \exp^{-ikr} \quad (\text{A1.19})$$

where  $A$  and  $B$  are constants introduced from the solution to Equation A1.18 and represent the magnitudes of the two wave solutions. The first term represents a wave traveling from left to right and the second term represents a wave traveling right to left. The wave number for both terms,  $k$ , is given as:

$$k(r) = \sqrt{\frac{2m_r (E - V(r))}{\hbar^2}} \quad (\text{A1.20})$$

Another region of interest is the region where the coulomb potential dominates the nuclear potential, but the kinetic energy is greater than the Coulomb potential. In this region  $r > r_c$ , (where  $r_c$  is the distance at which the kinetic and potential energies are equal). Since  $E > V(r)$  the form of the solution is the same as in region I and the wave also propagates. The solution to the wave equation in this region is given as:

$$u_{\text{III}}(r) = E \exp^{ikr} + F \exp^{-ikr} \quad (\text{A1.21})$$

where E and F are constants introduced from the differential equation and represent the magnitudes of the forward and reverse traveling waves. The expression for the wave number remains the same as in region I (as given by Equation A1.20), although the values will be different since the potential  $V(r)$  for  $r > r_c$  is dominated by the Coulomb potential whereas in region I the nuclear potential dominates. The key similarity between regions I and III is that since the wavenumber  $k$  is real ( $E > V(r)$ ) the solutions to the equations result in traveling waves that are oscillatory. Whereas in region II the wavenumber  $k$  is imaginary and the wave is evanescent.

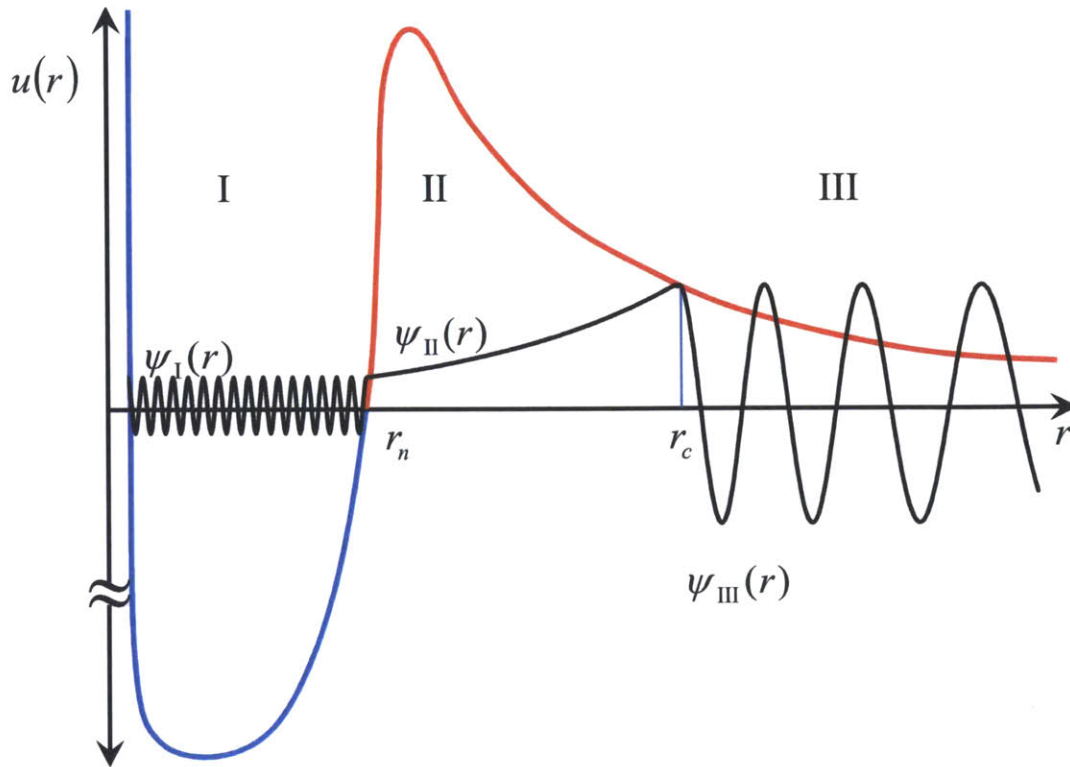
The region of most interested for tunneling is the region between  $r_n < r < r_c$ , where  $E < V(r)$ , which under classical representation would not allow the particle to penetrate. In this region under the quantum mechanical representation the wave is no longer freely propagating as it was given by the wave-function solutions in A1.19 and A1.21, but is expressed as an evanescent wave that decays exponentially from  $r_c$  to  $r_n$ . The solution to the wave function in this region is given as:

$$u_{\text{II}}(r) = C \exp^{\kappa r} + D \exp^{-\kappa r} \quad (\text{A1.22})$$

where C and D are constants introduced from the differential equation and represent the magnitudes of the two evanescent wave solutions. The decay constant,  $\kappa$  is given as:

$$\kappa(r) = \sqrt{\frac{2m_r(V(r) - E)}{\hbar^2}} \quad (\text{A1.23})$$

The behavior of the wave function for all three regions is given in **Figure 28**.



**Figure 28. The wave-function solution to the Schrodinger equation for the fusion problem.**

From the wave-functions in each region, the tunneling probability is determined by solving for the wave function magnitudes taking into account the appropriate boundary and continuity conditions. The derivation is somewhat involved, but in the end the probability is determined to be:

$$P_{Tun} = \exp^{-2G} \quad (A1.24)$$

Here G is a new parameter called the Gamow factor and is given as:

$$G = \int_{r_n}^{r_c} \sqrt{\frac{2m_r}{\hbar^2} (V_{eff}(r) - E)} dr \quad (A1.25)$$

In many cases of interest, the Coulomb potential dominates the nuclear potential and the angular momentum repulsive force (as given previously in A1.17) so that the effective



potential can be approximated as just the Coulomb potential. Taking the potential to be the Coulomb potential, the Gamow energy expression is reduced to:

$$G = \int_{r_n}^{r_c} \sqrt{\frac{2m_r}{\hbar^2} \left( \frac{Z_1 Z_2 q^2}{4\pi\epsilon_0 r} - E \right)} dr \quad (\text{A1.26})$$

which, when solving for the integral, gives the following relation:

$$G = \sqrt{\frac{2m_r}{\hbar^2 E} \frac{Z_1 Z_2 q^2}{4\pi\epsilon_0}} \left[ \cos^{-1} \sqrt{\frac{r_n}{r_c}} - \sqrt{\frac{r_n}{r_c} \left( 1 - \frac{r_n}{r_c} \right)} \right] \quad (\text{A1.27})$$

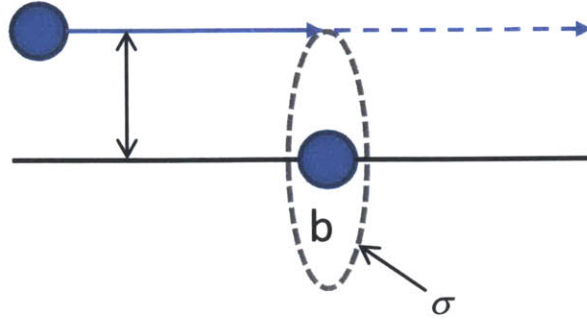
When the kinetic energy of the particle (E) is significantly less than the peak potential energy ( $V_{\text{Max}}$ ),  $E \ll V_{\text{Max}}$ , then  $r_n \ll r_c$  and A1.27 reduces to:

$$G = \sqrt{\frac{2m_r}{\hbar^2 E} \frac{Z_1 Z_2 q^2}{4\pi\epsilon_0}} \frac{\pi}{2} \quad (\text{A1.28})$$

In this form we can express the probability of tunneling as a function of energy as:

$$P_{\text{Tun}}(E) = \exp\left(-\sqrt{\frac{E_G}{E}}\right), \text{ where } E_G = \frac{Z_1^2 Z_2^2 q^4 m_r}{8\epsilon_0 \hbar^2} \quad (\text{A1.29})$$

With the probability of two particles tunneling as a function of energy determined, we now look to the nuclear reaction rate itself. The collision between two nuclei can be characterized in terms of the vertical separation between two particles that are passing by each other. A "collision" between the two particles is defined in terms of the vertical separation such that for a particle passing a distance greater than some value  $b$  is taken as the two particles missing, whereas any particle passing a distance less than  $b$  is taken as the two particles colliding. The defining distance between a collision and a miss is known as the impact parameter  $b$  and is illustrated in Figure 29.



**Figure 29. Impact parameter  $b$ , and cross section of nuclear collision.**

In addition, the impact parameter  $b$  defines a surface within which a collision will occur. This surface is known as the nuclear cross section ( $\sigma$ ) and is given by  $\sigma = \pi b^2$ . A reasonable approximation for the impact parameter is obtained from the conservation of angular momentum. Classically, the angular momentum of the reduced particle in the center of mass frame can be shown to be equal to  $bm_r v$ , where  $b$  is the impact parameter,  $m_r$  is the reduced mass and  $v$  is the reduced particle velocity. On the other hand from equation A1.14, we see that for low impact parameters, the quantum mechanical angular momentum is on the order of  $\hbar$ . Therefore, in order for a collision to occur,  $bm_r v \leq \hbar$ . Expressed in terms of the kinetic energy:

$$b \leq \frac{\hbar}{\sqrt{2m_r}} \frac{1}{E^{1/2}} \quad (\text{A1.30})$$

Even if the particles collide, fusion will only occur if the particles are able to tunnel through the Coulomb barrier. Therefore, the full nuclear cross section taking into account the tunneling probability is given as:

$$\sigma = \pi b^2 \cdot P_{Tun} \quad (\text{A1.31})$$

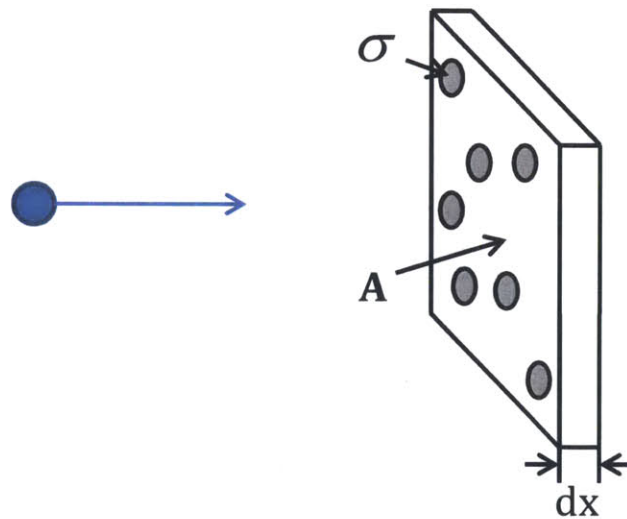
Substituting in A1.30 and A1.31 gives the cross section as a function of energy:

$$\sigma(E) = \frac{\pi \hbar^2}{2m_r} \cdot \frac{1}{E} \cdot \exp\left(-\sqrt{\frac{E_G}{E}}\right), \quad \text{where} \quad E_G = \frac{Z_1^2 Z_2^2 q^4 m_r}{8\epsilon_0 \hbar^2} \quad (\text{A1.32})$$

Now consider the case where instead of two particles colliding, a single particle is launched into a sea of target particles with density  $n_2$  [ $\text{m}^{-3}$ ]. The probability of a collision in this case is given as the ratio of the surface area covered by target particles to the total area. This ratio is given as:

$$P_{Rn} = \frac{N\sigma}{A} = \frac{n_2 A \sigma dx}{A} = n_2 \sigma dx \quad (\text{A1.33})$$

where  $P_{Rn}$  is the probability of a reaction,  $N$  is the number of target particles,  $A$  is the area of the incremental volume,  $n_2$  is the density of target particles, and  $dx$  is the differential thickness of the volume. The situation is illustrated in Figure 30.



**Figure 30. Fusion collisions with a density of target particles.**

In this case the differential thickness of the reaction volume can be expressed in terms of the velocity:  $dx = v \cdot dt$ . By substituting into A1.33 and dividing by  $dt$  we get the single particle reaction rate:

$$R = \frac{P_{Rn}}{dt} = n_2 \sigma v \quad (\text{A1.34})$$

Now when there is more than just one particle, but rather a whole density ( $n_1$ ) of particles moving toward the target particles, this reaction rate is just the single particle reaction rate times the source particle density. This gives the general fusion reaction rate for two particle densities:

$$R_{12}(v) = n_1 n_2 \sigma(v) v \quad (\text{A1.35})$$

where  $\sigma$  is also a function of the relative velocity between the particles. For practical situations the velocities of each species is not constant and collisions are happening in three dimensions. In this case the particle species is characterized by a Maxwellian velocity distribution as given by Equation A1.36:

$$f_i(v_i) = \left( \frac{m_i}{2\pi k_B T} \right)^{3/2} \exp\left( -\frac{m_i v_i^2}{2k_B T} \right) \quad (\text{A1.36})$$

where  $i$  is the particle species,  $f$  is the velocity distribution function,  $m$  is mass of species  $i$ ,  $k_B$  is Boltzman's constant, and  $T$  is the species temperature. When both species 1 and 2 have separate distribution functions, the reaction rate between the species can be expressed as:

$$R_{12}(v) = \iint \sigma(\mathbf{v}_1 - \mathbf{v}_2) |\mathbf{v}_1 - \mathbf{v}_2| f_1(\mathbf{v}_1) f_2(\mathbf{v}_2) d^3 \mathbf{v}_1 d^3 \mathbf{v}_2 \quad (\text{A1.37})$$

When integrated over the entire velocity distributions of both species this is commonly expressed as

$$R_{12} = n_1 n_2 \langle \sigma v \rangle \quad (\text{A1.38})$$

where  $\langle \sigma v \rangle$  is the rate coefficient and represents the average nuclear reaction rate over both species' velocity distributions. Since the velocity terms are integrated out, by looking at Equation A1.36 one can see that the rate coefficient and therefore fusion reaction rate is only a function of the plasma temperature.

## Appendix 2: MIT Linear Electrostatic Ion Accelerator (LEIA) Ion Beam Current Measurements (Faraday Cup)

The MIT Linear Electrostatic Ion Accelerator (LEIA) [56] is an accelerator-based fusion product generator at the MIT Plasma Science and Fusion center that is primarily used for nuclear diagnostic development for diagnostics fielded in the OMEGA [10] laser, the Z-Machine [8], and the National Ignition Facility [9]. LEIA is capable of producing DD and D<sup>3</sup>He fusion products at rates on the order of  $10^7 \text{ s}^{-1}$  and  $10^6 \text{ s}^{-1}$  respectively. An image of LEIA is given in the figure below.



**Figure 31. Linear Electrostatic Ion Accelerator (LEIA).**

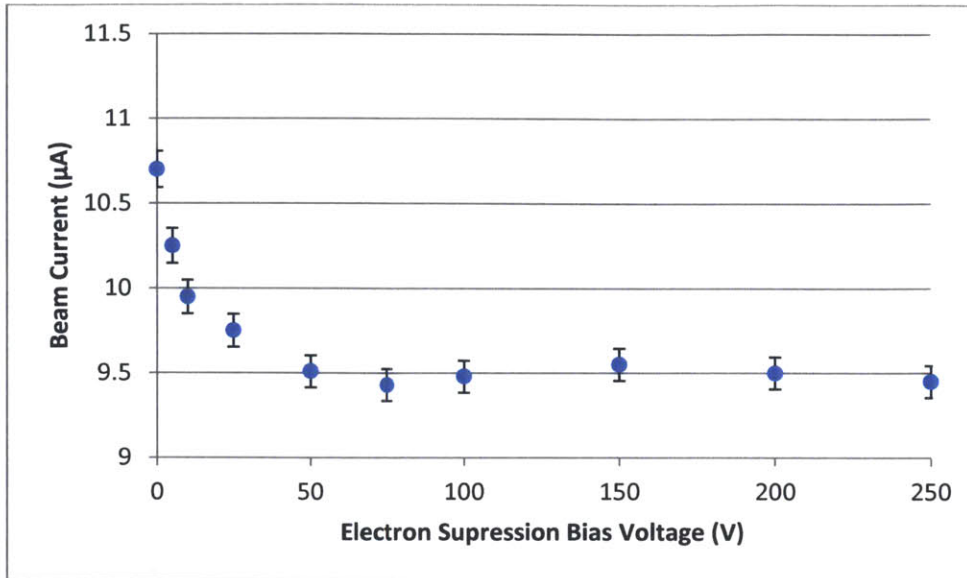
In the accelerator, DD or D<sup>3</sup>He gas is fed into a glass bottle that is ionized using an RF source. After ionization, a  $\sim 5\text{kV}$  probe voltage is used to extract the ions from which they are focused by a  $\sim 3.5\text{kV}$  focus supply and then accelerated down a  $135\text{kV}$  acceleration tube. The ions travel the length of the accelerator to the target chamber where they collide with an erbium deuteride target creating DD or D<sup>3</sup>He fusion products depending on the gas used and target doping (often times the target is doped with <sup>3</sup>He and then hit with a D beam to create D<sup>3</sup>He fusion products instead of running a <sup>3</sup>He beam into the target directly). Energies and yields from the charged particles are then measured using a surface barrier semiconductor detector. A complete overview of LEIA can be found in Sinenian et al [56].

As part of a recent upgrade to the accelerator, a National Electrostatics Corporation FC-50 faraday cup was installed to measure the beam current in-situ during operation. The cup consists of a tantalum collector to limit neutron production and an electron suppression ring to limit electron emission from the cup. The beam current gathered by the collector (on the order of micro amps) is sent to a log-linear operational amplifier that converts the beam current to a  $\pm 10$  V signal. The signal is then read by an Acromag IP network controller which sends the measured signal in real-time to the LEIA control and data acquisition computer where the software converts the  $\pm 10$  V signal back to the actual beam current.

To obtain absolute beam current measurements, the electron suppression ring must be properly biased to direct emitted electrons back into the collector cup. A negative bias creates a field between the suppressor ring and the collector that accelerates electrons toward the collector, while a positively biased suppressor ring accelerates electrons away from the cup and has the effect of increasing the measured current reading above what the beam current actual is.

To determine the optimum bias voltage, a bias voltage sweep was conducted to test the effect of negative polarity biases on the measured beam current. For all sweeps a deuterium beam was used with a beam energy of 120keV. The probe voltage was set to 5.025 kV, and the focus voltage was set to 3.55 kV. The gas pressure in the plasma bottle was set to  $75 \pm 1$  mTorr and the probe current remained constant at 0.9 mA. The measured beam currents for the negative polarity sweep at voltage settings between 0 V and -250 V are given in **Figure 32**. In the plot we see that the initial voltage without any electron suppression is  $10.7 \mu\text{A}$ . As the electron suppression voltage ramps up between 0 and  $\sim -75\text{V}$  the current measurement reduces to around  $9.5 \mu\text{A}$  and then hits a plateau that continues all the way to -500V (although only data points through -500V are given in the plot).

From this we conclude that at ion energies of 120keV, which is in the standard range for LEIA operation (maximum energy being 150keV), the negatively biased electron suppression voltage should be set no less than at -75V in order to obtain accurate beam current measurements by accelerating emitted electrons back into the collector.



**Figure 32. LEIA faraday cup beam current measurements with a negatively biased electron suppression voltages.**





## Appendix 3: Radiochromic Film Slit Width Verification on OMEGA Charged Particle Spectrometers

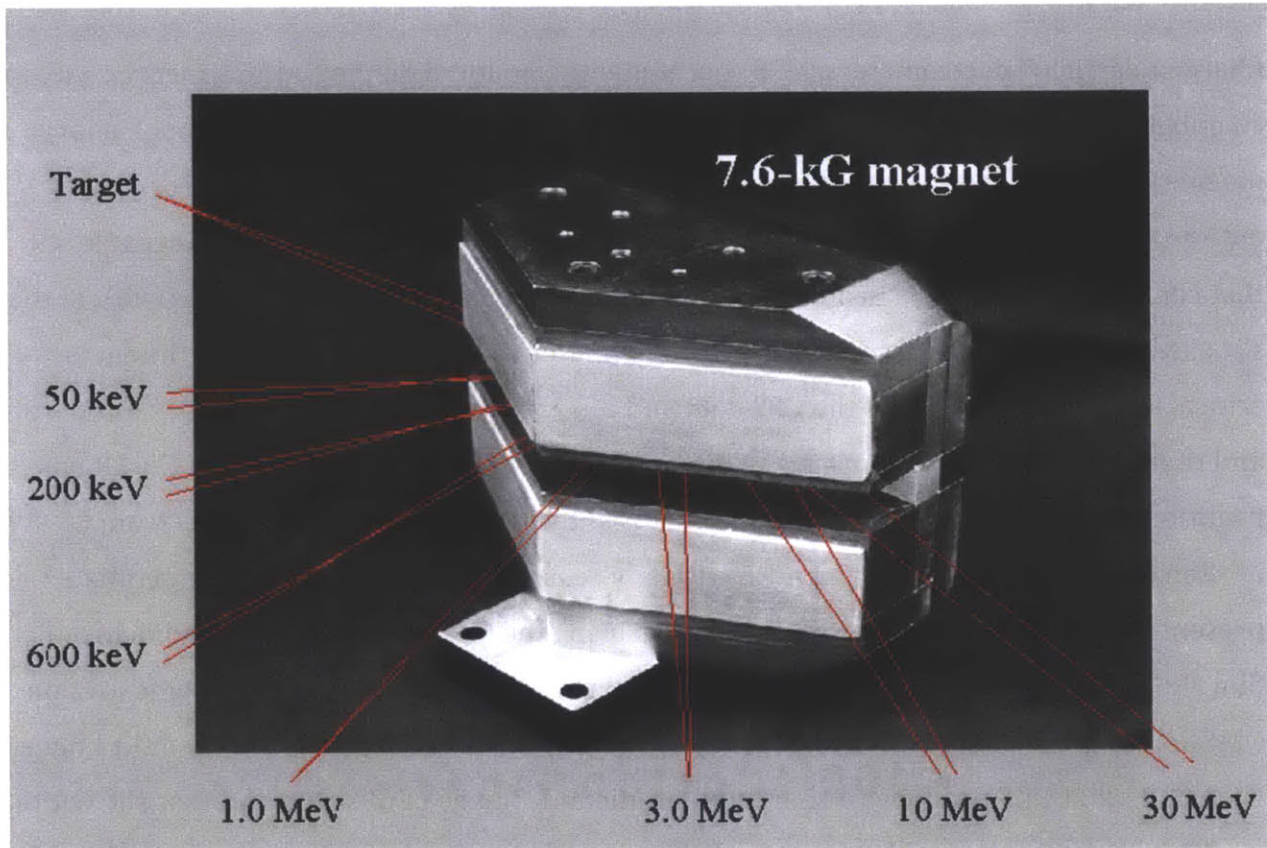
### A4.1 Introduction

Charged Particle Spectrometers (CPS) permanently mounted on the OMEGA target chamber are used to measure energy spectra by passing charged particles through a large magnetic field which separates the particles based on their mass and energy. Prior to entering the magnetic field, the stream of particles passes through an interchangeable slit that collimates the particle beam and limits the influx of particles based on the width of the slit used. Knowing the correct width of the collimator slit fielded on each experiment is critical for proper analysis of the CPS data and it is therefore desirable to have a consistent and repeatable way of verifying the width of the slit used for each experiment. CR-39 has traditionally been used to verify the collimator slit width, but the image quality from CR-39 is often too poor to infer the slit width with any reasonable accuracy. In this appendix I present the results of a new approach to measuring the CPS slit-width using radiochromic film (RCF) instead of CR-39. Nominal and actual slit widths for the two CPS diagnostics on OMEGA are given along with a brief study looking at the effect of parallax on the slit image. I conclude that RCF produces a sharp and predictable image of CPS slits and that slit-width verification can be accomplished using RCF in a consistent and repeatable way. A table of measured slit widths and RCF slit images from all the slits in the CPS1 and CPS2 collimator slit inventories is provided for use as a benchmark for verifying the CPS slit width on future experiments.

### A4.2 Overview

Two Charged Particle Spectrometers (CPS1 and CPS2), that are permanently mounted on the OMEGA target chamber, are used to measure charged particle energy spectra and yields by directing charged particles through a 7.6 kG uniform magnetic field which alters the particles' trajectory based the particle's mass and energy. The position at which particles are detected is determined by the particle gyroradius. An image of the magnet used in both

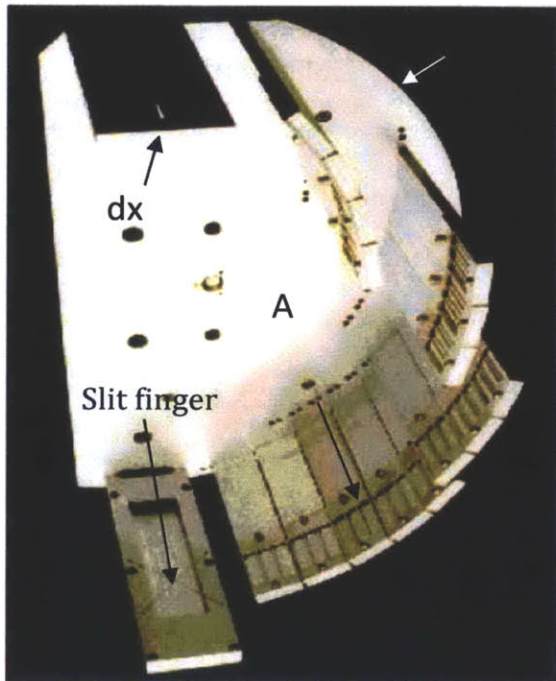
CPS1 and CPS2 is given in **Figure 33** and illustrates where the charged particles enter the magnet from the “target” end as well as multiple possible deflection angles based on particle energy.



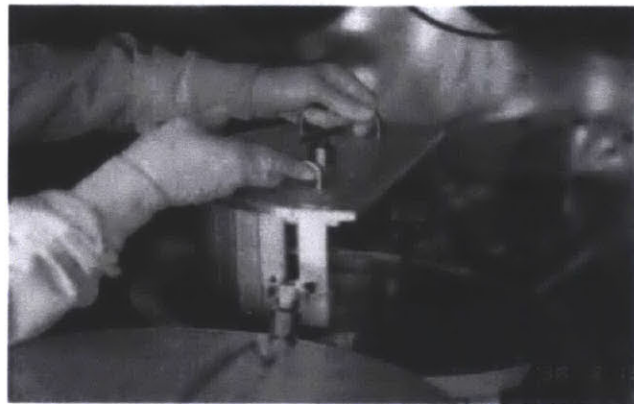
**Figure 33. Magnet used for both CPS1 and CPS2 with particles entering from the “target” end and being deflected based on particle energy (Figure courtesy of LLE standard operating procedure D-ES-P-092).**

Prior to entering the magnetic field, the stream of particles passes through an aperture that consists of an interchangeable slit which collimates the particles into a beam and limits the influx of particles based on the width of the slit. For CPS1, which is located outside the target chamber, the slit is cut into a “finger” that extends down from the baseplate of the CPS data cartridge assembly that is housed over the magnet. Several other “fingers” also protrude down from the data cartridge base plate and are equipped with CR-39 nuclear track detectors that detect the deflected particles at various angles. A third type of finger

extends down directly across from the slit finger and is used to measure the width of the collimator slit during each experiment by recording x-rays that pass through the slit unaffected by the magnet. Traditionally, CR-39 has also been used on the slit-width x-ray finger for x-ray detection. An image of the CPS data cartridge assembly showing the baseplate and the various fingers is given in **Figure 34(a)**, and an image of the data cartridge assembly being mounted over the magnet on CPS1 is shown in **Figure 34(b)**.



(a)

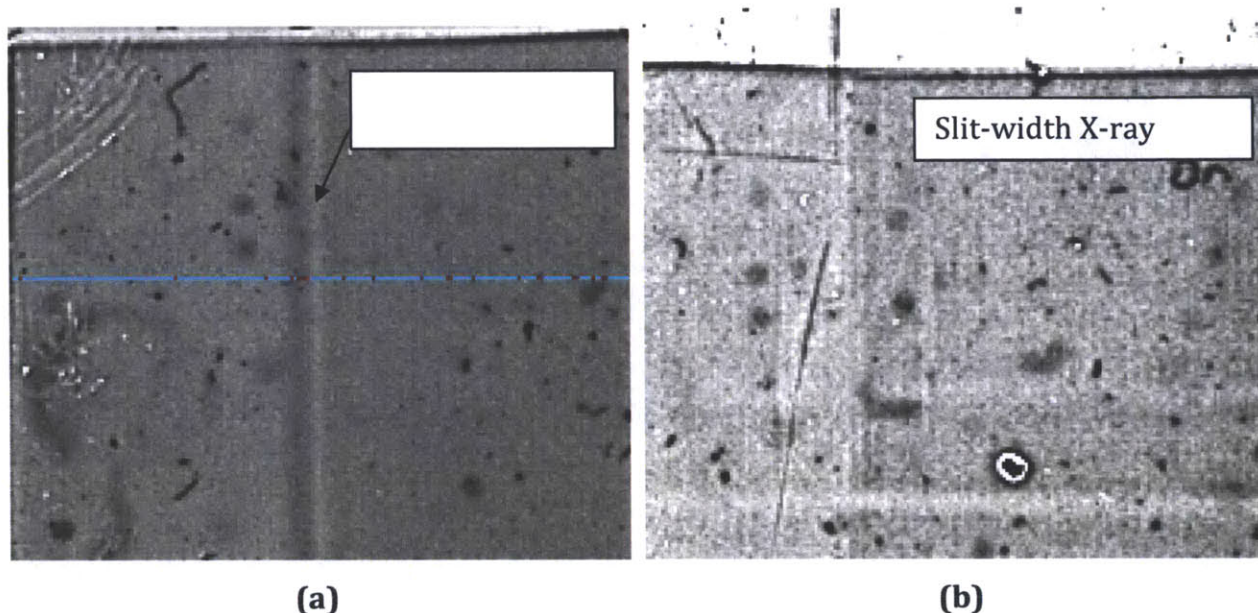


(b)

**Figure 34. (a) CPS data cartridge assembly showing the baseplate, slit finger, CR-39 nuclear track detector fingers, and slit-width x-ray finger. (b) Data cartridge assembly being mounted over the magnet in CPS1 (Both figures courtesy of LLE standard operating procedure D-ES-P-092).**

For each experiment, knowing the correct width of the collimator slit fielded is critical for determining yields and linewidths, and it is therefore desirable to have a consistent and repeatable way of verifying the width of the slit used. As mentioned previously, CR-39 has traditionally been used for CPS slit-width verification, but the image quality has proven to be quite poor and it is often difficult to infer accurate slit widths from the data. In **Figure 35**, two collimator slit images using CR-39 are given. Figure 35(a) gives the slit image from

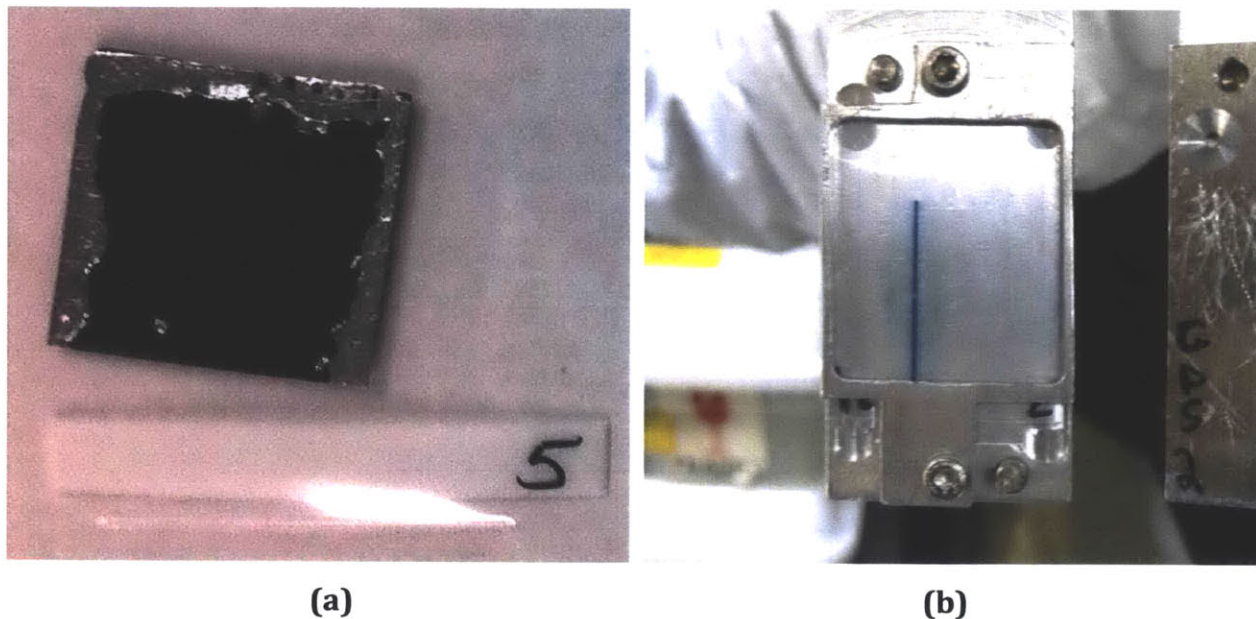
CPS1 on OMEGA shot 59484 and Figure 35(b) gives the slit image from CPS2 on OMEGA shot 59489. The slit in Figure 35(a), is identifiable, although very faint, and runs vertical along the center of the image. In contrast, in Figure 35(b), there is no discernible image of the slit from which the slit-width can be inferred. Other CR-39 slit images show similar results and illustrate why CR-39 is not a dependable detector for measuring collimator slit widths accurately and consistently.



**Figure 35. (a) CR-39 slit image from CPS1 (OMEGA shot 59484), slit is discernible. (b) CR-39 slit width image for CPS2 (OMEGA shot 59489), slit is not discernible.**

Because of difficulty in interpreting CR-39 slit image data, two alternative detectors were fielded on D<sup>3</sup>He exploding pusher shots conducted on May 25<sup>th</sup>, 2011 on both CPS1 and CPS2 to determine whether an alternative detector could produce a clearer image of the slit. The detectors fielded include BIOMEX x-ray film and radiochromic film (RCF). Images of the developed BIOMEX x-ray film and RCF fielded on the May 25<sup>th</sup> shots are given in **Figure 36**. Due to light sensitivity, the x-ray film required special preparation and had to be placed in a light-tight foil package to prevent premature exposure. The process of preparing the film in this manner was tedious as the foil, being only a few microns thin to maximize x-ray penetration, tore easily and adhering the foil to the film in a dark room required significant effort. Radiochromic film on the other hand is not light sensitive and does not require the same kind of special treatment. Upon irradiation, the color of the film

turns a shade of blue with the darkness increasing as a function of the intensity of the radiation source. Other advantages of RCF include high spatial resolution and low spectral sensitivity.



**Figure 36. (a) BIOMAX x-ray film fielded on OMEGA shot 62412 on CPS1. (b) Radiochromic film fielded on OMEGA shot 62407 on CPS2.**

As can be seen in Figure 36(a), the x-ray film is completely exposed and there is no discernible image of the slit. This was true of all six pieces of x-ray film fielded on CPS1 and CPS2 for shots 62409, 62411, and 62412. The cause of the complete exposure has yet to be determined, but with all the steps involved in preparing the film having little room for error, there were many opportunities for premature exposure. This suggests that even if the x-ray film had produced an image of the slit, in practice it would have been a difficult detector to work with. In Figure 36(b), however, you see the radiochromic film providing a much clearer and more sharply contrasted image of the slit than the CR-39 slit image given in Figure 35(a).

Following the success of the RCF slit images obtained on May 25<sup>th</sup>, a follow-up experiment was conducted on June 29<sup>th</sup>, 2011 as a ride-along to a series of spherical RT shots. The experimental setup was nearly the same for every shot and consisted of 54 lasers incident on the target with an addition 6 lasers incident on a foil backlighter. The

goal of the ride-along experiment was to obtain images of every slit in the CPS1 and CPS2 slit inventories and benchmark the width of the slit image recorded on the RCF with the nominal width of the slit. A list of the nominal slit widths currently available from the OMEGA collimator slit inventory for CPS1 and CPS2 is given in **Table 7**.

**Table 7. Inventory of slits for CPS1 and CPS2.**

CPS 1	CPS 2
0.09mm	0.1mm
0.2mm	0.25mm
0.5mm	0.5mm
1.0mm	1.0mm
2.0mm	2.0mm
3.0mm	3.0mm
4.0mm	4.0mm
5.0mm	5.0mm
--	7.0mm
10.0mm	10.0mm

As previously mentioned, for CPS1 the slit is cut into a finger that is directly mounted to the data cartridge assembly baseplate. An image of the inventory of CPS1 slits is given in **Figure 37**. In **Figure 38** we see the data obtained for all slits in the CPS1 slit inventory. As is readily apparent, all slit images are easily discernible by eye and scale appropriately with increasing nominal width. For CPS2, the magnet and data cartridge are mounted inside the target chamber and are attached to a retractable housing that allows CPS2 to be located closer to the target chamber center (TCC). This is done to provide better counting statistics and higher resolution. To accommodate the retractable housing, the collimator slit is not directly mounted to the data cartridge baseplate, as is the case with CPS1, but is mounted to the housing separately. Images of the collimator slit inventory for CPS2 along with slit image data obtained on the June 29<sup>th</sup> shots is given in **Figure 39**.

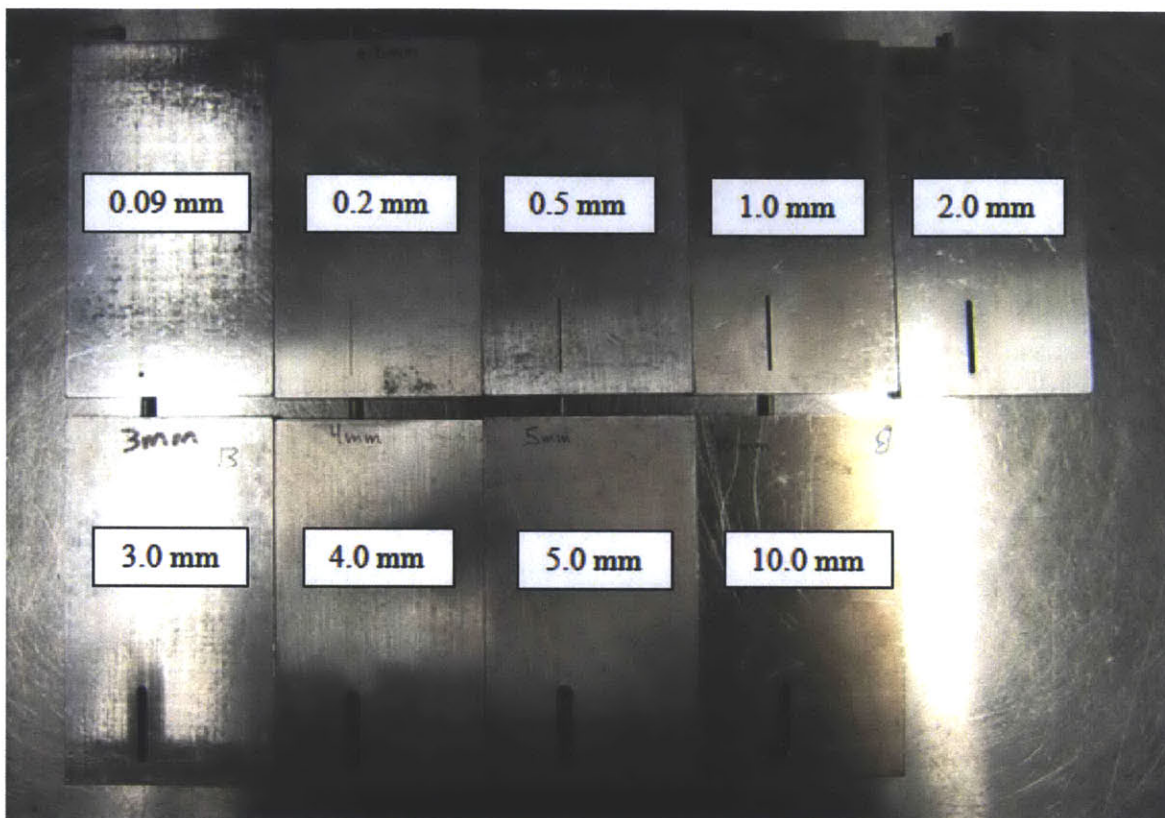


Figure 37. Inventory of CPS1 slits include nominal widths of 0.09mm, 0.2mm, 0.5mm, 1.0mm, 2.0mm, 3.0mm, 4.0mm, 5.0mm, and 10.0mm.

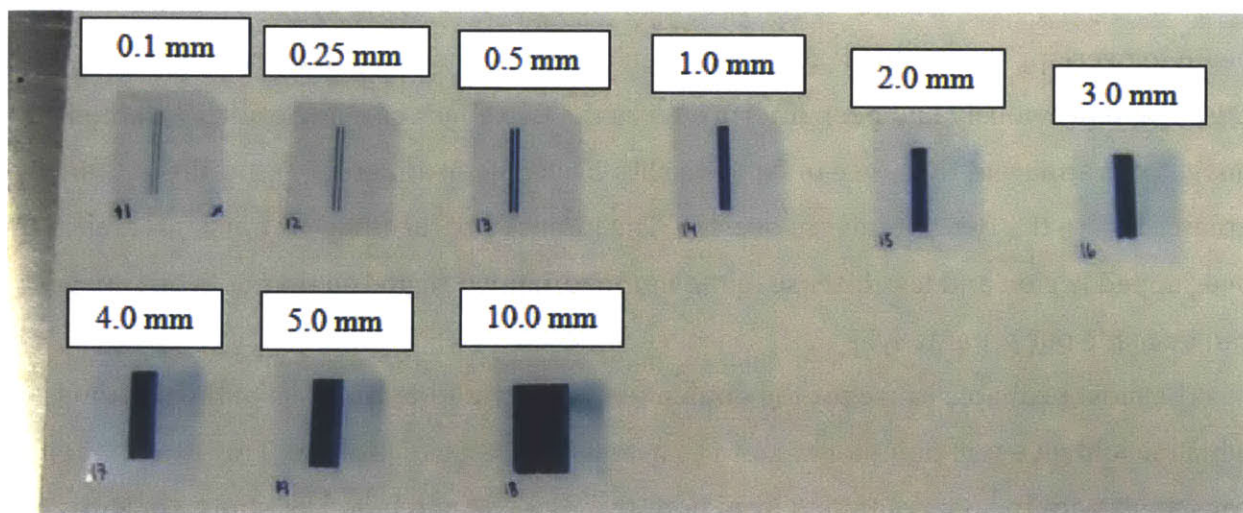
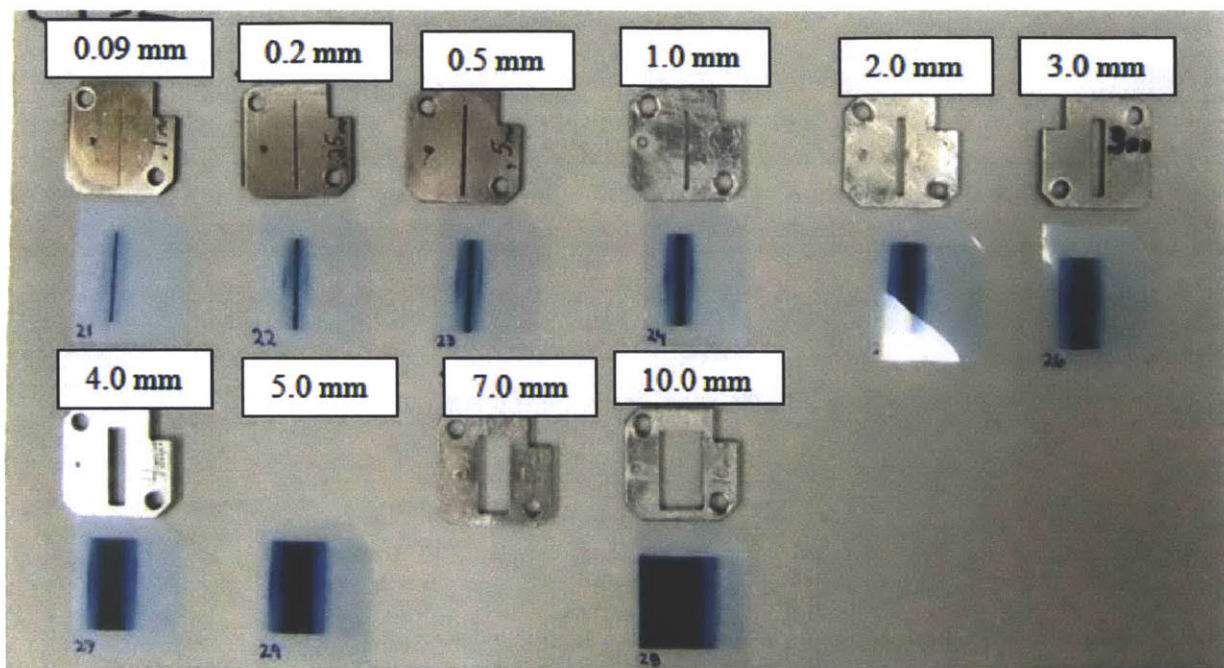


Figure 38. Slit images obtained for the CPS1 slit inventory on June 29th, 2011 using RCF.



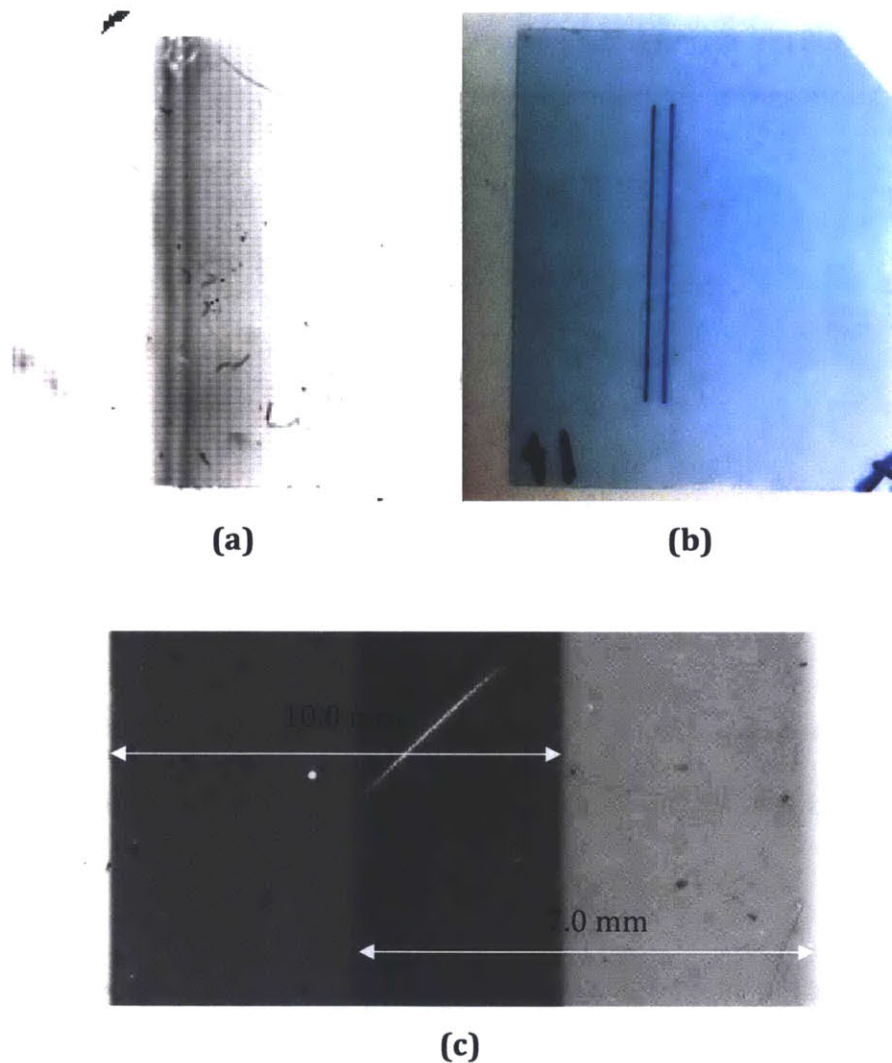
**Figure 39. Slit images obtained for CPS2 on June 29th, 2011 using RCF along with CPS2 collimator slit inventory (all slit images included except for 7.0mm, and all slit inventory included except 5.0mm).**

One notable difference between the CPS1 and CPS2 data is the presence of a double feature in the CPS1 data where two slit images are observed instead of one. For the 0.09mm, 0.2mm, and 0.5mm slits these features are distinctly separate, but by the 1.0mm slit, they begin to overlap. The double feature has been observed in slit-width images recorded with CR-39, and previously had been interpreted as the two edges of a single slit. With the RCF images it is apparent there are in fact two slits. This is even apparent in the slits 1.0mm and greater where the two slit images overlap. The intensity of the image is much greater in the overlapped region and less intense in the non-overlapped region so that both slit images can be made out separately.

The most probable cause for the double feature is the additional use of the backlighter, which would give two point x-ray sources near TCC instead of just one. This explanation is consistent with the data obtained from both the May 25<sup>th</sup> and June 29<sup>th</sup> shots. On May 25<sup>th</sup> no backlighter was used and no double feature was observed, whereas the double feature is seen on the June 29<sup>th</sup> shots as well as OMEGA shot 61082, both of which used a backlighter. In addition, when looking closely at the RCF data, one image is observably

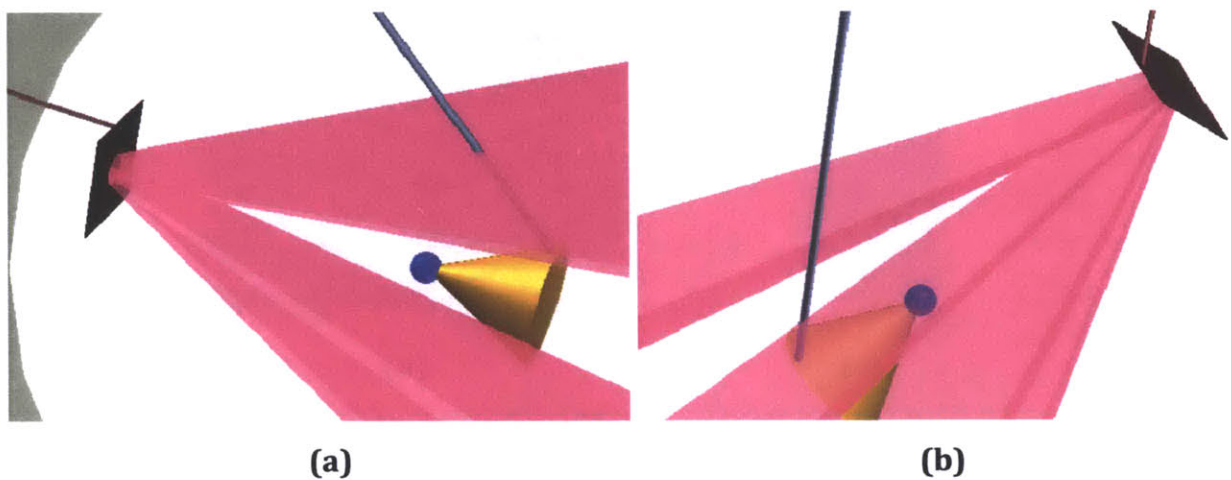


darker than the other which suggests the x-ray source for one image is more intense than the other. This is consistent with more x-rays being generated by the 54 lasers incident on the target compared to the x-rays generated from only 6 lasers incident on the backlighter foil. Images of the double feature appearing in earlier CR-39 data and the June 29<sup>th</sup> shots, as well as an image of slit overlap for the 2.0mm slit on CPS1, are given in **Figure 40**.



**Figure 40. (a) Double feature appearing in CR-39 slit image for CPS1 (OMEGA shot 61082). (b) Double Feature appearing in RCF slit image for CPS1 (OMEGA shot 62754). (c) Overlapping target and backlighter images from 2.0mm slit on CPS1.**

What remains to be explained is why the double feature is only seen in CPS1 data and not with CPS2. One explanation is that this is due to the location of CPS1 and CPS2 relative to the target and backlighter. When viewing TCC from CPS1 if the target and the backlighter do not overlap in the field of view, they would both be seen as two distinct point sources. On the other hand, when viewing the target and backlighter from CPS2 if the target is in the field of view but the backlighter source is covered, then all that would be seen would be a single point source. This explanation is verified when looking at the VisRad setup for the June 29<sup>th</sup> 2011 shots as shown in **Figure 41**.



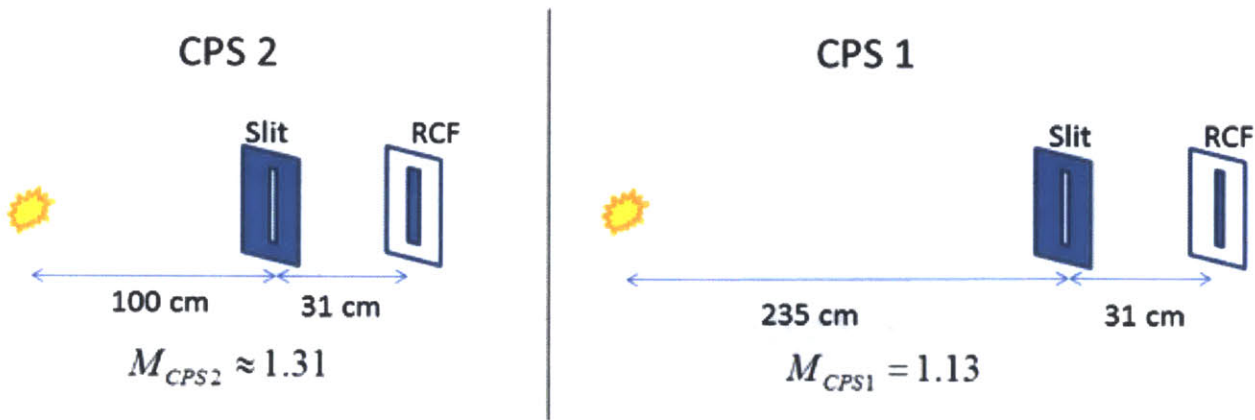
**Figure 41. View of target capsule and backlighter foil from (a) CPS 2, and (b) CPS 1. In (a) both the front of the back lighter foil and the target are in the field of view providing to point X-ray sources. In (b) the target is in the field of view but the back of the backlighter foil seen which may limit X-ray emissions.**

### A4.3 Results

From the collimator slit images obtained from the June 29<sup>th</sup>, 2011 shots, we create a table of measured widths that are inferred from the images to use as a benchmark for verifying the collimator slit width of RCF slit image data taken on future shots. As part of the benchmarking table, we include the calculated width of the image on the RCF taking into account magnification effects. If we treat each implosion as a simple x-ray point source at TCC, then the magnification of the collimator slit as seen on the RCF film is given as:

$$M = \frac{W_{RCF}}{W_{Slit}} = \frac{L_{TCC-Slit} + L_{Slit-RCF}}{L_{TCC-Slit}}$$

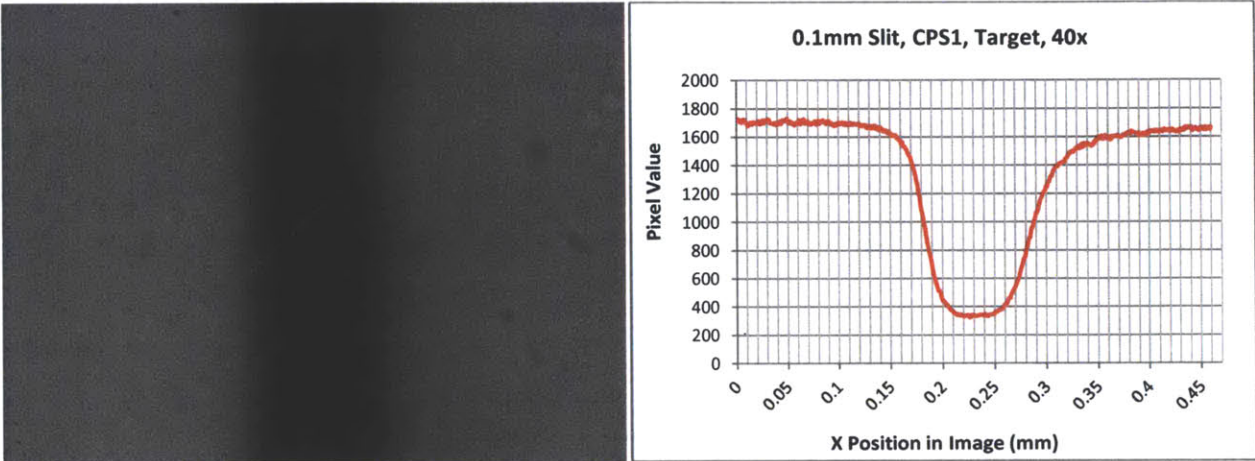
where  $W_{RCF}$  is the width of the slit image on the RCF,  $W_{Slit}$  is the actual width of the slit,  $L_{TCC-Slit}$  is the distance from TCC to the slit, and  $L_{Slit-RCF}$  is the distance from the slit to the RCF. The distance between TCC and the slit is documented for both CPS1 and CPS 2 where  $L_{TCC-Slit} = 235\text{cm}$  for CPS1 and  $L_{TCC-Slit} = 100\text{cm}$  for CPS2. For CPS1,  $L_{Slit-RCF}$  has been measured to be 31cm and the distance should be the same for CPS2 according to Damien Hicks' thesis[57], although this needs to be measured and verified. Magnification factors for both CPS1 and CPS2 along with both experimental configurations are given in **Figure 42**.



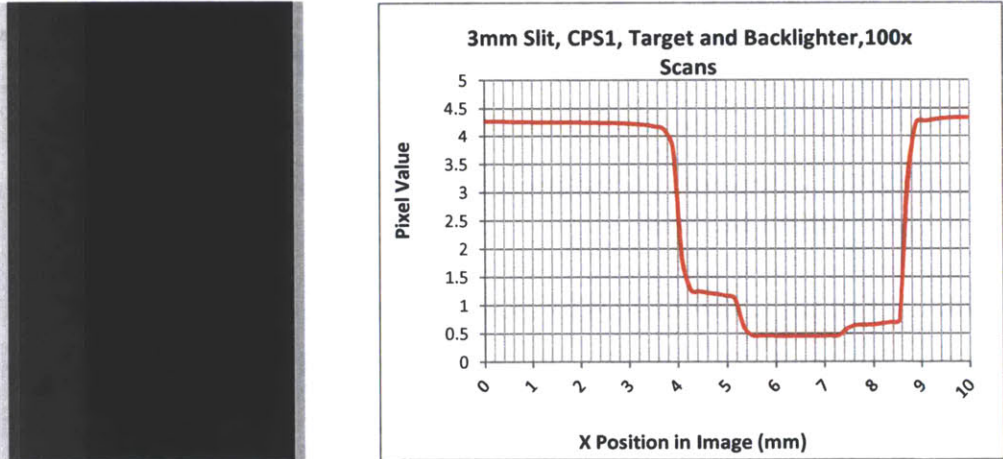
**Figure 42. Experimental configuration for CPS1 and CPS2 with corresponding magnification factors.**

To obtain the slit width images for the 0.09mm to 2.0mm slits, the RCF was observed under a microscope and a lineout was obtained by integrating the signal vertically over 1000 pixels to reduce noise. The slits 3.0mm and greater were too large to fit in a single frame and instead were scanned to create an image containing multiple frames each at 100x magnification. As each frame is 0.178mm wide at 100x magnification, the total width was determined by multiplying the number of frames by the frame width. For slits 1.00mm and smaller, lineouts were made for both the target and backlighter slit images. For slits 2.00mm and larger, a single lineout was made of the overlapping target and backlighter

images. The lineout of the target image for the 0.1mm slit on CPS1 is given in **Figure 43**, showing how the slit width was determined from a slit image that fit under a single microscope frame. **Figure 44**, which shows overlapping target and backlighter slit images of the 3mm slit on CPS1, provides an example of how the lineout was determined from a scan using multiple frames at 100x magnification.



**Figure 43. Target slit image for 0.1mm slit on CPS1 with lineout showing slit thickness (microscope magnification set to 100x).**

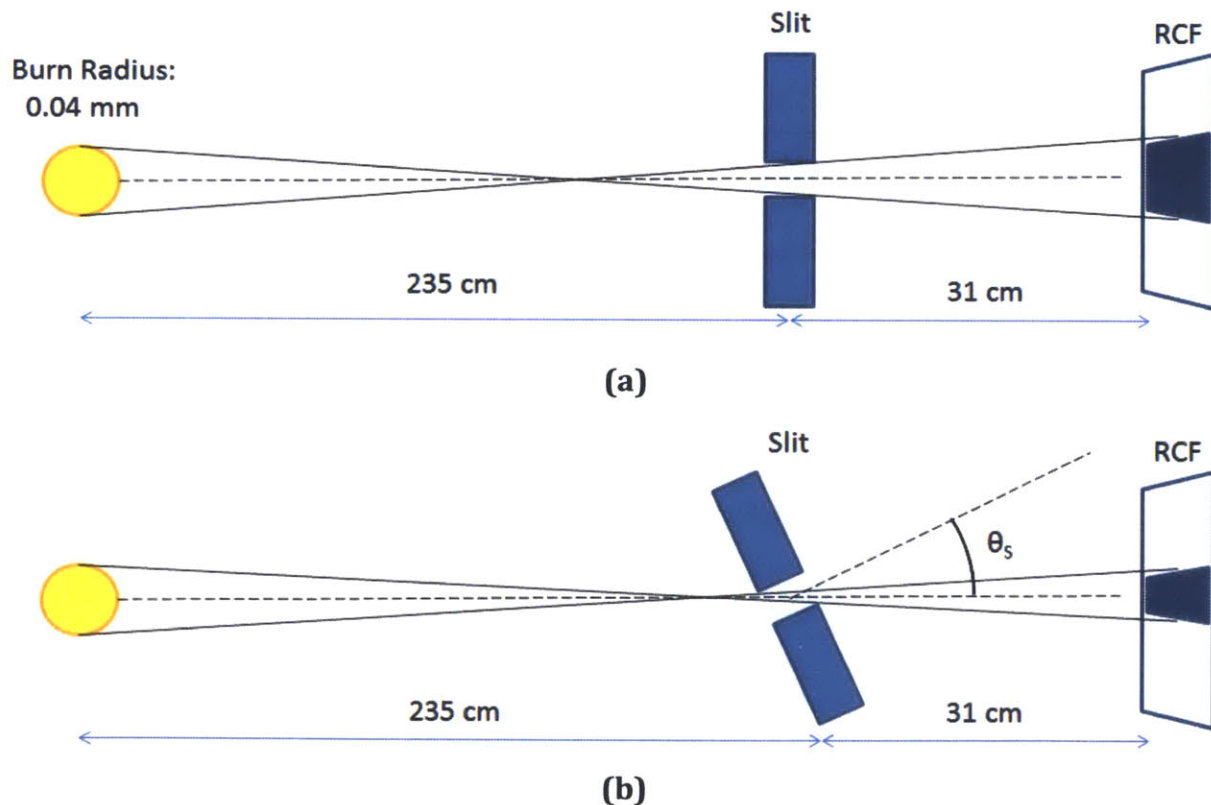


**Figure 44. Overlapping target and backlighter image for 3mm slit on CPS1 with lineout showing slit thickness (microscope set to 100x in scanning mode).**

Although both methods provide well characterized images of the slit, the resolution of the scanning method is limited by frame size at 100x magnification which introduces an error of  $\pm 0.178\text{mm}$ . For measurement, the width of each slit is given as the FWHM of the

intensity on each lineout. Using this definition for slit width, we obtain the measured widths of the CPS1 and CPS2 collimator slit inventories as given in **Table 8**. For CPS1, widths are given for both the target and backlighter images separately. For the 2.0mm and larger slits where the target and backlighter images overlap, this was done by using the change in contrast in the overlapped region as can be seen in Figure 40(c).

In addition, a study was also conducted to look into the effect of small rotational perturbations in slit alignment on the width of the RCF slit image. Nominally the slit is perfectly orthogonal to the line of sight between capsule and the RCF as shown in **Figure 45(a)**. However, small rotational perturbations ( $\theta_s$ ) limit the fluence passing through the slit which will result in a smaller yield measurement and a narrower slit image on the RCF. This effect of small rotational perturbations is illustrated in Figure **45(b)**. Calculations of the angle needed for a 20% reduction in yield are also given in **Table 9**.



**Figure 45. Effect of rotational perturbation on slit image width: (a) no rotation, (b) rotation of angle  $\theta_s$ .**

**Table 8. Benchmarked measured and calculated widths of slits in CPS1 and CPS2 inventory. For CPS1, both widths from the target and backlighter (BL) images are given separately.**

Slit Width	CPS	Source	Measured Width	Calculated Width
0.09mm	1	Target	0.107mm	0.113mm
	1	Backlighter	0.175mm	0.113mm
0.1mm	2	Target + BL	0.376mm	0.131mm
0.2mm	1	Target	0.240mm	0.226mm
	1	Backlighter	0.266mm	0.226mm
0.25mm	2	Target + BL	0.568mm	0.328mm
0.5mm	1	Target	0.593mm	0.566mm
	1	Backlighter	0.594mm	0.566mm
	2	Target + BL	0.94mm	0.655mm
1.0mm	1	Target	1.133mm	1.132mm
	1	Backlighter	1.174mm	1.132mm
	2	Target + BL	1.487mm	1.31mm
2.0mm	1	Target	2.284mm	2.264mm
	1	Backlighter	2.306mm	2.264mm
	2	Target + BL	2.927mm	2.62mm
3.0mm	1	Target	3.38 ±0.178mm	3.39mm
	1	Backlighter	3.38 ±0.178mm	3.39mm
	2	Target + BL	3.92 ±0.178mm	3.93mm
4.0mm	1	Target	4.63 ±0.178mm	4.52mm
	1	Backlighter	4.63 ±0.178mm	4.52mm
	2	Target + BL	5.52 ±0.178mm	5.24mm
5.0mm	1	Target	5.70 ±0.178mm	5.65mm
	1	Backlighter	5.70 ±0.178mm	5.65mm
	2	Target + BL	6.59 ±0.178mm	6.55mm
10.0mm	1	Target	11.40 ±0.178mm	11.30mm
	1	Backlighter	11.40 ±0.178mm	11.30mm
	2	Target + BL	13.10 ±0.178mm	13.10mm

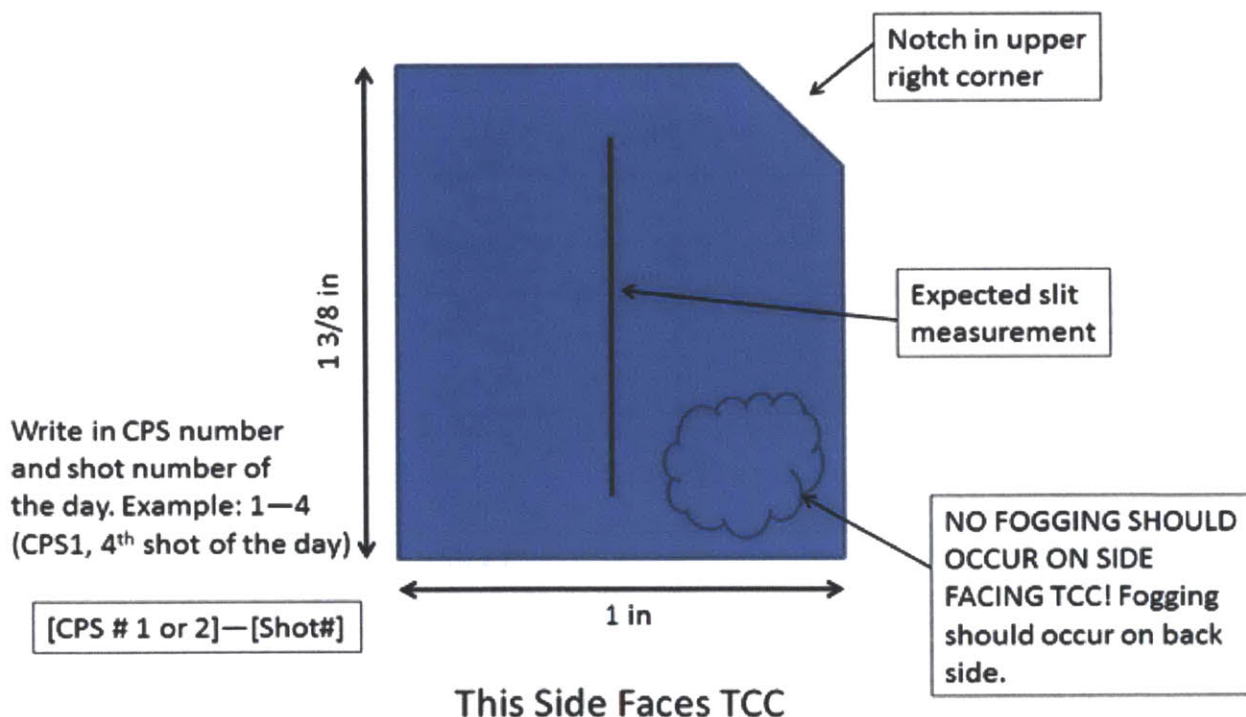
Overall the measured widths show good agreement with the calculated widths except for CPS2 on the narrower slits (0.1mm, 0.25mm, 0.5mm, 1.0mm, and 2.0mm).

**Table 9. Measured slit width and slit depths, calculated and measured RCF slit images and the angle of rotational perturbation needed to reduce the yield measurement by 20%.**

Nominal Width	CPS	Measured	Measured	RCF Image	RCF Image	$\theta_s$
		Width	Depth	Calculated	Measured	
0.09mm	1	-	2.5	0.107	0.107	2.29
0.1mm	2	0.102	1.323	0.131	0.376	4.45
0.2mm	1	0.210	2.545	0.231	0.240	4.70
0.25mm	2	0.262	1.519	0.328	0.568	9.87
0.5mm	1	0.501	2.47	0.566	0.593	11.47
	2	0.517	1.535	0.655	0.94	18.59
1.0mm	1	1.044	2.69	1.13	1.133	21.18
	2	0.976	2.518	1.31	1.487	21.23
2.0mm	1	-	-	2.26	2.284	-
	2	2.052	2.883	2.62	2.927	35.48
3.0mm	1	-	-	3.40	3.38	-
	2	-	-	3.93	3.92	-
4.0mm	1	-	-	4.53	4.63	-
	2	-	-	5.24	5.52	-
5.0mm	1	-	-	5.66	5.70	-
	2	-	-	6.55	6.59	-
10.0mm	1	-	-	11.32	11.40	-
	2	-	-	13.10	13.10	-

#### A4.4 Radiochromic Film Setup

This section establishes the guidelines for setting up the RCF to be used for slit width verification on CPS1 and CPS2. Each piece should be  $1\frac{3}{8}$ in x 1in to fit the holder on the x-ray slit-width finger. A notch is made in the upper right hand corner to distinguish the front side from back side of the RCF. This is important as the organic microcrystal monomer layer must be facing TCC. To determine which side is the layered side, breathe softly on the film and note whether or not the film fogs up. The side that is not layered will fog while the side layered with the organic microcrystal monomer will not. To label each piece, use a Sharpie to carefully write in the bottom left hand corner a two number identifier where the first digit stands for the CPS number and the second digit(s) stand for the shot number for that day (e.g. 25 would be CPS2, shot 5 and 112 would be CPS1 shot 12). Although a more sophisticated identification system would be valuable to uniquely identify each piece regardless of the shot day, recording more than 3 digits would be difficult without taking up needed surface area on the film.



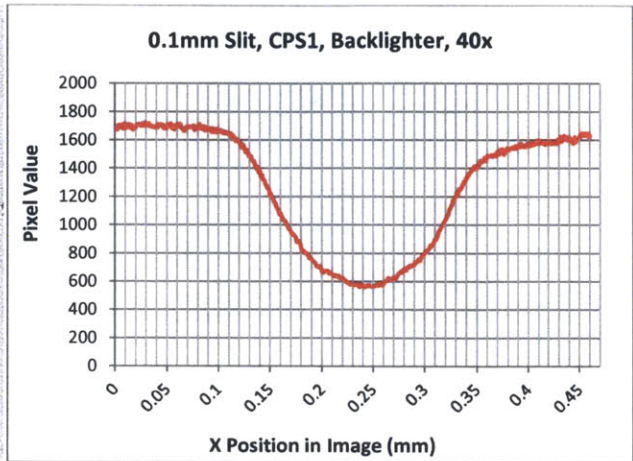
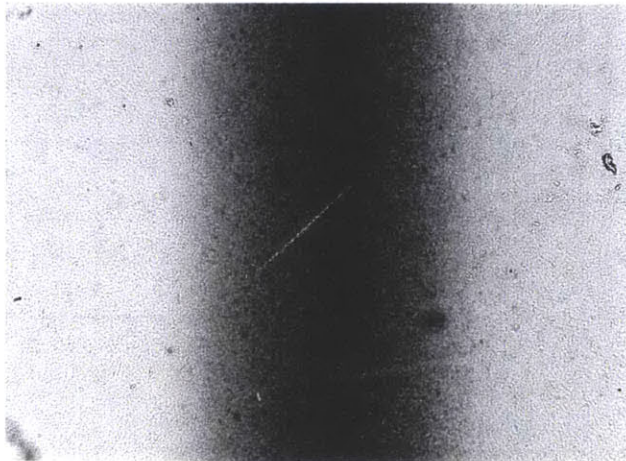
**Figure 46. Preparation specifications for RCF used for imaging collimator slit width on CPS1 and CPS2.**



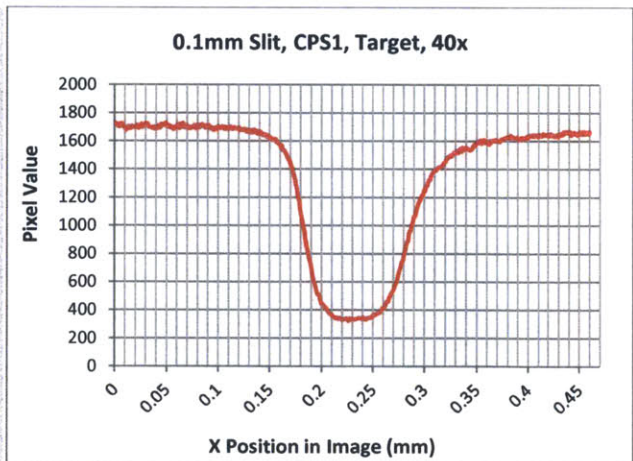
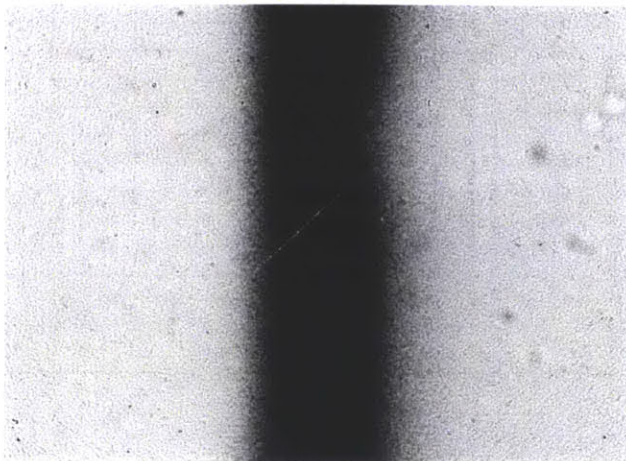
# A4.5 Data

June 29th 2011

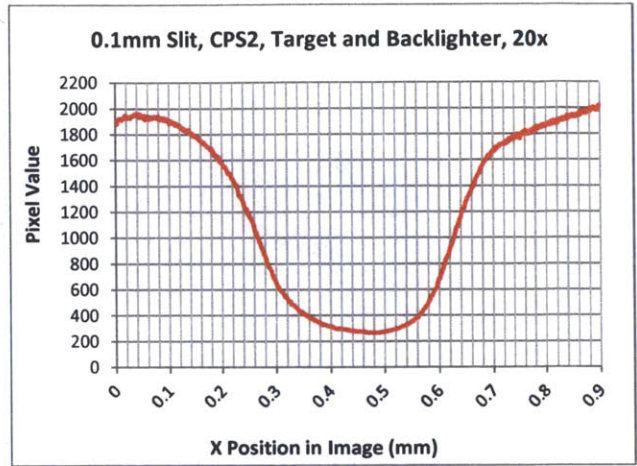
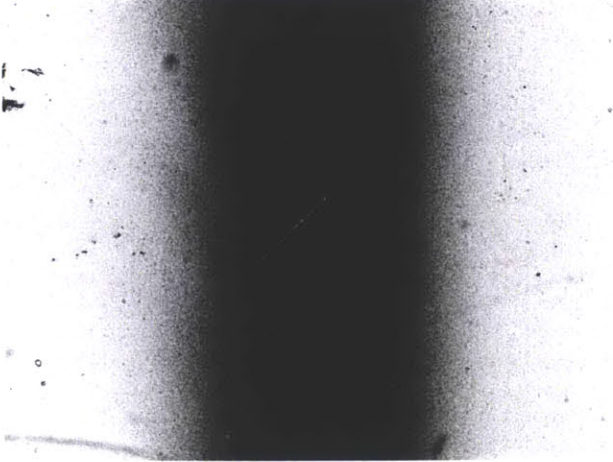
0.1mm Backlighter Image, CPS1



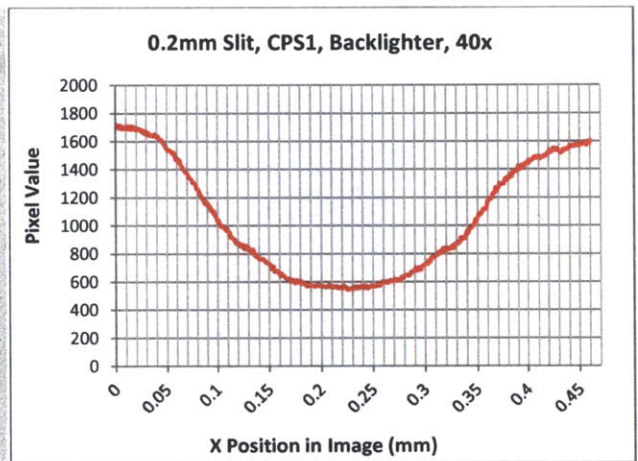
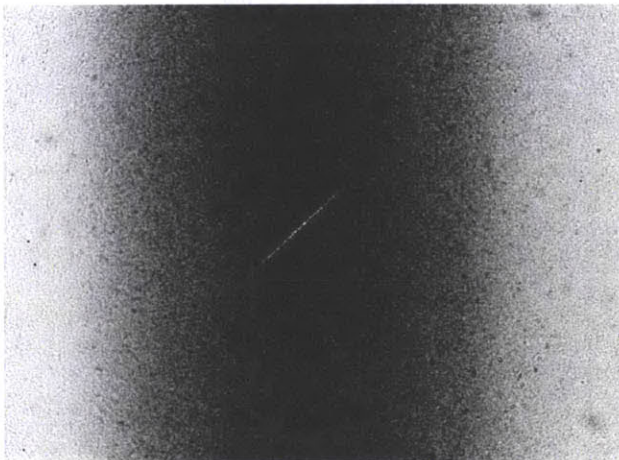
0.1mm Target Image, CPS1



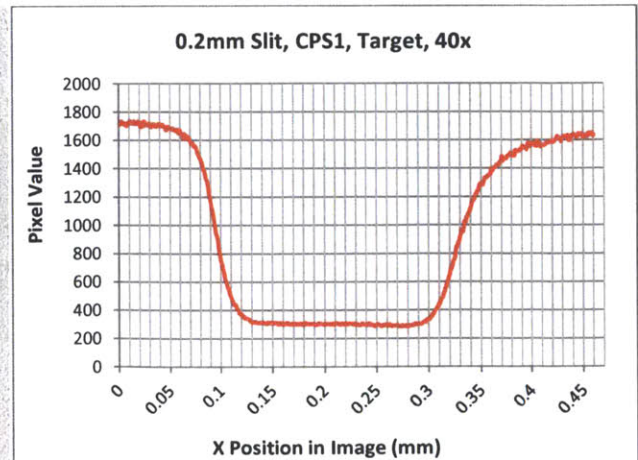
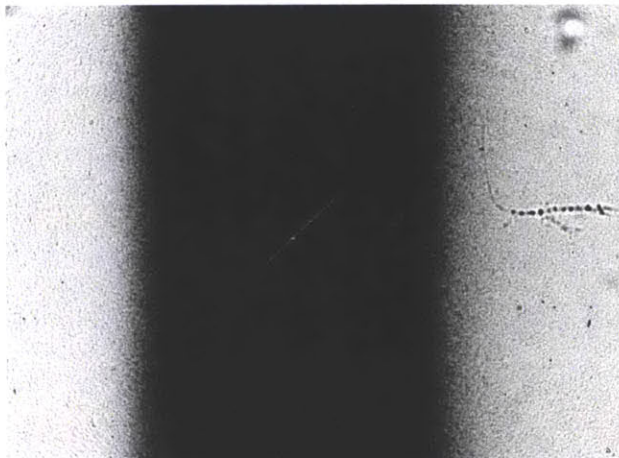
0.1mm Target and Backlighter Image, CPS2



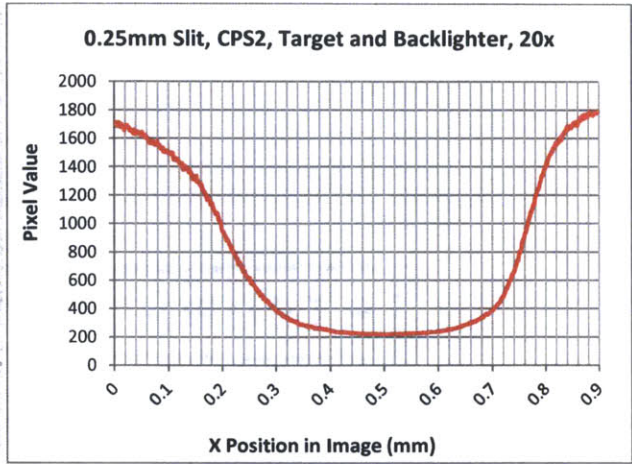
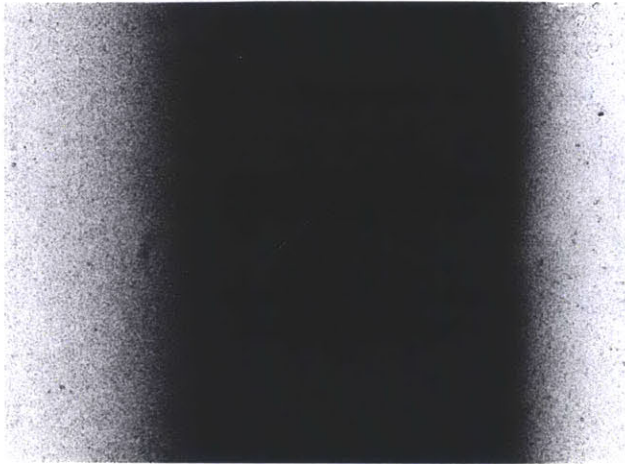
0.2mm Backlighter Image, CPS1



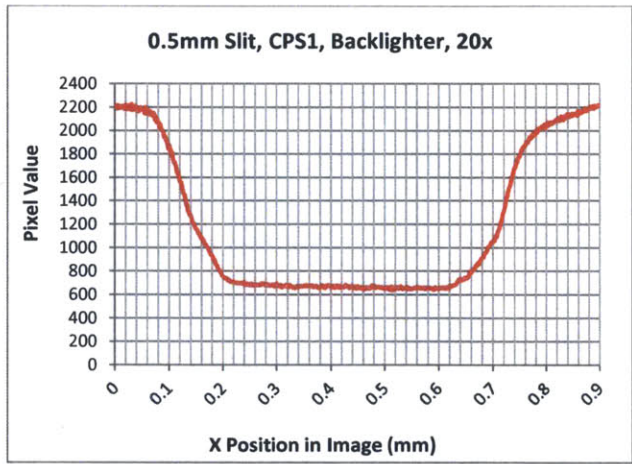
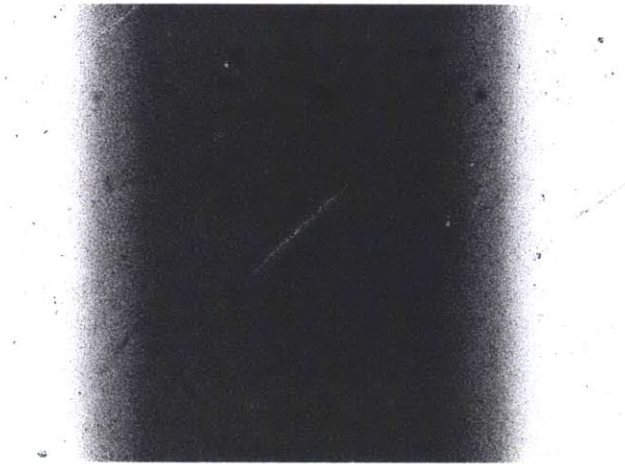
0.2mm Target Image, CPS1



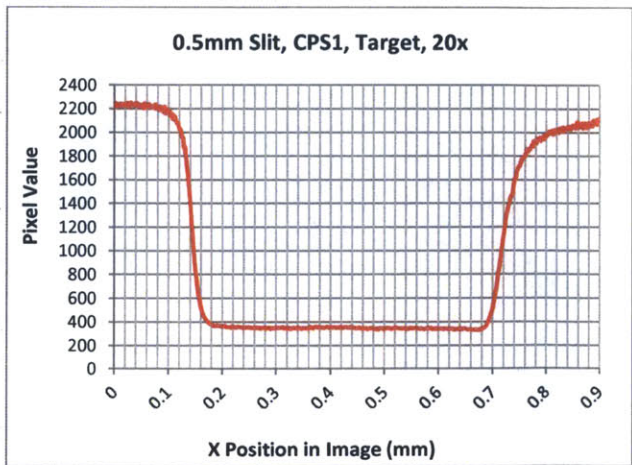
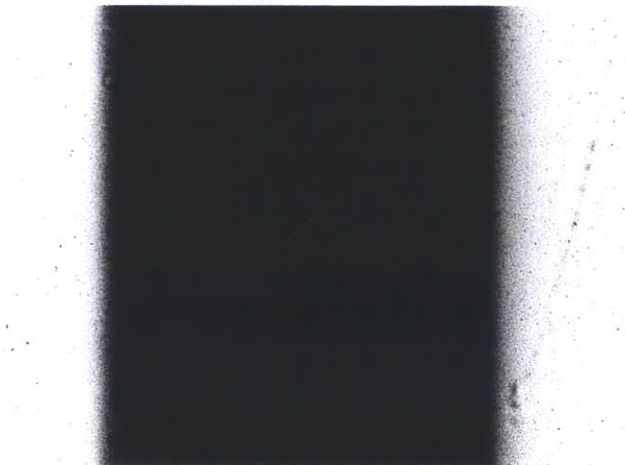
0.25mm Overlapped Target and Backlighter Image, CPS2



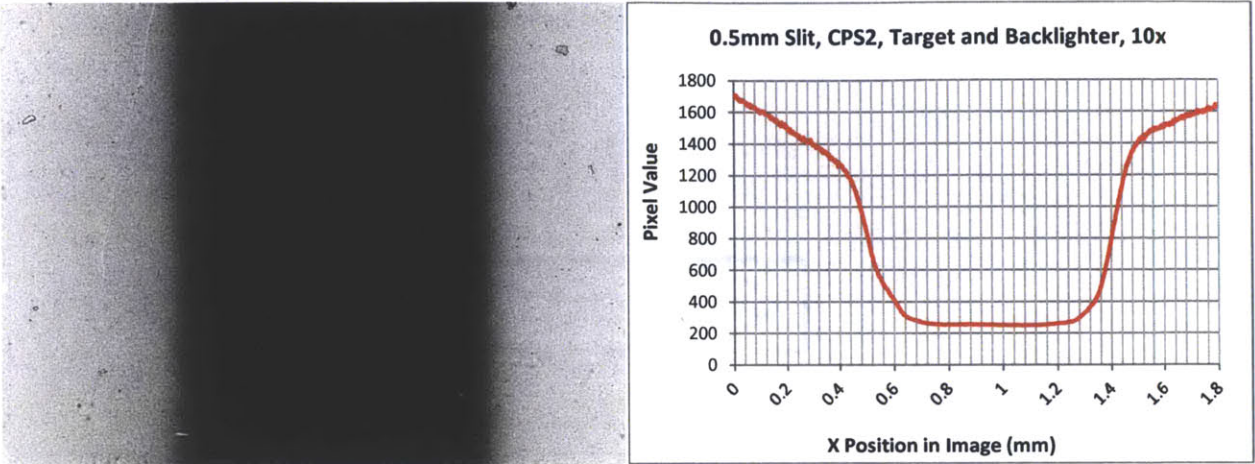
0.5mm Backlighter Image, CPS1



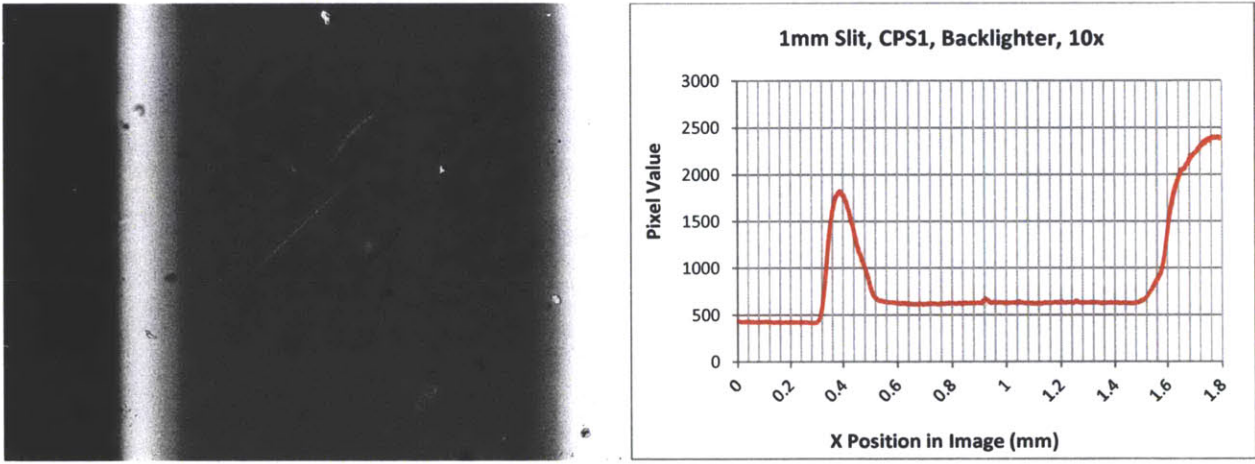
0.5mm Target Image, CPS1



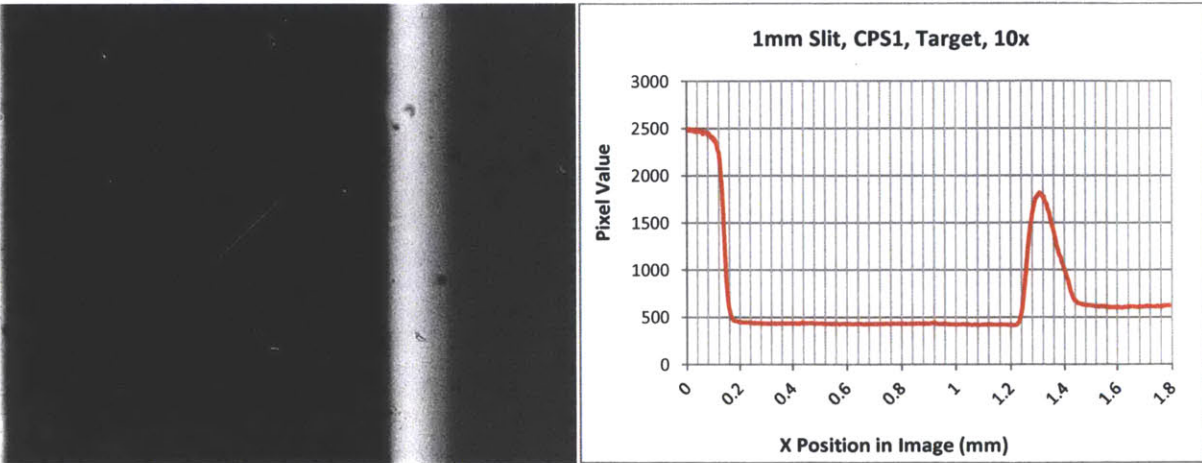
0.5mm Overlapped Target and Backlighter Image, CPS2



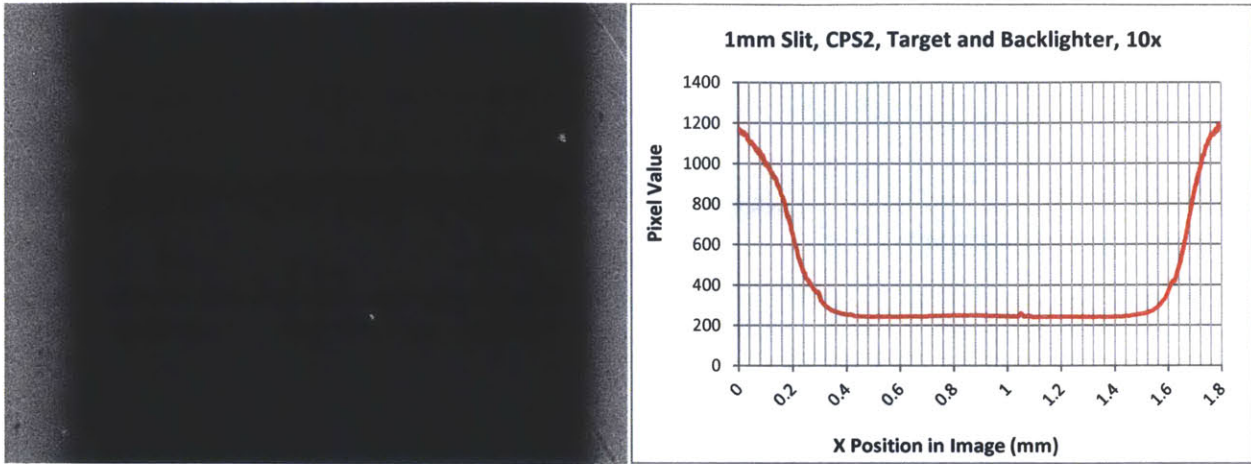
1mm Backlighter Image, CPS1



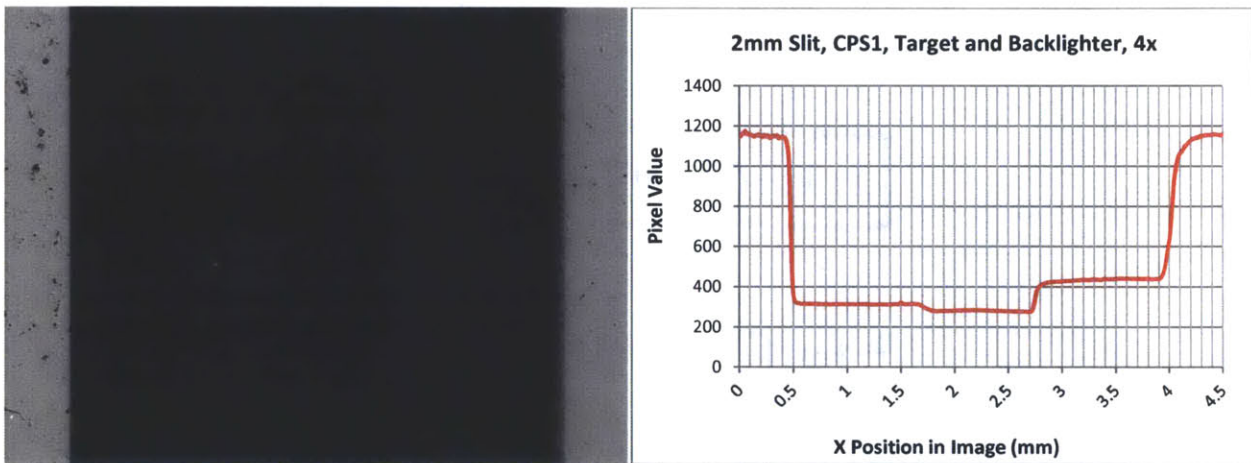
1mm Target Image, CPS1



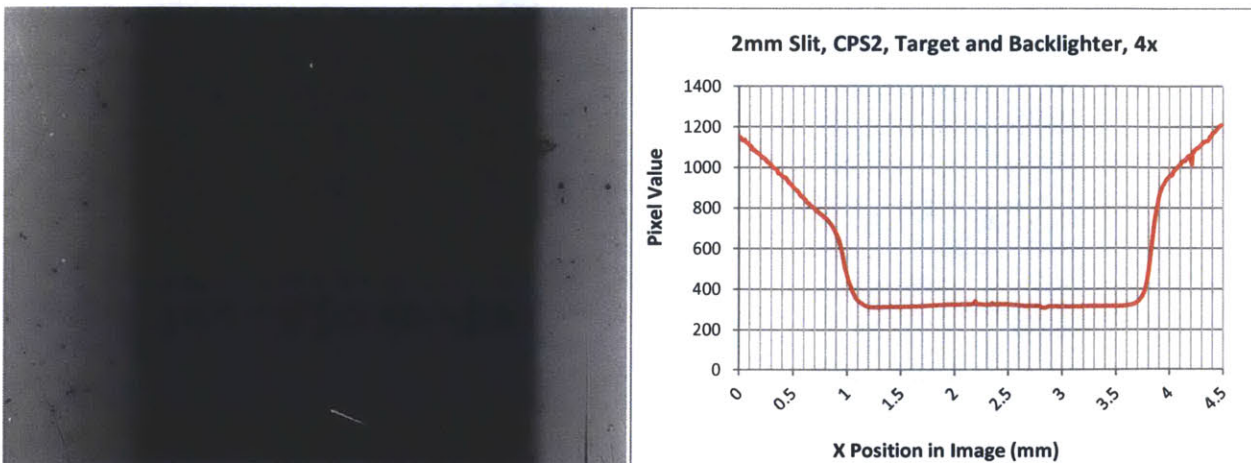
1mm Overlapped Target and Backlighter Image, CPS2



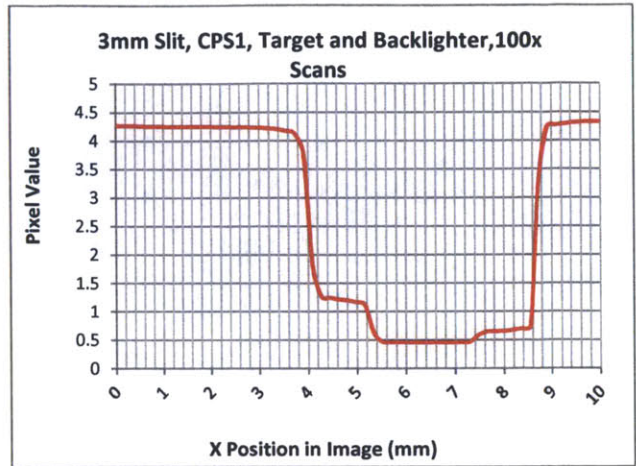
2mm Overlapped Target and Backlighter Image, CPS1



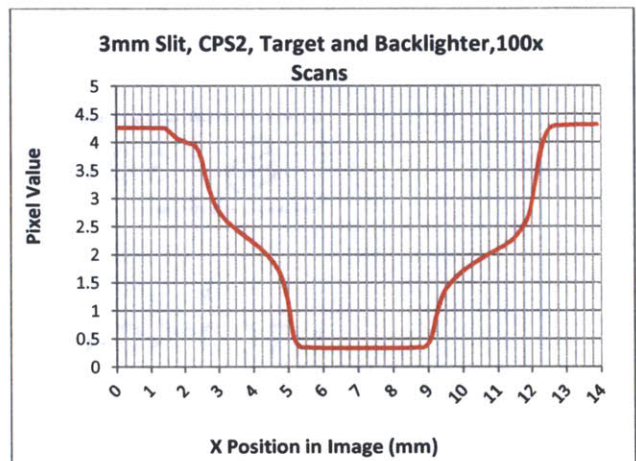
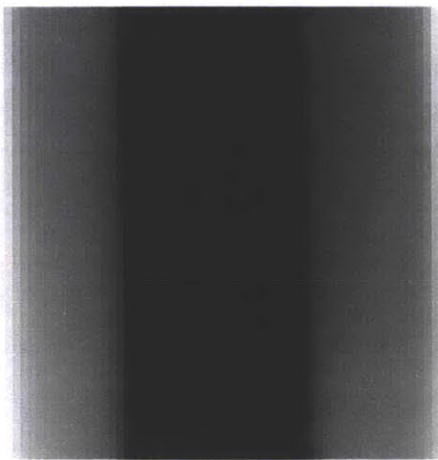
2mm Overlapped Target and Backlighter Image, CPS2



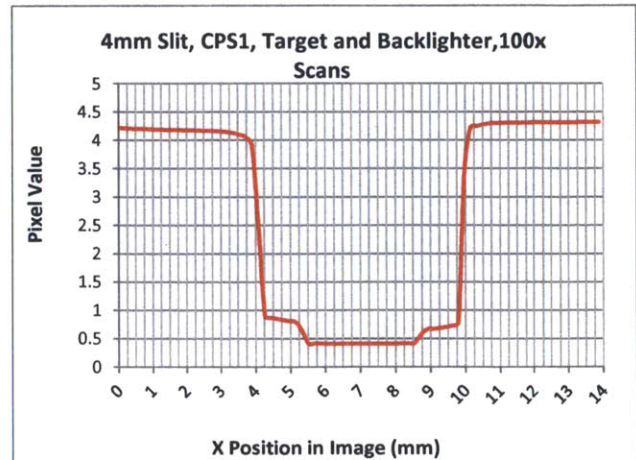
3mm Overlapped Target and Backlighter Image, CPS1



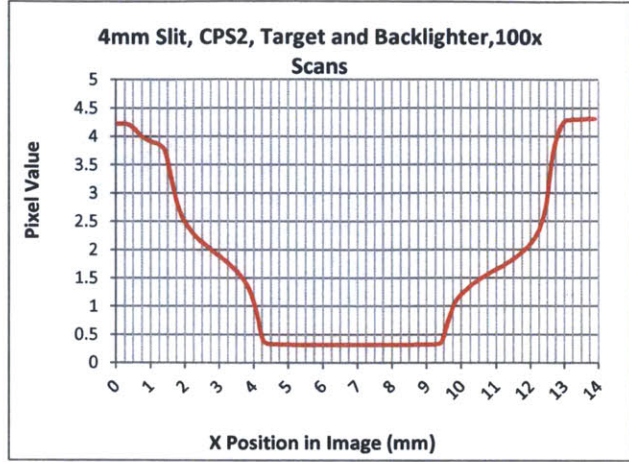
3mm Overlapped Target and Backlighter Image, CPS2



4mm Overlapped Target and Backlighter Image, CPS1



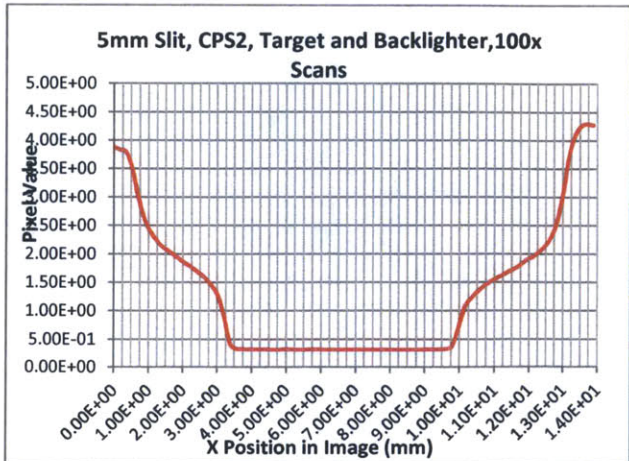
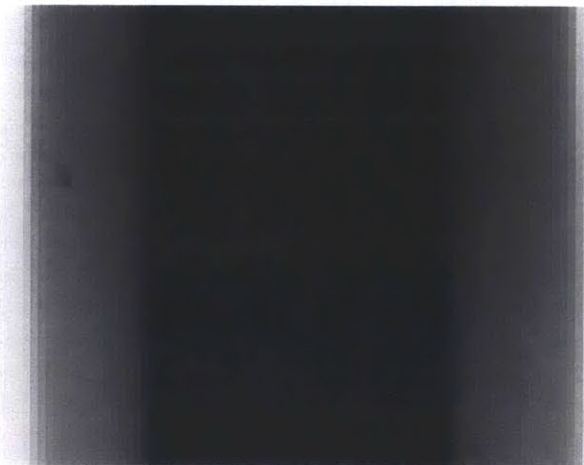
4mm Overlapped Target and Backlighter Image, CPS2



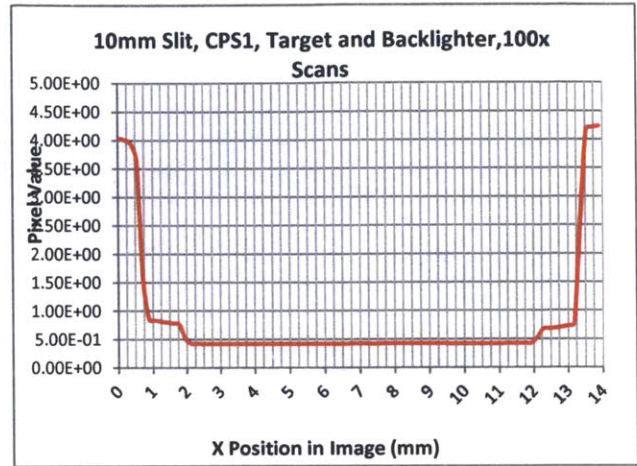
5mm Overlapped Target and Backlighter Image, CPS1



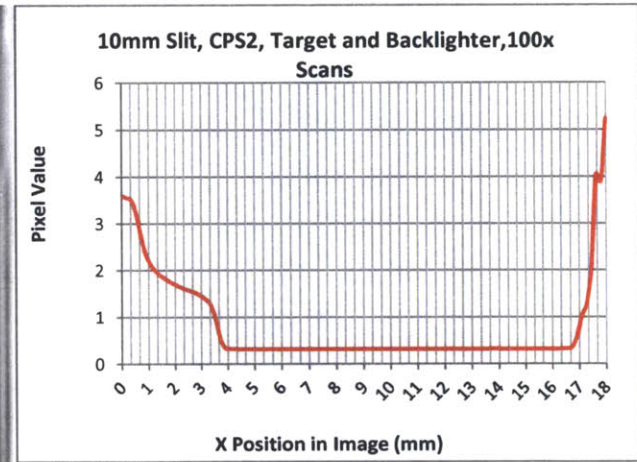
5mm Overlapped Target and Backlighter Image, CPS2



10mm Overlapped Target and Backlighter Image, CPS1

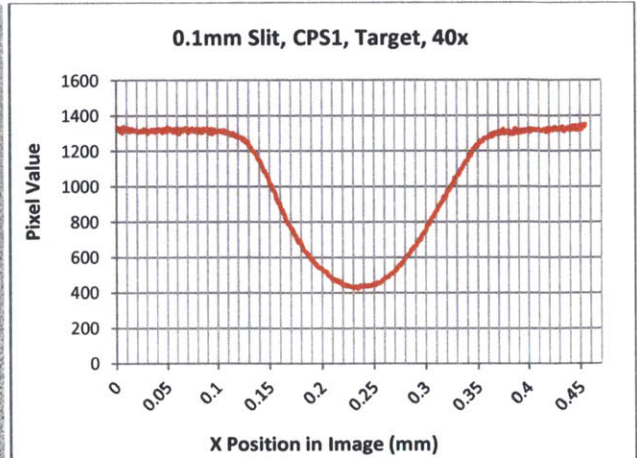
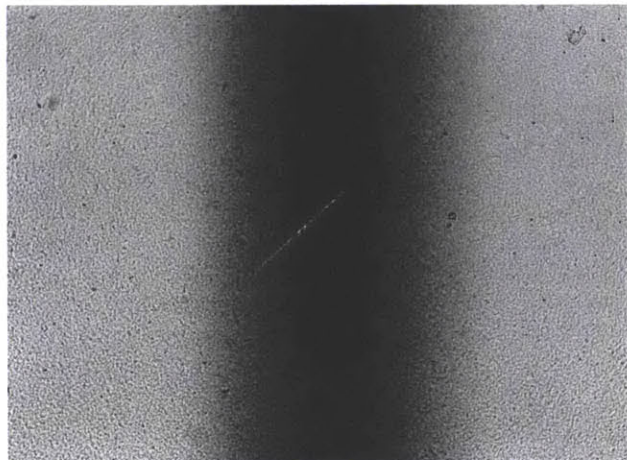


10mm Overlapped Target and Backlighter Image, CPS2



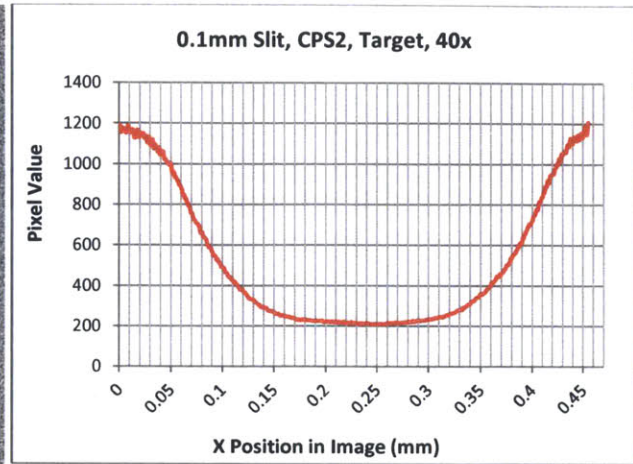
May 25<sup>th</sup> 2011

0.1mm Target Image, CPS1, Shot 62407

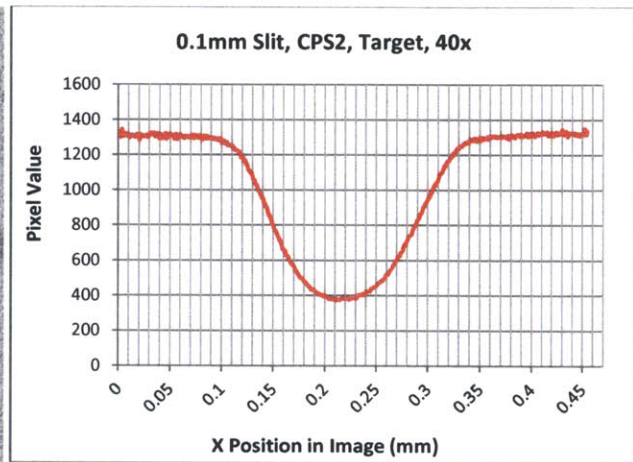
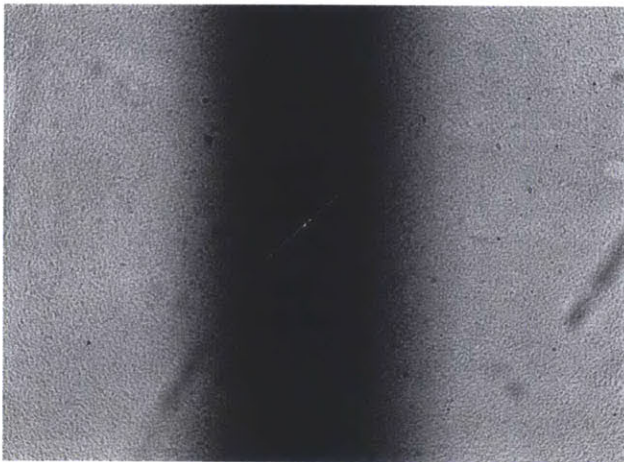




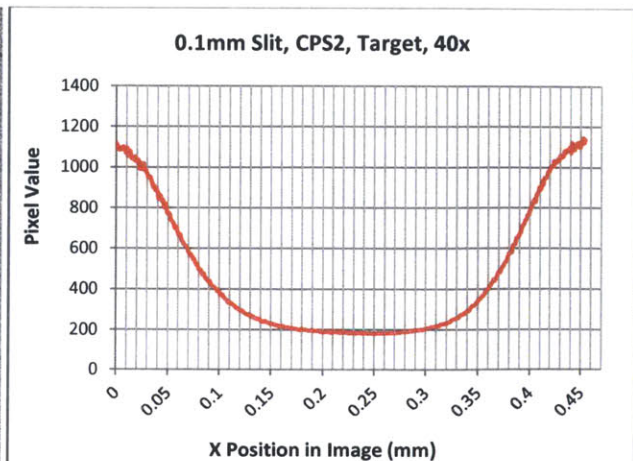
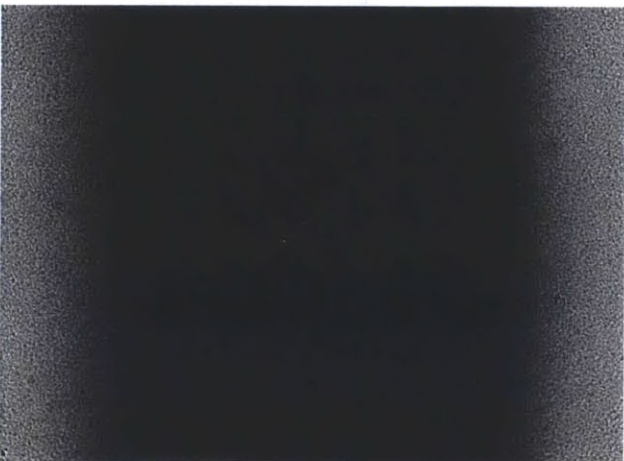
0.1mm Target Image, CPS2, Shot 62407



0.1mm Target Image, CPS1, Shot 62408



0.1mm Target Image, CPS2, Shot 62408





## Appendix 4: Stage Etching of High Fluence Range Filter CR-39 Modules On Omega

It has been shown previously that CR-39 solid state nuclear track plastic, used as a charged particle detector on the “back-end” of OMEGA and NIF diagnostics/spectrometers, is ideally suited to record particle fluences up to  $3 \times 10^4$  tracks/cm<sup>2</sup> [31]. However, often times conditions on OMEGA and the NIF can result in fluences two orders of magnitude greater than this. Typically the optimal etch time for CR-39 to fully uncover charged particle tracks is 5 hours. By using shorter etch times than the standard 5 hour, and by cross calibrating to CR-39 shot on the MIT Linear Electrostatic Ion Accelerator (LEIA) to fluences equivalent to what is seen on inertial confinement fusion experiments on OMEGA and the NIF, the dynamic fluence range of the CR-39 can be significantly extended. Work conducted to extend the range of the CR-39 fluence from OMEGA D3He exploding pusher shots is given here for the case of DD and D3He protons.

Under standard conditions, CR-39 is etched in a solution of sodium hydroxide for 5 hours in order to full expose the charged particle tracks for detection under a 40x scanning microscope and to etch the track diameters to a sufficient size so as to ensure good signal to noise separation. An image depicting how the track diameter change as a function of etch time is given in **Figure 47**. At a 5 hour etch, counting efficiencies of 100% are obtained under both 40x and 100x magnification. Longer etch times are also beneficial for improving signal to noise separation in the analysis. With fluences up to  $3 \times 10^4$ /cm<sup>2</sup>, tracks are easily distinguished and little overlap occurs. However, as the fluence increases beyond this, tracks begin to overlap and are rejected by the scanning software as depicted in **Figure 47**.

The dynamic range of CR-39 can be significantly extended by reducing the etch time which by so doing reduces the track diameter. However, if the etch time is reduce too much the track will not be discerned by the scanning microscope which will result in track undercounting and poor signal to noise separation. For a given fluence, then, there is an optimal etch time span which is long enough so that track undercounting does not occur, but at the same time is short enough so that tracks have not yet begun to overlap. An image

depicting the track undercount regime, optimal etch range, and track overlap regime is given in Figure 49.

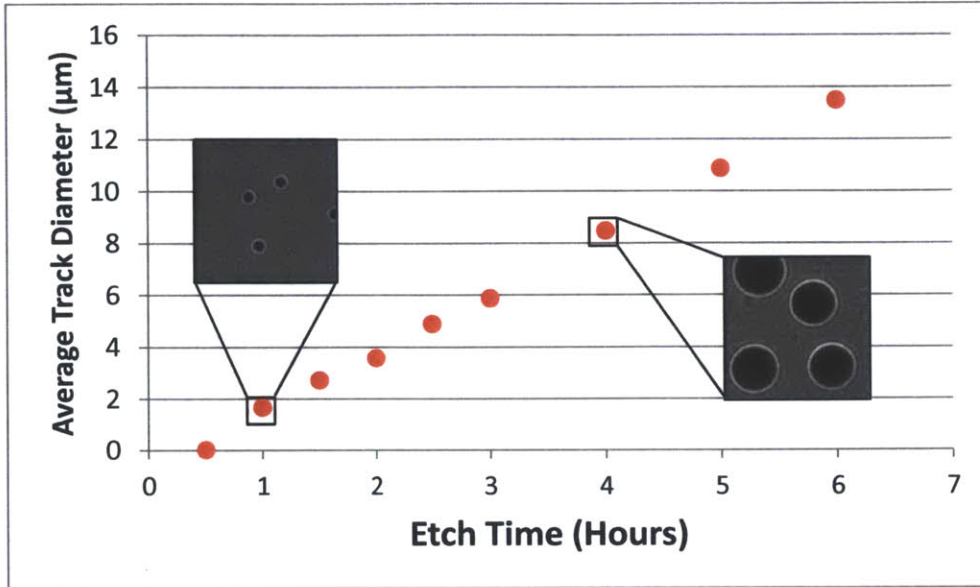


Figure 47. Average track diameter vs. etch time for CR-39 etched in a sodium hydroxide solution.



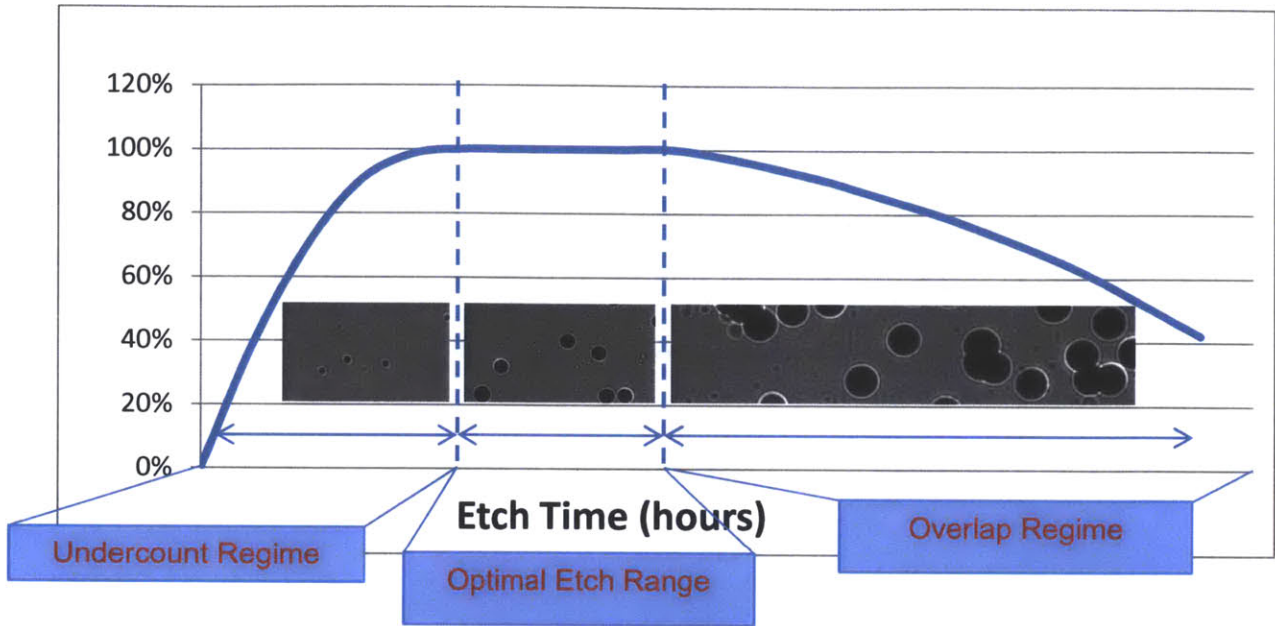


Figure 49. The qualitative detection efficiency of CR-39 as a function of etch time. The track undercount, optimal etch range, and track overlap regime for CR-39 are also identified.

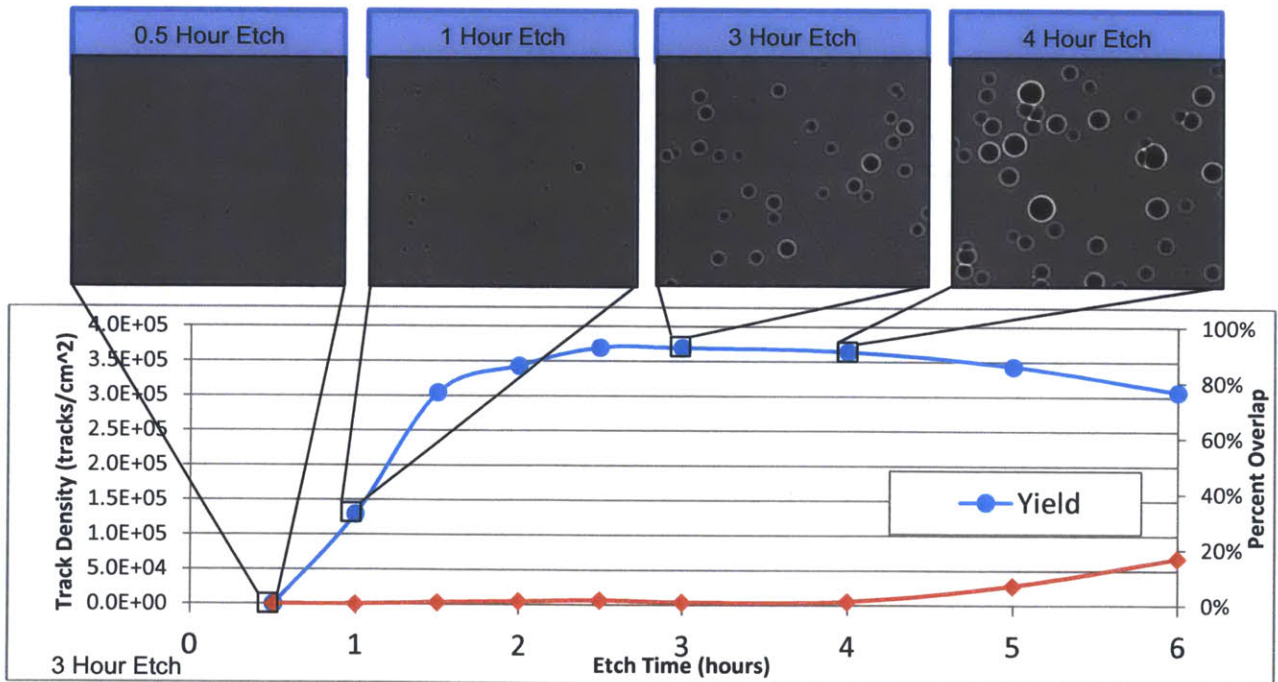


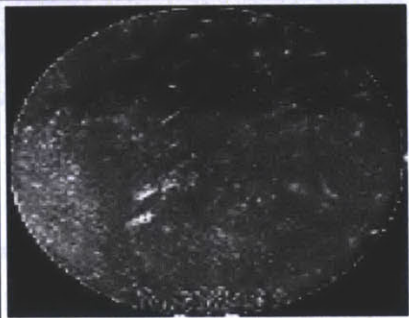
Figure 50. The actual etch time vs. track detection rate for OMEGA Shot 62409 which had a D3He-p fluence of 3.69x10<sup>5</sup> tracks/cm<sup>2</sup>.



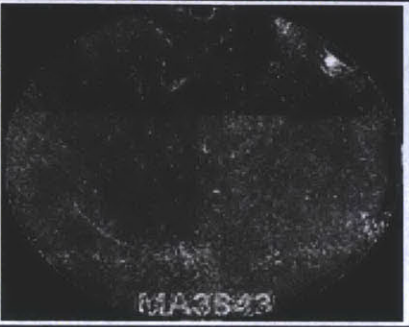
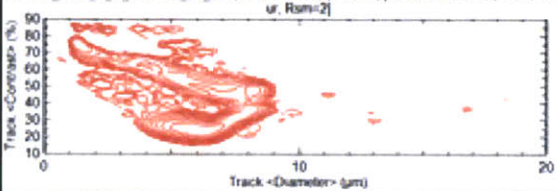
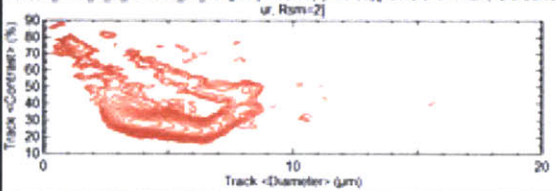
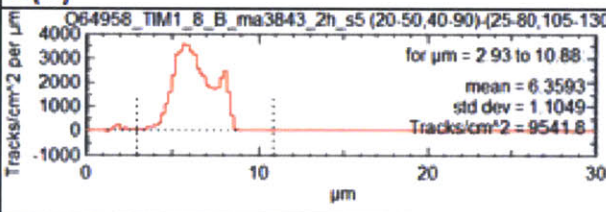
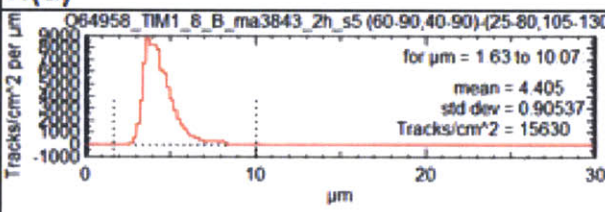
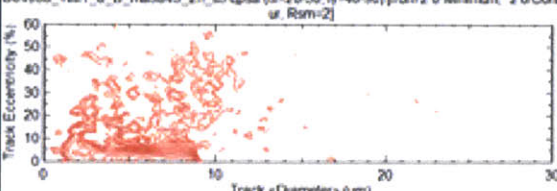
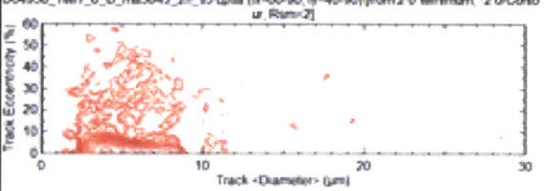
## Appendix 5: Absolute DDp Measurements taken on Exploding Pushers on OMEGA (February 7<sup>th</sup> and 9<sup>th</sup>, 2012)

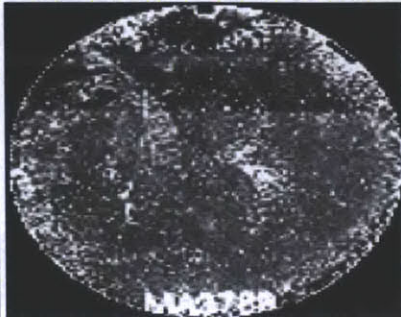
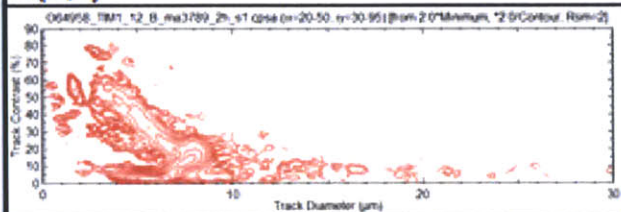
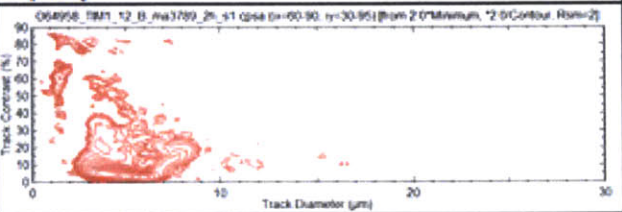
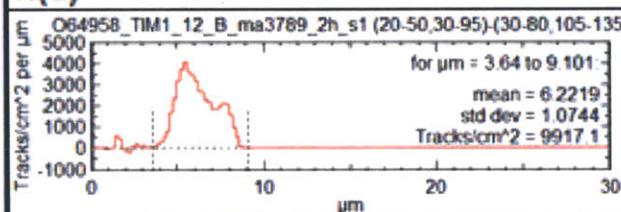
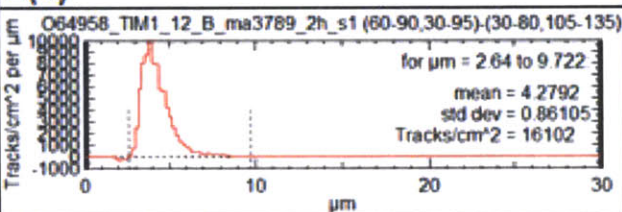
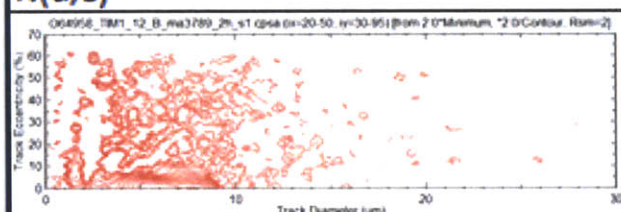
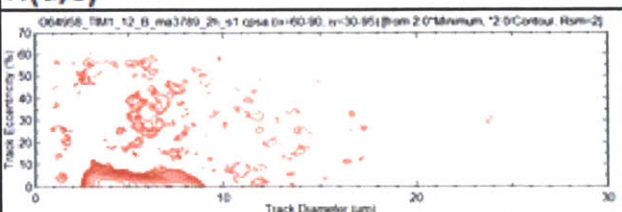
This appendix documents the details of the analysis of CR-39 to obtain DD proton yields for use of calibrating the OMEGA nTOF detector for Campaigns A and B for a series of shots conducted on February 7<sup>th</sup> and 9<sup>th</sup>, 2012. For each analysis a header specified the following: TIM and trident location of the CR-39 (e.g. TIM 1, 4:00), shot number, the amount of time (in hours) that the piece was etched in a sodium hydroxide bath, the distance of the piece (in cm) from OMEGA TCC, and the magnification used for the scanning software (standard being 40x). In addition, we include the analysis parameters that specify the analysis software setup for analyzing both the 50 $\mu$ m and 25 $\mu$ m steps. These parameters designate: Limit Area (the data area on the CR-39 to include in the analysis), Background (the area on the CR-39 with no signal that is used for background subtraction), Limit c% (the limit placed on the contrast of a track to aid in signal to noise separation), Limit e% (the limit placed on the eccentricity of a track to aid in signal to noise separation). Next, three plots are given to visualize the data by plotting all track by diameter vs. eccentricity— $N(d,c)$ , diameter vs. contrast— $N(d,e)$ , and then just a histogram of track diameters. The diameter vs. eccentricity and diameter vs. contrast are used to determine the signal to noise cutoffs used in the analysis parameters (i.e. Limit c% and Limit e%). With signal separated from the noise, an average track diameter is given along with a calculated track fluence in terms of tracks/cm<sup>2</sup>. The yield is then obtained by multiplying the track fluence over the target chamber solid angle. For a complete discussion on the analysis of charged particle tracks in CR-39 refer to Sequin et al. [31].

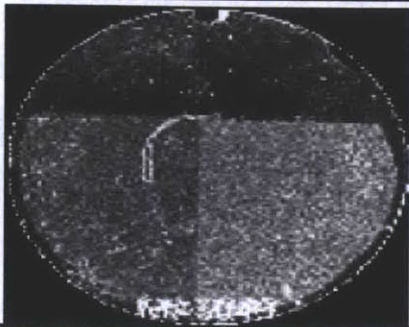
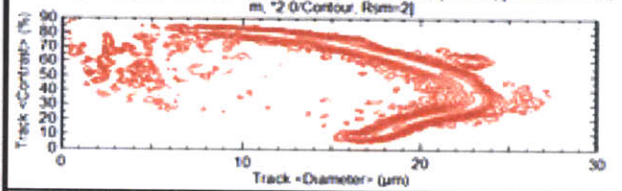
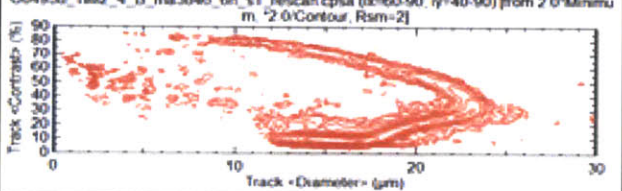
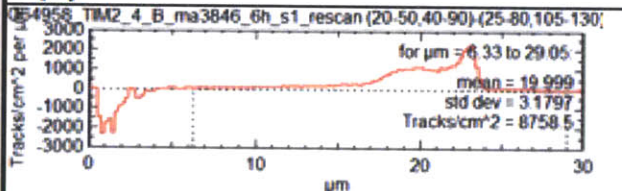
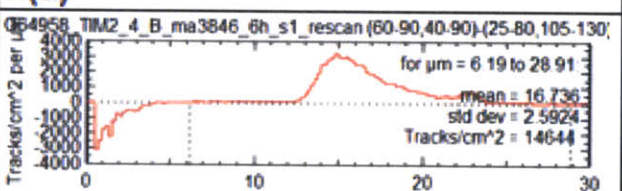
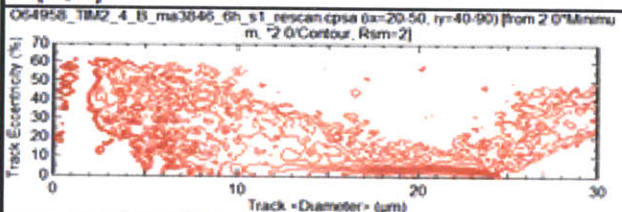
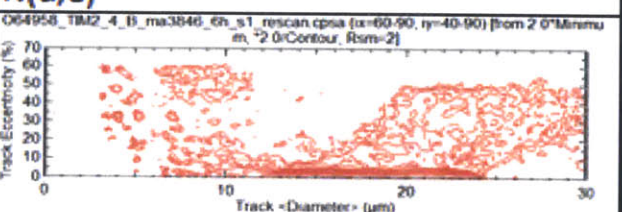
Shot 64958


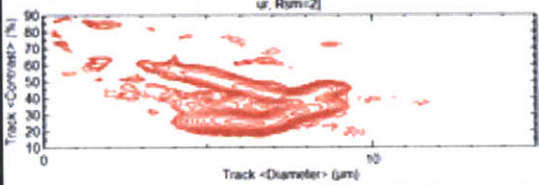
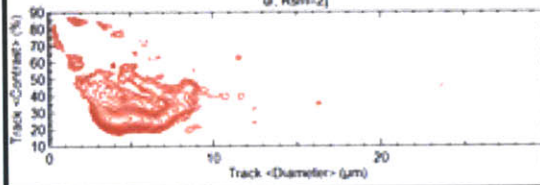
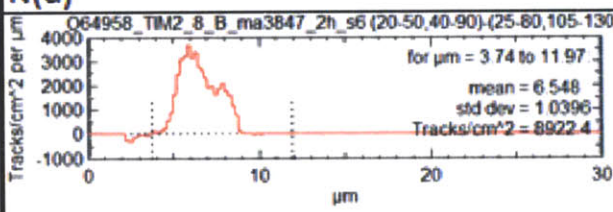
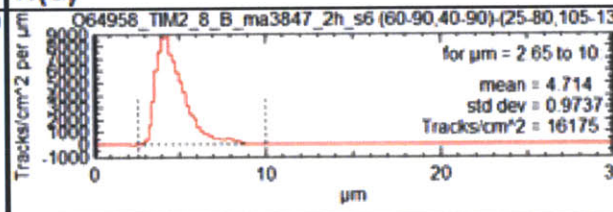
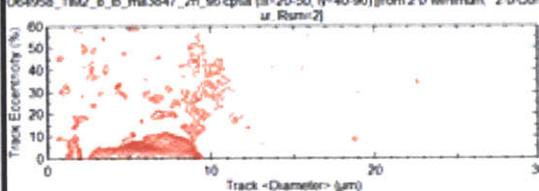
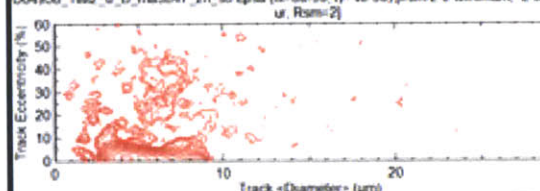
Tim 1, 4:00						
Shot	64958	Piece	ma3841	Type	Bert	
Etch Time (hours)	6	Distance (cm)	150	Magnification	40x	
<i>Step (um):</i>	50		<i>Step (um):</i>	25		
Limit c (%)	0 ≤ c ≤ 85		Limit c (%)	0 ≤ c ≤ 80		
Limit e (%)	0 ≤ e ≤ 15		Limit e (%)	0 ≤ e ≤ 15		
Limit Area	20 ≤ x ≤ 50 40 ≤ y ≤ 90		Limit Area	60 ≤ x ≤ 90 40 ≤ y ≤ 90		
Background	25 ≤ x ≤ 80 105 ≤ y ≤ 130		Background	25 ≤ x ≤ 80 105 ≤ y ≤ 130		
<b>N(d,c)</b>			<b>N(d,c)</b>			
<b>N(d)</b>			<b>N(d)</b>			
<b>N(d,e)</b>			<b>N(d,e)</b>			
<b>Average d (um)</b>	19.963		<b>Average d (um)</b>	16.774		
<b>Fluence (tracks/cm^2)</b>	9.02E+03		<b>Fluence (tracks/cm^2)</b>	1.43E+04		
<b>Yield</b>	2.55E+09		<b>Yield</b>	4.03E+09		



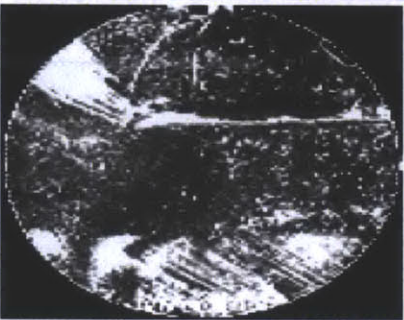
Tim 1, 8:00						
Shot	64958	Piece	ma3843	Type	Bert	
Etch Time (hours)	2	Distance (cm)	150	Magnification	40x	
<b>Step (um):</b>	50		<b>Step (um):</b>	25		
<b>Limit c (%)</b>	$0 \leq c \leq 70$		<b>Limit c (%)</b>	$0 \leq c \leq 60$		
<b>Limit e (%)</b>	$0 \leq e \leq 15$		<b>Limit e (%)</b>	$0 \leq e \leq 15$		
<b>Limit Area</b>	$20 \leq x \leq 50$ $40 \leq y \leq 90$		<b>Limit Area</b>	$60 \leq x \leq 90$ $40 \leq y \leq 90$		
<b>Background</b>	$25 \leq x \leq 80$ $105 \leq y \leq 130$		<b>Background</b>	$25 \leq x \leq 80$ $105 \leq y \leq 130$		
<b>N(d,c)</b>			<b>N(d,c)</b>			
<b>N(d)</b>			<b>N(d)</b>			
<b>N(d,e)</b>			<b>N(d,e)</b>			
<b>Average d (um)</b>	6.3593		<b>Average d (um)</b>	4.405		
<b>Fluence (tracks/cm^2)</b>	9.54E+03		<b>Fluence (tracks/cm^2)</b>	1.56E+04		
<b>Yield</b>	2.70E+09		<b>Yield</b>	4.42E+09		

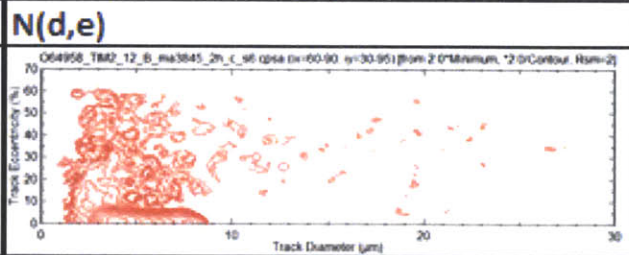
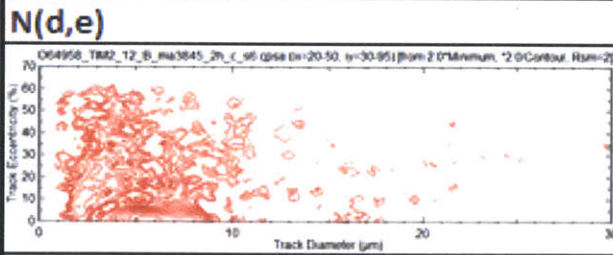
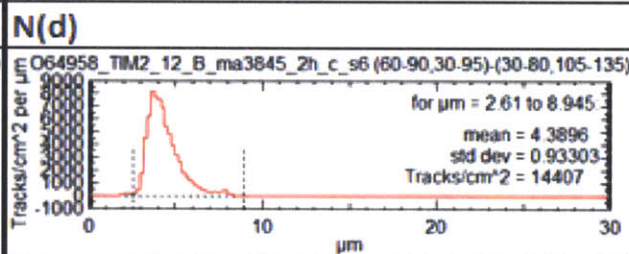
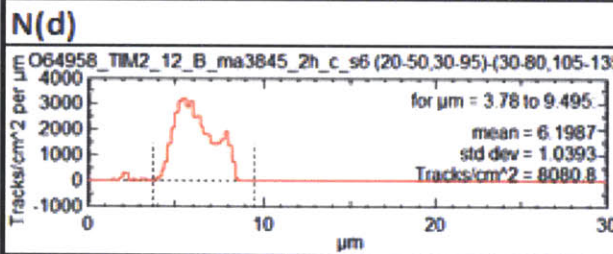
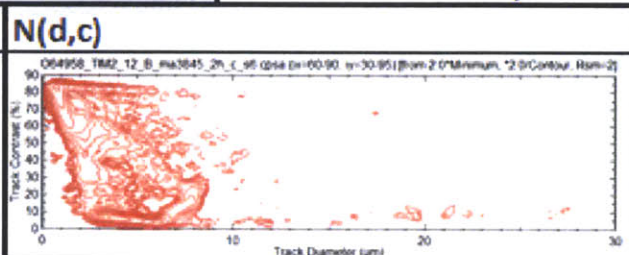
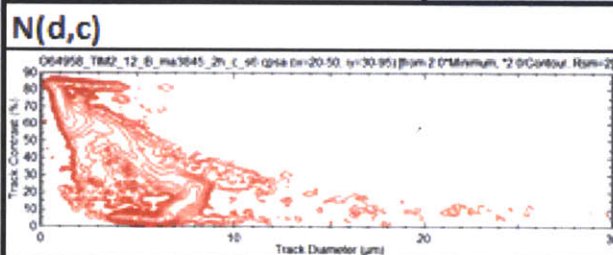
Tim 1, 12:00					
Shot	64958	Piece	ma3789	Type	Bert
Etch Time (hours)	2	Distance (cm)	150	Magnification	40x
Step (um):	50		Step (um):	25	
Limit c (%)	$0 \leq c \leq 62$		Limit c (%)	$0 \leq c \leq 40$	
Limit e (%)	$0 \leq e \leq 11$		Limit e (%)	$0 \leq e \leq 11$	
Limit Area	$20 \leq x \leq 50$ $30 \leq y \leq 95$		Limit Area	$60 \leq x \leq 90$ $30 \leq y \leq 95$	
Background	$30 \leq x \leq 80$ $105 \leq y \leq 135$		Background	$30 \leq x \leq 80$ $105 \leq y \leq 135$	
N(d,c)			N(d,c)		
					
N(d)		N(d)			
					
N(d,e)		N(d,e)			
					
Average d (um)	6.2219	Average d (um)	4.2792		
Fluence (tracks/cm^2)	9.92E+03	Fluence (tracks/cm^2)	1.61E+04		
Yield	2.80E+09	Yield	4.55E+09		

Tim 2, 4:00					
Shot	64958	Piece	ma3846	Type	Bert
Etch Time (hours)	6	Distance (cm)	150	Magnification	40x
<i>Step (um):</i>	50		<i>Step (um):</i>	25	
Limit c (%)	$0 \leq c \leq 85$		Limit c (%)	$0 \leq c \leq 85$	
Limit e (%)	$0 \leq e \leq 15$		Limit e (%)	$0 \leq e \leq 15$	
Limit Area	$20 \leq x \leq 50$ $40 \leq y \leq 90$		Limit Area	$60 \leq x \leq 90$ $40 \leq y \leq 90$	
Background	$25 \leq x \leq 80$ $105 \leq y \leq 130$		Background	$25 \leq x \leq 80$ $105 \leq y \leq 130$	
<b>N(d,c)</b>			<b>N(d,c)</b>		
					
<b>N(d)</b>		<b>N(d)</b>			
					
<b>N(d,e)</b>		<b>N(d,e)</b>			
					
<b>Average d (um)</b>	19.999	<b>Average d (um)</b>	16.736		
<b>Fluence (tracks/cm^2)</b>	8.76E+03	<b>Fluence (tracks/cm^2)</b>	1.46E+04		
<b>Yield</b>	2.48E+09	<b>Yield</b>	4.14E+09		

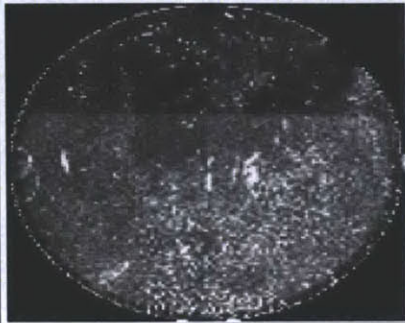
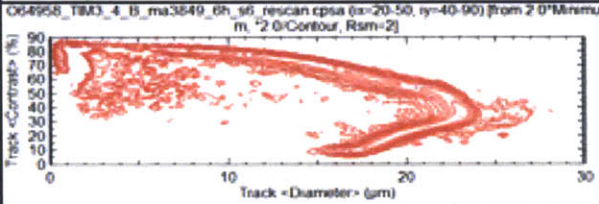
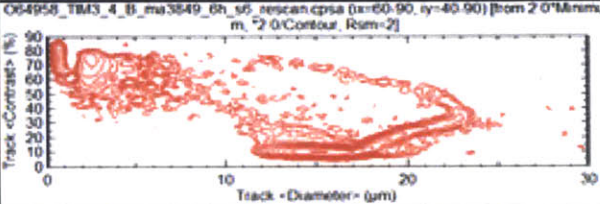
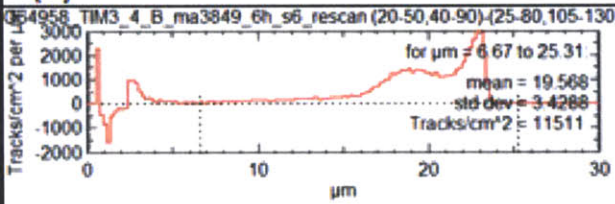
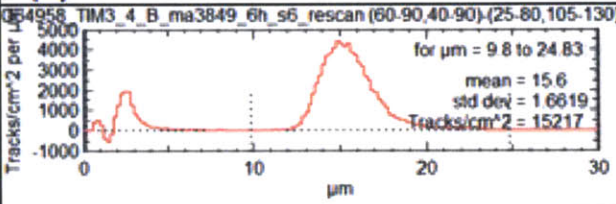
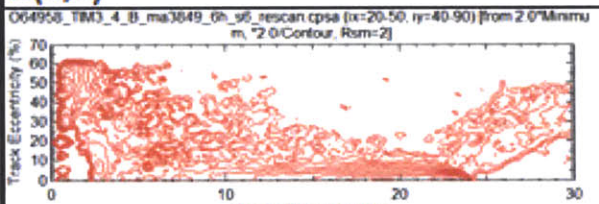
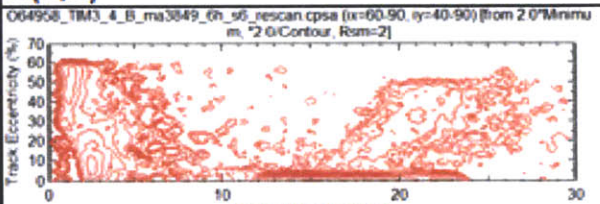
Tim 2, 8:00					
Shot	64958	Piece	ma3847	Type	Bert
Etch Time (hours)	2	Distance (cm)	150	Magnification	40x
<b>Step (um):</b>	50			<b>Step (um):</b>	25
<b>Limit c (%)</b>	0 ≤ c ≤ 65			<b>Limit c (%)</b>	0 ≤ c ≤ 60
<b>Limit e (%)</b>	0 ≤ e ≤ 15			<b>Limit e (%)</b>	0 ≤ e ≤ 15
<b>Limit Area</b>	20 ≤ x ≤ 50 40 ≤ y ≤ 90			<b>Limit Area</b>	60 ≤ x ≤ 90 40 ≤ y ≤ 90
<b>Background</b>	25 ≤ x ≤ 80 105 ≤ y ≤ 130			<b>Background</b>	25 ≤ x ≤ 80 105 ≤ y ≤ 130
<b>N(d,c)</b>		<b>N(d,c)</b>			
					
<b>N(d)</b>		<b>N(d)</b>			
					
<b>N(d,e)</b>		<b>N(d,e)</b>			
					
<b>Average d (um)</b>	6.548	<b>Average d (um)</b>	4.714		
<b>Fluence (tracks/cm^2)</b>	8.92E+03	<b>Fluence (tracks/cm^2)</b>	1.62E+04		
<b>Yield</b>	2.52E+09	<b>Yield</b>	4.57E+09		


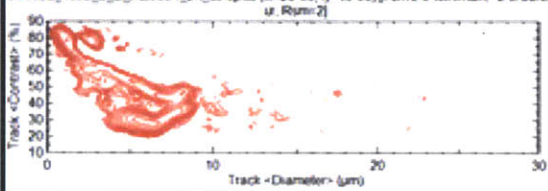
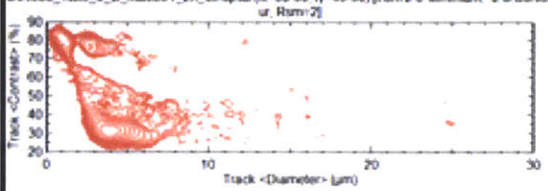
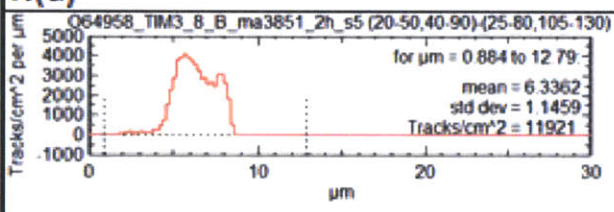
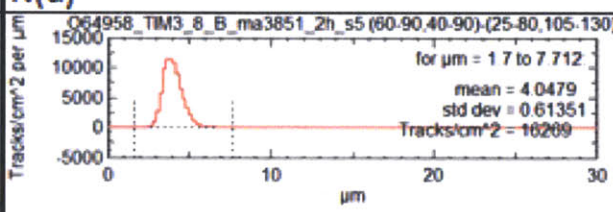
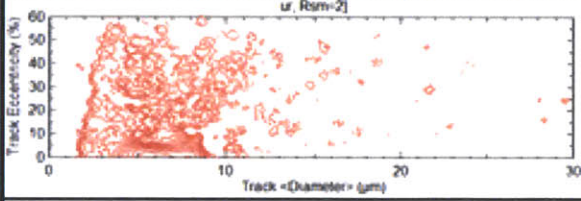
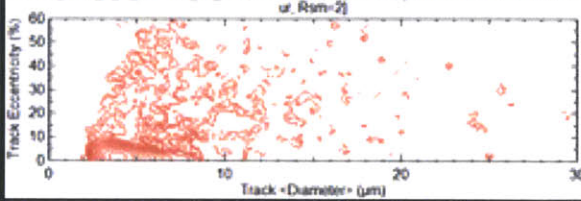
Tim 2, 12:00

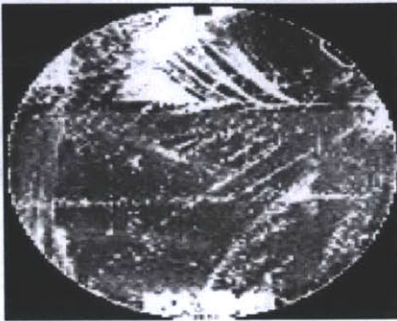
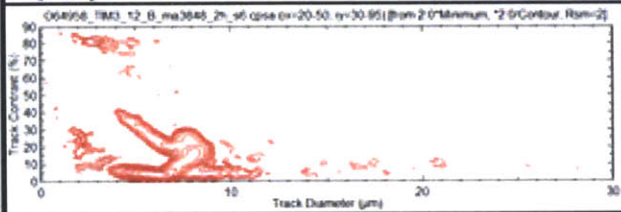
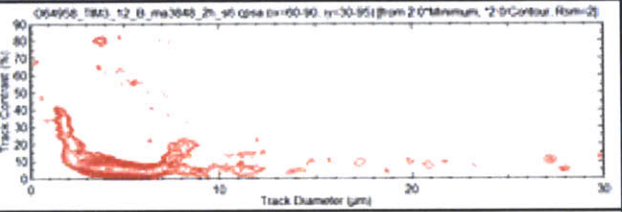
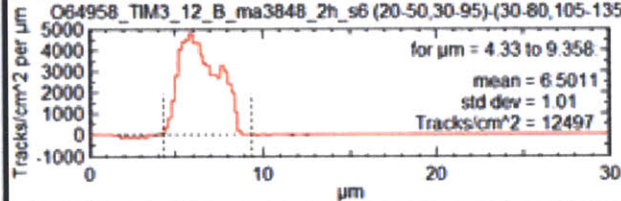
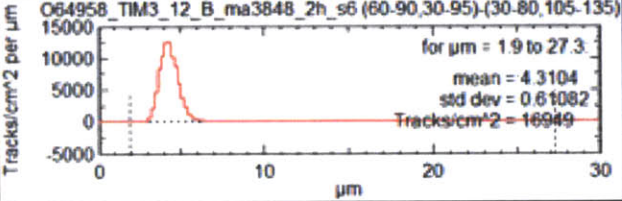
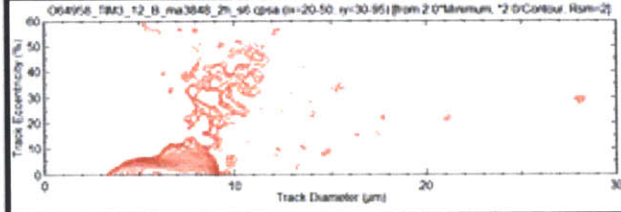
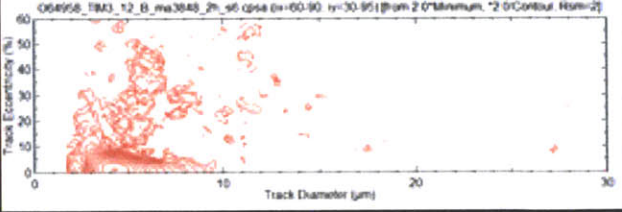
<b>Shot</b>	<b>64958</b>	<b>Piece</b>	<b>ma3845</b>	<b>Type</b>	<b>Bert</b>
<b>Etch Time (hours)</b>	<b>2</b>	<b>Distance (cm)</b>	<b>150</b>	<b>Magnification</b>	<b>40x</b>
<b>Step (um):</b>	<b>50</b>			<b>Step (um):</b>	<b>25</b>
<b>Limit c (%)</b>	$0 \leq c \leq 37$			<b>Limit c (%)</b>	$0 \leq c \leq 31$
<b>Limit e (%)</b>	$0 \leq e \leq 9$			<b>Limit e (%)</b>	$0 \leq e \leq 9$
<b>Limit Area</b>	$20 \leq x \leq 50$ $30 \leq y \leq 95$			<b>Limit Area</b>	$60 \leq x \leq 90$ $30 \leq y \leq 95$
<b>Background</b>	$30 \leq x \leq 80$ $105 \leq y \leq 135$			<b>Background</b>	$30 \leq x \leq 80$ $105 \leq y \leq 135$



<b>Average d (um)</b>	<b>6.1987</b>	<b>Average d (um)</b>	<b>4.3896</b>
<b>Fluence (tracks/cm^2)</b>	<b>8.08E+03</b>	<b>Fluence (tracks/cm^2)</b>	<b>1.44E+04</b>
<b>Yield</b>	<b>2.28E+09</b>	<b>Yield</b>	<b>4.07E+09</b>

Tim 3, 4:00					
Shot	64958	Piece	ma3849	Type	Bert
Etch Time (hours)	6	Distance (cm)	150	Magnification	40x
<b>Step (um):</b>	50		<b>Step (um):</b>	25	
<b>Limit c (%)</b>	0 ≤ c ≤ 85		<b>Limit c (%)</b>	0 ≤ c ≤ 75	
<b>Limit e (%)</b>	0 ≤ e ≤ 15		<b>Limit e (%)</b>	0 ≤ e ≤ 15	
<b>Limit Area</b>	20 ≤ x ≤ 50 40 ≤ y ≤ 90		<b>Limit Area</b>	60 ≤ x ≤ 90 40 ≤ y ≤ 90	
<b>Background</b>	25 ≤ x ≤ 80 105 ≤ y ≤ 130		<b>Background</b>	25 ≤ x ≤ 80 105 ≤ y ≤ 130	
<b>N(d,c)</b>					
<b>N(d)</b>	 <p>for <math>\mu\text{m} = 6.67</math> to <math>25.31</math>  mean = 19.568  std dev = 3.4288  Tracks/cm<sup>2</sup> = 11511</p>		 <p>for <math>\mu\text{m} = 9.8</math> to <math>24.83</math>  mean = 15.6  std dev = 1.6619  Tracks/cm<sup>2</sup> = 15217</p>		
<b>N(d,e)</b>					
<b>Average d (um)</b>	19.568	<b>Average d (um)</b>	15.6		
<b>Fluence (tracks/cm^2)</b>	1.15E+04	<b>Fluence (tracks/cm^2)</b>	1.52E+04		
<b>Yield</b>	3.25E+09	<b>Yield</b>	4.30E+09		

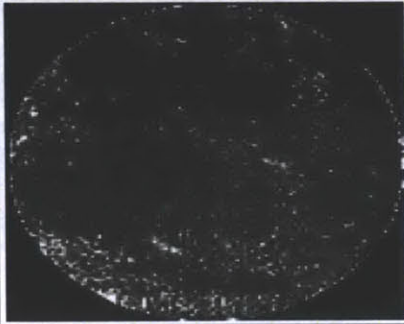
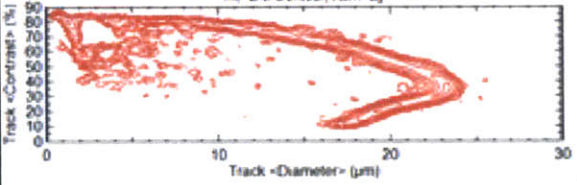
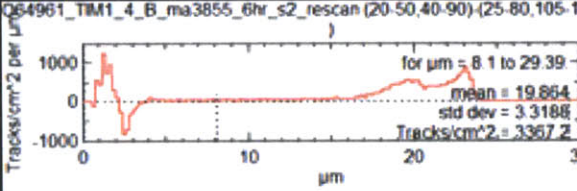
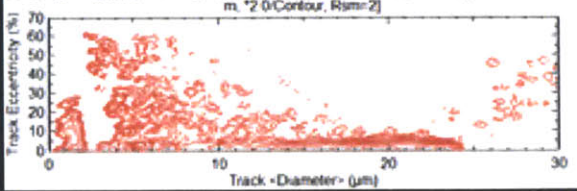
Tim 3, 8:00					
Shot	64958	Piece	ma3851	Type	Bert
Etch Time (hours)	2	Distance (cm)	150	Magnification	40x
<b>Step (um):</b>	50		<b>Step (um):</b>	25	
<b>Limit c (%)</b>	0 ≤ c ≤ 60		<b>Limit c (%)</b>	0 ≤ c ≤ 50	
<b>Limit e (%)</b>	0 ≤ e ≤ 15		<b>Limit e (%)</b>	0 ≤ e ≤ 15	
<b>Limit Area</b>	20 ≤ x ≤ 50 40 ≤ y ≤ 90		<b>Limit Area</b>	60 ≤ x ≤ 90 40 ≤ y ≤ 90	
<b>Background</b>	25 ≤ x ≤ 80 105 ≤ y ≤ 130		<b>Background</b>	25 ≤ x ≤ 80 105 ≤ y ≤ 130	
<b>N(d,c)</b>					
<b>N(d)</b>					
<b>N(d,e)</b>					
<b>Average d (um)</b>	6.3362	<b>Average d (um)</b>	4.0479		
<b>Fluence (tracks/cm^2)</b>	1.19E+04	<b>Fluence (tracks/cm^2)</b>	1.63E+04		
<b>Yield</b>	3.37E+09	<b>Yield</b>	4.60E+09		


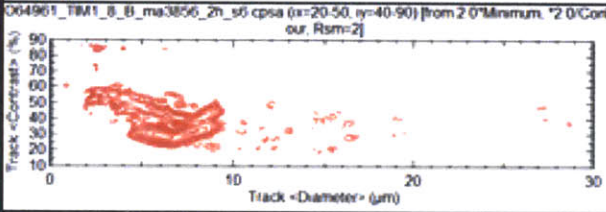
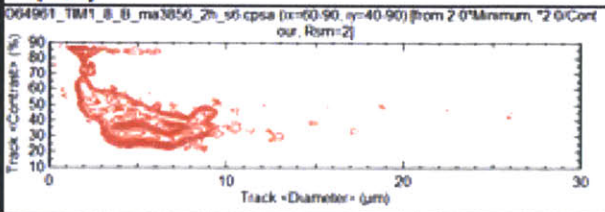
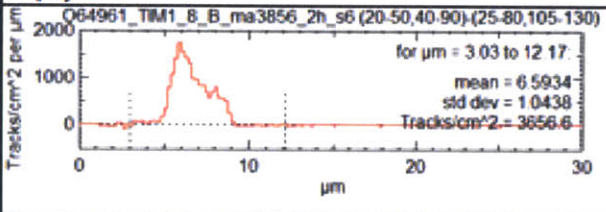
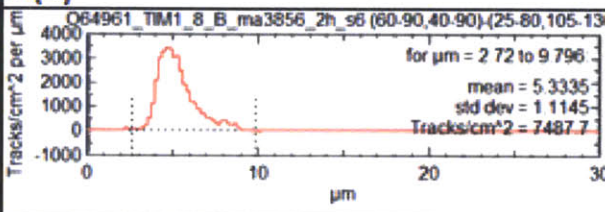
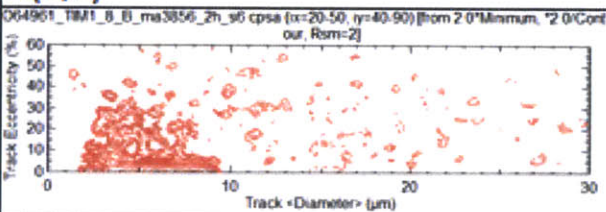
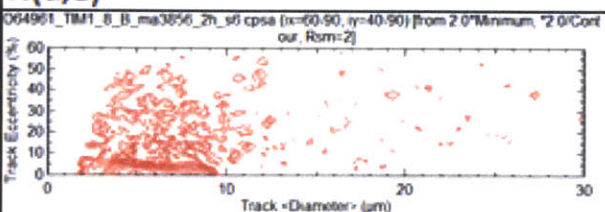
Tim 3, 12:00					
Shot	64958	Piece	ma3848	Type	Bert
Etch Time (hours)	2	Distance (cm)	150	Magnification	40x
<b>Step (um):</b>	50		<b>Step (um):</b>	25	
<b>Limit c (%)</b>	$0 \leq c \leq 42$		<b>Limit c (%)</b>	$0 \leq c \leq 15$	
<b>Limit e (%)</b>	$0 \leq e \leq 14$		<b>Limit e (%)</b>	$0 \leq e \leq 11$	
<b>Limit Area</b>	$20 \leq x \leq 50$ $30 \leq y \leq 95$		<b>Limit Area</b>	$60 \leq x \leq 90$ $30 \leq y \leq 95$	
<b>Background</b>	$30 \leq x \leq 80$ $105 \leq y \leq 135$		<b>Background</b>	$30 \leq x \leq 80$ $105 \leq y \leq 135$	
<b>N(d,c)</b>			<b>N(d,c)</b>		
<b>N(d)</b>	 O64958_TIM3_12_B_ma3848_2h_s6 (20-50,30-95)(from 2 0'Minimum, *2 0'Contour, Rom=2) for $\mu\text{m} = 4.33$ to $9.358$ mean = 6.5011 std dev = 1.01 Tracks/cm <sup>2</sup> = 12497		<b>N(d)</b>		 O64958_TIM3_12_B_ma3848_2h_s6 (60-90,30-95)(30-80,105-135) for $\mu\text{m} = 1.9$ to $27.3$ mean = 4.3104 std dev = 0.61082 Tracks/cm <sup>2</sup> = 16949
<b>N(d,e)</b>			<b>N(d,e)</b>		
<b>Average d (um)</b>	6.5011		<b>Average d (um)</b>	4.3104	
<b>Fluence (tracks/cm<sup>2</sup>)</b>	1.25E+04		<b>Fluence (tracks/cm<sup>2</sup>)</b>	1.69E+04	
<b>Yield</b>	3.53E+09		<b>Yield</b>	4.79E+09	

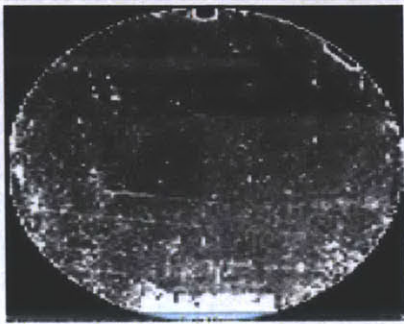
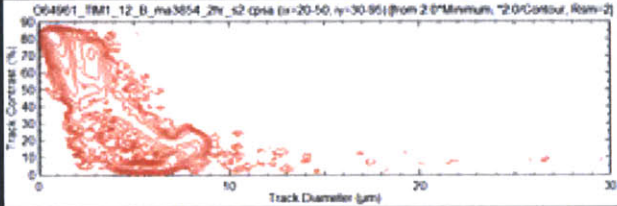
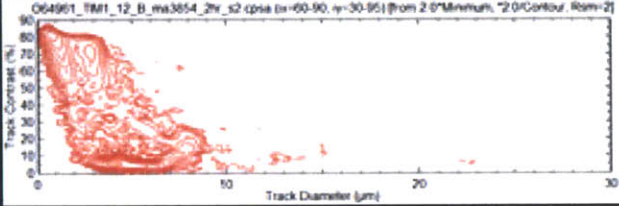
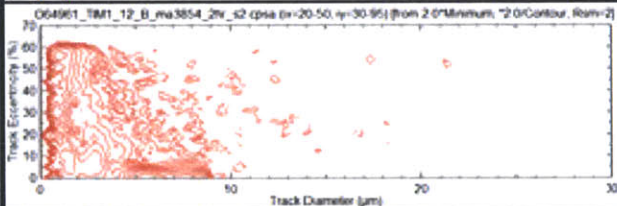
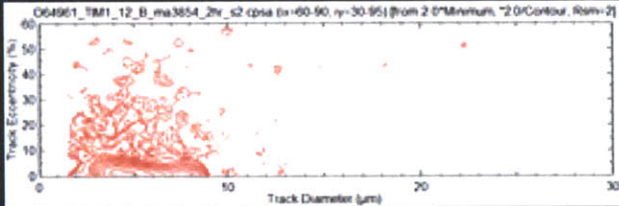
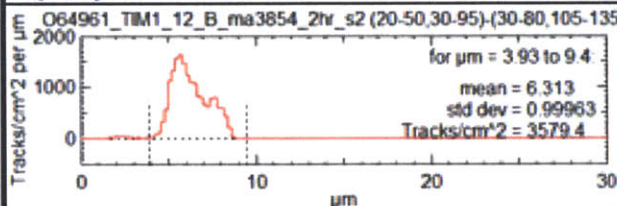
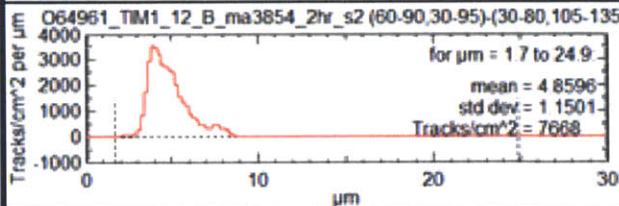


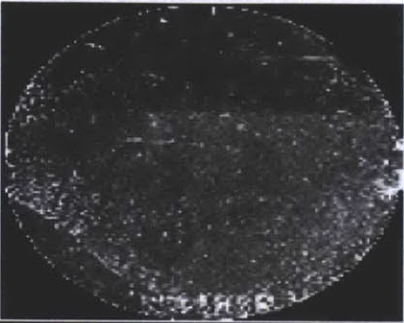
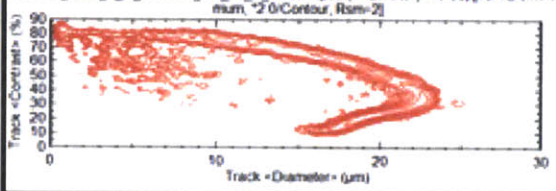
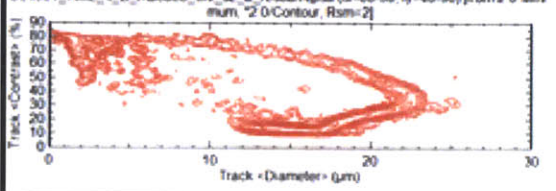
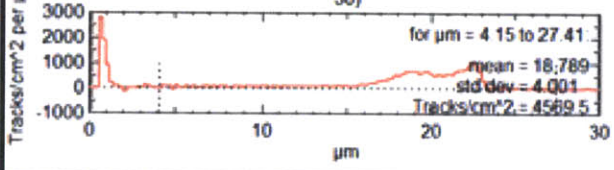
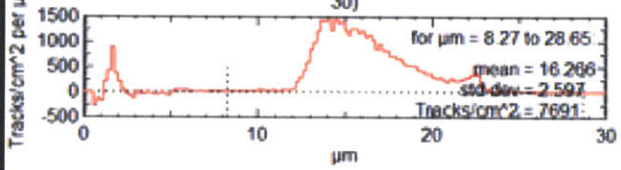
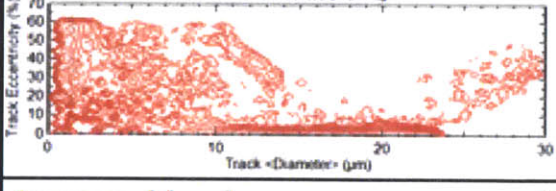
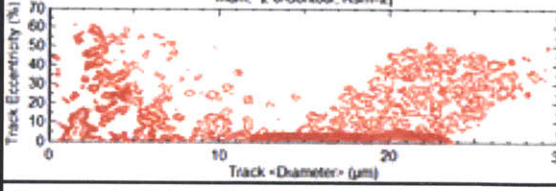
TIM 5					
Shot	64958	Piece	ma3853	Type	Bert
Etch Time (hours)	3	Distance (cm)	150	Magnification	40x
<b>Step (um):</b>	50		<b>Step (um):</b>	25	
<b>Limit c (%)</b>	$0 \leq c \leq 80$		<b>Limit c (%)</b>	$0 \leq c \leq 60$	
<b>Limit e (%)</b>	$0 \leq e \leq 15$		<b>Limit e (%)</b>	$0 \leq e \leq 15$	
<b>Limit Area</b>	$20 \leq x \leq 50$ $40 \leq y \leq 90$		<b>Limit Area</b>	$60 \leq x \leq 90$ $40 \leq y \leq 90$	
<b>Background</b>	$25 \leq x \leq 80$ $105 \leq y \leq 130$		<b>Background</b>	$25 \leq x \leq 80$ $105 \leq y \leq 130$	
<b>N(d,c)</b>			<b>N(d,c)</b>		
<p>O64958_TIM5_B_ma3853_3h_s5 cpsa (x=20-50, y=40-90) [from 2.0° Minimum, 2.0° Contour, Rsm=2]</p>		<p>O64958_TIM5_B_ma3853_3h_s5 cpsa (x=60-90, y=40-90) [from 2.0° Minimum, 2.0° Contour, Rsm=2]</p>			
<b>N(d)</b>		<b>N(d)</b>			
<p>O64958_TIM5_B_ma3853_3h_s5 (20-50,40-90)-(25-80,105-130) for <math>\mu\text{m} = 4.01</math> to <math>14.29</math> mean = 9.6019 std dev = 1.6098 Tracks/cm<sup>2</sup> = 8880.2</p>		<p>O64958_TIM5_B_ma3853_3h_s5 (60-90,40-90)-(25-80,105-130) for <math>\mu\text{m} = 3.47</math> to <math>14.15</math> mean = 6.8849 std dev = 1.2249 Tracks/cm<sup>2</sup> = 13889</p>			
<b>N(d,e)</b>		<b>N(d,e)</b>			
<p>O64958_TIM5_B_ma3853_3h_s5 cpsa (x=20-50, y=40-90) [from 2.0° Minimum, 2.0° Contour, Rsm=2]</p>		<p>O64958_TIM5_B_ma3853_3h_s5 cpsa (x=60-90, y=40-90) [from 2.0° Minimum, 2.0° Contour, Rsm=2]</p>			
<b>Average d (um)</b>	9.6019	<b>Average d (um)</b>	6.8849		
<b>Fluence (tracks/cm^2)</b>	8.88E+03	<b>Fluence (tracks/cm^2)</b>	1.39E+04		
<b>Yield</b>	2.51E+09	<b>Yield</b>	3.93E+09		

Shot 64961

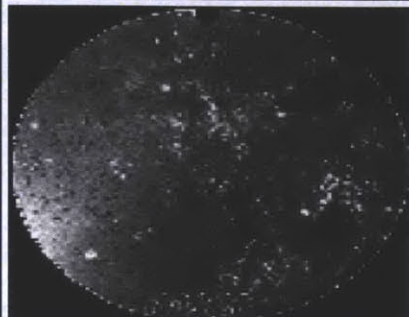
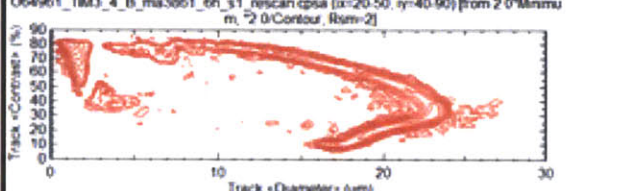
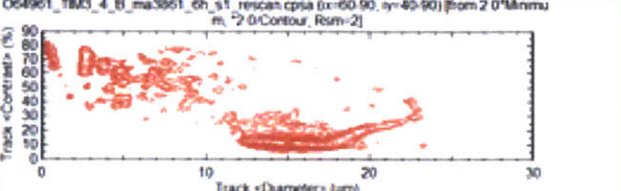
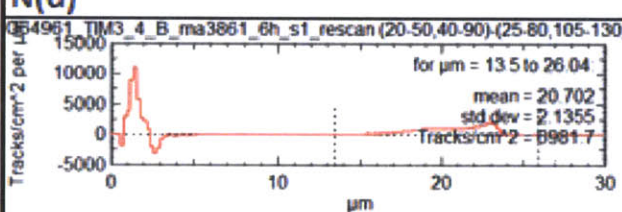
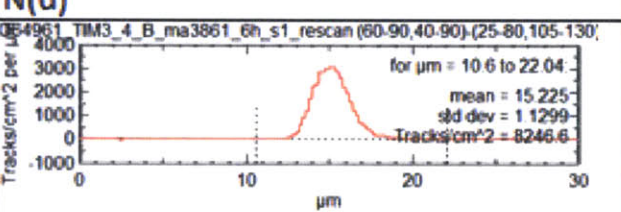
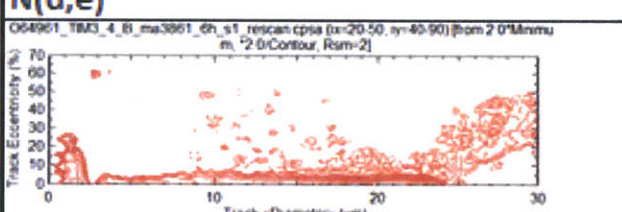
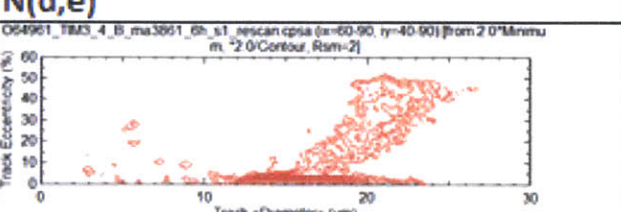
Tim 1, 4:00					
Shot	64961	Piece	ma3855	Type	Bert
Etch Time (hours)	6	Distance (cm)	150	Magnification	40x
<i>Step (um):</i>	50		<i>Step (um):</i>	25	
Limit c (%)	0 ≤ c ≤ 85		Limit c (%)	0 ≤ c ≤ 85	
Limit e (%)	0 ≤ e ≤ 15		Limit e (%)	0 ≤ e ≤ 15	
Limit Area	20 ≤ x ≤ 50 40 ≤ y ≤ 90		Limit Area	60 ≤ x ≤ 90 40 ≤ y ≤ 90	
Background	25 ≤ x ≤ 80 105 ≤ y ≤ 130		Background	25 ≤ x ≤ 80 105 ≤ y ≤ 130	
<b>N(d,c)</b>			<b>N(d,c)</b>		
<b>N(d)</b>			<b>N(d)</b>		
<b>N(d,e)</b>			<b>N(d,e)</b>		
<b>Average d (um)</b>	19.864	<b>Average d (um)</b>	17.051		
<b>Fluence (tracks/cm^2)</b>	3.37E+03	<b>Fluence (tracks/cm^2)</b>	6.64E+03		
<b>Yield</b>	9.52E+08	<b>Yield</b>	1.88E+09		

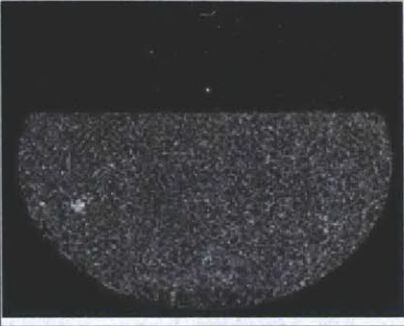
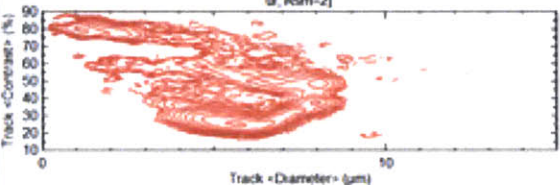
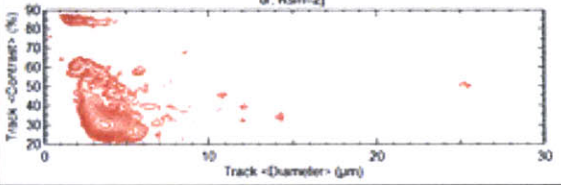
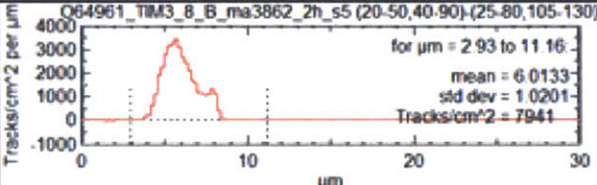
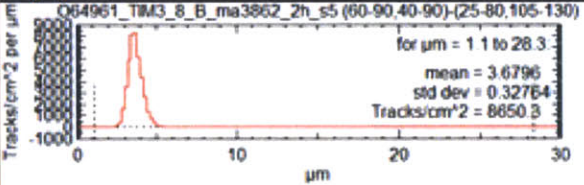
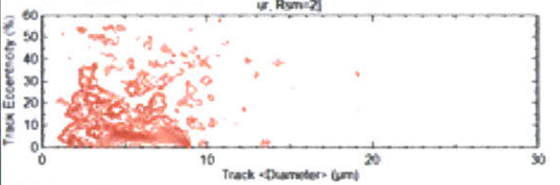
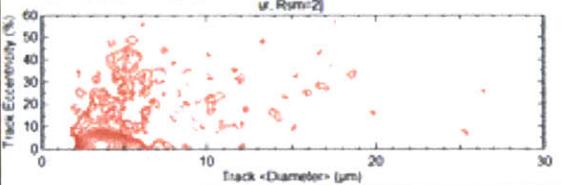
Tim 1, 8:00				
Shot	64961	Piece	ma3856	Type Bert
Etch Time (hours)	2	Distance (cm)	150	Magnification 40x
Step (um):	50			Step (um): 25
Limit c (%)	$0 \leq c \leq 60$			Limit c (%) $0 \leq c \leq 50$
Limit e (%)	$0 \leq e \leq 15$			Limit e (%) $0 \leq e \leq 15$
Limit Area	$20 \leq x \leq 50$ $40 \leq y \leq 90$			Limit Area $60 \leq x \leq 90$ $40 \leq y \leq 90$
Background	$25 \leq x \leq 80$ $105 \leq y \leq 130$			Background $25 \leq x \leq 80$ $105 \leq y \leq 130$
<b>N(d,c)</b>				<b>N(d,c)</b>
				
<b>N(d)</b>		<b>N(d)</b>		
				
<b>N(d,e)</b>		<b>N(d,e)</b>		
				
Average d (um)	6.5934	Average d (um)	5.3335	
Fluence (tracks/cm^2)	3.66E+03	Fluence (tracks/cm^2)	7.49E+03	
Yield	1.03E+09	Yield	2.12E+09	

Tim 1, 12:00					
Shot	64961	Piece	ma3854	Type	Bert
Etch Time (hours)	2	Distance (cm)	150	Magnification	40x
Step (um):	50		Step (um):	25	
Limit c (%)	$0 \leq c \leq 30$		Limit c (%)	$0 \leq c \leq 29$	
Limit e (%)	$0 \leq e \leq 9$		Limit e (%)	$0 \leq e \leq 9$	
Limit Area	$20 \leq x \leq 50$ $30 \leq y \leq 95$		Limit Area	$60 \leq x \leq 90$ $30 \leq y \leq 95$	
Background	$30 \leq x \leq 80$ $105 \leq y \leq 135$		Background	$30 \leq x \leq 80$ $105 \leq y \leq 135$	
N(d,c)			N(d,c)		
					
N(d)		N(d)			
					
N(d,e)		N(d,e)			
					
Average d (um)		6.313	Average d (um)		
Fluence (tracks/cm^2)		3.58E+03	Fluence (tracks/cm^2)		
Yield		1.01E+09	Yield		
			2.17E+09		

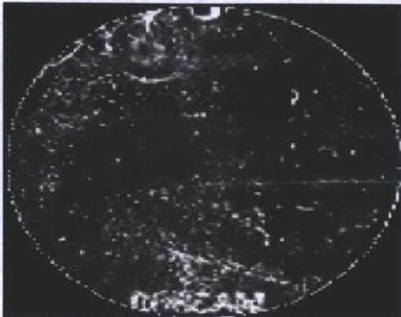
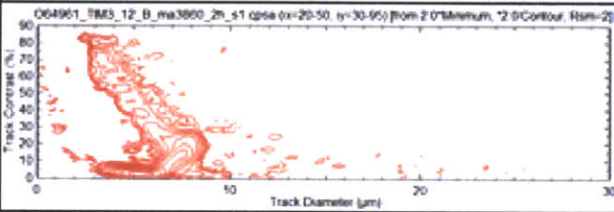
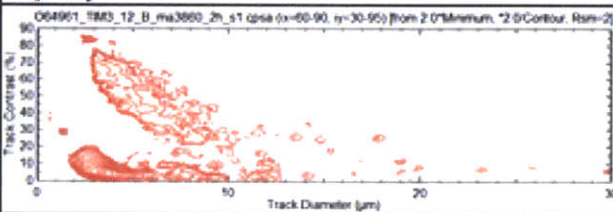
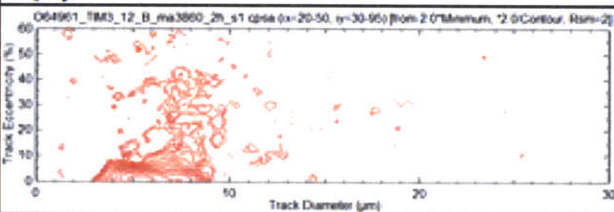
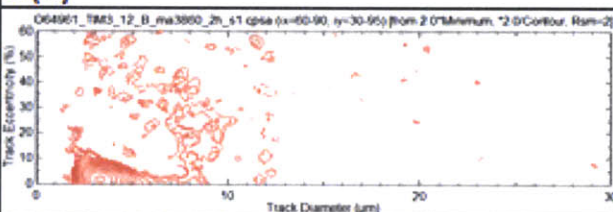
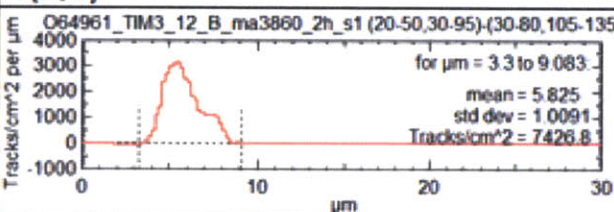
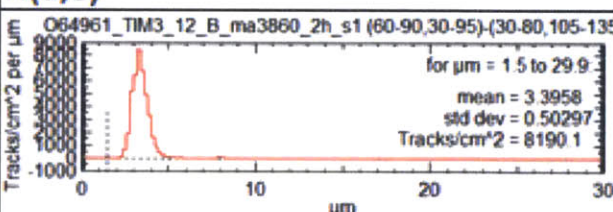
Tim 2, 4:00						
Shot	64961	Piece	ma3858	Type	Bert	
Etch Time (hours)	6	Distance (cm)	150	Magnification	40x	
<b>Step (um):</b>	50		<b>Step (um):</b>	25		
<b>Limit c (%)</b>	$0 \leq c \leq 85$		<b>Limit c (%)</b>	$0 \leq c \leq 85$		
<b>Limit e (%)</b>	$0 \leq e \leq 15$		<b>Limit e (%)</b>	$0 \leq e \leq 15$		
<b>Limit Area</b>	$20 \leq x \leq 50$ $40 \leq y \leq 90$		<b>Limit Area</b>	$60 \leq x \leq 90$ $40 \leq y \leq 90$		
<b>Background</b>	$25 \leq x \leq 80$ $105 \leq y \leq 130$		<b>Background</b>	$25 \leq x \leq 80$ $105 \leq y \leq 130$		
<b>N(d,c)</b>			<b>N(d,c)</b>			
<b>N(d)</b>			<b>N(d)</b>			
<b>N(d,e)</b>			<b>N(d,e)</b>			
<b>Average d (um)</b>	18.789		<b>Average d (um)</b>		16.266	
<b>Fluence (tracks/cm^2)</b>	4.57E+03		<b>Fluence (tracks/cm^2)</b>		7.69E+03	
<b>Yield</b>	1.29E+09		<b>Yield</b>		2.17E+09	

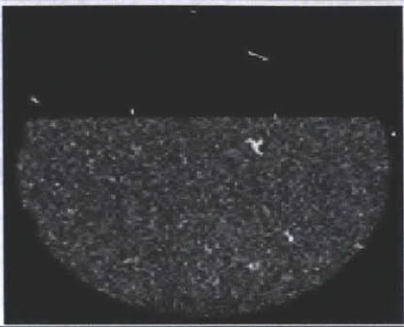
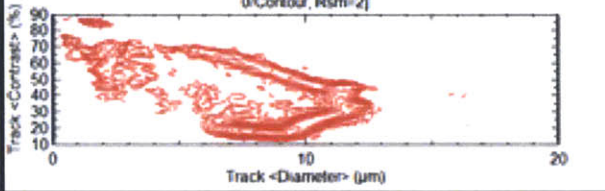
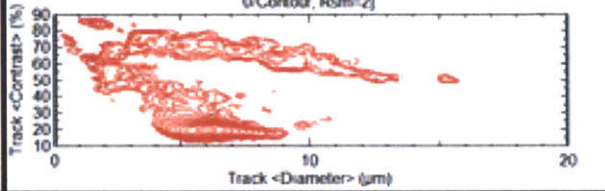
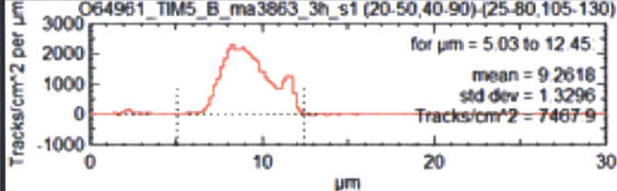
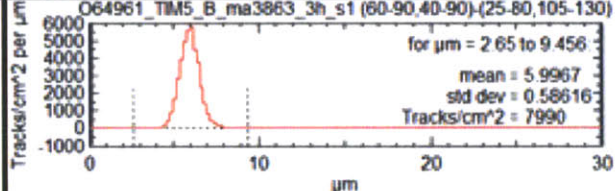
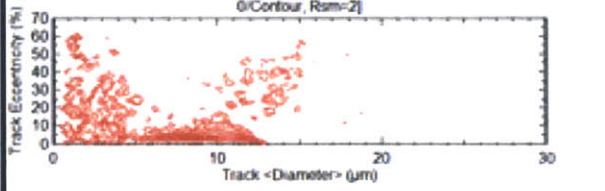
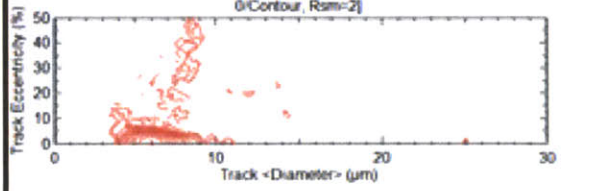
Tim 2, 8:00					
Shot	64961	Piece	ma3859	Type	Bert
Etch Time (hours)	2	Distance (cm)	150	Magnification	40x
<b>Step (um):</b>	50			<b>Step (um):</b>	25
<b>Limit c (%)</b>	0 ≤ c ≤ 70			<b>Limit c (%)</b>	0 ≤ c ≤ 50
<b>Limit e (%)</b>	0 ≤ e ≤ 15			<b>Limit e (%)</b>	0 ≤ e ≤ 15
<b>Limit Area</b>	20 ≤ x ≤ 50 40 ≤ y ≤ 90			<b>Limit Area</b>	60 ≤ x ≤ 90 40 ≤ y ≤ 90
<b>Background</b>	25 ≤ x ≤ 80 105 ≤ y ≤ 130			<b>Background</b>	25 ≤ x ≤ 80 105 ≤ y ≤ 130
<b>N(d,c)</b>					
<b>N(d)</b>					
<b>N(d,e)</b>					
<b>Average d (um)</b>	6.3028		<b>Average d (um)</b>		4.5244
<b>Fluence (tracks/cm^2)</b>	3.94E+03		<b>Fluence (tracks/cm^2)</b>		6.67E+03
<b>Yield</b>	1.11E+09		<b>Yield</b>		1.89E+09

Tim 3, 4:00					
Shot	64961	Piece	ma3861	Type	Bert
Etch Time (hours)	6	Distance (cm)	150	Magnification	40x
<b>Step (um):</b>	50		<b>Step (um):</b>	25	
<b>Limit c (%)</b>	$0 \leq c \leq 85$		<b>Limit c (%)</b>	$0 \leq c \leq 40$	
<b>Limit e (%)</b>	$0 \leq e \leq 15$		<b>Limit e (%)</b>	$0 \leq e \leq 15$	
<b>Limit Area</b>	$20 \leq x \leq 50$ $40 \leq y \leq 90$		<b>Limit Area</b>	$60 \leq x \leq 90$ $40 \leq y \leq 90$	
<b>Background</b>	$25 \leq x \leq 80$ $105 \leq y \leq 130$		<b>Background</b>	$25 \leq x \leq 80$ $105 \leq y \leq 130$	
<b>N(d,c)</b>			<b>N(d,c)</b>		
					
<b>N(d)</b>		<b>N(d)</b>			
					
<b>N(d,e)</b>		<b>N(d,e)</b>			
					
<b>Average d (um)</b>	20.702	<b>Average d (um)</b>	15.225		
<b>Fluence (tracks/cm^2)</b>	6.98E+03	<b>Fluence (tracks/cm^2)</b>	8.25E+03		
<b>Yield</b>	1.97E+09	<b>Yield</b>	2.33E+09		

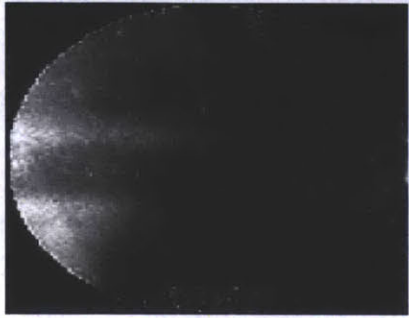
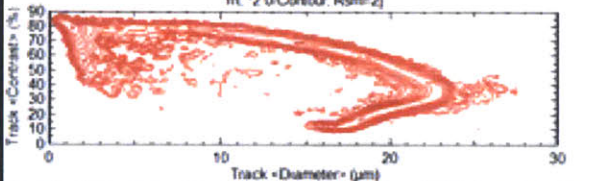
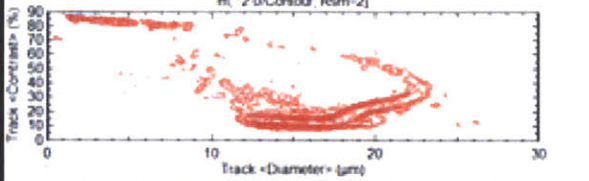
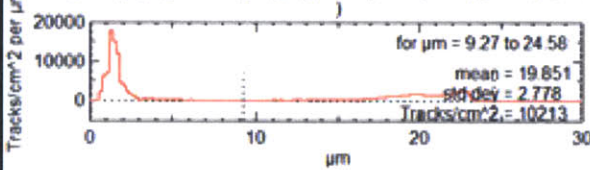
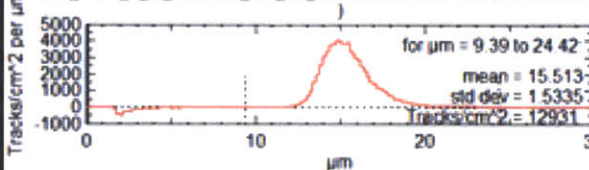
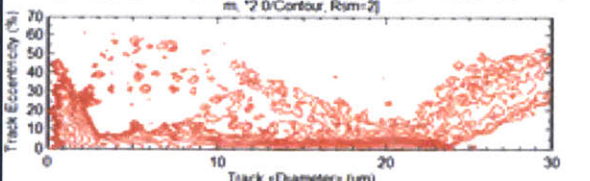
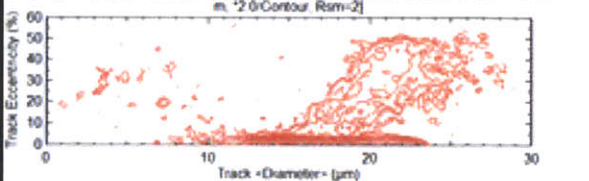
Tim 3, 8:00					
Shot	64961	Piece	ma3862	Type	Bert
Etch Time (hours)	2	Distance (cm)	150	Magnification	40x
<i>Step (um):</i>	50		<i>Step (um):</i>	25	
Limit c (%)	$0 \leq c \leq 65$		Limit c (%)	$0 \leq c \leq 55$	
Limit e (%)	$0 \leq e \leq 15$		Limit e (%)	$0 \leq e \leq 15$	
Limit Area	$20 \leq x \leq 50$ $40 \leq y \leq 90$		Limit Area	$60 \leq x \leq 90$ $40 \leq y \leq 90$	
Background	$25 \leq x \leq 80$ $105 \leq y \leq 130$		Background	$25 \leq x \leq 80$ $105 \leq y \leq 130$	
<b>N(d,c)</b>			<b>N(d,c)</b>		
					
<b>N(d)</b>		<b>N(d)</b>			
					
<b>N(d,e)</b>		<b>N(d,e)</b>			
					
<b>Average d (um)</b>		6.0133	<b>Average d (um)</b>		3.6796
<b>Fluence (tracks/cm^2)</b>		7.94E+03	<b>Fluence (tracks/cm^2)</b>		8.65E+03
<b>Yield</b>		2.25E+09	<b>Yield</b>		2.45E+09


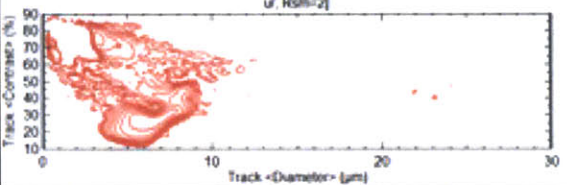
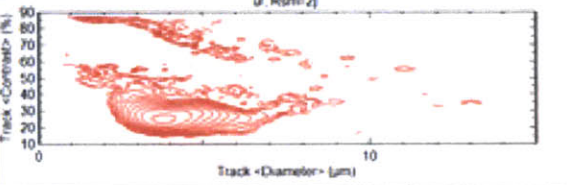
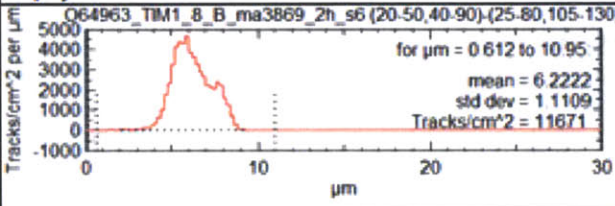
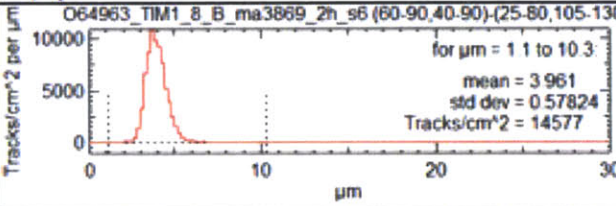
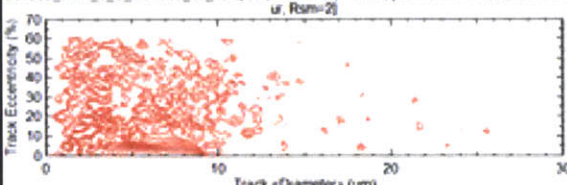
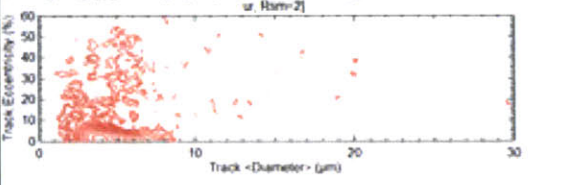


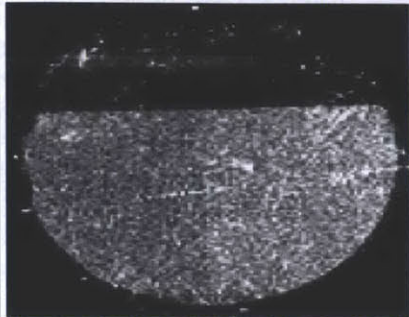
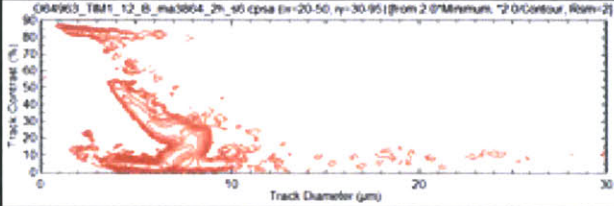
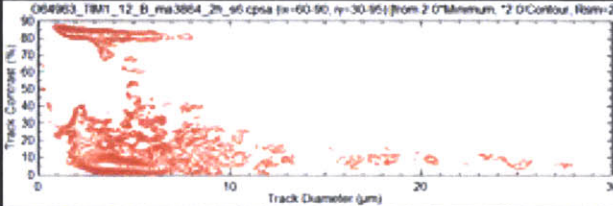
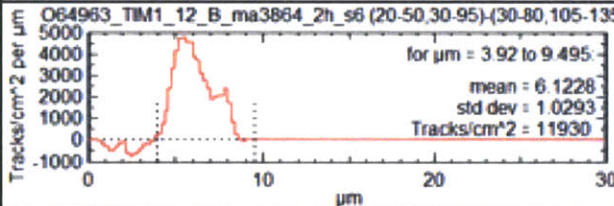
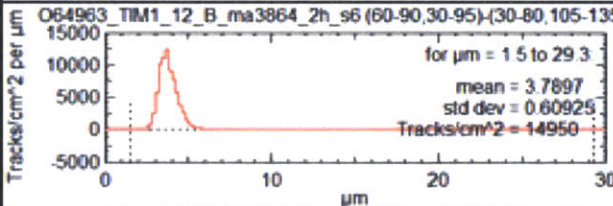
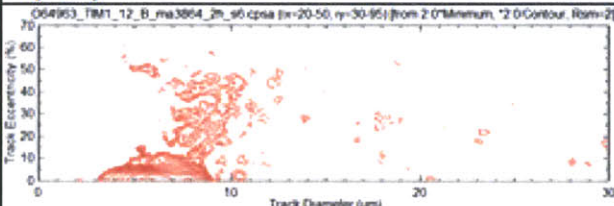
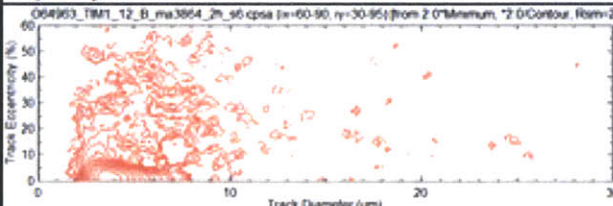
Tim 3, 12:00					
Shot	64961	Piece		Type	Bert
Etch Time (hours)	2	Distance (cm)	150	Magnification	40x
Step (um):	50			Step (um):	25
Limit c (%)	$0 \leq c \leq 28$			Limit c (%)	$0 \leq c \leq 20$
Limit e (%)	$0 \leq e \leq 12$			Limit e (%)	$0 \leq e \leq 14$
Limit Area	$20 \leq x \leq 50$ $30 \leq y \leq 95$			Limit Area	$60 \leq x \leq 90$ $30 \leq y \leq 95$
Background	$30 \leq x \leq 80$ $105 \leq y \leq 135$			Background	$30 \leq x \leq 80$ $105 \leq y \leq 135$
<b>N(d,c)</b>			<b>N(d,c)</b>		
					
<b>N(d)</b>			<b>N(d)</b>		
					
<b>N(d,e)</b>			<b>N(d,e)</b>		
					
Average d (um)	5.825		Average d (um)	3.3858	
Fluence (tracks/cm^2)	7.43E+03		Fluence (tracks/cm^2)	8.19E+03	
Yield	2.10E+09		Yield	2.32E+09	

TIM 5					
Shot	64961	Piece	ma3863	Type	Bert
Etch Time (hours)	3	Distance (cm)	150	Magnification	40x
Step (um):	50		Step (um):	25	
Limit c (%)	$0 \leq c \leq 70$		Limit c (%)	$0 \leq c \leq 40$	
Limit e (%)	$0 \leq e \leq 15$		Limit e (%)	$0 \leq e \leq 15$	
Limit Area	$20 \leq x \leq 50$ $40 \leq y \leq 90$		Limit Area	$60 \leq x \leq 90$ $40 \leq y \leq 90$	
Background	$25 \leq x \leq 80$ $105 \leq y \leq 130$		Background	$25 \leq x \leq 80$ $105 \leq y \leq 130$	
<b>N(d,c)</b>			<b>N(d,c)</b>		
					
<b>N(d)</b>		<b>N(d)</b>			
					
<b>N(d,e)</b>		<b>N(d,e)</b>			
					
Average d (um)	9.2618	Average d (um)	5.9967		
Fluence (tracks/cm^2)	7.47E+03	Fluence (tracks/cm^2)	7.99E+03		
Yield	2.11E+09	Yield	2.26E+09		

Shot 64963

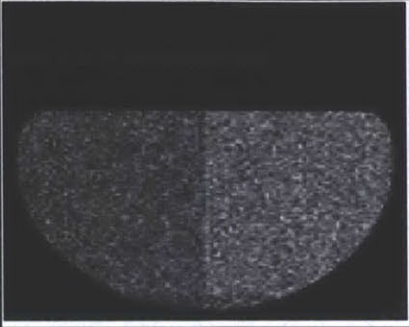
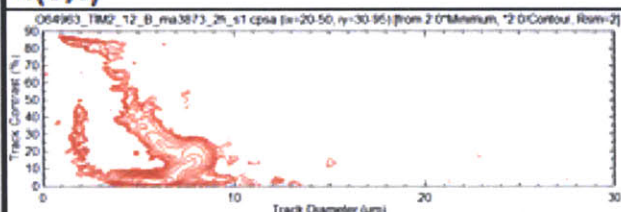
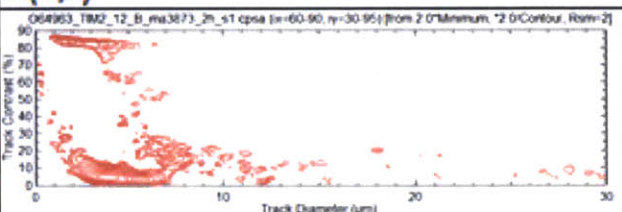
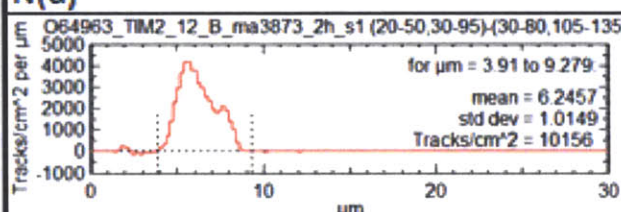
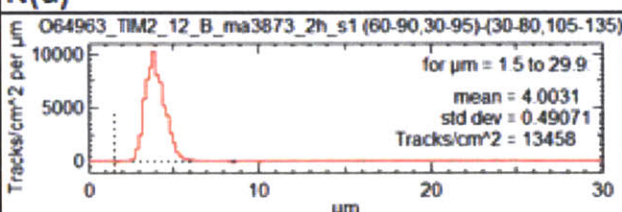
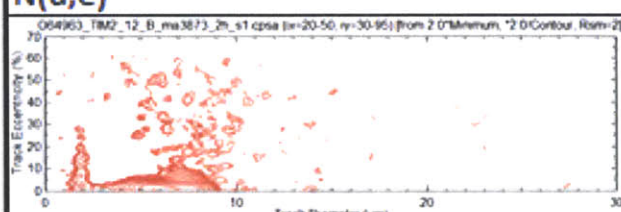
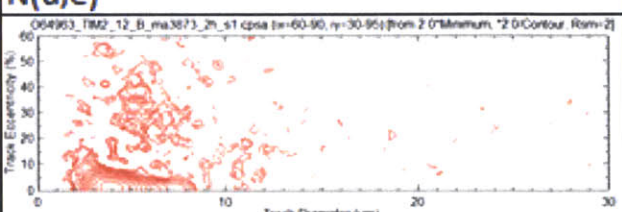
Tim 1, 4:00					
Shot	64963	Piece	ma3865	Type	Bert
Etch Time (hours)	6	Distance (cm)	150	Magnification	40x
<b>Step (um):</b>	50		<b>Step (um):</b>	25	
<b>Limit c (%)</b>	0 ≤ c ≤ 85		<b>Limit c (%)</b>	0 ≤ c ≤ 60	
<b>Limit e (%)</b>	0 ≤ e ≤ 15		<b>Limit e (%)</b>	0 ≤ e ≤ 15	
<b>Limit Area</b>	20 ≤ x ≤ 50 40 ≤ y ≤ 90		<b>Limit Area</b>	60 ≤ x ≤ 90 40 ≤ y ≤ 90	
<b>Background</b>	25 ≤ x ≤ 80 105 ≤ y ≤ 130		<b>Background</b>	25 ≤ x ≤ 80 105 ≤ y ≤ 130	
<b>N(d,c)</b>			<b>N(d,c)</b>		
					
<b>N(d)</b>			<b>N(d)</b>		
					
<b>N(d,e)</b>			<b>N(d,e)</b>		
					
<b>Average d (um)</b>	19.851	<b>Average d (um)</b>	15.513		
<b>Fluence (tracks/cm^2)</b>	1.02E+04	<b>Fluence (tracks/cm^2)</b>	1.29E+04		
<b>Yield</b>	2.89E+09	<b>Yield</b>	3.66E+09		

Tim 1, 8:00					
Shot	64963	Piece	ma3869	Type	Bert
Etch Time (hours)	2	Distance (cm)	150	Magnification	40x
Step (um):	50		Step (um):	25	
Limit c (%)	0 ≤ c ≤ 60		Limit c (%)	0 ≤ c ≤ 55	
Limit e (%)	0 ≤ e ≤ 15		Limit e (%)	0 ≤ e ≤ 15	
Limit Area	20 ≤ x ≤ 50 40 ≤ y ≤ 90		Limit Area	60 ≤ x ≤ 90 40 ≤ y ≤ 90	
Background	25 ≤ x ≤ 80 105 ≤ y ≤ 130		Background	25 ≤ x ≤ 80 105 ≤ y ≤ 130	
<b>N(d,c)</b>			<b>N(d,c)</b>		
					
<b>N(d)</b>			<b>N(d)</b>		
					
<b>N(d,e)</b>			<b>N(d,e)</b>		
					
<b>Average d (um)</b>		6.2222	<b>Average d (um)</b>		3.961
<b>Fluence (tracks/cm^2)</b>		1.17E+04	<b>Fluence (tracks/cm^2)</b>		1.46E+04
<b>Yield</b>		3.30E+09	<b>Yield</b>		4.12E+09


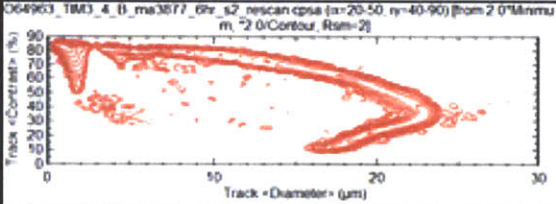
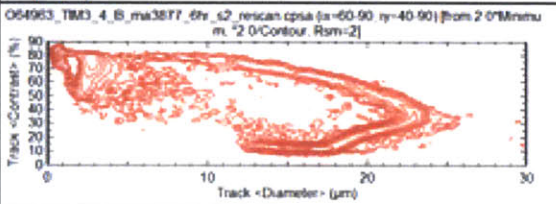
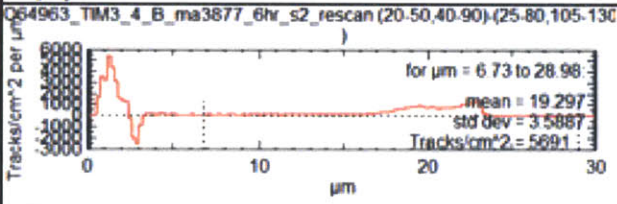
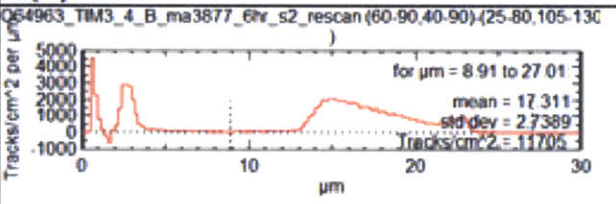
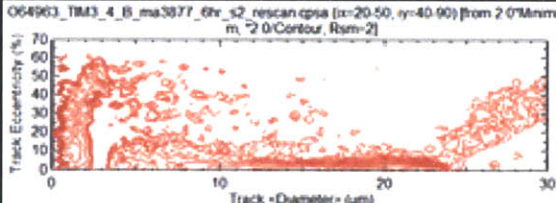
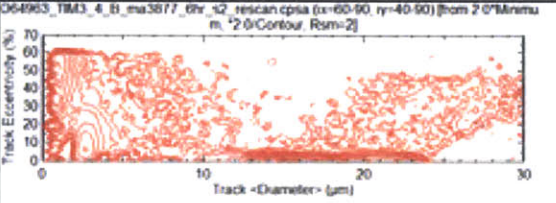
Tim 1, 12:00					
Shot	64963	Piece	ma3864	Type	Bert
Etch Time (hours)	2	Distance (cm)	150	Magnification	40x
Step (um):	50		Step (um):	25	
Limit c (%)	0 ≤ c ≤ 55		Limit c (%)	0 ≤ c ≤ 15	
Limit e (%)	0 ≤ e ≤ 13		Limit e (%)	0 ≤ e ≤ 11	
Limit Area	20 ≤ x ≤ 50 30 ≤ y ≤ 95		Limit Area	60 ≤ x ≤ 90 30 ≤ y ≤ 95	
Background	30 ≤ x ≤ 80 105 ≤ y ≤ 135		Background	30 ≤ x ≤ 80 105 ≤ y ≤ 135	
N(d,c)			N(d,c)		
					
N(d)		N(d)			
					
N(d,e)		N(d,e)			
					
Average d (um)	6.1228	Average d (um)	3.7897		
Fluence (tracks/cm^2)	1.19E+04	Fluence (tracks/cm^2)	1.50E+04		
Yield	3.37E+09	Yield	4.23E+09		

Tim 2, 4:00					
Shot	64963	Piece	ma3874	Type	Bert
Etch Time (hours)	6	Distance (cm)	150	Magnification	40x
<i>Step (um):</i>	50		<i>Step (um):</i>	25	
Limit c (%)	$0 \leq c \leq 85$		Limit c (%)	$0 \leq c \leq 70$	
Limit e (%)	$0 \leq e \leq 15$		Limit e (%)	$0 \leq e \leq 15$	
Limit Area	$20 \leq x \leq 50$ $40 \leq y \leq 90$		Limit Area	$60 \leq x \leq 90$ $40 \leq y \leq 90$	
Background	$25 \leq x \leq 80$ $105 \leq y \leq 130$		Background	$25 \leq x \leq 80$ $105 \leq y \leq 130$	
<b>N(d,c)</b>		<b>N(d,c)</b>			
<b>N(d)</b>		<b>N(d)</b>			
<b>N(d,e)</b>		<b>N(d,e)</b>			
<b>Average d (um)</b>	20.078	<b>Average d (um)</b>	15.307		
<b>Fluence (tracks/cm^2)</b>	9.57E+03	<b>Fluence (tracks/cm^2)</b>	1.30E+04		
<b>Yield</b>	2.71E+09	<b>Yield</b>	3.67E+09		

Tim 2, 8:00						
Shot	64963	Piece	ma3875	Type	Bert	
Etch Time (hours)	2	Distance (cm)	150	Magnification	40x	
Step (um):	50			Step (um):	25	
Limit c (%)	$0 \leq c \leq 75$			Limit c (%)	$0 \leq c \leq 55$	
Limit e (%)	$0 \leq e \leq 15$			Limit e (%)	$0 \leq e \leq 15$	
Limit Area	$20 \leq x \leq 50$ $40 \leq y \leq 90$			Limit Area	$60 \leq x \leq 90$ $40 \leq y \leq 90$	
Background	$25 \leq x \leq 80$ $105 \leq y \leq 130$			Background	$25 \leq x \leq 80$ $105 \leq y \leq 130$	
<b>N(d,c)</b>					<b>N(d,c)</b>	
<p>064963_TIM2_8_B_ma3875_2hr_s2 cpsia (x=20-50, y=40-90) from 2 0'Minimum, 2 0'Cont our, Rsm=2</p>					<p>064963_TIM2_8_B_ma3875_2hr_s2 cpsia (x=60-90, y=40-90) from 2 0'Minimum, 2 0'Cont our, Rsm=2</p>	
<b>N(d)</b>					<b>N(d)</b>	
<p>064963_TIM2_8_B_ma3875_2hr_s2 (20-50,40-90).(25-80,105-130) for <math>\mu\text{m} = 3.95</math> to <math>10.82</math> mean = 6.3779 std dev = 1.0484 Tracks/cm<sup>2</sup> = 10310</p>					<p>064963_TIM2_8_B_ma3875_2hr_s2 (60-90,40-90).(25-80,105-130) for <math>\mu\text{m} = 1.3</math> to <math>10.02</math> mean = 4.063 std dev = 0.64104 Tracks/cm<sup>2</sup> = 13642</p>	
<b>N(d,e)</b>					<b>N(d,e)</b>	
<p>064963_TIM2_8_B_ma3875_2hr_s2 cpsia (x=20-50, y=40-90) from 2 0'Minimum, 2 0'Cont our, Rsm=2</p>					<p>064963_TIM2_8_B_ma3875_2hr_s2 cpsia (x=60-90, y=40-90) from 2 0'Minimum, 2 0'Cont our, Rsm=2</p>	
Average d (um)		6.3779	Average d (um)		4.063	
Fluence (tracks/cm <sup>2</sup> )		1.03E+04	Fluence (tracks/cm <sup>2</sup> )		1.36E+04	
Yield		2.92E+09	Yield		3.86E+09	

Tim 2, 12:00					
Shot	64963	Piece	ma3873	Type	Bert
Etch Time (hours)	2	Distance (cm)	150	Magnification	40x
Step (um):	50		Step (um):	25	
Limit c (%)	$0 \leq c \leq 50$		Limit c (%)	$0 \leq c \leq 22$	
Limit e (%)	$0 \leq e \leq 11$		Limit e (%)	$0 \leq e \leq 12$	
Limit Area	$20 \leq x \leq 50$ $30 \leq y \leq 95$		Limit Area	$60 \leq x \leq 90$ $30 \leq y \leq 95$	
Background	$30 \leq x \leq 80$ $105 \leq y \leq 135$		Background	$30 \leq x \leq 80$ $105 \leq y \leq 135$	
<b>N(d,c)</b>		<b>N(d,c)</b>			
					
<b>N(d)</b>		<b>N(d)</b>			
					
<b>N(d,e)</b>		<b>N(d,e)</b>			
					
Average d (um)	6.2457	Average d (um)	4.0031		
Fluence (tracks/cm^2)	1.02E+04	Fluence (tracks/cm^2)	1.35E+04		
Yield	2.87E+09	Yield	3.81E+09		

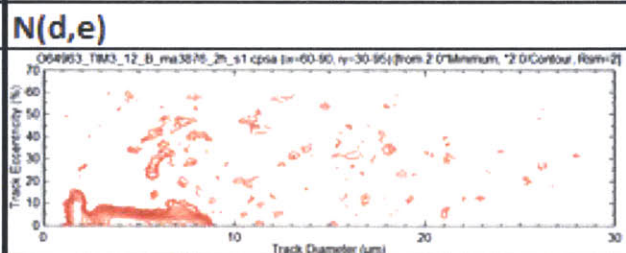
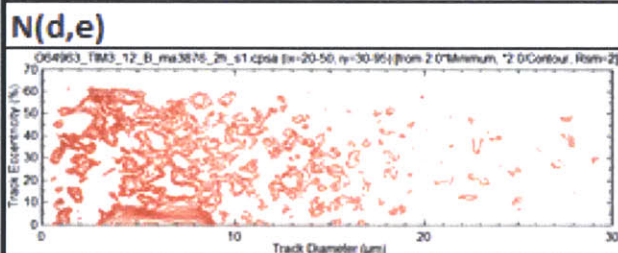
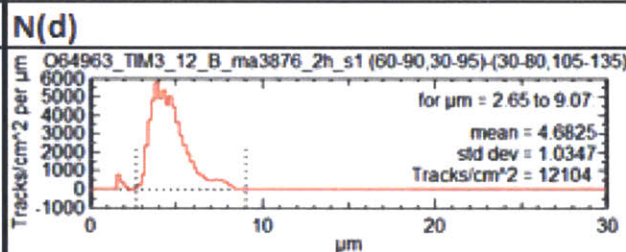
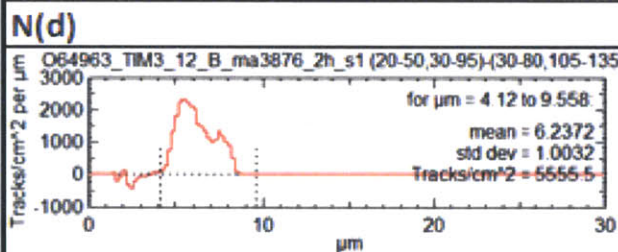
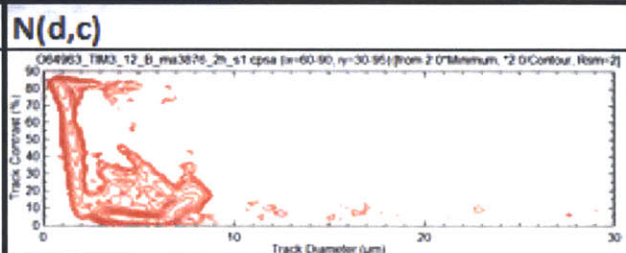
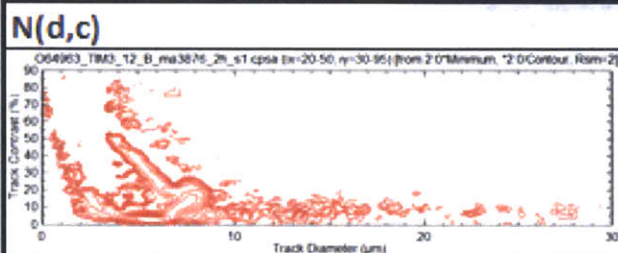


Tim 3, 4:00						
Shot	64963	Piece	ma3877	Type	Bert	
Etch Time (hours)	6	Distance (cm)	150	Magnification	40x	
<b>Step (um):</b>	50		<b>Step (um):</b>	25		
<b>Limit c (%)</b>	0 ≤ c ≤ 85		<b>Limit c (%)</b>	0 ≤ c ≤ 85		
<b>Limit e (%)</b>	0 ≤ e ≤ 15		<b>Limit e (%)</b>	0 ≤ e ≤ 15		
<b>Limit Area</b>	20 ≤ x ≤ 50 40 ≤ y ≤ 90		<b>Limit Area</b>	60 ≤ x ≤ 90 40 ≤ y ≤ 90		
<b>Background</b>	25 ≤ x ≤ 80 105 ≤ y ≤ 130		<b>Background</b>	25 ≤ x ≤ 80 105 ≤ y ≤ 130		
<b>N(d,c)</b>			<b>N(d,c)</b>			
<b>N(d)</b>			<b>N(d)</b>			
<b>N(d,e)</b>			<b>N(d,e)</b>			
<b>Average d (um)</b>	19.297	<b>Average d (um)</b>	17.311			
<b>Fluence (tracks/cm^2)</b>	5.69E+03	<b>Fluence (tracks/cm^2)</b>	1.17E+04			
<b>Yield</b>	1.61E+09	<b>Yield</b>	3.31E+09			

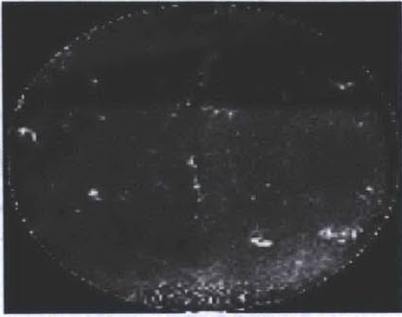
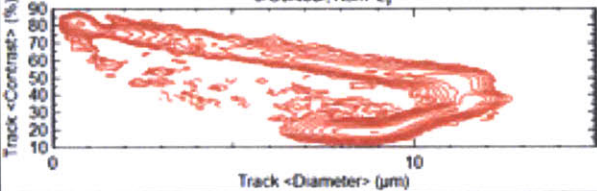
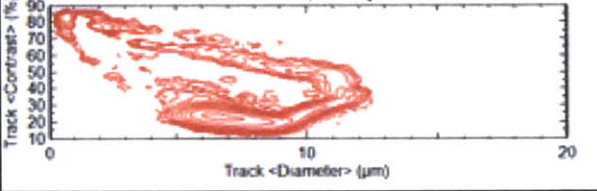
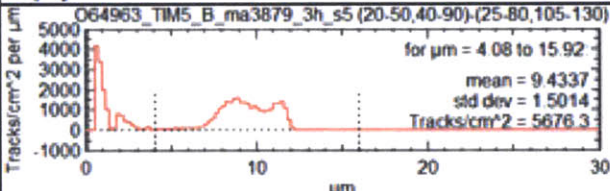
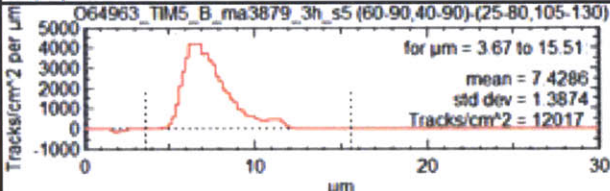
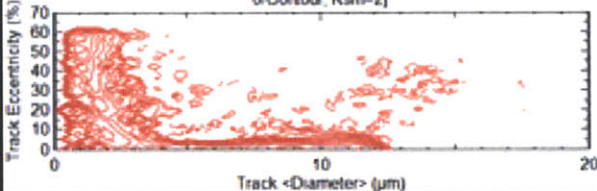
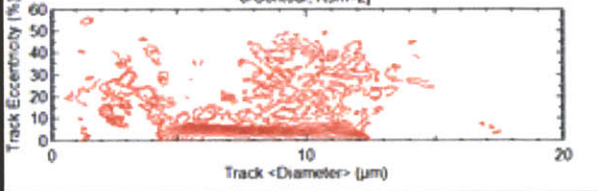
Tim 3, 8:00					
Shot	64963	Piece	ma3878	Type	Bert
Etch Time (hours)	2	Distance (cm)	150	Magnification	40x
Step (um):	50			Step (um):	25
Limit c (%)	0 ≤ c ≤ 60			Limit c (%)	0 ≤ c ≤ 60
Limit e (%)	0 ≤ e ≤ 15			Limit e (%)	0 ≤ e ≤ 15
Limit Area	20 ≤ x ≤ 50 40 ≤ y ≤ 90			Limit Area	60 ≤ x ≤ 90 40 ≤ y ≤ 90
Background	25 ≤ x ≤ 80 105 ≤ y ≤ 130			Background	25 ≤ x ≤ 80 105 ≤ y ≤ 130
<b>N(d,c)</b>			<b>N(d,c)</b>		
<p>064963_TIM3_8_B_ma3878_2hr_s2 (x=20-50, y=40-90) [from 2.0° Minimum, *2.0° Contour, Rsm=2]</p>			<p>064963_TIM3_8_B_ma3878_2hr_s2 (x=60-90, y=40-90) [from 2.0° Minimum, *2.0° Contour, Rsm=2]</p>		
<b>N(d)</b>			<b>N(d)</b>		
<p>064963_TIM3_8_B_ma3878_2hr_s2 (20-50,40-90)-(25-80,105-130) for µm = 2.93 to 12.59 mean = 6.2432 std dev = 1.0749 Tracks/cm² = 6096</p>			<p>064963_TIM3_8_B_ma3878_2hr_s2 (60-90,40-90)-(25-80,105-130) for µm = 2.59 to 10.34 mean = 4.739 std dev = 1.0696 Tracks/cm² = 13409</p>		
<b>N(d,e)</b>			<b>N(d,e)</b>		
<p>064963_TIM3_8_B_ma3878_2hr_s2 (x=20-50, y=40-90) [from 2.0° Minimum, *2.0° Contour, Rsm=2]</p>			<p>064963_TIM3_8_B_ma3878_2hr_s2 (x=60-90, y=40-90) [from 2.0° Minimum, *2.0° Contour, Rsm=2]</p>		
<b>Average d (um)</b>		6.2432	<b>Average d (um)</b>		4.739
<b>Fluence (tracks/cm²)</b>		6.10E+03	<b>Fluence (tracks/cm²)</b>		1.34E+04
<b>Yield</b>		1.72E+09	<b>Yield</b>		3.79E+09

**Tim 3, 12:00**

<b>Shot</b>	<b>64963</b>	<b>Piece</b>	<b>ma3876</b>	<b>Type</b>	<b>Bert</b>
<b>Etch Time (hours)</b>	<b>2</b>	<b>Distance (cm)</b>	<b>150</b>	<b>Magnification</b>	<b>40x</b>
<b>Step (um):</b>	<b>50</b>			<b>Step (um):</b>	<b>25</b>
<b>Limit c (%)</b>	<b>0 ≤ c ≤ 54</b>			<b>Limit c (%)</b>	<b>0 ≤ c ≤ 36</b>
<b>Limit e (%)</b>	<b>0 ≤ e ≤ 13</b>			<b>Limit e (%)</b>	<b>0 ≤ e ≤ 11</b>
<b>Limit Area</b>	<b>20 ≤ x ≤ 50</b> <b>30 ≤ y ≤ 95</b>			<b>Limit Area</b>	<b>60 ≤ x ≤ 90</b> <b>30 ≤ y ≤ 95</b>
<b>Background</b>	<b>30 ≤ x ≤ 80</b> <b>105 ≤ y ≤ 135</b>			<b>Background</b>	<b>30 ≤ x ≤ 80</b> <b>105 ≤ y ≤ 135</b>



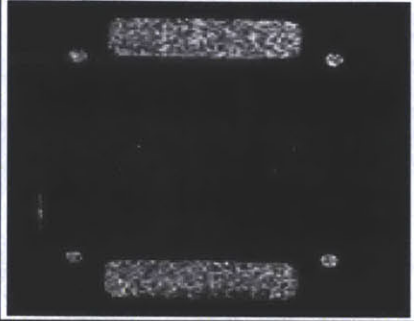
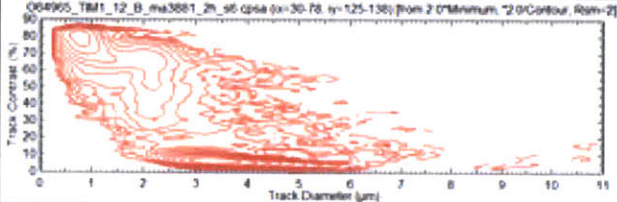
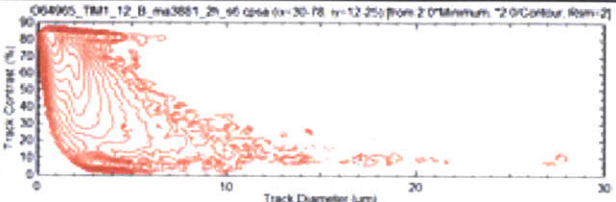
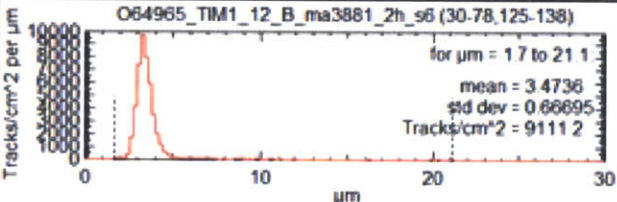
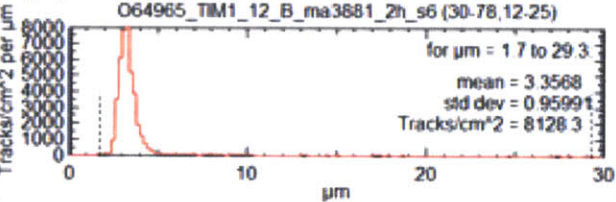
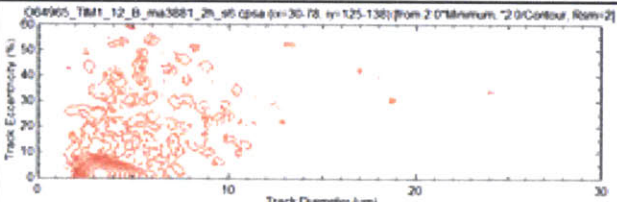
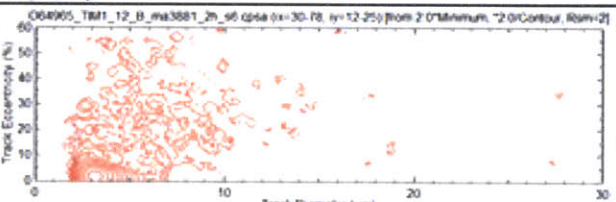
<b>Average d (um)</b>	<b>6.2372</b>	<b>Average d (um)</b>	<b>4.6825</b>
<b>Fluence (tracks/cm^2)</b>	<b>5.56E+03</b>	<b>Fluence (tracks/cm^2)</b>	<b>1.21E+04</b>
<b>Yield</b>	<b>1.57E+09</b>	<b>Yield</b>	<b>3.42E+09</b>

TIM 5					
Shot	64963	Piece	ma3879	Type	Bert
Etch Time (hours)	3	Distance (cm)	150	Magnification	40x
Step (um):	50		Step (um):	25	
Limit c (%)	$0 \leq c \leq 80$		Limit c (%)	$0 \leq c \leq 65$	
Limit e (%)	$0 \leq e \leq 15$		Limit e (%)	$0 \leq e \leq 15$	
Limit Area	$20 \leq x \leq 50$ $40 \leq y \leq 90$		Limit Area	$60 \leq x \leq 90$ $40 \leq y \leq 90$	
Background	$25 \leq x \leq 80$ $105 \leq y \leq 130$		Background	$25 \leq x \leq 80$ $105 \leq y \leq 130$	
<b>N(d,c)</b>		<b>N(d,c)</b>			
					
<b>N(d)</b>		<b>N(d)</b>			
					
<b>N(d,e)</b>		<b>N(d,e)</b>			
					
Average d (um)	9.4337	Average d (um)	7.4286		
Fluence (tracks/cm^2)	5.68E+03	Fluence (tracks/cm^2)	1.20E+04		
Yield	1.60E+09	Yield	3.40E+09		

Shot 64965


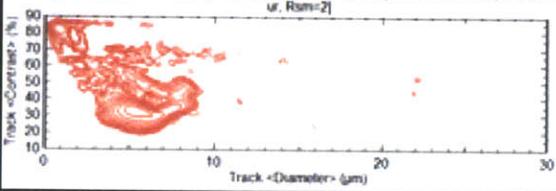
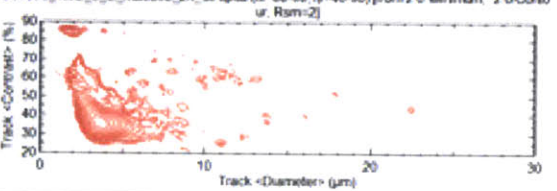
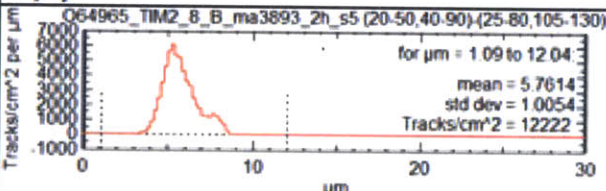
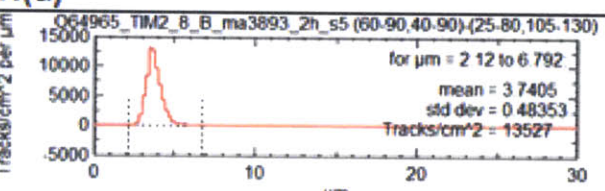
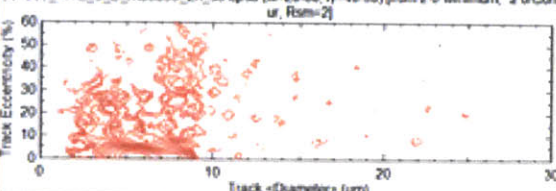
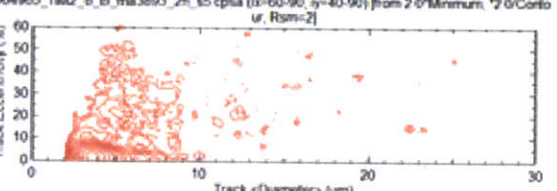
Tim 1, 4:00						
Shot	64965	Piece	ma3882	Type	Bert	
Etch Time (hours)	6	Distance (cm)	150	Magnification	40x	
<b>Step (um):</b>	50			<b>Step (um):</b>	25	
<b>Limit c (%)</b>	0 ≤ c ≤ 85			<b>Limit c (%)</b>	0 ≤ c ≤ 85	
<b>Limit e (%)</b>	0 ≤ e ≤ 15			<b>Limit e (%)</b>	0 ≤ e ≤ 15	
<b>Limit Area</b>	20 ≤ x ≤ 50 40 ≤ y ≤ 90			<b>Limit Area</b>	60 ≤ x ≤ 90 40 ≤ y ≤ 90	
<b>Background</b>	25 ≤ x ≤ 80 105 ≤ y ≤ 130			<b>Background</b>	25 ≤ x ≤ 80 105 ≤ y ≤ 130	
<b>N(d,c)</b>				<b>N(d,c)</b>		
<b>N(d)</b>			<b>N(d)</b>			
<b>N(d,e)</b>			<b>N(d,e)</b>			
<b>Average d (um)</b>	19.713		<b>Average d (um)</b>		14.18	
<b>Fluence (tracks/cm^2)</b>	1.41E+04		<b>Fluence (tracks/cm^2)</b>		1.76E+04	
<b>Yield</b>	3.99E+09		<b>Yield</b>		4.99E+09	

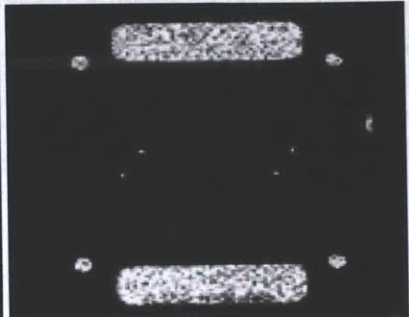
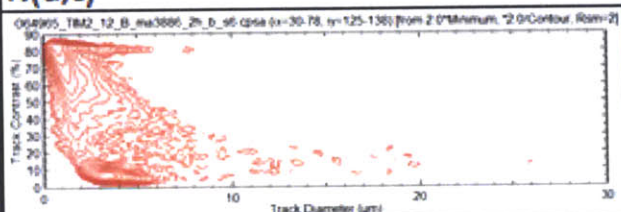
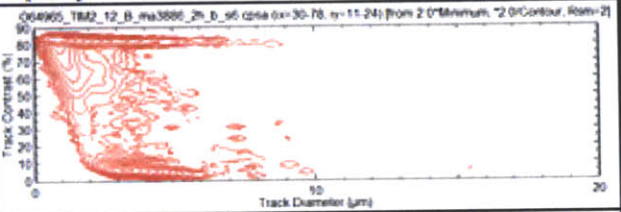
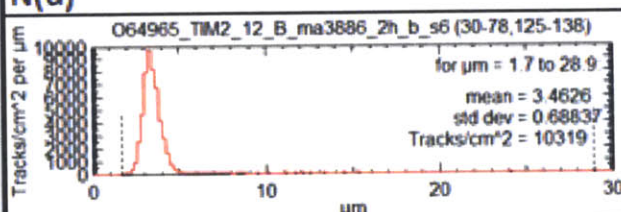
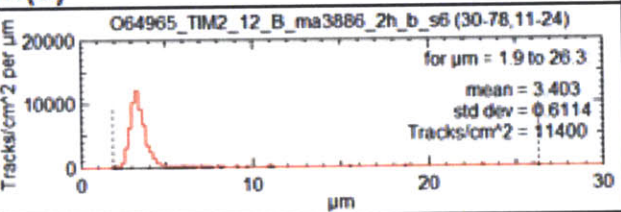
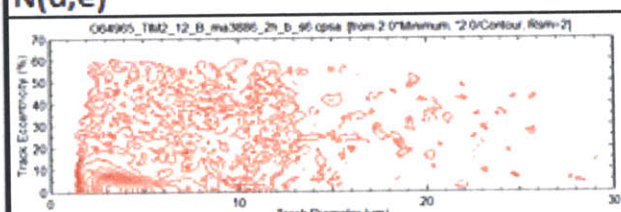
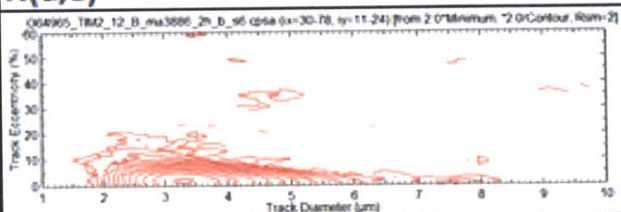
Tim 1, 8:00					
Shot	64965	Piece	ma3884	Type	Bert
Etch Time (hours)	2	Distance (cm)	150	Magnification	40x
<b>Step (um):</b>	50			<b>Step (um):</b>	25
<b>Limit c (%)</b>	0 ≤ c ≤ 70			<b>Limit c (%)</b>	0 ≤ c ≤ 50
<b>Limit e (%)</b>	0 ≤ e ≤ 15			<b>Limit e (%)</b>	0 ≤ e ≤ 15
<b>Limit Area</b>	20 ≤ x ≤ 50 40 ≤ y ≤ 90			<b>Limit Area</b>	60 ≤ x ≤ 90 40 ≤ y ≤ 90
<b>Background</b>	25 ≤ x ≤ 80 105 ≤ y ≤ 130			<b>Background</b>	25 ≤ x ≤ 80 105 ≤ y ≤ 130
<b>N(d,c)</b>					
<b>N(d)</b>					
<b>N(d,e)</b>					
<b>Average d (um)</b>	5.7738		<b>Average d (um)</b>		3.6434
<b>Fluence (tracks/cm^2)</b>	1.60E+04		<b>Fluence (tracks/cm^2)</b>		1.80E+04
<b>Yield</b>	4.53E+09		<b>Yield</b>		5.10E+09


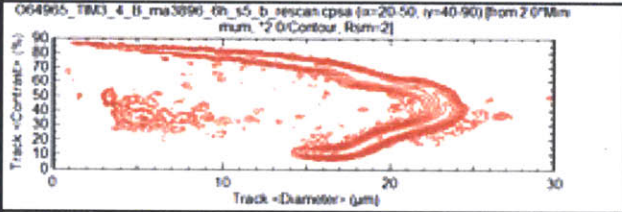
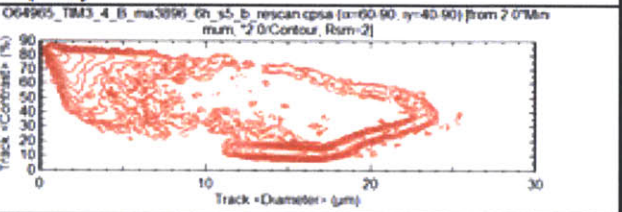
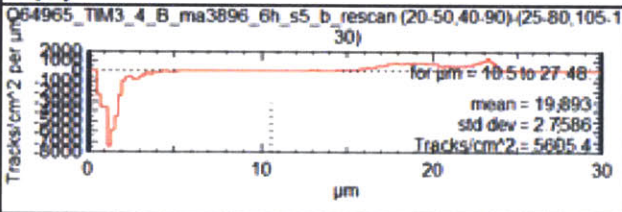
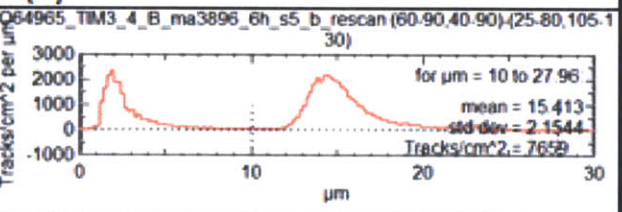
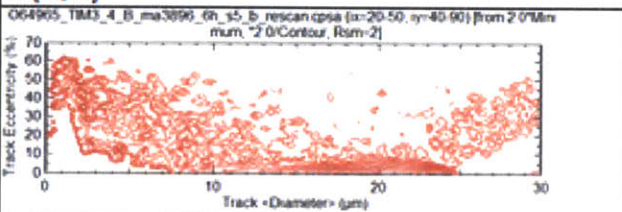
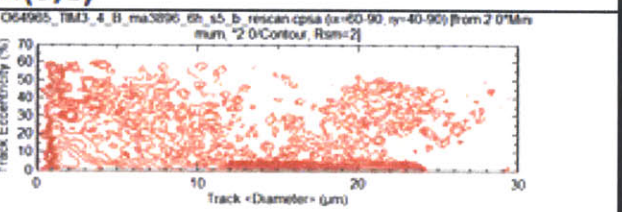
Tim 1, 12:00						
Shot	64965	Piece	ma3881	Type	WRF	
Etch Time (hours)	2	Distance (cm)	150	Magnification	40x	
D v. E Parameter (c)				Energy		
Limit c (%)				$0 \leq c \leq 16$	Sigma	
Limit e (%)				$0 \leq e \leq 11$		
Limit Area				$30 \leq x \leq 78$		
Top				$125 \leq y \leq 138$		
Limit Area	$30 \leq x \leq 78$	Bottom	$12 \leq y \leq 25$			
N(d,c)			N(d,c)			
						
N(d)			N(d)			
 O64965_TIM1_12_B_ma3881_2h_s6 (30-78,125-138) for $\mu\text{m} = 1.7$ to $21.1$ mean = 3.4736 std dev = 0.66695 Tracks/cm <sup>2</sup> = 9111.2			 O64965_TIM1_12_B_ma3881_2h_s6 (30-78,12-25) for $\mu\text{m} = 1.7$ to $29.3$ mean = 3.3568 std dev = 0.95991 Tracks/cm <sup>2</sup> = 8128.3			
N(d,e)			N(d,e)			
						
Average d (um)		3.4736	Average d (um)		3.3568	
Fluence (tracks/cm^2)		9.11E+03	Fluence (tracks/cm^2)		8.13E+03	
Yield		2.58E+09	Yield		2.30E+09	

Tim 2, 4:00					
Shot	64965	Piece	ma3887	Type	Bert
Etch Time (hours)	6	Distance (cm)	150	Magnification	40x
<i>Step (um):</i>	50	[Micrograph]	<i>Step (um):</i>	25	
Limit c (%)	0 ≤ c ≤ 85		Limit c (%)	0 ≤ c ≤ 50	
Limit e (%)	0 ≤ e ≤ 15		Limit e (%)	0 ≤ e ≤ 15	
Limit Area	20 ≤ x ≤ 50 40 ≤ y ≤ 90		Limit Area	60 ≤ x ≤ 90 40 ≤ y ≤ 90	
Background	25 ≤ x ≤ 80 105 ≤ y ≤ 130		Background	25 ≤ x ≤ 80 105 ≤ y ≤ 130	
<b>N(d,c)</b>		<b>N(d,c)</b>			
<p>064965_TIM2_4_B_ma3887_6h_s5_rescan cpsa (x=20-50, y=40-90) [from 2 0'Minmu m, *2 0'Contour, Rsm=2]</p>		<p>064965_TIM2_4_B_ma3887_6h_s5_rescan cpsa (x=60-90, y=40-90) [from 2 0'Minmu m, *2 0'Contour, Rsm=2]</p>			
<b>N(d)</b>		<b>N(d)</b>			
<p>064965_TIM2_4_B_ma3887_6h_s5_rescan (20-50,40-90)-(25-80,105-130)</p> <p>for <math>\mu\text{m} = 7.14</math> to <math>28.44</math>  mean = 19.809  std dev = 2.676  Tracks/cm<sup>2</sup> = 10031</p>		<p>064965_TIM2_4_B_ma3887_6h_s5_rescan (60-90,40-90)-(25-80,105-130)</p> <p>for <math>\mu\text{m} = 8.91</math> to <math>23.06</math>  mean = 14.523  std dev = 1.4097  Tracks/cm<sup>2</sup> = 11385</p>			
<b>N(d,e)</b>		<b>N(d,e)</b>			
<p>064965_TIM2_4_B_ma3887_6h_s5_rescan cpsa (x=20-50, y=40-90) [from 2 0'Minmu m, *2 0'Contour, Rsm=2]</p>		<p>064965_TIM2_4_B_ma3887_6h_s5_rescan cpsa (x=60-90, y=40-90) [from 2 0'Minmu m, *2 0'Contour, Rsm=2]</p>			
<b>Average d (um)</b>	19.809	<b>Average d (um)</b>	14.523		
<b>Fluence (tracks/cm^2)</b>	1.00E+04	<b>Fluence (tracks/cm^2)</b>	1.14E+04		
<b>Yield</b>	2.84E+09	<b>Yield</b>	3.22E+09		

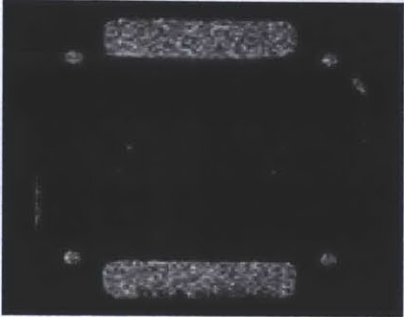
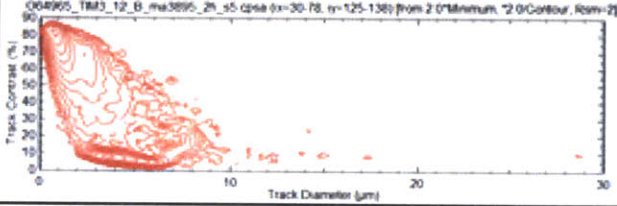
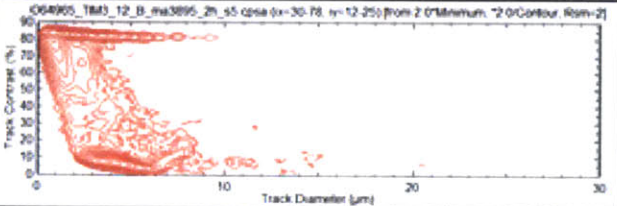
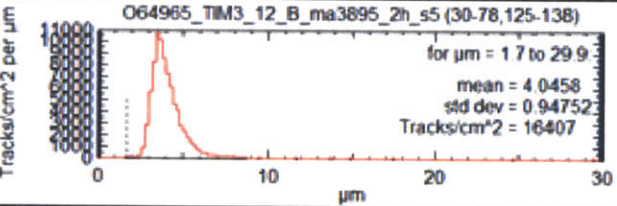
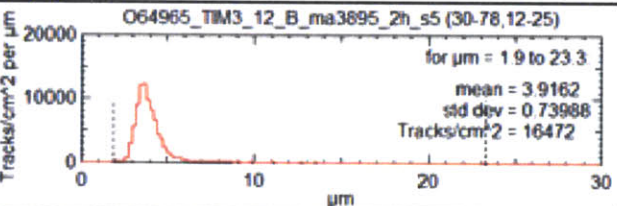
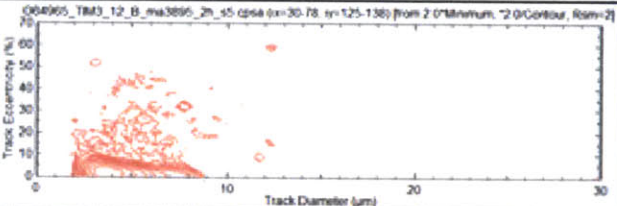
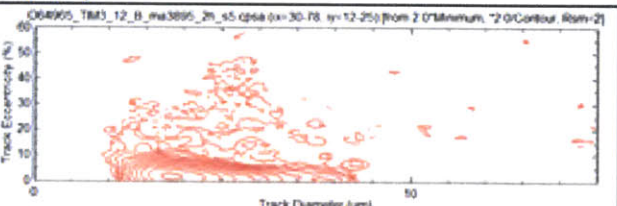


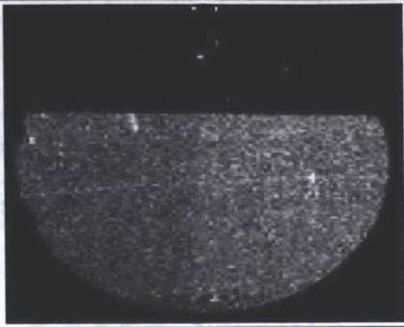
Tim 2, 8:00					
Shot	64965	Piece	ma3893	Type	Bert
Etch Time (hours)	2	Distance (cm)	150	Magnification	40x
<b>Step (um):</b>	50		<b>Step (um):</b>	25	
<b>Limit c (%)</b>	$0 \leq c \leq 60$		<b>Limit c (%)</b>	$0 \leq c \leq 50$	
<b>Limit e (%)</b>	$0 \leq e \leq 15$		<b>Limit e (%)</b>	$0 \leq e \leq 15$	
<b>Limit Area</b>	$20 \leq x \leq 50$ $40 \leq y \leq 90$		<b>Limit Area</b>	$60 \leq x \leq 90$ $40 \leq y \leq 90$	
<b>Background</b>	$25 \leq x \leq 80$ $105 \leq y \leq 130$		<b>Background</b>	$25 \leq x \leq 80$ $105 \leq y \leq 130$	
<b>N(d,c)</b>					
<b>N(d)</b>					
<b>N(d,e)</b>					
<b>Average d (um)</b>	5.7614	<b>Average d (um)</b>	3.7405		
<b>Fluence (tracks/cm^2)</b>	1.22E+04	<b>Fluence (tracks/cm^2)</b>	1.35E+04		
<b>Yield</b>	3.46E+09	<b>Yield</b>	3.82E+09		

Tim 2, 12:00						
Shot	64965	Piece	ma3886	Type	WRF	
Etch Time (hours)	2	Distance (cm)	150	Magnification	40x	
D v. E Parameter (c)				Energy		
Limit c (%)				$0 \leq c \leq 18$	Sigma	
Limit e (%)				$0 \leq e \leq 16$		
Limit Area				$30 \leq x \leq 78$		
Top				$125 \leq y \leq 138$		
Limit Area	$30 \leq x \leq 78$					
Bottom	$12 \leq y \leq 25$					
<b>N(d,c)</b>			<b>N(d,c)</b>			
						
<b>N(d)</b>			<b>N(d)</b>			
 <p>for <math>\mu\text{m} = 1.7</math> to <math>28.9</math>  mean = 3.4626  std dev = 0.68837  Tracks/cm<sup>2</sup> = 10319</p>			 <p>for <math>\mu\text{m} = 1.9</math> to <math>26.3</math>  mean = 3.403  std dev = 0.6114  Tracks/cm<sup>2</sup> = 11400</p>			
<b>N(d,e)</b>			<b>N(d,e)</b>			
						
Average d (um)	3.4626	Average d (um)	3.403			
Fluence (tracks/cm <sup>2</sup> )	1.03E+04	Fluence (tracks/cm <sup>2</sup> )	1.14E+04			
Yield	2.92E+09	Yield	3.22E+09			

Tim 3, 4:00					
Shot	64965	Piece	ma3896	Type	Bert
Etch Time (hours)	6	Distance (cm)	150	Magnification	40x
Step (um):	50		Step (um):	25	
Limit c (%)	$0 \leq c \leq 85$		Limit c (%)	$0 \leq c \leq 75$	
Limit e (%)	$0 \leq e \leq 15$		Limit e (%)	$0 \leq e \leq 15$	
Limit Area	$20 \leq x \leq 50$ $40 \leq y \leq 90$		Limit Area	$60 \leq x \leq 90$ $40 \leq y \leq 90$	
Background	$25 \leq x \leq 80$ $105 \leq y \leq 130$		Background	$25 \leq x \leq 80$ $105 \leq y \leq 130$	
<b>N(d,c)</b>			<b>N(d,c)</b>		
					
<b>N(d)</b>		<b>N(d)</b>			
					
<b>N(d,e)</b>		<b>N(d,e)</b>			
					
Average d (um)	19.893	Average d (um)	15.412		
Fluence (tracks/cm^2)	5.61E+03	Fluence (tracks/cm^2)	7.66E+03		
Yield	1.58E+09	Yield	2.17E+09		

Tim 3, 8:00					
Shot	64965	Piece	ma3900	Type	Bert
Etch Time (hours)	2	Distance (cm)	150	Magnification	40x
<b>Step (um):</b>	50			<b>Step (um):</b>	25
<b>Limit c (%)</b>	$0 \leq c \leq 65$			<b>Limit c (%)</b>	$0 \leq c \leq 50$
<b>Limit e (%)</b>	$0 \leq e \leq 15$			<b>Limit e (%)</b>	$0 \leq e \leq 15$
<b>Limit Area</b>	$20 \leq x \leq 50$ $40 \leq y \leq 90$			<b>Limit Area</b>	$60 \leq x \leq 90$ $40 \leq y \leq 90$
<b>Background</b>	$25 \leq x \leq 80$ $105 \leq y \leq 130$			<b>Background</b>	$25 \leq x \leq 80$ $105 \leq y \leq 130$
<b>N(d,c)</b>				<b>N(d,c)</b>	
<p>O64965_TIM3_8_B_ma3900_2hr_s2 cpsa (x=20-50, y=40-90) [from 2.0 Minimum * 2.0 Contrast, Rsm=2]</p>		<p>O64965_TIM3_8_B_ma3900_2hr_s2 cpsa (x=60-90, y=40-90) [from 2.0 Minimum * 2.0 Contrast, Rsm=2]</p>			
<b>N(d)</b>		<b>N(d)</b>			
<p>O64965_TIM3_8_B_ma3900_2hr_s2 (20-50,40-90)-(25-80,105-130) for <math>\mu\text{m} = 3.61</math> to <math>10.54</math> mean = 5.8377 std dev = 1.079 Tracks/cm<sup>2</sup> = 12545</p>		<p>O64965_TIM3_8_B_ma3900_2hr_s2 (60-90,40-90)-(25-80,105-130) for <math>\mu\text{m} = 1.44</math> to <math>10.02</math> mean = 3.6543 std dev = 0.69569 Tracks/cm<sup>2</sup> = 13477</p>			
<b>N(d,e)</b>		<b>N(d,e)</b>			
<p>O64965_TIM3_8_B_ma3900_2hr_s2 cpsa (x=20-50, y=40-90) [from 2.0 Minimum * 2.0 Contrast, Rsm=2]</p>		<p>O64965_TIM3_8_B_ma3900_2hr_s2 cpsa (x=60-90, y=40-90) [from 2.0 Minimum * 2.0 Contrast, Rsm=2]</p>			
<b>Average d (um)</b>		5.8377	<b>Average d (um)</b>		3.6543
<b>Fluence (tracks/cm^2)</b>		1.25E+04	<b>Fluence (tracks/cm^2)</b>		1.35E+04
<b>Yield</b>		3.55E+09	<b>Yield</b>		3.81E+09

Tim 3, 12:00						
Shot	64965	Piece	ma3895	Type	WRF	
Etch Time (hours)	2	Distance (cm)	150	Magnification	40x	
D v. E Parameter (c)				Energy		
Limit c (%)				$0 \leq c \leq 23$	Sigma	
Limit e (%)				$0 \leq e \leq 12$		
Limit Area				$30 \leq x \leq 78$		
Top				$125 \leq y \leq 138$		
Limit Area				$30 \leq x \leq 78$		
Bottom	$12 \leq y \leq 25$					
N(d,c)			N(d,c)			
						
N(d)			N(d)			
						
N(d,e)			N(d,e)			
						
Average d (um)		4.0458	Average d (um)		3.9162	
Fluence (tracks/cm^2)		1.64E+04	Fluence (tracks/cm^2)		1.65E+04	
Yield		4.64E+09	Yield		4.66E+09	

TIM 5					
Shot	64965	Piece	ma3902	Type	Bert
Etch Time (hours)	3	Distance (cm)	150	Magnification	40x
Step (um):	50		Step (um):	25	
Limit c (%)	$0 \leq c \leq 80$		Limit c (%)	$0 \leq c \leq 50$	
Limit e (%)	$0 \leq e \leq 15$		Limit e (%)	$0 \leq e \leq 15$	
Limit Area	$20 \leq x \leq 50$ $40 \leq y \leq 90$		Limit Area	$60 \leq x \leq 90$ $40 \leq y \leq 90$	
Background	$25 \leq x \leq 80$ $105 \leq y \leq 130$		Background	$25 \leq x \leq 80$ $105 \leq y \leq 130$	
<b>N(d,c)</b>			<b>N(d,c)</b>		
<p>064965_TIM5_B_ma3902_3h_s1 cpsa (ix=20-50, iy=40-90) [from 2.0° Minimum, *2.0° Contour, Rsm=2]</p>		<p>064965_TIM5_B_ma3902_3h_s1 cpsa (ix=60-90, iy=40-90) [from 2.0° Minimum, *2.0° Contour, Rsm=2]</p>			
<b>N(d)</b>		<b>N(d)</b>			
<p>064965_TIM5_B_ma3902_3h_s1 (20-50,40-90)-(25-80,105-130)</p> <p>for <math>\mu\text{m} = 3.4</math> to <math>15.44</math>  mean = 8.9648  std dev = 1.5106  Tracks/cm<sup>2</sup> = 14715</p>		<p>064965_TIM5_B_ma3902_3h_s1 (60-90,40-90)-(25-80,105-130)</p> <p>for <math>\mu\text{m} = 1.17</math> to <math>13.25</math>  mean = 5.8999  std dev = 0.87486  Tracks/cm<sup>2</sup> = 20038</p>			
<b>N(d,e)</b>		<b>N(d,e)</b>			
<p>064965_TIM5_B_ma3902_3h_s1 cpsa (ix=20-50, iy=40-90) [from 2.0° Minimum, *2.0° Contour, Rsm=2]</p>		<p>064965_TIM5_B_ma3902_3h_s1 cpsa (ix=60-90, iy=40-90) [from 2.0° Minimum, *2.0° Contour, Rsm=2]</p>			
Average d (um)		8.9648	Average d (um)		5.8999
Fluence (tracks/cm <sup>2</sup> )		1.47E+04	Fluence (tracks/cm <sup>2</sup> )		2.00E+04
Yield		4.16E+09	Yield		5.67E+09


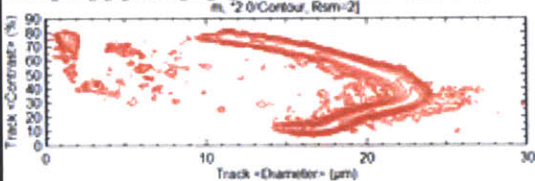
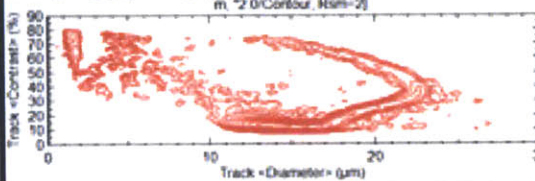
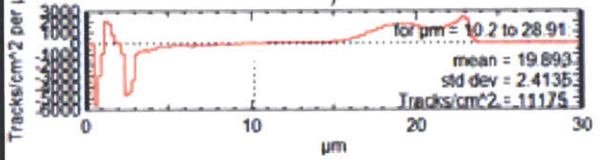
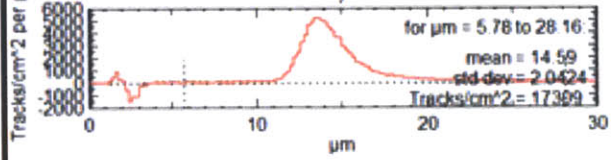
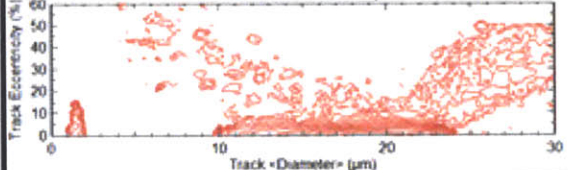
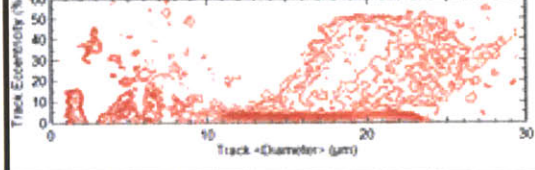
Shot 64967


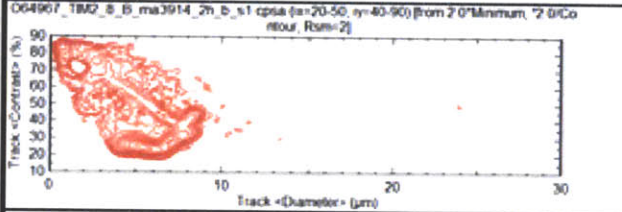
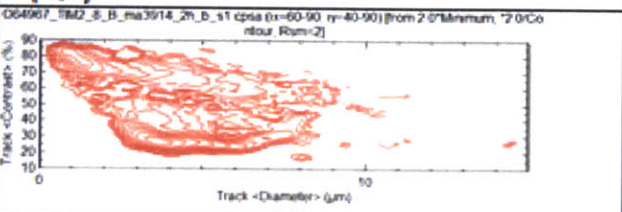
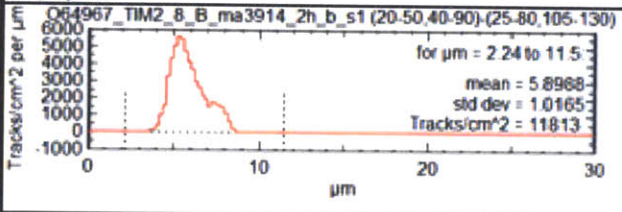
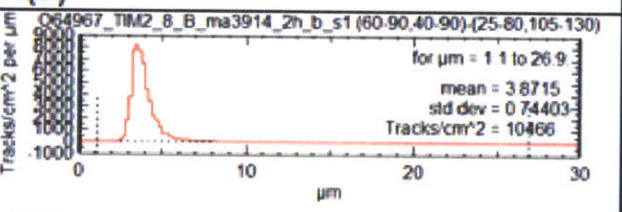
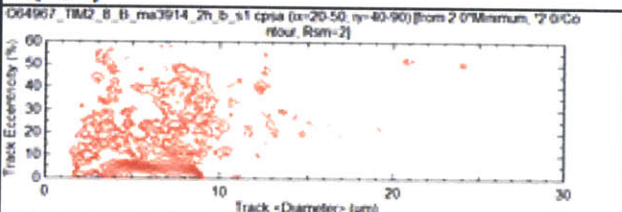
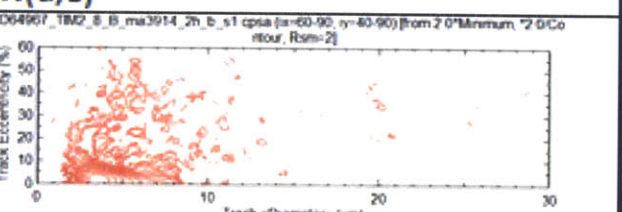
Tim 1, 4:00					
Shot	64967	Piece	ma3906	Type	Bert
Etch Time (hours)	6	Distance (cm)	150	Magnification	40x
<b>Step (um):</b>	50			<b>Step (um):</b>	25
<b>Limit c (%)</b>	0 ≤ c ≤ 85			<b>Limit c (%)</b>	0 ≤ c ≤ 80
<b>Limit e (%)</b>	0 ≤ e ≤ 15			<b>Limit e (%)</b>	0 ≤ e ≤ 15
<b>Limit Area</b>	20 ≤ x ≤ 50 40 ≤ y ≤ 90			<b>Limit Area</b>	60 ≤ x ≤ 90 40 ≤ y ≤ 90
<b>Background</b>	25 ≤ x ≤ 80 105 ≤ y ≤ 130			<b>Background</b>	25 ≤ x ≤ 80 105 ≤ y ≤ 130
<b>N(d,c)</b>		<b>N(d,c)</b>			
<b>N(d)</b>		<b>N(d)</b>			
<b>N(d,e)</b>		<b>N(d,e)</b>			
<b>Average d (um)</b>	19.546	<b>Average d (um)</b>	14.347		
<b>Fluence (tracks/cm^2)</b>	1.09E+04	<b>Fluence (tracks/cm^2)</b>	1.16E+04		
<b>Yield</b>	3.07E+09	<b>Yield</b>	3.28E+09		

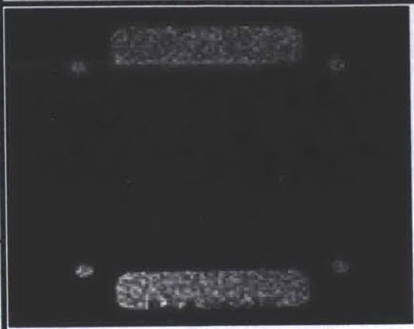
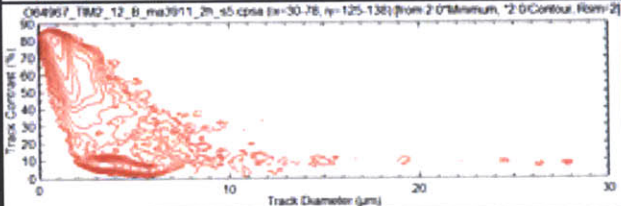
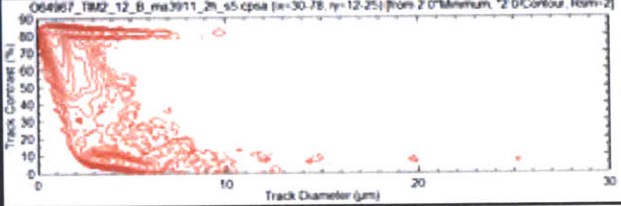
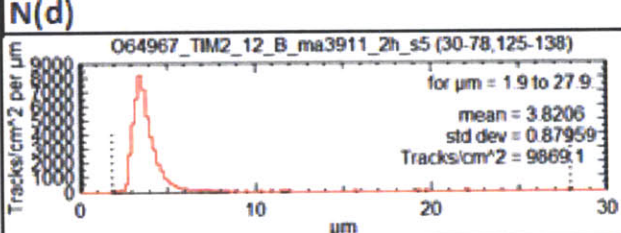
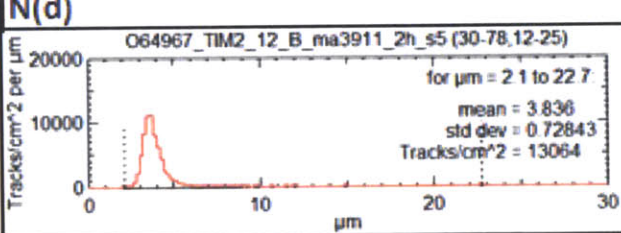
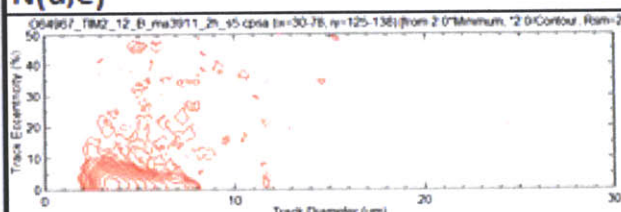
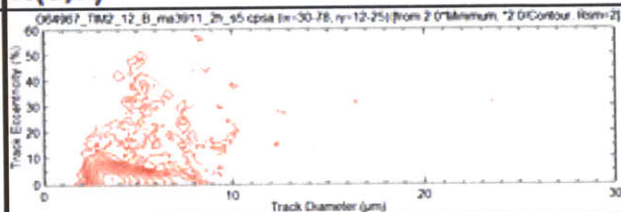
Tim 1, 8:00					
Shot	64967	Piece	ma3908	Type	Bert
Etch Time (hours)	2	Distance (cm)	150	Magnification	40x
<b>Step (um):</b>	50			<b>Step (um):</b>	25
<b>Limit c (%)</b>	$0 \leq c \leq 60$			<b>Limit c (%)</b>	$0 \leq c \leq 55$
<b>Limit e (%)</b>	$0 \leq e \leq 15$			<b>Limit e (%)</b>	$0 \leq e \leq 15$
<b>Limit Area</b>	$20 \leq x \leq 50$ $40 \leq y \leq 90$			<b>Limit Area</b>	$60 \leq x \leq 90$ $40 \leq y \leq 90$
<b>Background</b>	$25 \leq x \leq 80$ $105 \leq y \leq 130$			<b>Background</b>	$25 \leq x \leq 80$ $105 \leq y \leq 130$
<b>N(d,c)</b>				<b>N(d,c)</b>	
<b>N(d)</b>		<b>N(d)</b>			
<b>N(d,e)</b>		<b>N(d,e)</b>			
<b>Average d (um)</b>	5.6453	<b>Average d (um)</b>	3.4928		
<b>Fluence (tracks/cm^2)</b>	1.52E+04	<b>Fluence (tracks/cm^2)</b>	1.56E+04		
<b>Yield</b>	4.31E+09	<b>Yield</b>	4.42E+09		



Tim 1, 12:00					
Shot	64967	Piece	ma3905	Type	WRF
Etch Time (hours)	2	Distance (cm)	150	Magnification	40x
D v. E Parameter (c)				Energy	
Limit c (%)	$0 \leq c \leq 20$			Sigma	
Limit e (%)	$0 \leq e \leq 13$				
Limit Area	$30 \leq x \leq 78$				
Top	$125 \leq y \leq 138$				
Limit Area	$30 \leq x \leq 78$				
Bottom	$12 \leq y \leq 25$				
N(d,c)		N(d,c)			
N(d)		N(d)			
N(d,e)		N(d,e)			
Average d (um)	3.7584	Average d (um)	3.8536		
Fluence (tracks/cm^2)	1.55E+04	Fluence (tracks/cm^2)	1.10E+04		
Yield	4.39E+09	Yield	3.10E+09		

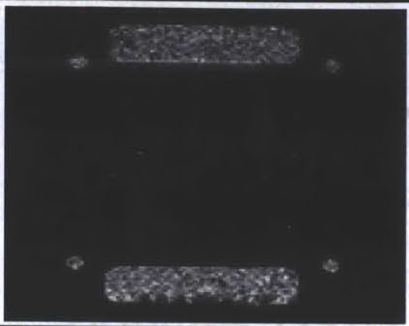
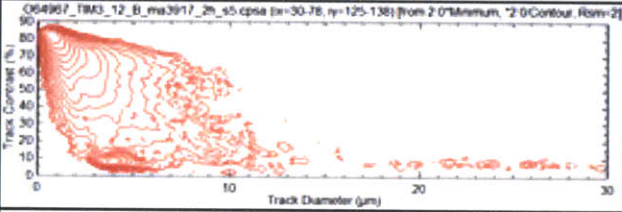
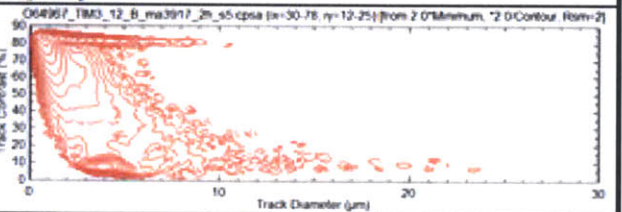
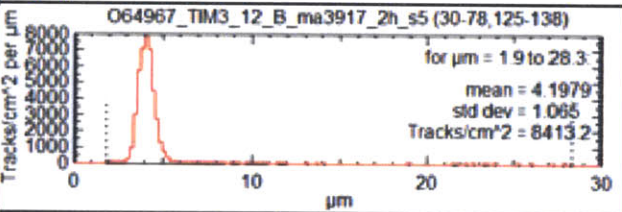
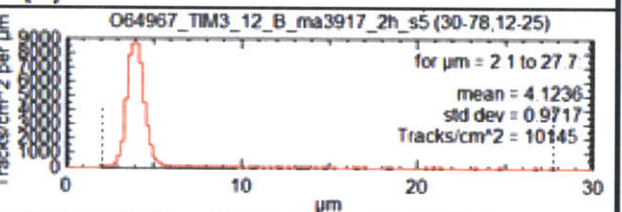
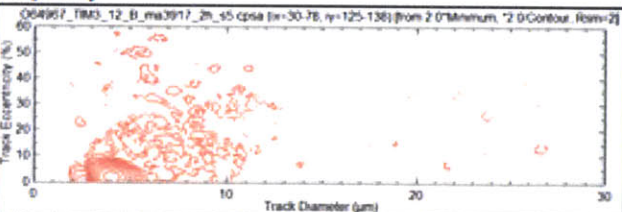
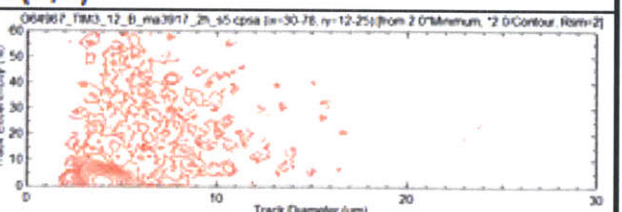
Tim 2, 4:00					
Shot	64967	Piece	ma3912	Type	Bert
Etch Time (hours)	6	Distance (cm)	150	Magnification	40x
<b>Step (um):</b>	50			<b>Step (um):</b>	25
<b>Limit c (%)</b>	$0 \leq c \leq 85$			<b>Limit c (%)</b>	$0 \leq c \leq 75$
<b>Limit e (%)</b>	$0 \leq e \leq 15$			<b>Limit e (%)</b>	$0 \leq e \leq 15$
<b>Limit Area</b>	$60 \leq x \leq 90$ $40 \leq y \leq 90$			<b>Limit Area</b>	$60 \leq x \leq 90$ $40 \leq y \leq 90$
<b>Background</b>	$25 \leq x \leq 80$ $105 \leq y \leq 130$			<b>Background</b>	$25 \leq x \leq 80$ $105 \leq y \leq 130$
<b>N(d,c)</b>				<b>N(d,c)</b>	
					
<b>N(d)</b>		<b>N(d)</b>			
					
<b>N(d,e)</b>		<b>N(d,e)</b>			
					
<b>Average d (um)</b>	19.893	<b>Average d (um)</b>	14.59		
<b>Fluence (tracks/cm^2)</b>	1.12E+04	<b>Fluence (tracks/cm^2)</b>	1.73E+04		
<b>Yield</b>	3.16E+09	<b>Yield</b>	4.89E+09		

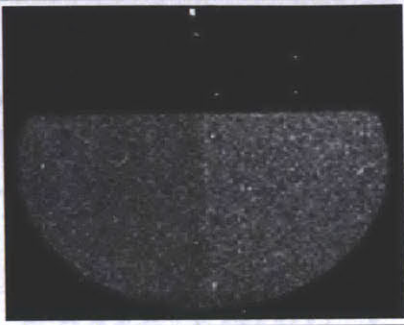
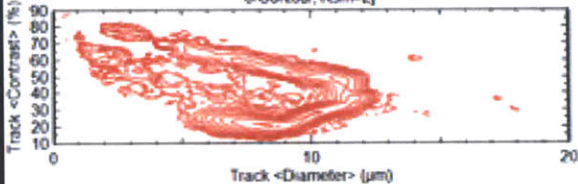
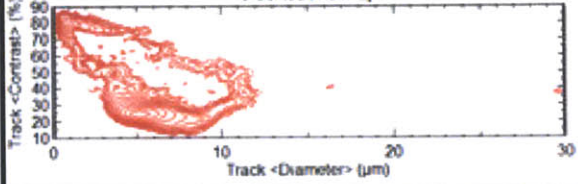
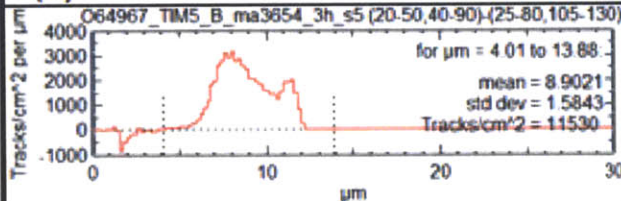
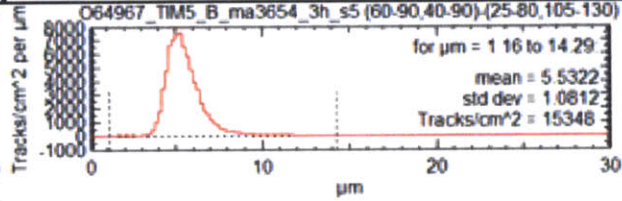
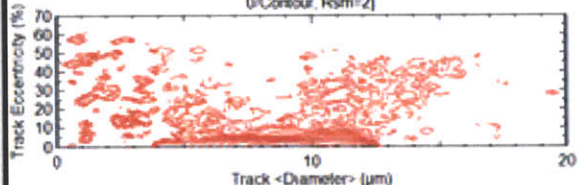
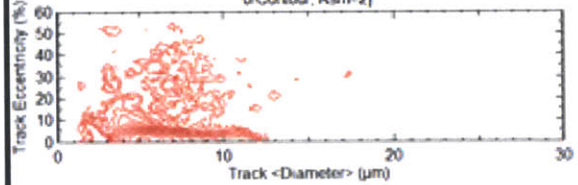
Tim 2, 8:00					
Shot	64967	Piece	ma3914	Type	Bert
Etch Time (hours)	2	Distance (cm)	150	Magnification	40x
<i>Step (um):</i>	50		<i>Step (um):</i>	25	
Limit c (%)	$0 \leq c \leq 50$		Limit c (%)	$0 \leq c \leq 55$	
Limit e (%)	$0 \leq e \leq 15$		Limit e (%)	$0 \leq e \leq 15$	
Limit Area	$20 \leq x \leq 50$ $40 \leq y \leq 90$		Limit Area	$60 \leq x \leq 90$ $40 \leq y \leq 90$	
Background	$25 \leq x \leq 80$ $105 \leq y \leq 130$		Background	$25 \leq x \leq 80$ $105 \leq y \leq 130$	
<b>N(d,c)</b>			<b>N(d,c)</b>		
					
<b>N(d)</b>		<b>N(d)</b>			
					
<b>N(d,e)</b>		<b>N(d,e)</b>			
					
Average d (um)	5.8988	Average d (um)	3.8715		
Fluence (tracks/cm^2)	1.18E+04	Fluence (tracks/cm^2)	1.05E+04		
Yield	3.34E+09	Yield	2.96E+09		

Tim 2, 12:00						
Shot	64967	Piece	ma3911	Type	WRF	
Etch Time (hours)	2	Distance (cm)	150	Magnification	40x	
D v. E Parameter (c)				Energy		
Limit c (%)				$0 \leq c \leq 16$	Sigma	
Limit e (%)				$0 \leq e \leq 12$		
Limit Area				$30 \leq x \leq 78$		
Top				$125 \leq y \leq 138$		
Limit Area				$30 \leq x \leq 78$		
Bottom	$12 \leq y \leq 25$					
N(d,c)		N(d,c)				
						
N(d)		N(d)				
						
N(d,e)		N(d,e)				
						
Average d (um)	3.8206	Average d (um)	3.836			
Fluence (tracks/cm^2)	9.87E+03	Fluence (tracks/cm^2)	1.31E+04			
Yield	2.79E+09	Yield	3.69E+09			

Tim 3, 4:00					
Shot	64967	Piece	ma3918	Type	Bert
Etch Time (hours)	6	Distance (cm)	150	Magnification	40x
<b>Step (um):</b>	50			<b>Step (um):</b>	25
<b>Limit c (%)</b>	$0 \leq c \leq 85$			<b>Limit c (%)</b>	$0 \leq c \leq 50$
<b>Limit e (%)</b>	$0 \leq e \leq 15$			<b>Limit e (%)</b>	$0 \leq e \leq 15$
<b>Limit Area</b>	$20 \leq x \leq 50$ $40 \leq y \leq 90$			<b>Limit Area</b>	$60 \leq x \leq 90$ $40 \leq y \leq 90$
<b>Background</b>	$25 \leq x \leq 80$ $105 \leq y \leq 130$			<b>Background</b>	$25 \leq x \leq 80$ $105 \leq y \leq 130$
<b>N(d,c)</b>				<b>N(d,c)</b>	
<p>064967_TIM3_4_B_ma3918_6h_s5_rescan cpsa (x=20-50, y=40-90) [from 2.0 Minmu m, 2.0 Contour, Rsm=2]</p>		<p>064967_TIM3_4_B_ma3918_6h_s5_rescan cpsa (x=60-90, y=40-90) [from 2.0 Minmu m, 2.0 Contour, Rsm=2]</p>			
<b>N(d)</b>		<b>N(d)</b>			
<p>064967_TIM3_4_B_ma3918_6h_s5_rescan (20-50,40-90) (25-80,105-130)</p> <p>for <math>\mu\text{m} = 7.76</math> to <math>28.23</math>  mean = 19.862  std dev = 2.3909  Tracks/cm<sup>2</sup> = 12973</p>		<p>064967_TIM3_4_B_ma3918_6h_s5_rescan (60-90,40-90) (25-80,105-130)</p> <p>for <math>\mu\text{m} = 7.96</math> to <math>22.04</math>  mean = 13.862  std dev = 1.1843  Tracks/cm<sup>2</sup> = 16844</p>			
<b>N(d,e)</b>		<b>N(d,e)</b>			
<p>064967_TIM3_4_B_ma3918_6h_s5_rescan cpsa (x=20-50, y=40-90) [from 2.0 Minmu m, 2.0 Contour, Rsm=2]</p>		<p>064967_TIM3_4_B_ma3918_6h_s5_rescan cpsa (x=60-90, y=40-90) [from 2.0 Minmu m, 2.0 Contour, Rsm=2]</p>			
<b>Average d (um)</b>	19.862	<b>Average d (um)</b>	13.862		
<b>Fluence (tracks/cm^2)</b>	1.30E+04	<b>Fluence (tracks/cm^2)</b>	1.68E+04		
<b>Yield</b>	3.67E+09	<b>Yield</b>	4.76E+09		

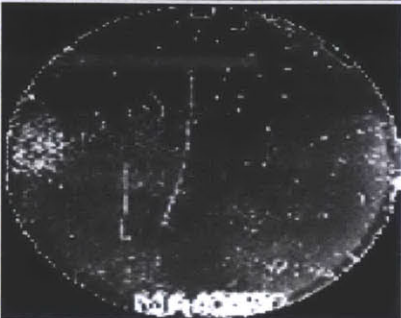
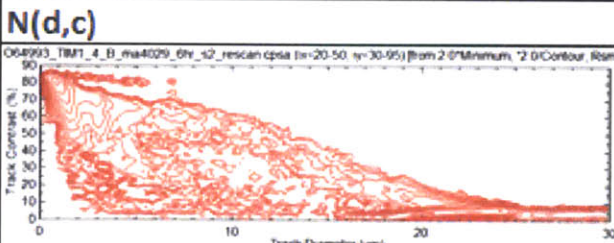
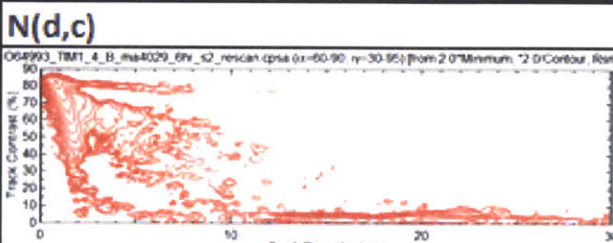
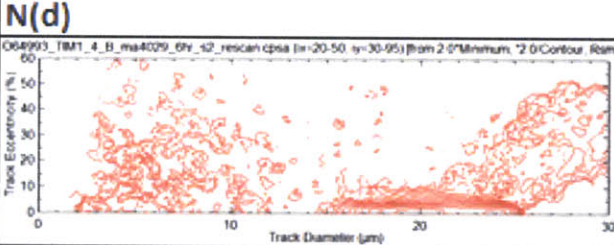
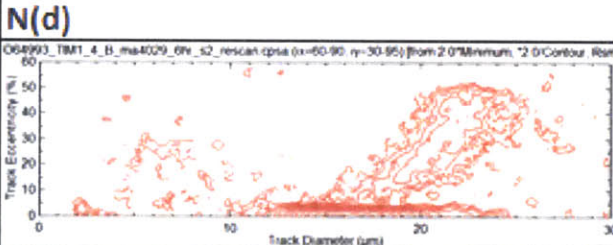
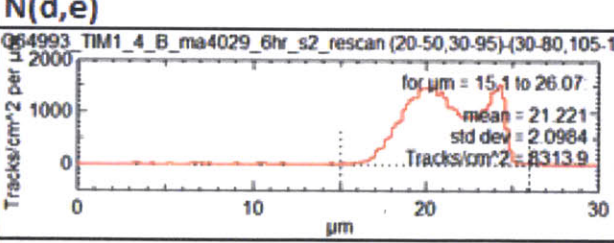
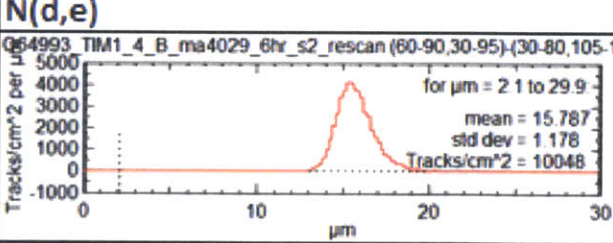
Tim 3, 8:00					
Shot	64967	Piece	ma3920	Type	Bert
Etch Time (hours)	2	Distance (cm)	150	Magnification	40x
<b>Step (um):</b>	50			<b>Step (um):</b>	25
<b>Limit c (%)</b>	$0 \leq c \leq 60$			<b>Limit c (%)</b>	$0 \leq c \leq 45$
<b>Limit e (%)</b>	$0 \leq e \leq 15$			<b>Limit e (%)</b>	$0 \leq e \leq 15$
<b>Limit Area</b>	$20 \leq x \leq 50$ $40 \leq y \leq 90$			<b>Limit Area</b>	$60 \leq x \leq 90$ $40 \leq y \leq 90$
<b>Background</b>	$25 \leq x \leq 80$ $105 \leq y \leq 130$			<b>Background</b>	$25 \leq x \leq 80$ $105 \leq y \leq 130$
<b>N(d,c)</b>			<b>N(d,c)</b>		
<b>N(d)</b>			<b>N(d)</b>		
<b>N(d,e)</b>			<b>N(d,e)</b>		
<b>Average d (um)</b>		5.5994	<b>Average d (um)</b>		3.5089
<b>Fluence (tracks/cm^2)</b>		1.30E+04	<b>Fluence (tracks/cm^2)</b>		1.50E+04
<b>Yield</b>		3.68E+09	<b>Yield</b>		4.25E+09

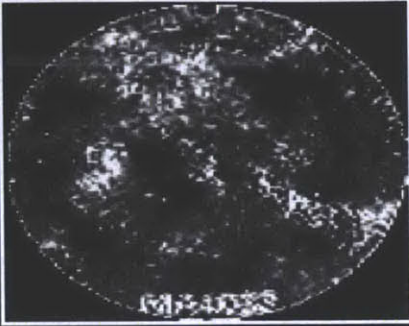
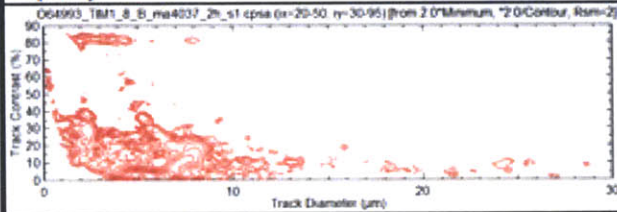
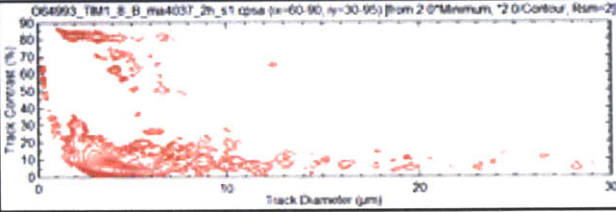
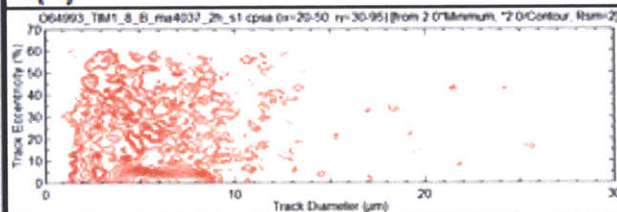
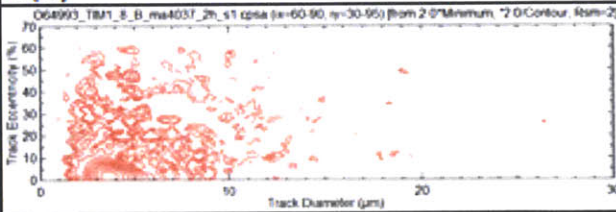
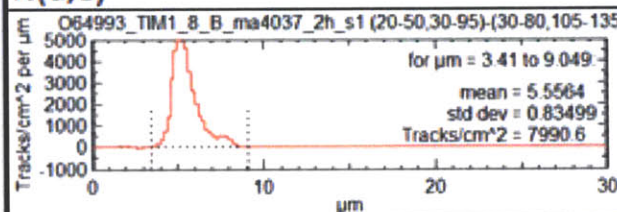
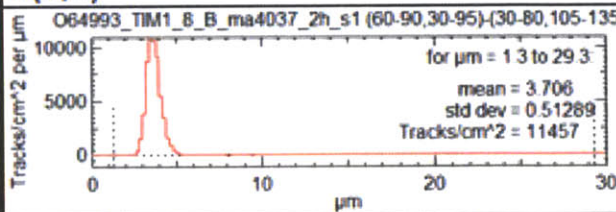
Tim 3, 12:00					
Shot	64967	Piece		Type	WRF
Etch Time (hours)	2	Distance (cm)	150	Magnification	40x
D v. E Parameter (c)				Energy	
Limit c (%)	$0 \leq c \leq 18$			Sigma	
Limit e (%)	$0 \leq e \leq 12$				
Limit Area	$30 \leq x \leq 78$				
Top	$125 \leq y \leq 138$				
Limit Area	$30 \leq x \leq 78$				
Bottom	$12 \leq y \leq 25$				
N(d,c)		N(d,c)			
					
N(d)		N(d)			
					
N(d,e)		N(d,e)			
					
Average d (um)	4.1979	Average d (um)	4.1236		
Fluence (tracks/cm^2)	8.41E+03	Fluence (tracks/cm^2)	1.01E+04		
Yield	2.38E+09	Yield	2.87E+09		

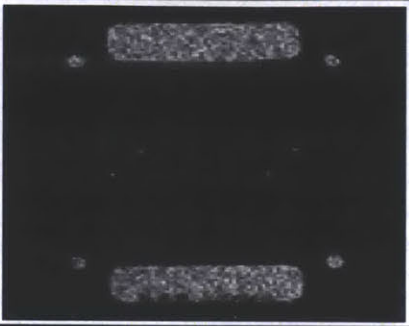
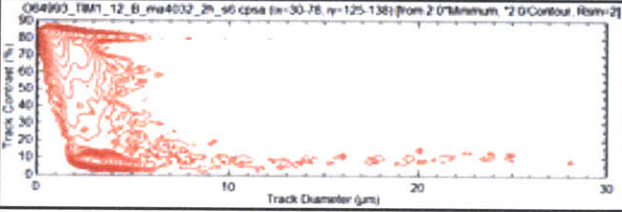
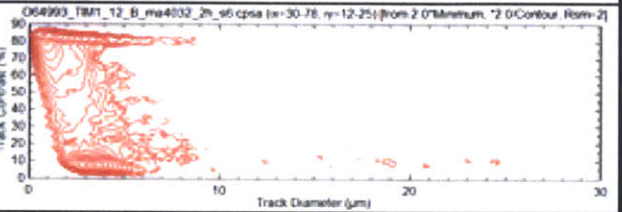
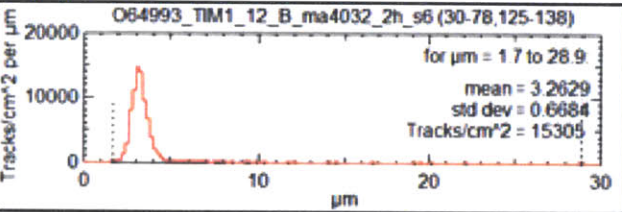
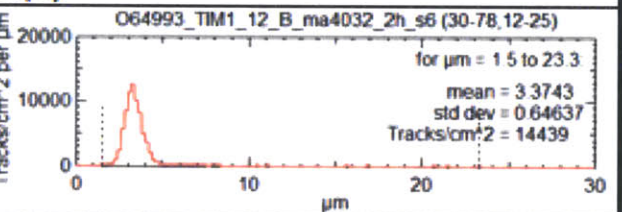
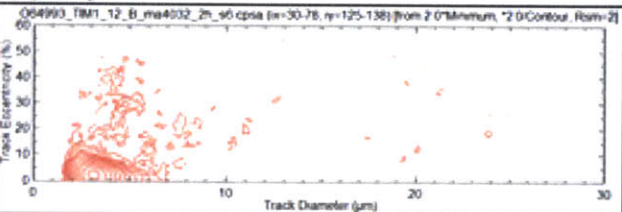
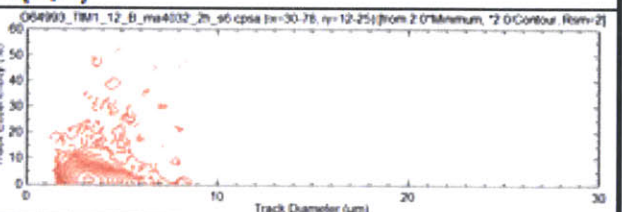
TIM 5					
Shot	64967	Piece	ma3654	Type	Bert
Etch Time (hours)	3	Distance (cm)	150	Magnification	40x
Step (um):	50		Step (um):	25	
Limit c (%)	$0 \leq c \leq 60$		Limit c (%)	$0 \leq c \leq 55$	
Limit e (%)	$0 \leq e \leq 15$		Limit e (%)	$0 \leq e \leq 15$	
Limit Area	$20 \leq x \leq 50$ $40 \leq y \leq 90$		Limit Area	$60 \leq x \leq 90$ $40 \leq y \leq 90$	
Background	$25 \leq x \leq 80$ $105 \leq y \leq 130$		Background	$25 \leq x \leq 80$ $105 \leq y \leq 130$	
N(d,c)			N(d,c)		
					
N(d)		N(d)			
					
N(d,e)		N(d,e)			
					
Average d (um)	8.9021	Average d (um)	5.5322		
Fluence (tracks/cm^2)	1.15E+04	Fluence (tracks/cm^2)	1.53E+04		
Yield	3.26E+09	Yield	4.34E+09		

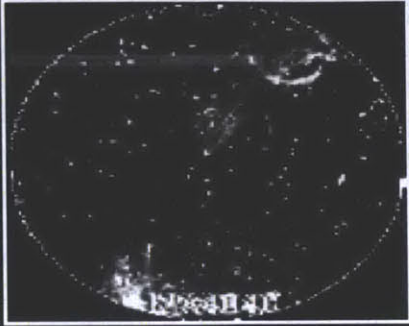
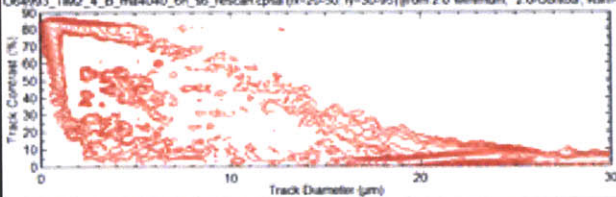
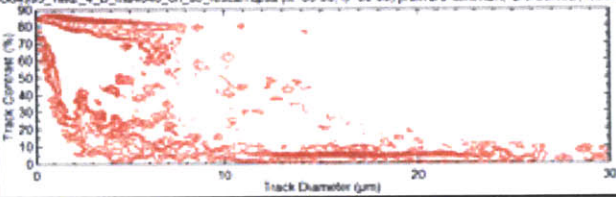
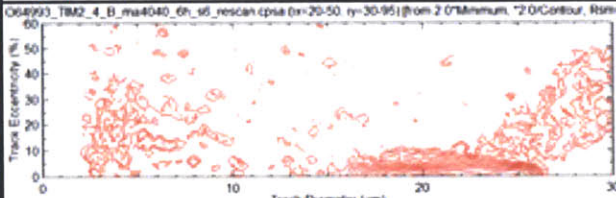
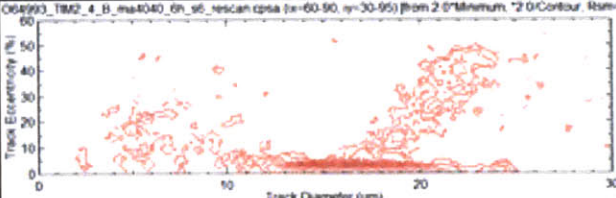
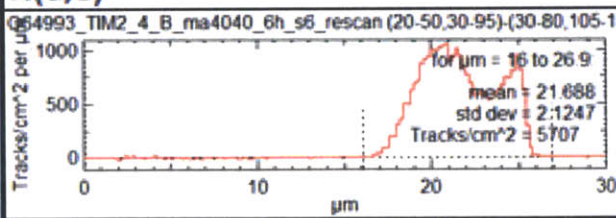
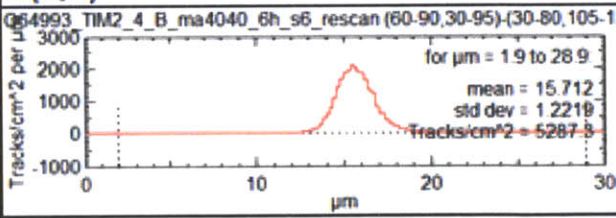


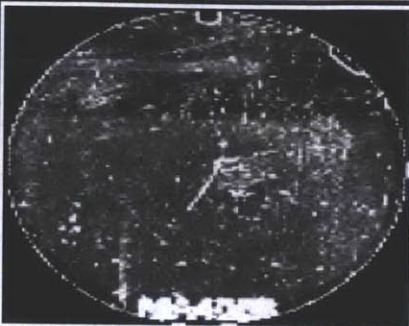
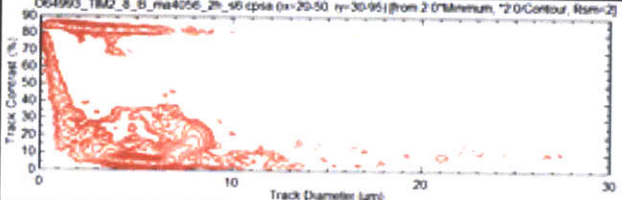
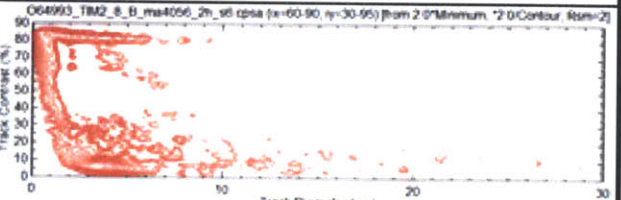
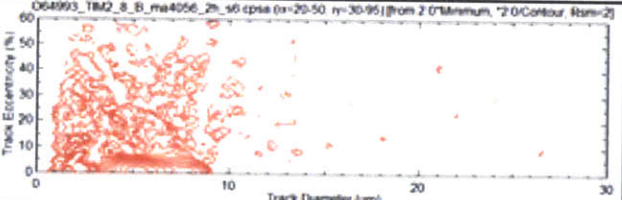
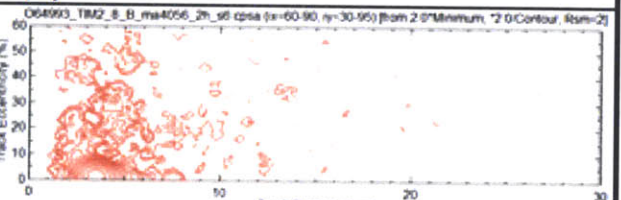
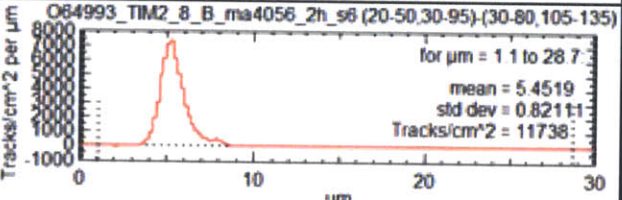
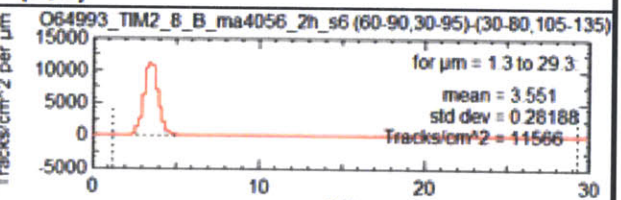
Shot 64993

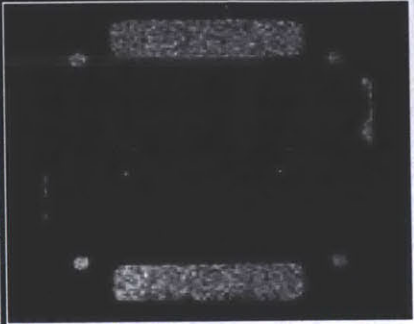
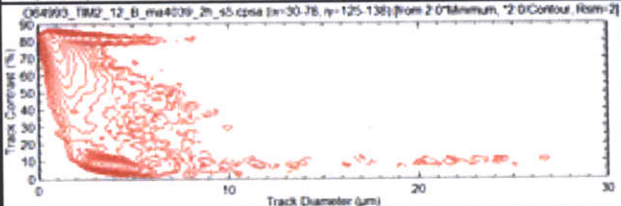
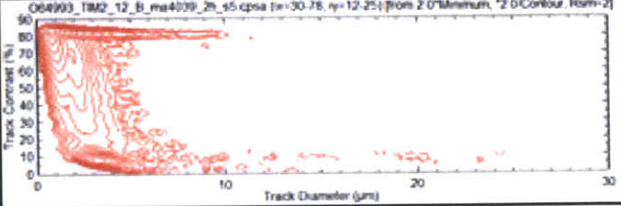
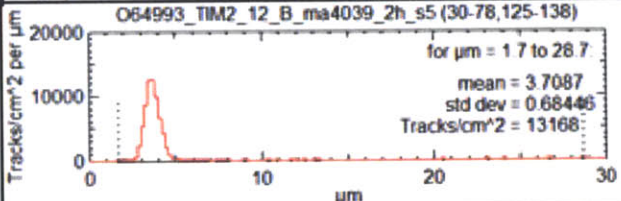
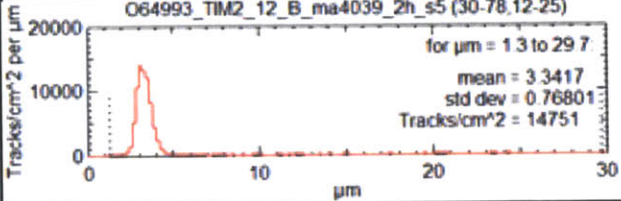
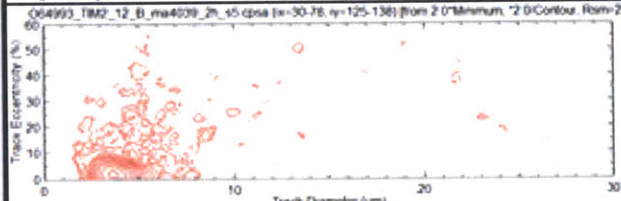
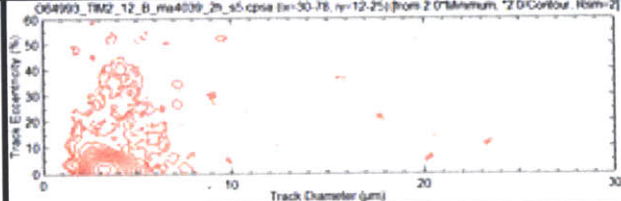
Tim 1, 4:00					
Shot	64993	Piece	ma4029	Type	Bert
Etch Time (hours)	6	Distance (cm)	150	Magnification	40x
<b>Step (um):</b>	50		<b>Step (um):</b>	25	
<b>Limit c (%)</b>	0 ≤ c ≤ 15		<b>Limit c (%)</b>	0 ≤ c ≤ 10	
<b>Limit e (%)</b>	0 ≤ e ≤ 10		<b>Limit e (%)</b>	0 ≤ e ≤ 7	
<b>Limit Area</b>	20 ≤ x ≤ 50 30 ≤ y ≤ 95		<b>Limit Area</b>	60 ≤ x ≤ 90 30 ≤ y ≤ 95	
<b>Background</b>	30 ≤ x ≤ 80 105 ≤ y ≤ 135		<b>Background</b>	30 ≤ x ≤ 80 105 ≤ y ≤ 135	
<b>N(d,c)</b>			<b>N(d,c)</b>		
<b>N(d)</b>			<b>N(d)</b>		
<b>N(d,e)</b>			<b>N(d,e)</b>		
<b>Average d (um)</b>	21.221		<b>Average d (um)</b>	15.787	
<b>Fluence (tracks/cm^2)</b>	8.31E+03		<b>Fluence (tracks/cm^2)</b>	1.01E+04	
<b>Yield</b>	2.35E+09		<b>Yield</b>	2.85E+09	

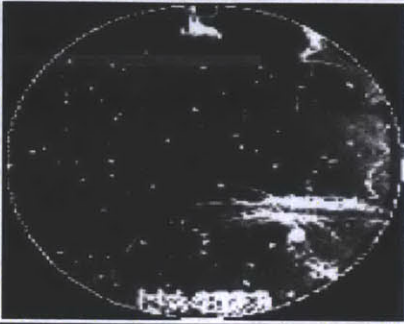
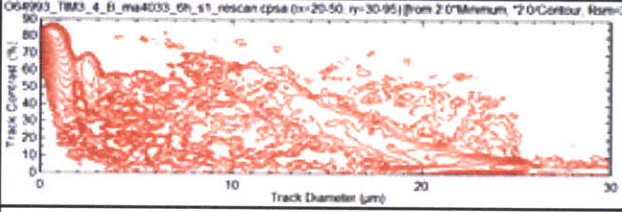
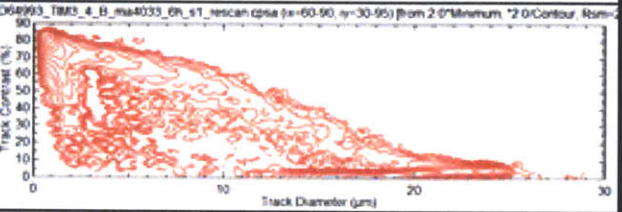
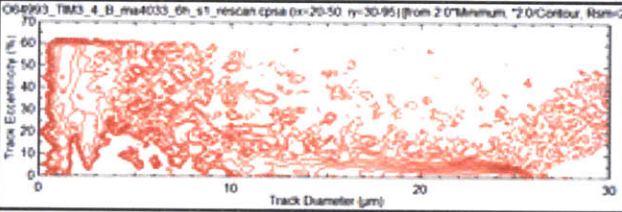
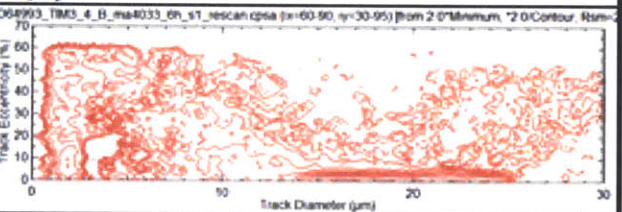
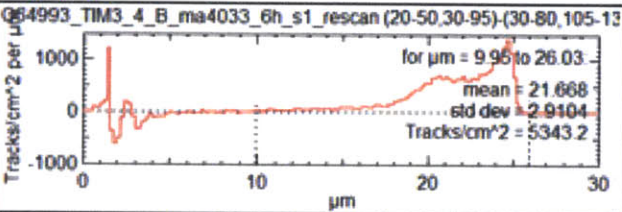
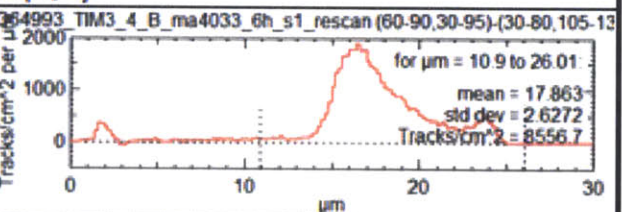
Tim 1, 8:00					
Shot	64993	Piece	ma4037	Type	Bert
Etch Time (hours)	2	Distance (cm)	150	Magnification	40x
Step (um):	50		Step (um):	25	
Limit c (%)	$0 \leq c \leq 25$		Limit c (%)	$0 \leq c \leq 25$	
Limit e (%)	$0 \leq e \leq 9$		Limit e (%)	$0 \leq e \leq 12$	
Limit Area	$20 \leq x \leq 50$ $30 \leq y \leq 95$		Limit Area	$60 \leq x \leq 90$ $30 \leq y \leq 95$	
Background	$30 \leq x \leq 80$ $105 \leq y \leq 135$		Background	$30 \leq x \leq 80$ $105 \leq y \leq 135$	
N(d,c)		N(d,c)			
					
N(d)		N(d)			
					
N(d,e)		N(d,e)			
					
Average d (um)		5.5564	Average d (um)		3.706
Fluence (tracks/cm^2)		7.99E+03	Fluence (tracks/cm^2)		1.15E+04
Yield		2.26E+09	Yield		3.24E+09

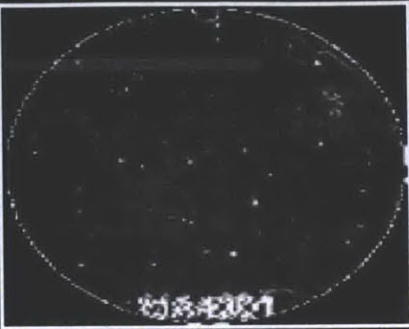
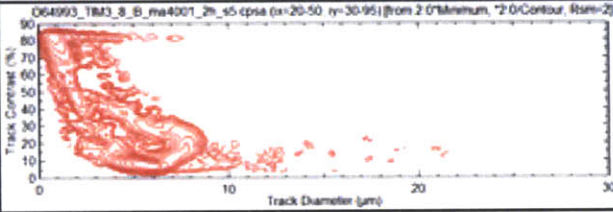
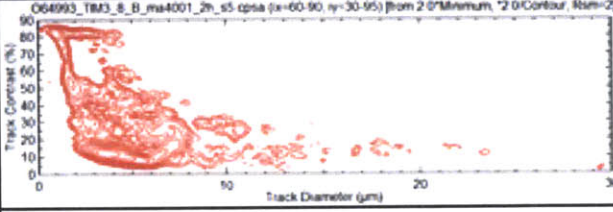
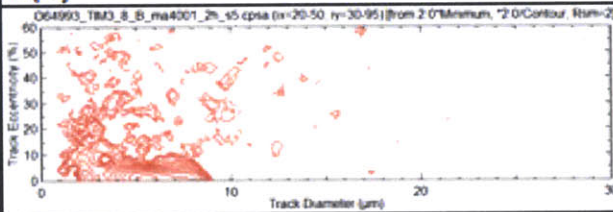
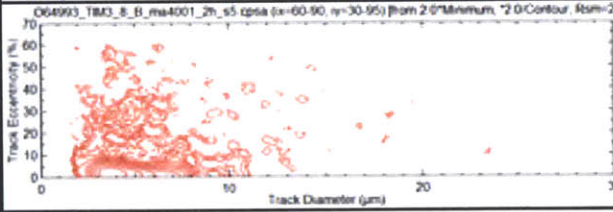
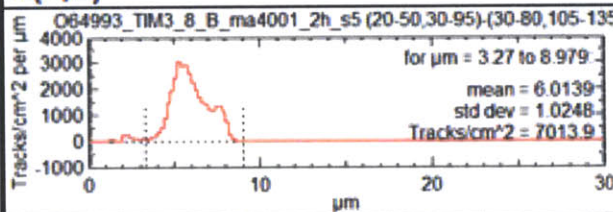
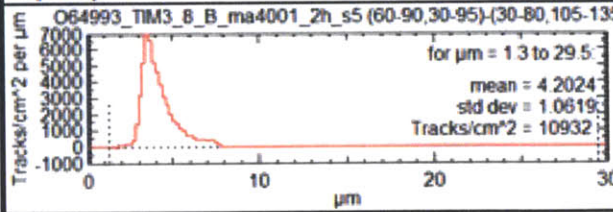
Tim 1, 12:00						
Shot	64993	Piece	ma4032	Type	WRF	
Etch Time (hours)	2	Distance (cm)	150	Magnification	40x	
D v. E Parameter (c)				Energy		
Limit c (%)				$0 \leq c \leq 18$	Sigma	
Limit e (%)				$0 \leq e \leq 14$		
Limit Area				$30 \leq x \leq 78$		
Top				$125 \leq y \leq 138$		
Limit Area	$30 \leq x \leq 78$	Bottom	$12 \leq y \leq 25$			
N(d,c)		N(d,c)				
						
N(d)		N(d)				
						
N(d,e)		N(d,e)				
						
Average d (um)	3.2629	Average d (um)	3.3743			
Fluence (tracks/cm^2)	1.53E+04	Fluence (tracks/cm^2)	1.44E+04			
Yield	4.33E+09	Yield	4.08E+09			

Tim 2, 4:00					
Shot	64993	Piece	ma4040	Type	Bert
Etch Time (hours)	6	Distance (cm)	150	Magnification	40x
Step (um):	50		Step (um):	25	
Limit c (%)	$0 \leq c \leq 15$		Limit c (%)	$0 \leq c \leq 8$	
Limit e (%)	$0 \leq e \leq 10$		Limit e (%)	$0 \leq e \leq 7$	
Limit Area	$20 \leq x \leq 50$ $30 \leq y \leq 95$		Limit Area	$60 \leq x \leq 90$ $30 \leq y \leq 95$	
Background	$30 \leq x \leq 80$ $105 \leq y \leq 135$		Background	$30 \leq x \leq 80$ $105 \leq y \leq 135$	
N(d,c)		N(d,c)			
					
N(d)		N(d)			
					
N(d,e)		N(d,e)			
					
Average d (um)	21.688	Average d (um)	15.712		
Fluence (tracks/cm^2)	5.71E+03	Fluence (tracks/cm^2)	5.29E+03		
Yield	1.61E+09	Yield	1.49E+09		

Tim 2, 8:00					
Shot	64993	Piece	ma4056	Type	Bert
Etch Time (hours)	2	Distance (cm)	150	Magnification	40x
Step (um):	50		Step (um):	25	
Limit c (%)	$0 \leq c \leq 30$		Limit c (%)	$0 \leq c \leq 25$	
Limit e (%)	$0 \leq e \leq 8$		Limit e (%)	$0 \leq e \leq 12$	
Limit Area	$20 \leq x \leq 50$ $30 \leq y \leq 95$		Limit Area	$60 \leq x \leq 90$ $30 \leq y \leq 95$	
Background	$30 \leq x \leq 80$ $105 \leq y \leq 135$		Background	$30 \leq x \leq 80$ $105 \leq y \leq 135$	
<b>N(d,c)</b>			<b>N(d,c)</b>		
					
<b>N(d)</b>		<b>N(d)</b>			
					
<b>N(d,e)</b>		<b>N(d,e)</b>			
					
Average d (um)	5.4519	Average d (um)	3.551		
Fluence (tracks/cm^2)	1.17E+04	Fluence (tracks/cm^2)	1.16E+04		
Yield	3.32E+09	Yield	3.27E+09		

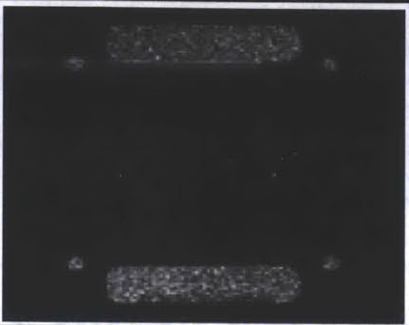
Tim 2, 12:00						
Shot	64993	Piece	ma4039	Type	WRF	
Etch Time (hours)	2	Distance (cm)	150	Magnification	40x	
D v. E Parameter (c)				Energy		
Limit c (%)				$0 \leq c \leq 18$	Sigma	
Limit e (%)				$0 \leq e \leq 13$		
Limit Area				$30 \leq x \leq 78$		
Top				$125 \leq y \leq 138$		
Limit Area	$30 \leq x \leq 78$					
Bottom	$12 \leq y \leq 25$					
<b>N(d,c)</b>		<b>N(d,c)</b>				
						
<b>N(d)</b>		<b>N(d)</b>				
						
<b>N(d,e)</b>		<b>N(d,e)</b>				
						
<b>Average d (um)</b>		3.7087	<b>Average d (um)</b>		3.3417	
<b>Fluence (tracks/cm^2)</b>		1.32E+04	<b>Fluence (tracks/cm^2)</b>		1.48E+04	
<b>Yield</b>		3.72E+09	<b>Yield</b>		4.17E+09	

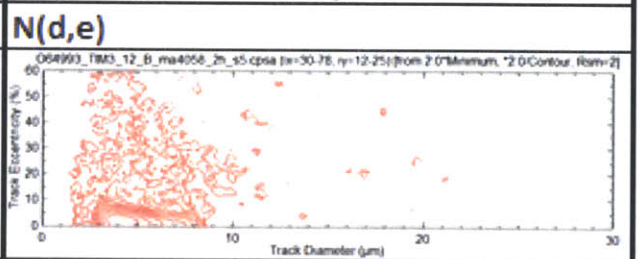
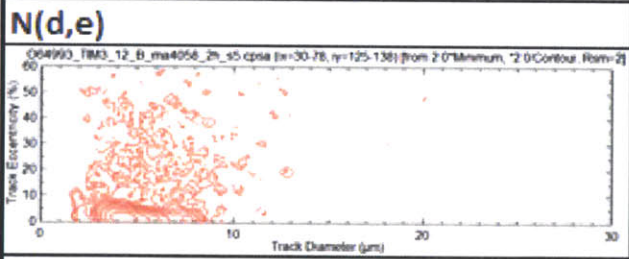
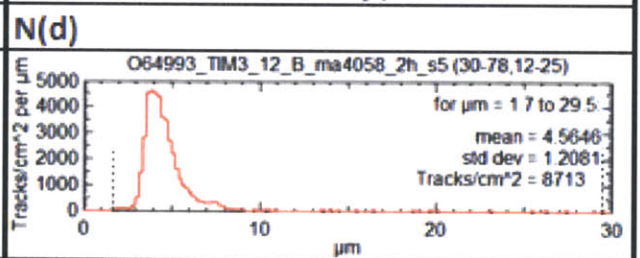
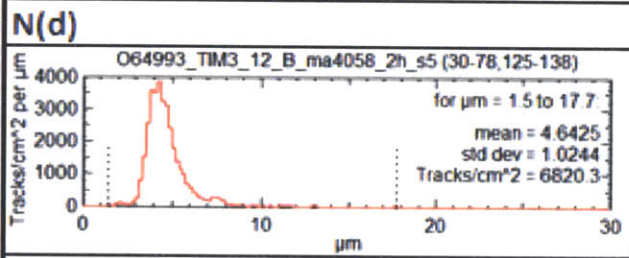
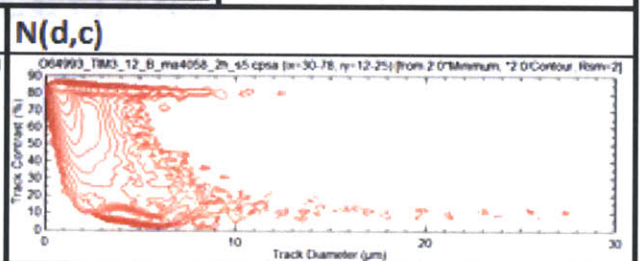
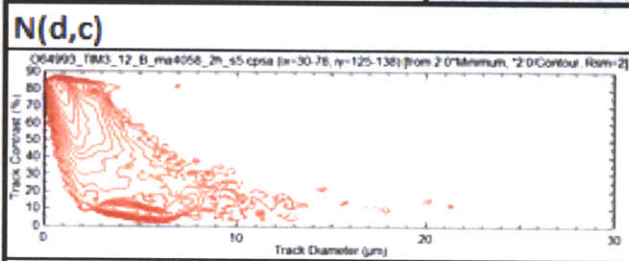
Tim 3, 4:00					
Shot	64993	Piece	ma4033	Type	Bert
Etch Time (hours)	6	Distance (cm)	150	Magnification	40x
<b>Step (um):</b>	50		<b>Step (um):</b>	25	
<b>Limit c (%)</b>	$0 \leq c \leq 65$		<b>Limit c (%)</b>	$0 \leq c \leq 50$	
<b>Limit e (%)</b>	$0 \leq e \leq 10$		<b>Limit e (%)</b>	$0 \leq e \leq 8$	
<b>Limit Area</b>	$20 \leq x \leq 50$ $30 \leq y \leq 95$		<b>Limit Area</b>	$20 \leq x \leq 50$ $30 \leq y \leq 95$	
<b>Background</b>	$30 \leq x \leq 80$ $105 \leq y \leq 135$		<b>Background</b>	$30 \leq x \leq 80$ $105 \leq y \leq 135$	
<b>N(d,c)</b>			<b>N(d,c)</b>		
					
<b>N(d)</b>		<b>N(d)</b>			
					
<b>N(d,e)</b>		<b>N(d,e)</b>			
					
<b>Average d (um)</b>	21.668	<b>Average d (um)</b>	17.863		
<b>Fluence (tracks/cm^2)</b>	5.34E+03	<b>Fluence (tracks/cm^2)</b>	8.56E+03		
<b>Yield</b>	1.51E+09	<b>Yield</b>	2.42E+09		

Tim 3, 8:00					
Shot	64993	Piece	ma4001	Type	Bert
Etch Time (hours)	2	Distance (cm)	150	Magnification	40x
<b>Step (um):</b>	50		<b>Step (um):</b>	25	
<b>Limit c (%)</b>	$0 \leq c \leq 45$		<b>Limit c (%)</b>	$0 \leq c \leq 40$	
<b>Limit e (%)</b>	$0 \leq e \leq 11$		<b>Limit e (%)</b>	$0 \leq e \leq 11$	
<b>Limit Area</b>	$20 \leq x \leq 50$ $30 \leq y \leq 95$		<b>Limit Area</b>	$60 \leq x \leq 95$ $30 \leq y \leq 95$	
<b>Background</b>	$30 \leq x \leq 80$ $105 \leq y \leq 135$		<b>Background</b>	$30 \leq x \leq 80$ $105 \leq y \leq 135$	
<b>N(d,c)</b>			<b>N(d,c)</b>		
<b>N(d)</b>			<b>N(d)</b>		
<b>N(d,e)</b>	 for $\mu\text{m} = 3.27$ to $8.979$ mean = 6.0139 std dev = 1.0248 Tracks/cm <sup>2</sup> = 7013.9		<b>N(d,e)</b>		 for $\mu\text{m} = 1.3$ to $29.5$ mean = 4.2024 std dev = 1.0619 Tracks/cm <sup>2</sup> = 10932
<b>Average d (um)</b>	6.0139		<b>Average d (um)</b>		4.2024
<b>Fluence (tracks/cm^2)</b>	7.01E+03		<b>Fluence (tracks/cm^2)</b>		1.09E+04
<b>Yield</b>	1.98E+09		<b>Yield</b>		3.09E+09

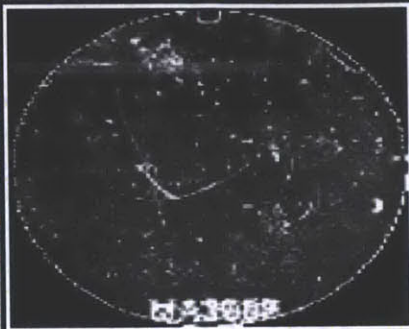
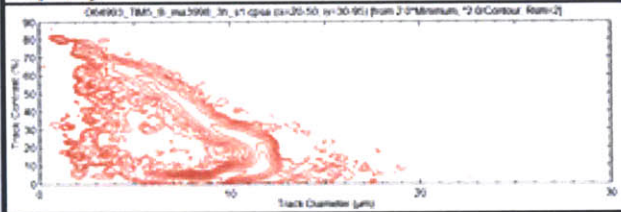
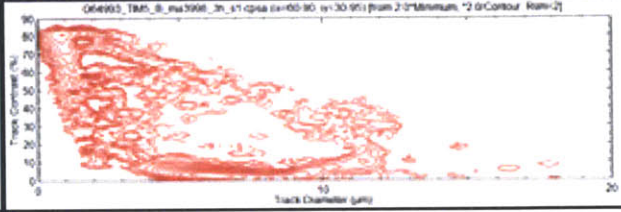
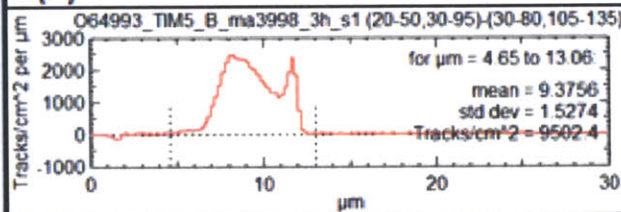
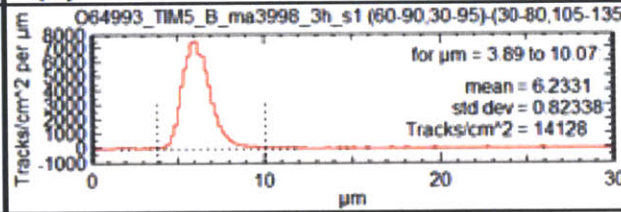
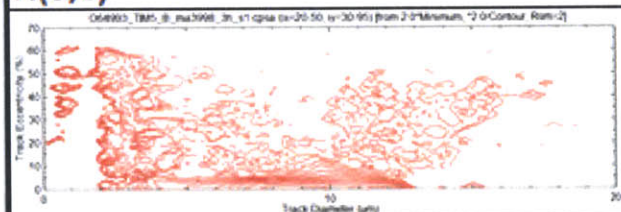
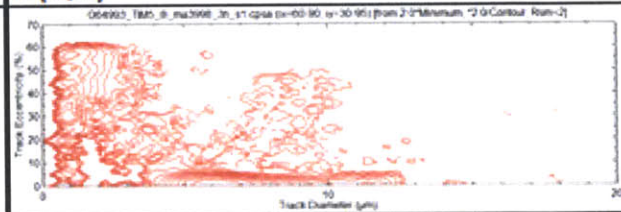


**Tim 3, 12:00**

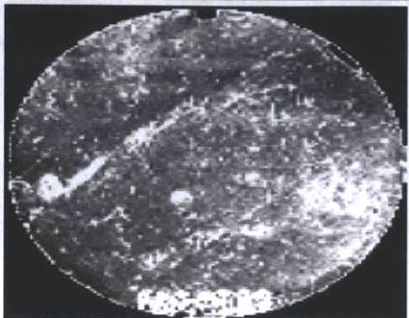
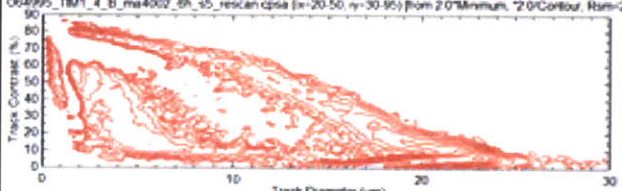
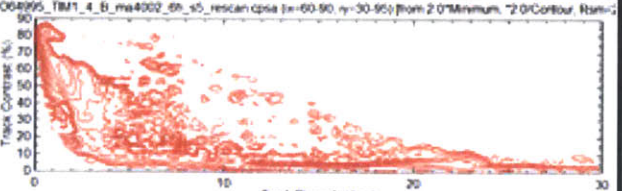
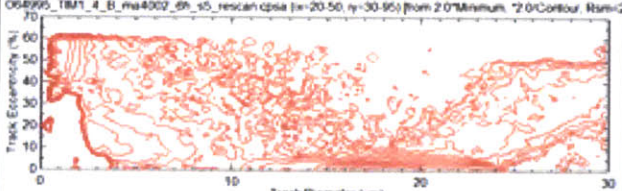
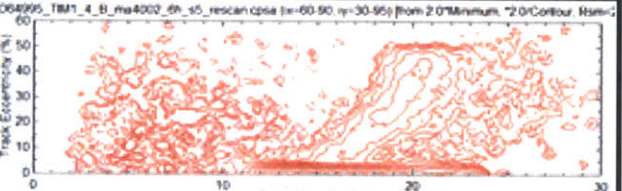
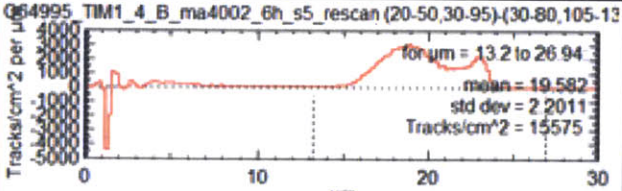
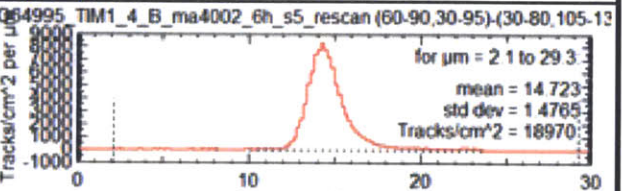
<b>Shot</b>	<b>64993</b>	<b>Piece</b>	<b>ma4058</b>	<b>Type</b>	<b>WRF</b>
<b>Etch Time (hours)</b>	<b>2</b>	<b>Distance (cm)</b>	<b>150</b>	<b>Magnification</b>	<b>40x</b>
<b>D v. E Parameter (c)</b>				<b>Energy</b>	
<b>Limit c (%)</b>	$0 \leq c \leq$	<b>20</b>		<b>Sigma</b>	
<b>Limit e (%)</b>	$0 \leq e \leq$	<b>11</b>			
<b>Limit Area</b>	$30 \leq x \leq$	<b>78</b>			
<b>Top</b>	$125 \leq y \leq$	<b>138</b>			
<b>Limit Area</b>	$30 \leq x \leq$	<b>78</b>			
<b>Bottom</b>	$12 \leq y \leq$	<b>25</b>			


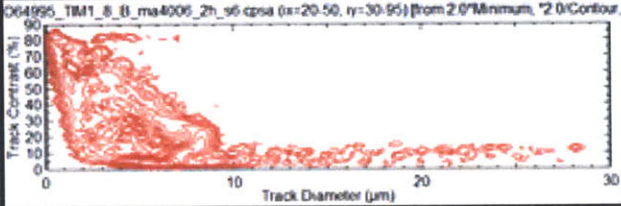
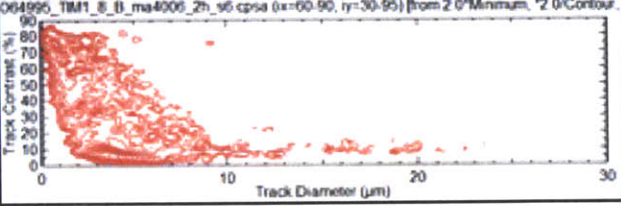
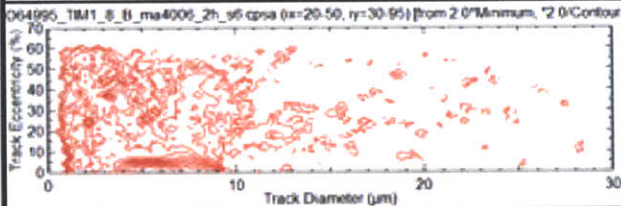
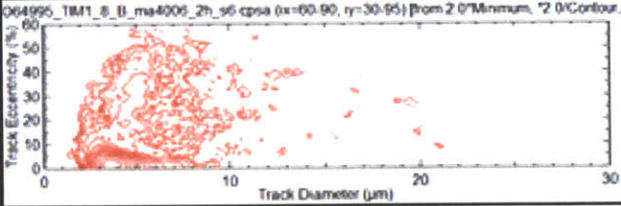
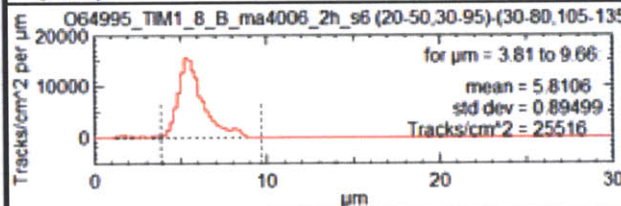
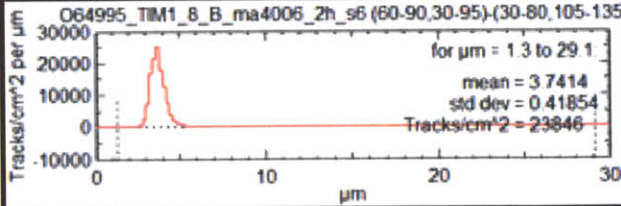


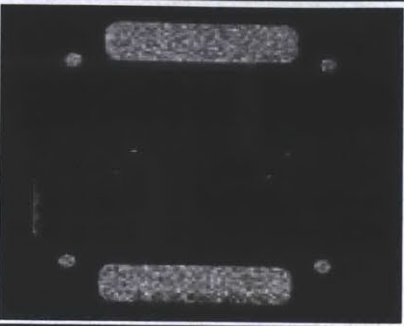
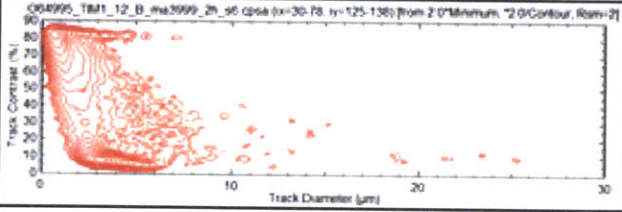
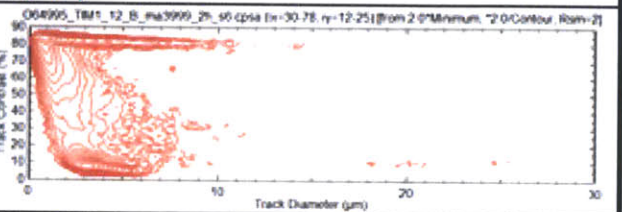
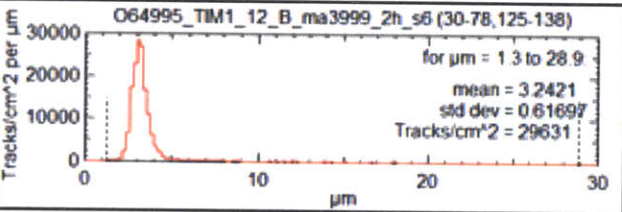
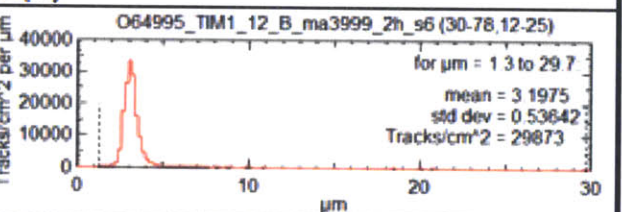
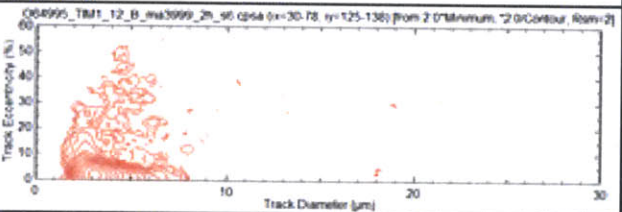
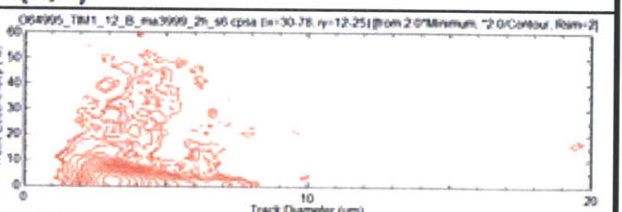
<b>Average d (um)</b>	<b>4.6425</b>	<b>Average d (um)</b>	<b>4.5646</b>
<b>Fluence (tracks/cm<sup>2</sup>)</b>	<b>6.82E+03</b>	<b>Fluence (tracks/cm<sup>2</sup>)</b>	<b>8.71E+03</b>
<b>Yield</b>	<b>1.93E+09</b>	<b>Yield</b>	<b>2.46E+09</b>

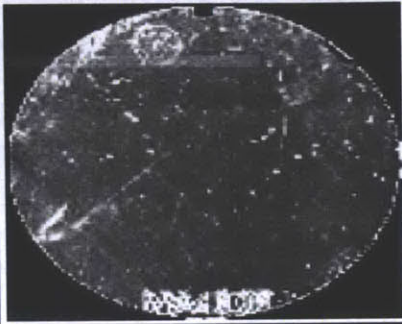
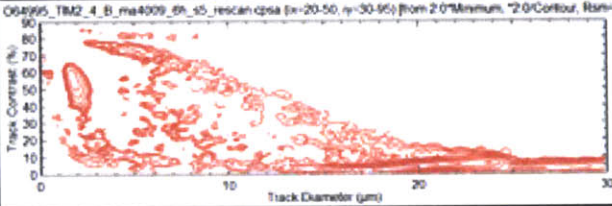
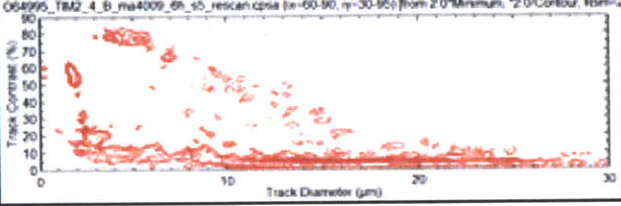
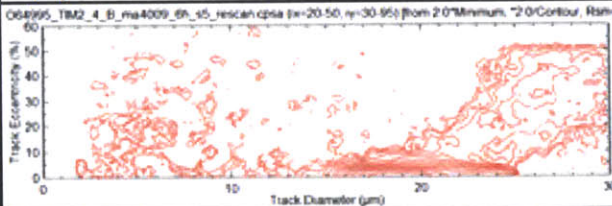
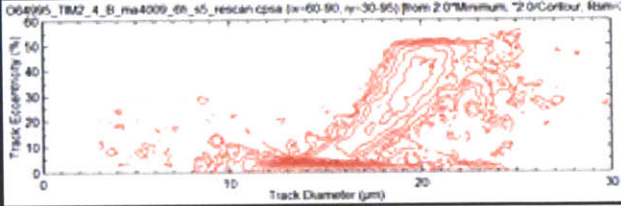
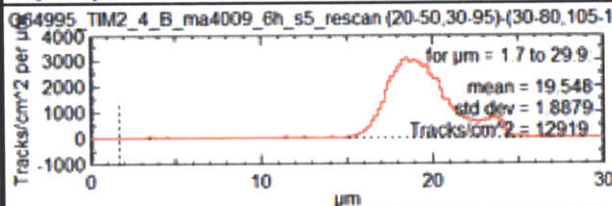
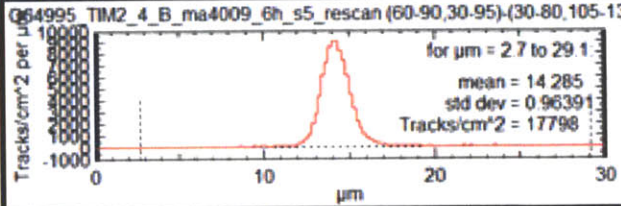
TIM 5					
Shot	64993	Piece	ma3998	Type	Bert
Etch Time (hours)	3	Distance (cm)	150	Magnification	40x
Step (um):	50		Step (um):	25	
Limit c (%)	$0 \leq c \leq 60$		Limit c (%)	$0 \leq c \leq 20$	
Limit e (%)	$0 \leq e \leq 12$		Limit e (%)	$0 \leq e \leq 8$	
Limit Area	$20 \leq x \leq 50$ $30 \leq y \leq 95$		Limit Area	$60 \leq x \leq 90$ $30 \leq y \leq 95$	
Background	$30 \leq x \leq 80$ $105 \leq y \leq 135$		Background	$30 \leq x \leq 80$ $105 \leq y \leq 135$	
N(d,c)			N(d,c)		
					
N(d)		N(d)			
					
N(d,e)		N(d,e)			
					
Average d (um)		9.3756	Average d (um)		6.2331
Fluence (tracks/cm^2)		9.50E+03	Fluence (tracks/cm^2)		1.41E+04
Yield		2.69E+09	Yield		3.99E+09


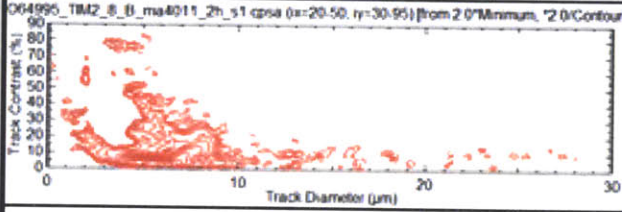
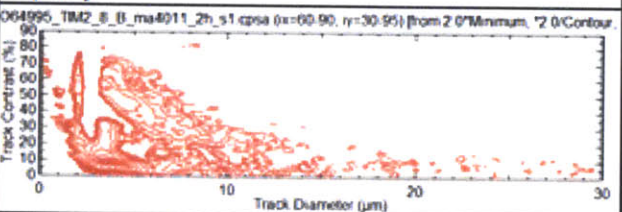
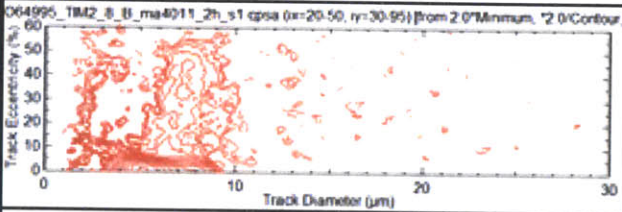
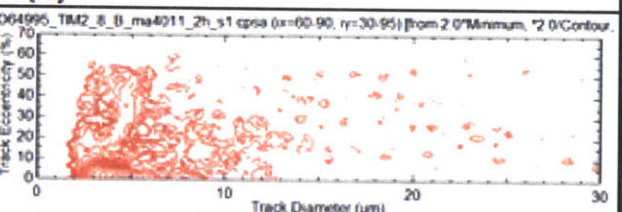
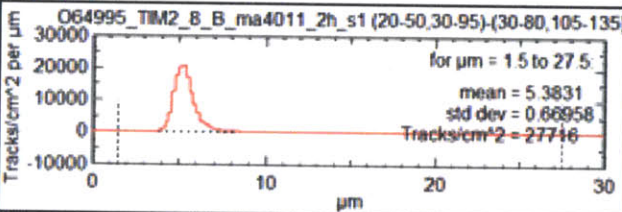
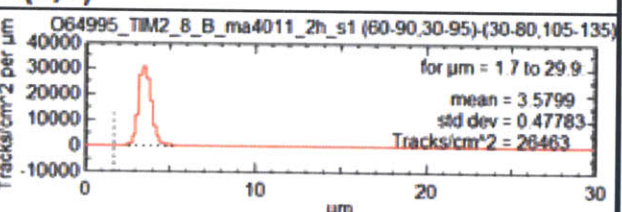
Shot 64995

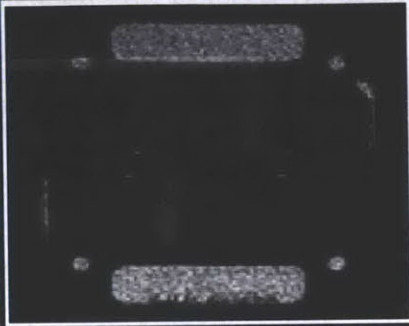
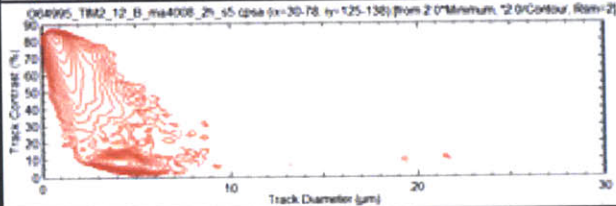
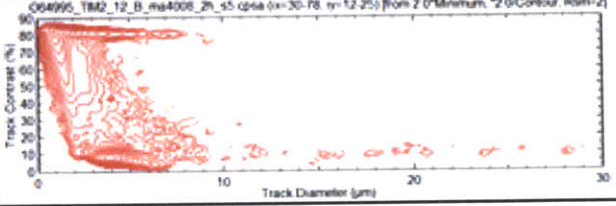
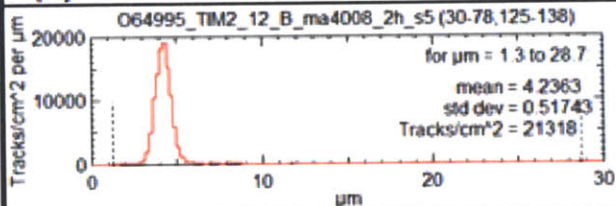
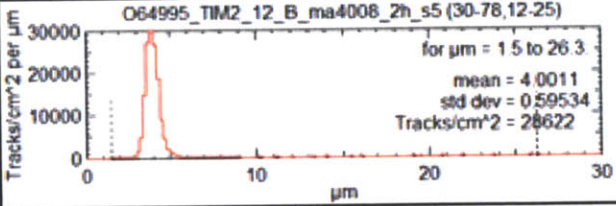
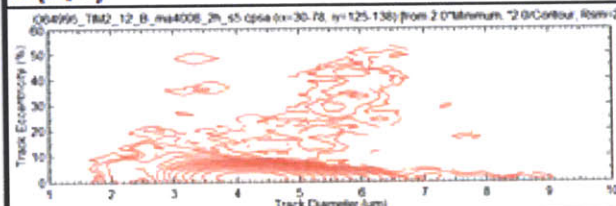
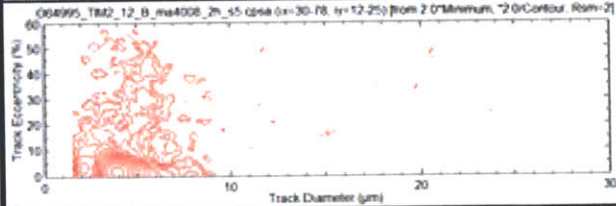
Tim 1, 4:00					
Shot	64995	Piece	ma4002	Type	Bert
Etch Time (hours)	6	Distance (cm)	150	Magnification	40x
<b>Step (um):</b>	50		<b>Step (um):</b>	25	
<b>Limit c (%)</b>	0 ≤ c ≤ 80		<b>Limit c (%)</b>	0 ≤ c ≤ 14	
<b>Limit e (%)</b>	0 ≤ e ≤ 11		<b>Limit e (%)</b>	0 ≤ e ≤ 7	
<b>Limit Area</b>	20 ≤ x ≤ 50 30 ≤ y ≤ 95		<b>Limit Area</b>	60 ≤ x ≤ 90 30 ≤ y ≤ 95	
<b>Background</b>	30 ≤ x ≤ 80 105 ≤ y ≤ 135		<b>Background</b>	30 ≤ x ≤ 80 105 ≤ y ≤ 135	
<b>N(d,c)</b>					
<b>N(d)</b>					
<b>N(d,e)</b>					
<b>Average d (um)</b>	19.582	<b>Average d (um)</b>	14.723		
<b>Fluence (tracks/cm^2)</b>	1.56E+04	<b>Fluence (tracks/cm^2)</b>	1.90E+04		
<b>Yield</b>	4.40E+09	<b>Yield</b>	5.36E+09		

Tim 1, 8:00					
Shot	64995	Piece	ma4006	Type	Bert
Etch Time (hours)	2	Distance (cm)	150	Magnification	40x
<b>Step (um):</b>	50		<b>Step (um):</b>	25	
<b>Limit c (%)</b>	$0 \leq c \leq 40$		<b>Limit c (%)</b>	$0 \leq c \leq 15$	
<b>Limit e (%)</b>	$0 \leq e \leq 11$		<b>Limit e (%)</b>	$0 \leq e \leq 12$	
<b>Limit Area</b>	$20 \leq x \leq 50$ $30 \leq y \leq 95$		<b>Limit Area</b>	$20 \leq x \leq 50$ $30 \leq y \leq 95$	
<b>Background</b>	$30 \leq x \leq 80$ $105 \leq y \leq 135$		<b>Background</b>	$30 \leq x \leq 80$ $105 \leq y \leq 135$	
<b>N(d,c)</b>			<b>N(d,c)</b>		
<b>N(d)</b>			<b>N(d)</b>		
<b>N(d,e)</b>			<b>N(d,e)</b>		
<b>Average d (um)</b>	5.8106		<b>Average d (um)</b>		3.7414
<b>Fluence (tracks/cm^2)</b>	2.55E+04		<b>Fluence (tracks/cm^2)</b>		2.38E+04
<b>Yield</b>	7.21E+09		<b>Yield</b>		6.74E+09

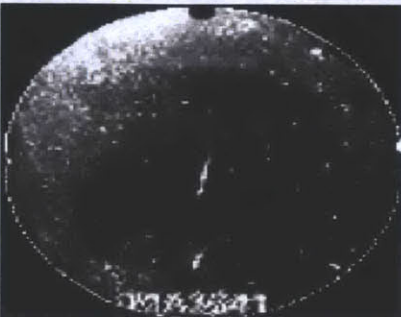
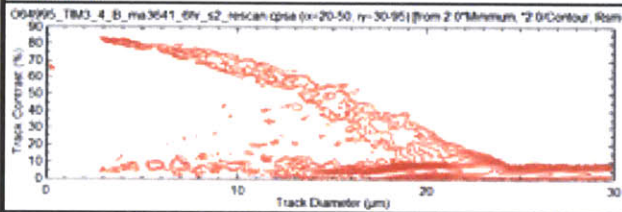
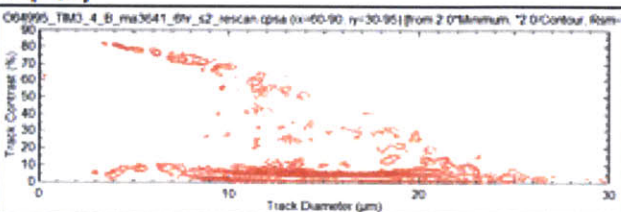
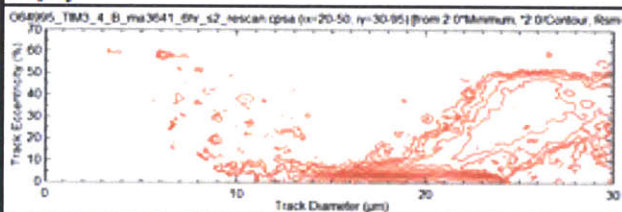
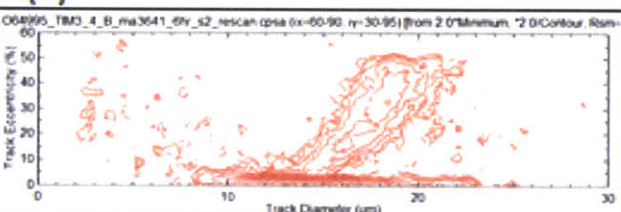
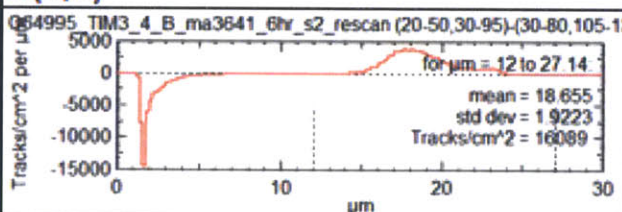
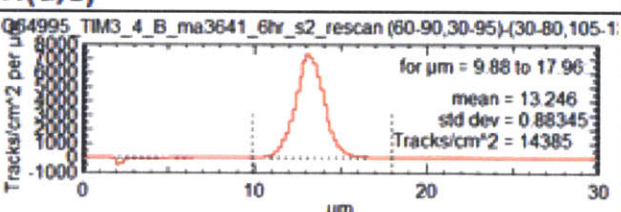
Tim 1, 12:00					
Shot	64993	Piece	ma3999	Type	WRF
Etch Time (hours)	2	Distance (cm)	150	Magnification	40x
D v. E Parameter (c)				Energy	
Limit c (%)	$0 \leq c \leq 29$			Sigma	
Limit e (%)	$0 \leq e \leq 15$				
Limit Area	$30 \leq x \leq 78$				
Top	$125 \leq y \leq 138$				
Limit Area	$30 \leq x \leq 78$				
Bottom	$12 \leq y \leq 25$				
N(d,c)		N(d,c)			
					
N(d)		N(d)			
					
N(d,e)		N(d,e)			
					
Average d (um)	3.2421	Average d (um)	3.1975		
Fluence (tracks/cm^2)	2.96E+04	Fluence (tracks/cm^2)	2.99E+04		
Yield	8.38E+09	Yield	8.45E+09		

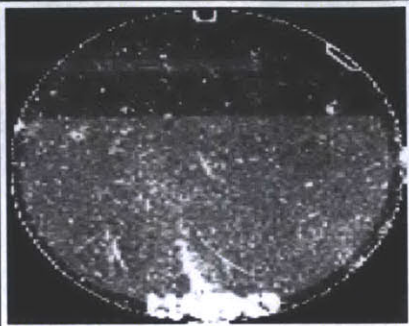
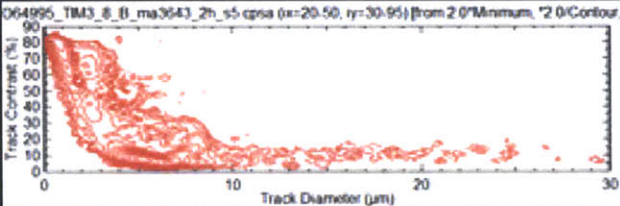
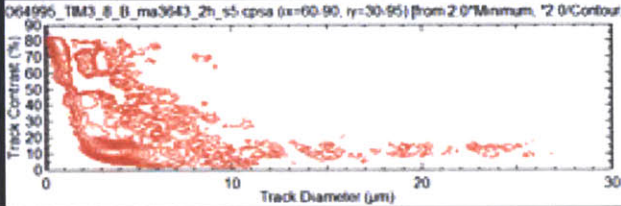
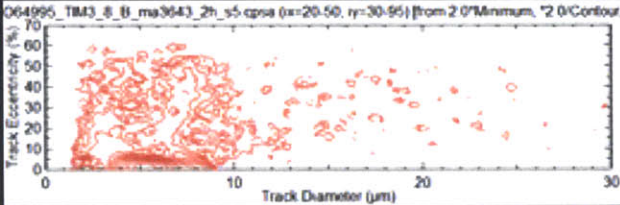
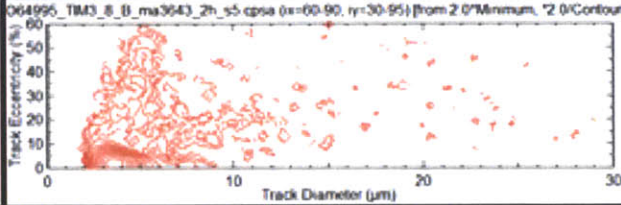
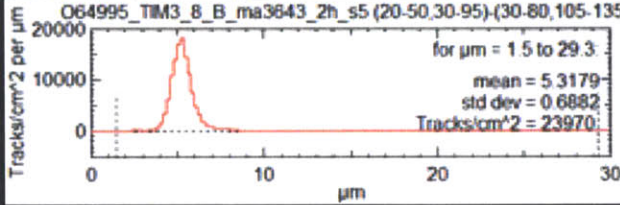
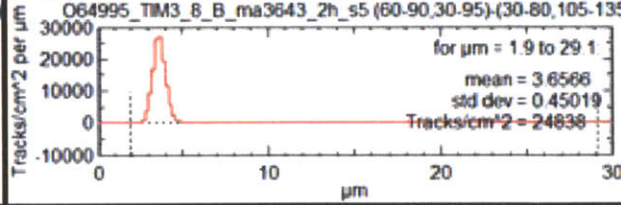
Tim 2, 4:00					
Shot	64995	Piece	ma4009	Type	Bert
Etch Time (hours)	6	Distance (cm)	150	Magnification	40x
<b>Step (um):</b>	50		<b>Step (um):</b>	25	
<b>Limit c (%)</b>	$0 \leq c \leq 15$		<b>Limit c (%)</b>	$0 \leq c \leq 8$	
<b>Limit e (%)</b>	$0 \leq e \leq 13$		<b>Limit e (%)</b>	$0 \leq e \leq 7$	
<b>Limit Area</b>	$20 \leq x \leq 50$ $30 \leq y \leq 95$		<b>Limit Area</b>	$60 \leq x \leq 90$ $30 \leq y \leq 95$	
<b>Background</b>	$30 \leq x \leq 80$ $105 \leq y \leq 135$		<b>Background</b>	$30 \leq x \leq 80$ $105 \leq y \leq 135$	
<b>N(d,c)</b>					
<b>N(d)</b>					
<b>N(d,e)</b>					
<b>Average d (um)</b>	19.548		<b>Average d (um)</b>		14.285
<b>Fluence (tracks/cm^2)</b>	1.29E+04		<b>Fluence (tracks/cm^2)</b>		1.78E+04
<b>Yield</b>	3.65E+09		<b>Yield</b>		5.03E+09

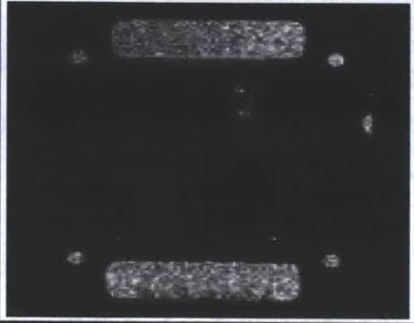
Tim 2, 8:00					
Shot	64995	Piece	ma4011	Type	Bert
Etch Time (hours)	2	Distance (cm)	150	Magnification	40x
Step (um):	50		Step (um):	25	
Limit c (%)	$0 \leq c \leq 30$		Limit c (%)	$0 \leq c \leq 20$	
Limit e (%)	$0 \leq e \leq 9$		Limit e (%)	$0 \leq e \leq 12$	
Limit Area	$20 \leq x \leq 50$ $30 \leq y \leq 95$		Limit Area	$60 \leq x \leq 90$ $30 \leq y \leq 95$	
Background	$30 \leq x \leq 80$ $105 \leq y \leq 135$		Background	$30 \leq x \leq 80$ $105 \leq y \leq 135$	
<b>N(d,c)</b>			<b>N(d,c)</b>		
					
<b>N(d)</b>		<b>N(d)</b>			
					
<b>N(d,e)</b>		<b>N(d,e)</b>			
					
Average d (um)	5.3831	Average d (um)	3.5799		
Fluence (tracks/cm^2)	2.77E+04	Fluence (tracks/cm^2)	2.65E+04		
Yield	7.84E+09	Yield	7.48E+09		

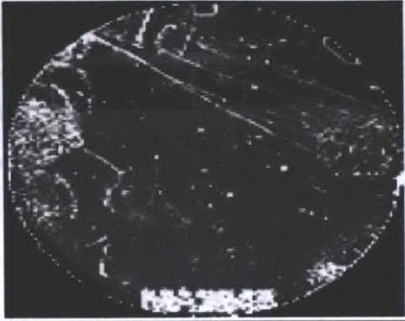
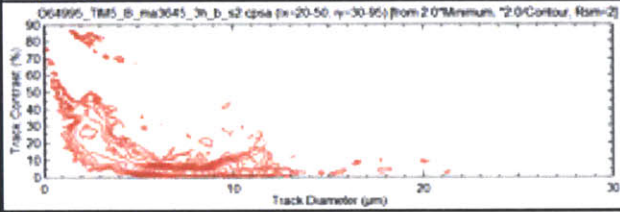
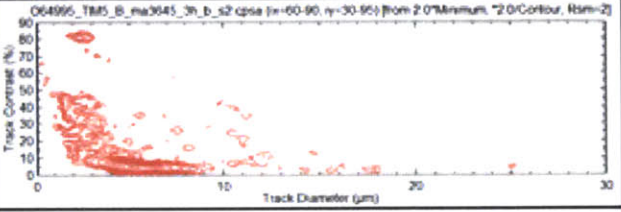
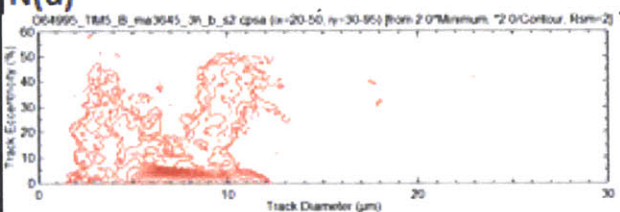
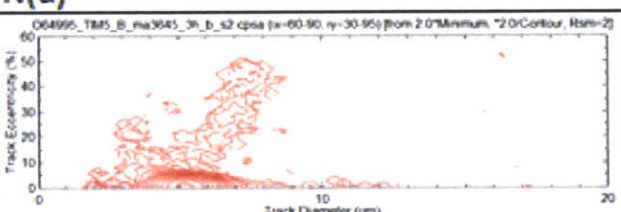
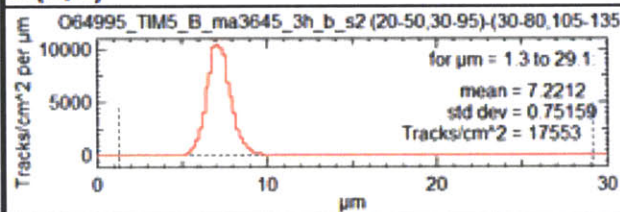
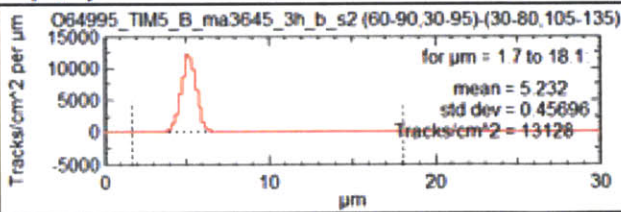
Tim 2, 12:00					
Shot	64993	Piece	ma4008	Type	WRF
Etch Time (hours)	2	Distance (cm)	150	Magnification	40x
D v. E Parameter (c)				Energy	
Limit c (%)	0 ≤ c ≤ 20			Sigma	
Limit e (%)	0 ≤ e ≤ 12				
Limit Area	30 ≤ x ≤ 78				
Top	125 ≤ y ≤ 138				
Limit Area	30 ≤ x ≤ 78				
Bottom	12 ≤ y ≤ 25				
N(d,c)			N(d,c)		
					
N(d)			N(d)		
					
N(d,e)			N(d,e)		
					
Average d (um)		4.2363	Average d (um)		4.0011
Fluence (tracks/cm^2)		2.13E+04	Fluence (tracks/cm^2)		2.86E+04
Yield		6.03E+09	Yield		8.09E+09



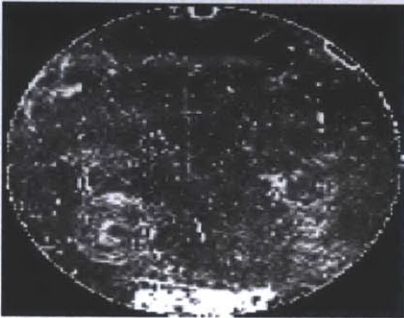
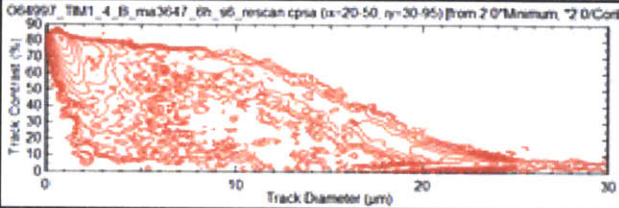
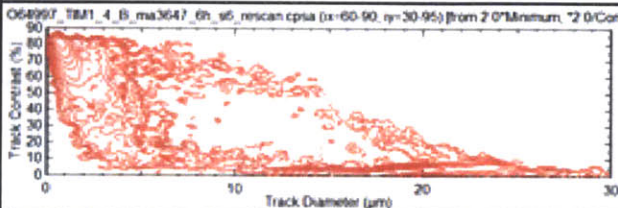
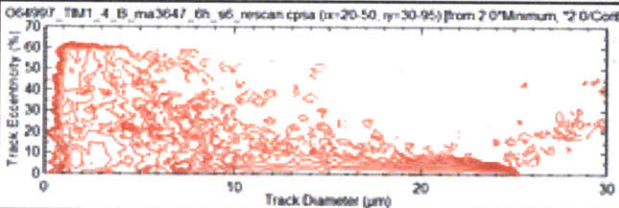
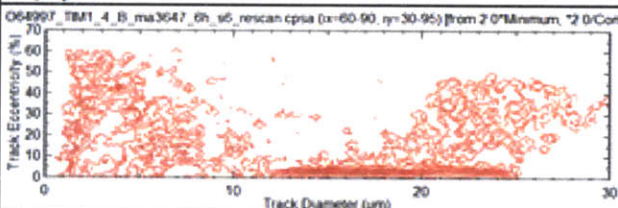
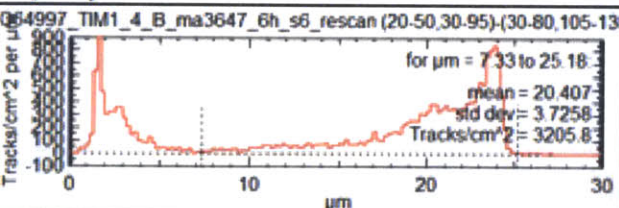
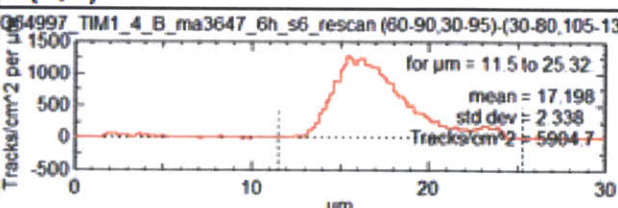
Tim 3, 4:00					
Shot	64995	Piece	ma3641	Type	Bert
Etch Time (hours)	6	Distance (cm)	150	Magnification	40x
Step (um):	50		Step (um):	25	
Limit c (%)	0 ≤ c ≤ 85		Limit c (%)	0 ≤ c ≤ 15	
Limit e (%)	0 ≤ e ≤ 11		Limit e (%)	0 ≤ e ≤ 7	
Limit Area	20 ≤ x ≤ 50 30 ≤ y ≤ 95		Limit Area	60 ≤ x ≤ 90 30 ≤ y ≤ 95	
Background	30 ≤ x ≤ 80 105 ≤ y ≤ 135		Background	30 ≤ x ≤ 80 105 ≤ y ≤ 135	
<b>N(d,c)</b>			<b>N(d,c)</b>		
					
<b>N(d)</b>			<b>N(d)</b>		
					
<b>N(d,e)</b>			<b>N(d,e)</b>		
					
Average d (um)	18.655	Average d (um)	13.246		
Fluence (tracks/cm^2)	1.61E+04	Fluence (tracks/cm^2)	1.44E+04		
Yield	4.55E+09	Yield	4.07E+09		

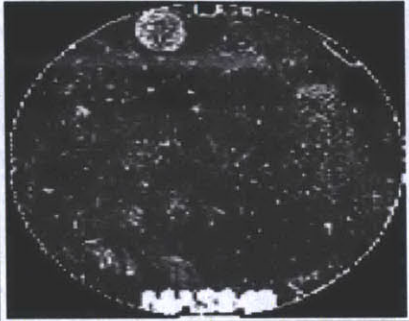
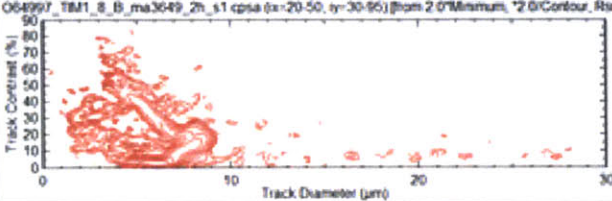
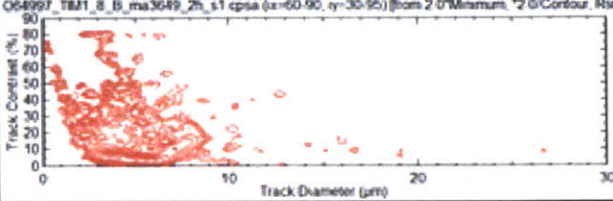
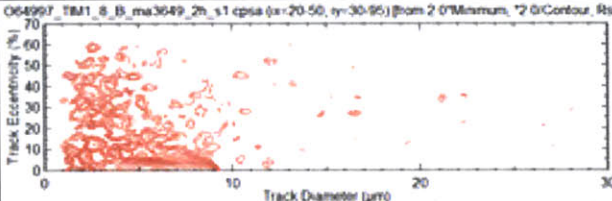
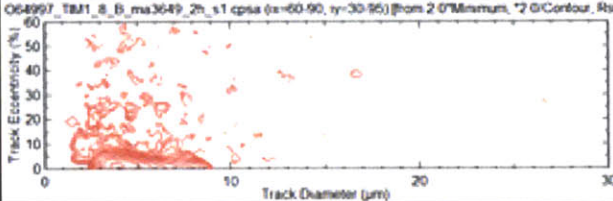
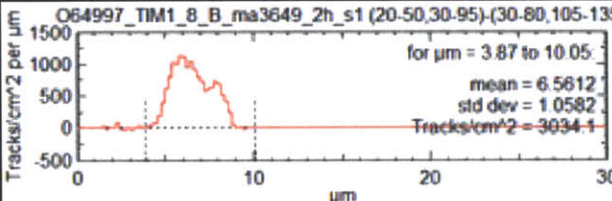
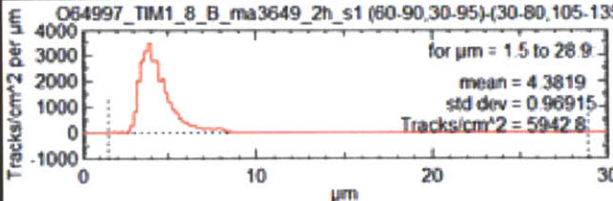
Tim 3, 8:00					
Shot	64995	Piece	ma3643	Type	Bert
Etch Time (hours)	2	Distance (cm)	150	Magnification	40x
<b>Step (um):</b>	50		<b>Step (um):</b>	25	
<b>Limit c (%)</b>	$0 \leq c \leq 35$		<b>Limit c (%)</b>	$0 \leq c \leq 20$	
<b>Limit e (%)</b>	$0 \leq e \leq 10$		<b>Limit e (%)</b>	$0 \leq e \leq 12$	
<b>Limit Area</b>	$20 \leq x \leq 50$ $30 \leq y \leq 95$		<b>Limit Area</b>	$60 \leq x \leq 90$ $30 \leq y \leq 95$	
<b>Background</b>	$30 \leq x \leq 80$ $105 \leq y \leq 135$		<b>Background</b>	$30 \leq x \leq 80$ $105 \leq y \leq 135$	
<b>N(d,c)</b>		<b>N(d,c)</b>			
					
<b>N(d)</b>		<b>N(d)</b>			
					
<b>N(d,e)</b>		<b>N(d,e)</b>			
					
<b>Average d (um)</b>		5.3179	<b>Average d (um)</b>		3.6566
<b>Fluence (tracks/cm^2)</b>		2.40E+04	<b>Fluence (tracks/cm^2)</b>		2.48E+04
<b>Yield</b>		6.78E+09	<b>Yield</b>		7.02E+09

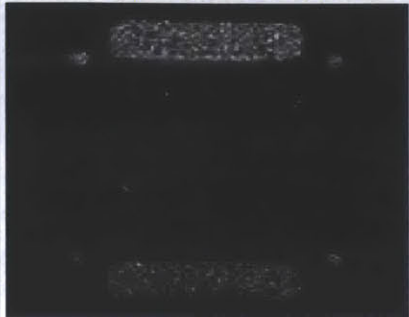
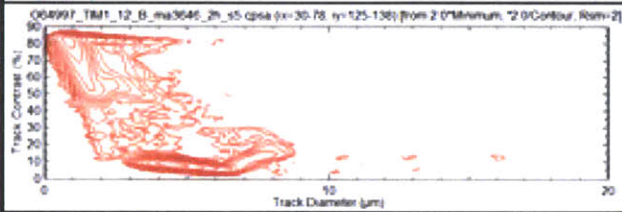
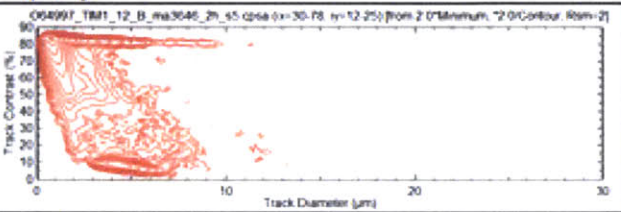
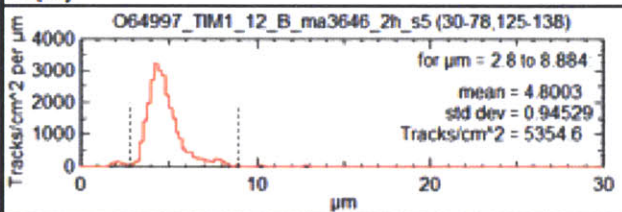
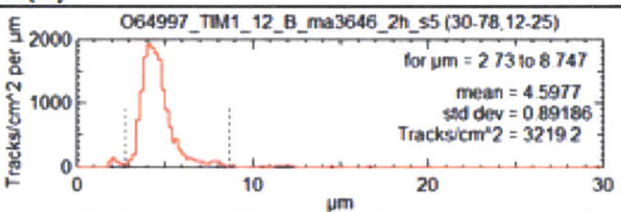
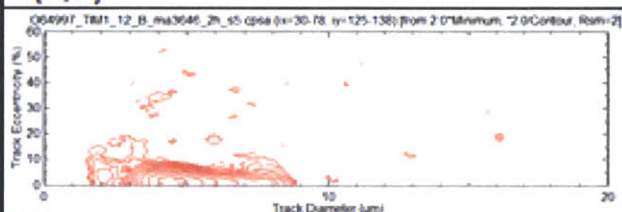
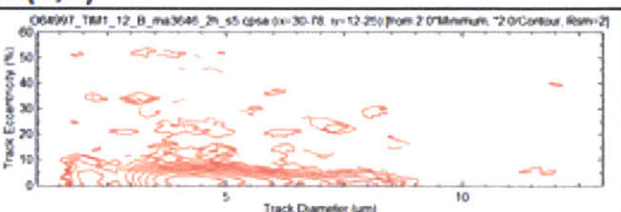
Tim 3, 12:00					
Shot	64993	Piece	ma4014	Type	WRF
Etch Time (hours)	2	Distance (cm)	150	Magnification	40x
D v. E Parameter (c)				Energy	
Limit c (%)	$0 \leq c \leq 23$			Sigma	
Limit e (%)	$0 \leq e \leq 12$				
Limit Area	$30 \leq x \leq 78$				
Top	$125 \leq y \leq 138$				
Limit Area	$30 \leq x \leq 78$				
Bottom	$12 \leq y \leq 25$				
N(d,c)		N(d,c)			
N(d)		N(d)			
N(d,e)		N(d,e)			
Average d (um)		3.764	Average d (um)		3.805
Fluence (tracks/cm²)		1.58E+04	Fluence (tracks/cm²)		1.76E+04
Yield		4.47E+09	Yield		4.97E+09

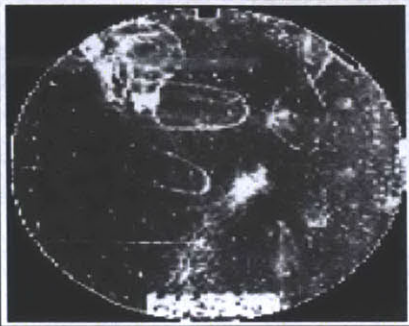
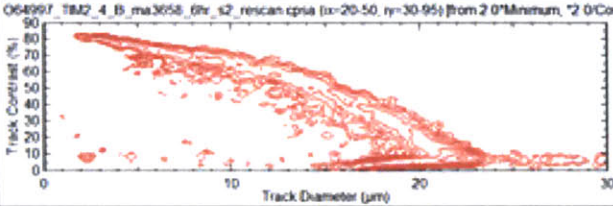
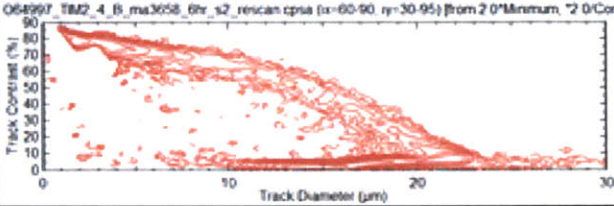
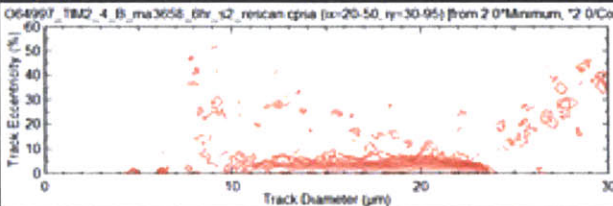
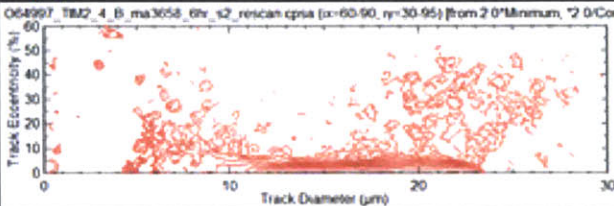
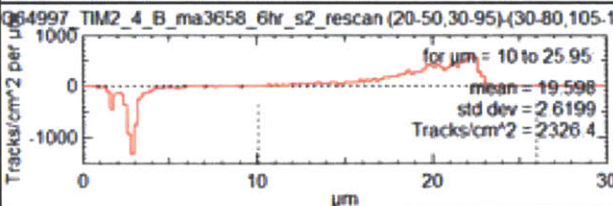
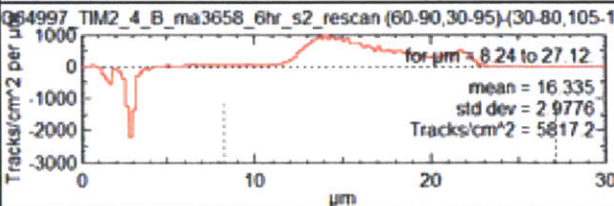
TIM 5					
Shot	64995	Piece	ma3645	Type	Bert
Etch Time (hours)	3	Distance (cm)	150	Magnification	40x
Step (um):	50		Step (um):	25	
Limit c (%)	$0 \leq c \leq 17$		Limit c (%)	$0 \leq c \leq 13$	
Limit e (%)	$0 \leq e \leq 8$		Limit e (%)	$0 \leq e \leq 8$	
Limit Area	$20 \leq x \leq 50$ $30 \leq y \leq 95$		Limit Area	$60 \leq x \leq 90$ $30 \leq y \leq 95$	
Background	$30 \leq x \leq 80$ $105 \leq y \leq 135$		Background	$30 \leq x \leq 80$ $105 \leq y \leq 135$	
N(d,c)			N(d,c)		
					
N(d)			N(d)		
					
N(d,e)			N(d,e)		
					
Average d (um)		7.2212	Average d (um)		5.232
Fluence (tracks/cm^2)		1.76E+04	Fluence (tracks/cm^2)		1.31E+04
Yield		4.96E+09	Yield		3.71E+09

Shot 64997

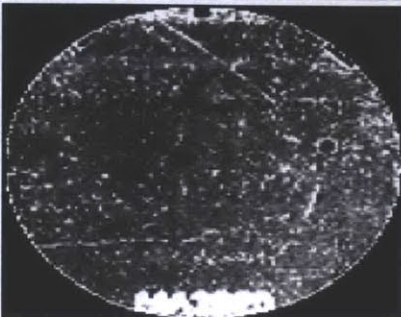
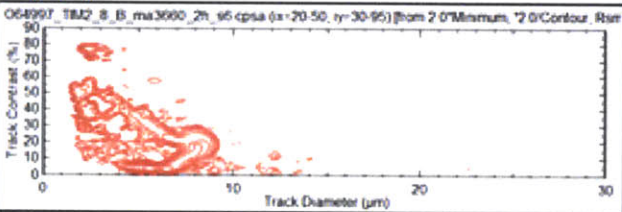
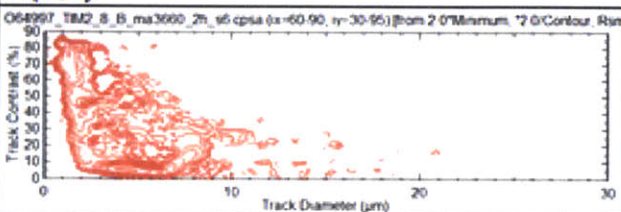
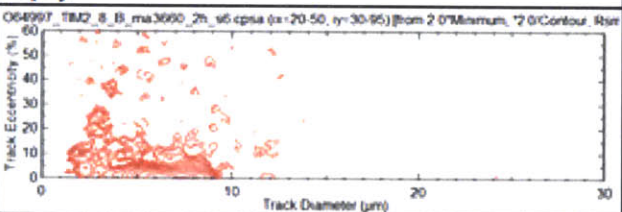
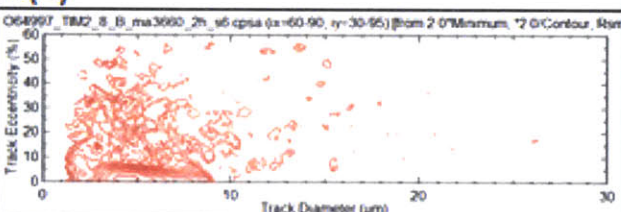
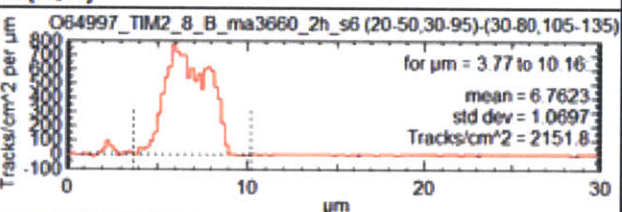
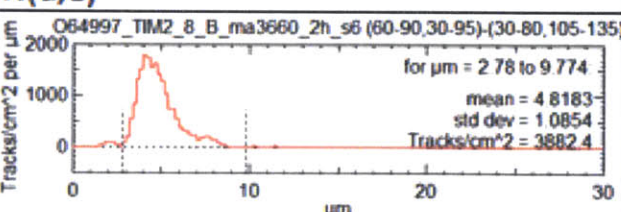
Tim 1, 4:00					
Shot	64997	Piece	ma3647	Type	Bert
Etch Time (hours)	6	Distance (cm)	150	Magnification	40x
<i>Step (um):</i>	50		<i>Step (um):</i>	25	
Limit c (%)	0 ≤ c ≤ 65		Limit c (%)	0 ≤ c ≤ 40	
Limit e (%)	0 ≤ e ≤ 10		Limit e (%)	0 ≤ e ≤ 9	
Limit Area	20 ≤ x ≤ 50 30 ≤ y ≤ 95		Limit Area	20 ≤ x ≤ 50 30 ≤ y ≤ 95	
Background	30 ≤ x ≤ 80 105 ≤ y ≤ 135		Background	30 ≤ x ≤ 80 105 ≤ y ≤ 135	
<b>N(d,c)</b>		<b>N(d,c)</b>			
					
<b>N(d)</b>		<b>N(d)</b>			
					
<b>N(d,e)</b>		<b>N(d,e)</b>			
					
<b>Average d (um)</b>	20.407	<b>Average d (um)</b>	17.198		
<b>Fluence (tracks/cm^2)</b>	3.21E+03	<b>Fluence (tracks/cm^2)</b>	5.90E+03		
<b>Yield</b>	9.06E+08	<b>Yield</b>	1.67E+09		

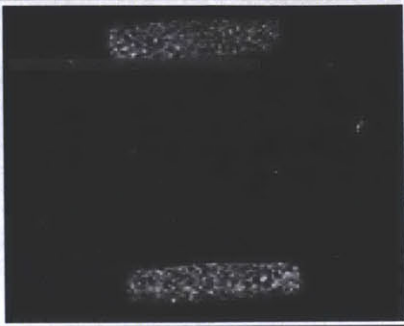
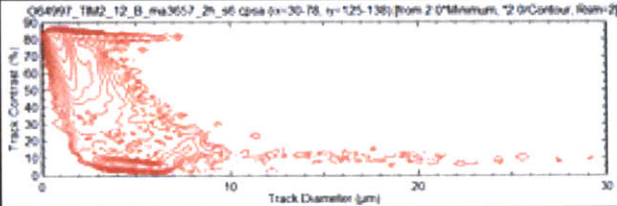
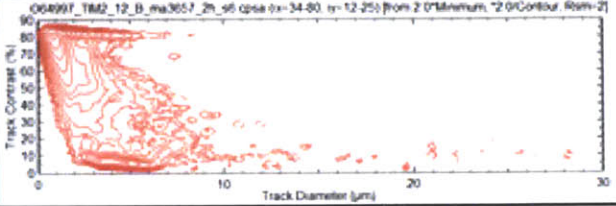
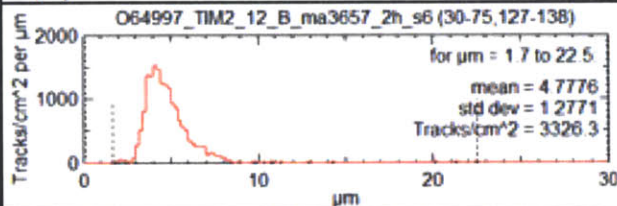
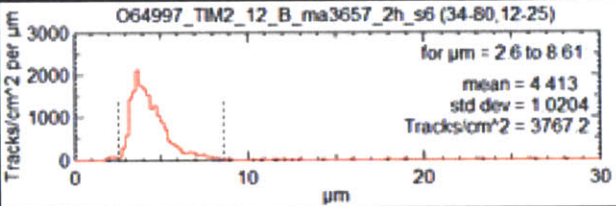
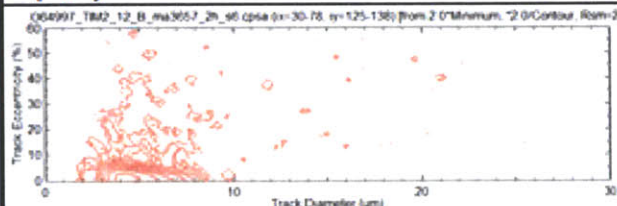
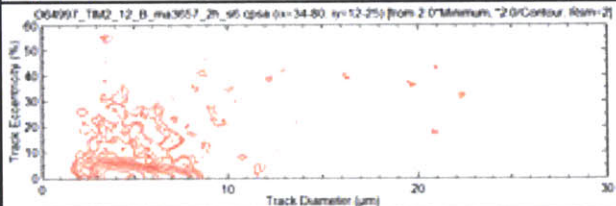
Tim 1, 8:00					
Shot	64997	Piece	ma3649	Type	Bert
Etch Time (hours)	2	Distance (cm)	150	Magnification	40x
Step (um):	50		Step (um):	25	
Limit c (%)	$0 \leq c \leq 50$		Limit c (%)	$0 \leq c \leq 27$	
Limit e (%)	$0 \leq e \leq 11$		Limit e (%)	$0 \leq e \leq 9$	
Limit Area	$20 \leq x \leq 50$ $30 \leq y \leq 95$		Limit Area	$20 \leq x \leq 50$ $30 \leq y \leq 95$	
Background	$30 \leq x \leq 80$ $105 \leq y \leq 135$		Background	$30 \leq x \leq 80$ $105 \leq y \leq 135$	
N(d,c)		N(d,c)			
					
N(d)		N(d)			
					
N(d,e)		N(d,e)			
					
Average d (um)	6.5612	Average d (um)	4.3819		
Fluence (tracks/cm^2)	3.03E+03	Fluence (tracks/cm^2)	5.94E+03		
Yield	8.58E+08	Yield	1.68E+09		

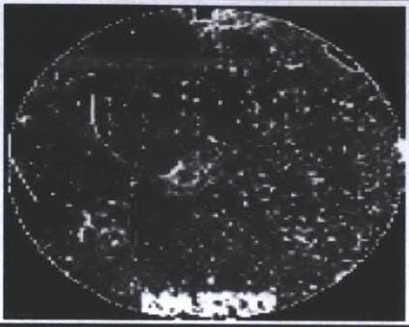
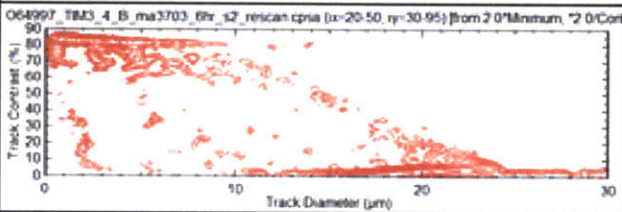
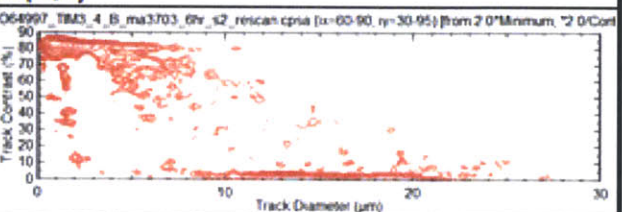
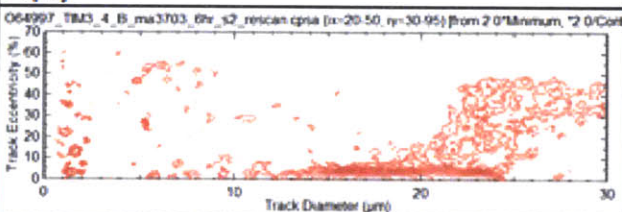
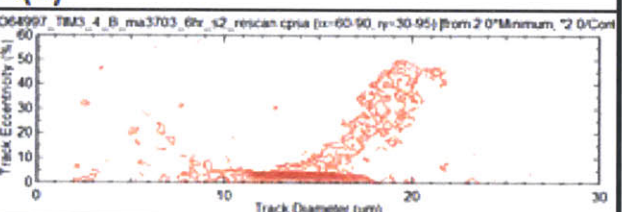
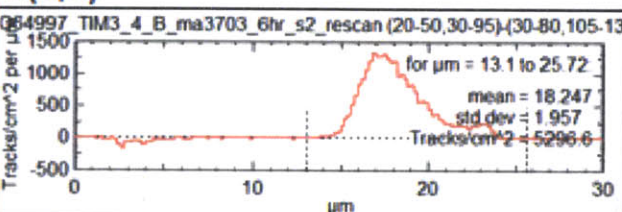
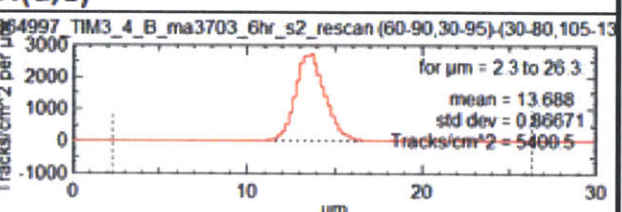
Tim 1, 12:00						
Shot	64993	Piece	ma3646	Type	WRF	
Etch Time (hours)	2	Distance (cm)	150	Magnification	40x	
D v. E Parameter (c)				Energy		
Limit c (%)				$0 \leq c \leq 30$	Sigma	
Limit e (%)				$0 \leq e \leq 12$		
Limit Area				$30 \leq x \leq 78$		
Top				$125 \leq y \leq 138$		
Limit Area	$30 \leq x \leq 78$					
Bottom	$12 \leq y \leq 25$					
N(d,c)			N(d,c)			
						
N(d)			N(d)			
						
N(d,e)			N(d,e)			
						
Average d (um)		4.8003	Average d (um)		4.5977	
Fluence (tracks/cm^2)		5.35E+03	Fluence (tracks/cm^2)		3.22E+03	
Yield		1.51E+09	Yield		9.10E+08	

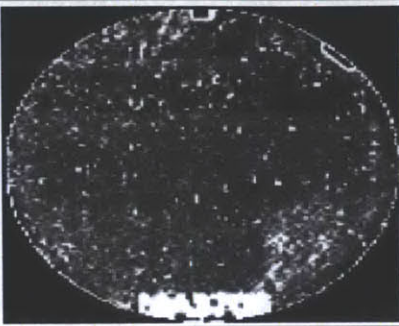
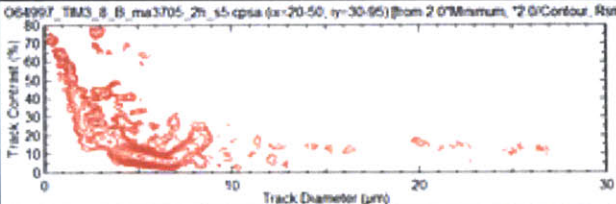
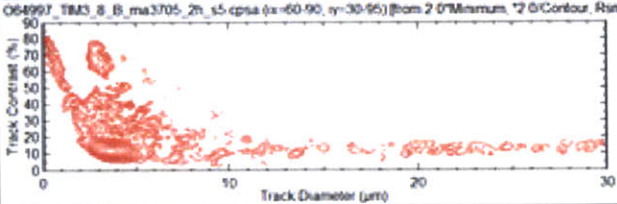
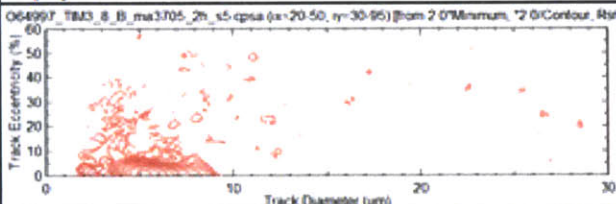
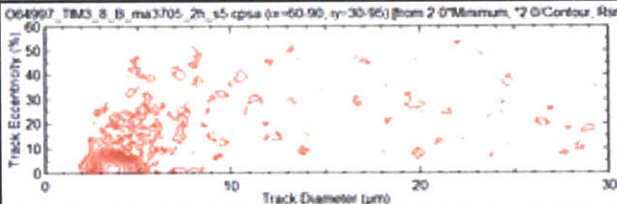
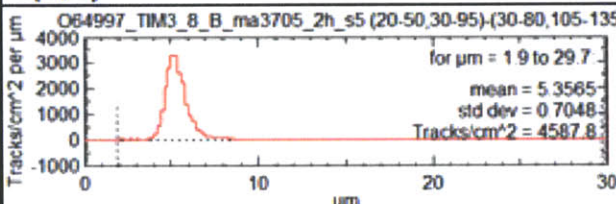
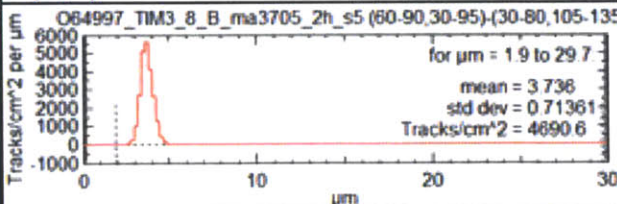
Tim 2, 4:00					
Shot	64997	Piece	ma3658	Type	Bert
Etch Time (hours)	6	Distance (cm)	150	Magnification	40x
<i>Step (um):</i>	50		<i>Step (um):</i>	25	
Limit c (%)	$0 \leq c \leq 60$		Limit c (%)	$0 \leq c \leq 70$	
Limit e (%)	$0 \leq e \leq 8$		Limit e (%)	$0 \leq e \leq 8$	
Limit Area	$20 \leq x \leq 50$ $30 \leq y \leq 95$		Limit Area	$20 \leq x \leq 50$ $30 \leq y \leq 95$	
Background	$30 \leq x \leq 80$ $105 \leq y \leq 135$		Background	$30 \leq x \leq 80$ $105 \leq y \leq 135$	
<b>N(d,c)</b>		<b>N(d,c)</b>			
					
<b>N(d)</b>		<b>N(d)</b>			
					
<b>N(d,e)</b>		<b>N(d,e)</b>			
					
Average d (um)		19.598	Average d (um)		16.335
Fluence (tracks/cm^2)		2.33E+03	Fluence (tracks/cm^2)		5.82E+03
Yield		6.58E+08	Yield		1.64E+09



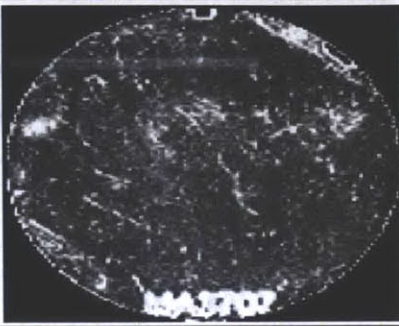
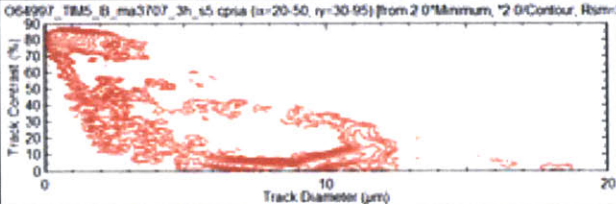
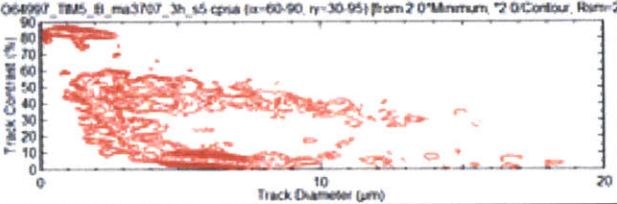
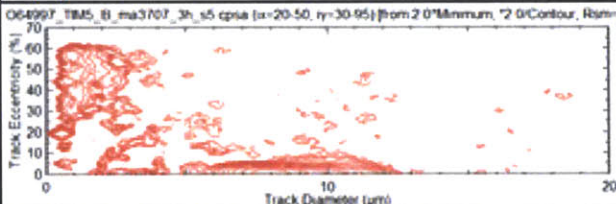
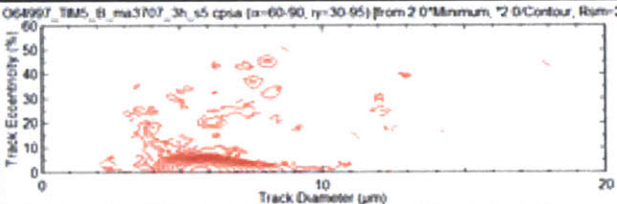
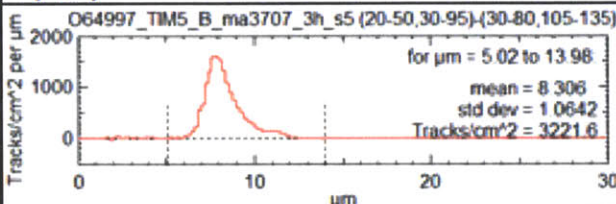
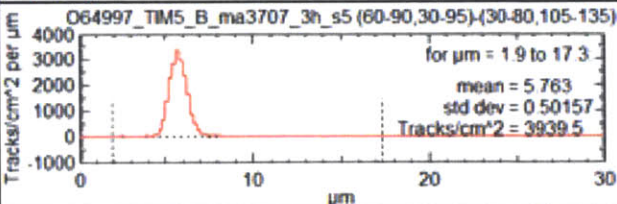
Tim 2, 8:00					
Shot	64997	Piece	ma3660	Type	Bert
Etch Time (hours)	2	Distance (cm)	150	Magnification	40x
<b>Step (um):</b>	50		<b>Step (um):</b>	25	
<b>Limit c (%)</b>	$0 \leq c \leq 41$		<b>Limit c (%)</b>	$0 \leq c \leq 30$	
<b>Limit e (%)</b>	$0 \leq e \leq 10$		<b>Limit e (%)</b>	$0 \leq e \leq 9$	
<b>Limit Area</b>	$20 \leq x \leq 50$ $30 \leq y \leq 95$		<b>Limit Area</b>	$20 \leq x \leq 50$ $30 \leq y \leq 95$	
<b>Background</b>	$30 \leq x \leq 80$ $105 \leq y \leq 135$		<b>Background</b>	$30 \leq x \leq 80$ $105 \leq y \leq 135$	
<b>N(d,c)</b>			<b>N(d,c)</b>		
					
<b>N(d)</b>		<b>N(d)</b>			
					
<b>N(d,e)</b>		<b>N(d,e)</b>			
					
<b>Average d (um)</b>	6.7623	<b>Average d (um)</b>	4.8183		
<b>Fluence (tracks/cm^2)</b>	2.15E+03	<b>Fluence (tracks/cm^2)</b>	3.88E+03		
<b>Yield</b>	6.08E+08	<b>Yield</b>	1.10E+09		

Tim 2, 12:00						
Shot	64993	Piece	ma3657	Type	WRF	
Etch Time (hours)	2	Distance (cm)	150	Magnification	40x	
D v. E Parameter (c)				Energy		
Limit c (%)				$0 \leq c \leq 16$	Sigma	
Limit e (%)				$0 \leq e \leq 11$		
Limit Area				$30 \leq x \leq 78$		
Top				$125 \leq y \leq 138$		
Limit Area				$30 \leq x \leq 78$		
Bottom	$12 \leq y \leq 25$					
N(d,c)						
N(d)						
N(d,e)						
Average d (µm)	4.7776		Average d (µm)	4.413		
Fluence (tracks/cm <sup>2</sup> )	3.33E+03		Fluence (tracks/cm <sup>2</sup> )	3.77E+03		
Yield	9.40E+08		Yield	1.07E+09		

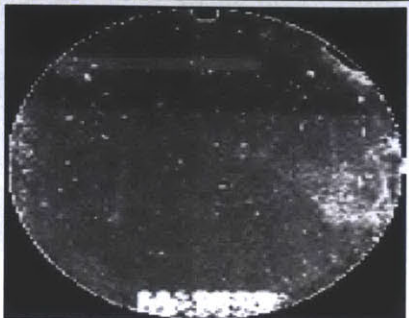
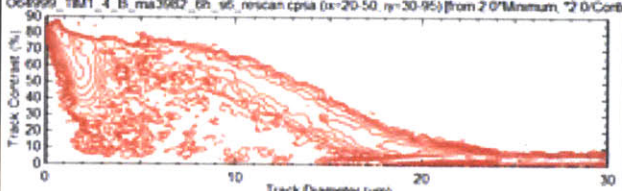
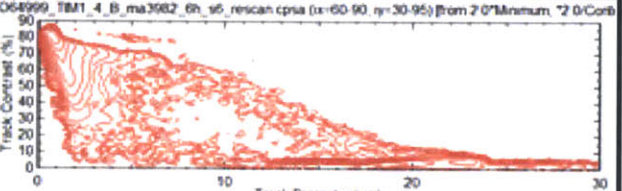
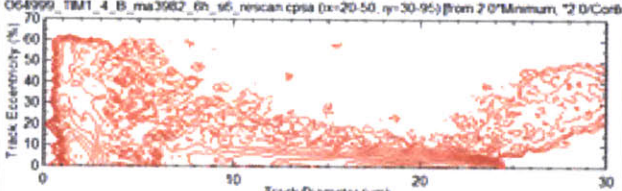
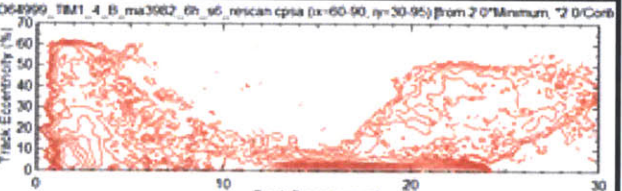
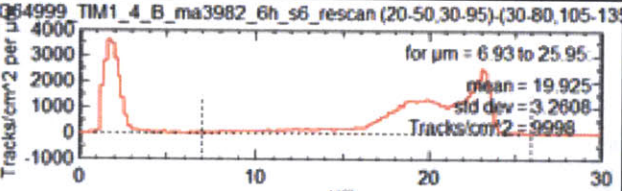
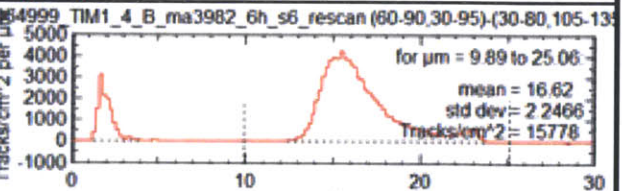
Tim 3, 4:00					
Shot	64997	Piece	ma3703	Type	Bert
Etch Time (hours)	6	Distance (cm)	150	Magnification	40x
<b>Step (um):</b>	50		<b>Step (um):</b>	25	
<b>Limit c (%)</b>	$0 \leq c \leq 55$		<b>Limit c (%)</b>	$0 \leq c \leq 7$	
<b>Limit e (%)</b>	$0 \leq e \leq 9$		<b>Limit e (%)</b>	$0 \leq e \leq 7$	
<b>Limit Area</b>	$20 \leq x \leq 50$ $30 \leq y \leq 95$		<b>Limit Area</b>	$20 \leq x \leq 50$ $30 \leq y \leq 95$	
<b>Background</b>	$30 \leq x \leq 80$ $105 \leq y \leq 135$		<b>Background</b>	$30 \leq x \leq 80$ $105 \leq y \leq 135$	
<b>N(d,c)</b>					
<b>N(d)</b>					
<b>N(d,e)</b>					
<b>Average d (um)</b>	18.247		<b>Average d (um)</b>		13.688
<b>Fluence (tracks/cm^2)</b>	5.30E+03		<b>Fluence (tracks/cm^2)</b>		5.40E+03
<b>Yield</b>	1.50E+09		<b>Yield</b>		1.53E+09

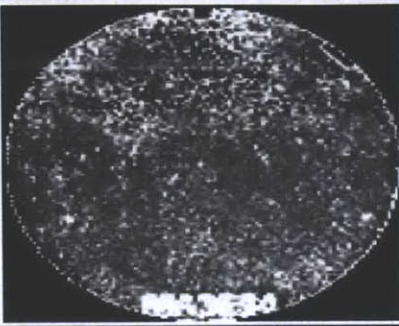
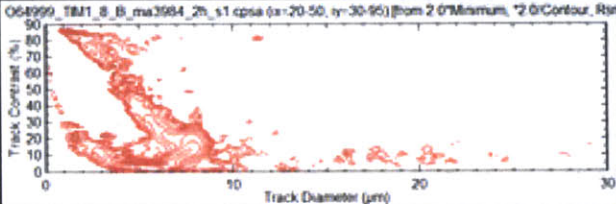
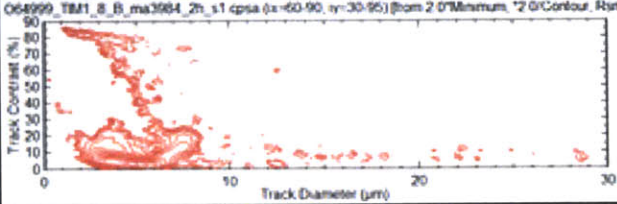
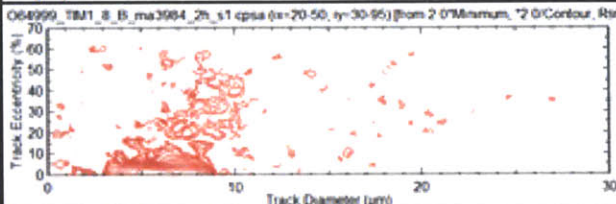
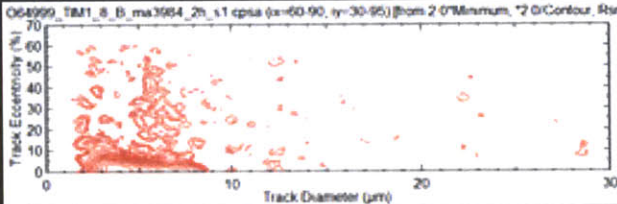
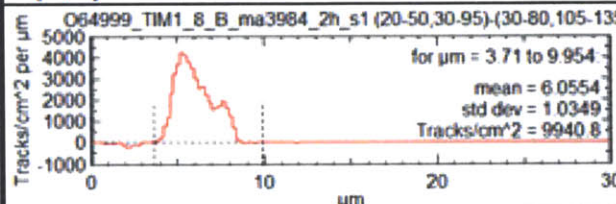
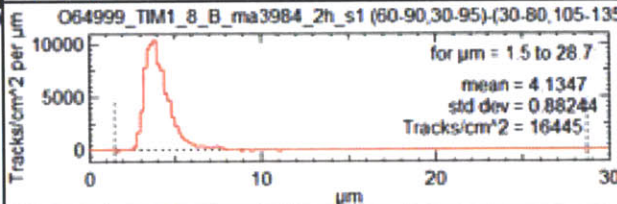
Tim 3, 8:00						
Shot	64997	Piece	ma3705	Type	Bert	
Etch Time (hours)	2	Distance (cm)	150	Magnification	40x	
<b>Step (um):</b>	50		<b>Step (um):</b>	25		
<b>Limit c (%)</b>	$0 \leq c \leq 25$		<b>Limit c (%)</b>	$0 \leq c \leq 21$		
<b>Limit e (%)</b>	$0 \leq e \leq 9$		<b>Limit e (%)</b>	$0 \leq e \leq 11$		
<b>Limit Area</b>	$20 \leq x \leq 50$ $30 \leq y \leq 95$		<b>Limit Area</b>	$20 \leq x \leq 50$ $30 \leq y \leq 95$		
<b>Background</b>	$30 \leq x \leq 80$ $105 \leq y \leq 135$		<b>Background</b>	$30 \leq x \leq 80$ $105 \leq y \leq 135$		
<b>N(d,c)</b>			<b>N(d,c)</b>			
<b>N(d)</b>			<b>N(d)</b>			
<b>N(d,e)</b>	 for $\mu\text{m} = 1.9$ to $29.7$ mean = 5.3565 std dev = 0.7048 Tracks/cm <sup>2</sup> = 4587.8		<b>N(d,e)</b>		 for $\mu\text{m} = 1.9$ to $29.7$ mean = 3.736 std dev = 0.71361 Tracks/cm <sup>2</sup> = 4690.6	
<b>Average d (um)</b>	5.3565		<b>Average d (um)</b>		3.736	
<b>Fluence (tracks/cm<sup>2</sup>)</b>	4.59E+03		<b>Fluence (tracks/cm<sup>2</sup>)</b>		4.69E+03	
<b>Yield</b>	1.30E+09		<b>Yield</b>		1.33E+09	

Tim 3, 12:00						
Shot	64993	Piece	ma3702	Type	WRF	
Etch Time (hours)	2	Distance (cm)	150	Magnification	40x	
D v. E Parameter (c)				Energy		
Limit c (%)				$0 \leq c \leq 18$	Sigma	
Limit e (%)				$0 \leq e \leq 15$		
Limit Area				$30 \leq x \leq 78$		
Top				$125 \leq y \leq 138$		
Limit Area				$30 \leq x \leq 78$		
Bottom	$12 \leq y \leq 25$					
N(d,c)			N(d,c)			
N(d)			N(d)			
<p>for <math>\mu\text{m} = 1.9</math> to <math>16.1</math>  mean = 3.7826  std dev = 0.54971  Tracks/cm<sup>2</sup> = 6298.3</p>			<p>for <math>\mu\text{m} = 1.5</math> to <math>25.7</math>  mean = 3.5828  std dev = 0.80088  Tracks/cm<sup>2</sup> = 4346.3</p>			
N(d,e)			N(d,e)			
Average d (um)		3.7826	Average d (um)		3.5828	
Fluence (tracks/cm^2)		6.30E+03	Fluence (tracks/cm^2)		4.35E+03	
Yield		1.78E+09	Yield		1.23E+09	

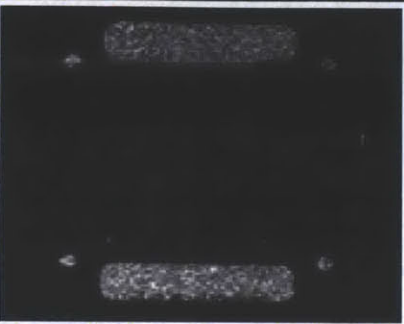
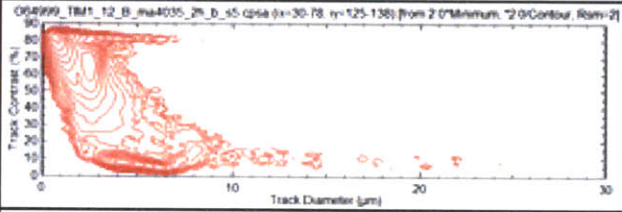
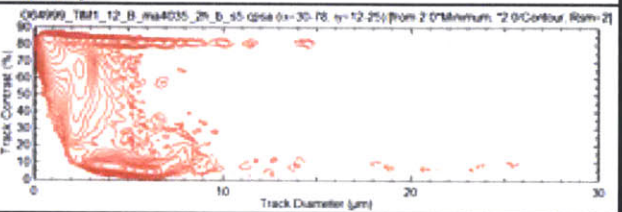
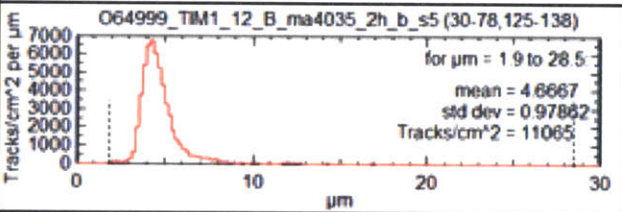
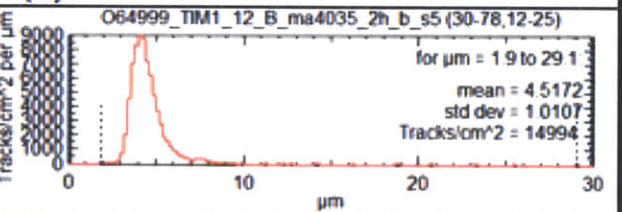
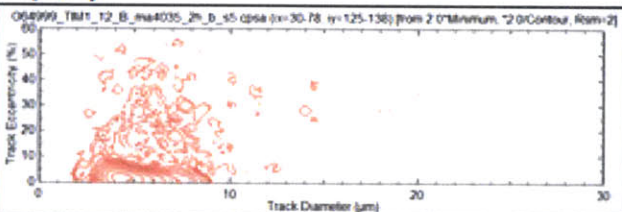
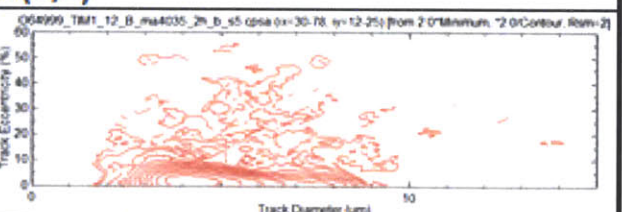
TIM 5					
Shot	64997	Piece	ma3707	Type	Bert
Etch Time (hours)	3	Distance (cm)	150	Magnification	40x
<b>Step (um):</b>	50		<b>Step (um):</b>	25	
<b>Limit c (%)</b>	$0 \leq c \leq 35$		<b>Limit c (%)</b>	$0 \leq c \leq 13$	
<b>Limit e (%)</b>	$0 \leq e \leq 11$		<b>Limit e (%)</b>	$0 \leq e \leq 9$	
<b>Limit Area</b>	$20 \leq x \leq 50$ $30 \leq y \leq 95$		<b>Limit Area</b>	$60 \leq x \leq 90$ $30 \leq y \leq 95$	
<b>Background</b>	$30 \leq x \leq 80$ $105 \leq y \leq 135$		<b>Background</b>	$30 \leq x \leq 80$ $105 \leq y \leq 135$	
<b>N(d,c)</b>			<b>N(d,c)</b>		
					
<b>N(d)</b>		<b>N(d)</b>			
					
<b>N(d,e)</b>		<b>N(d,e)</b>			
					
<b>Average d (um)</b>		8.306	<b>Average d (um)</b>		5.763
<b>Fluence (tracks/cm^2)</b>		3.22E+03	<b>Fluence (tracks/cm^2)</b>		3.94E+03
<b>Yield</b>		9.11E+08	<b>Yield</b>		1.11E+09

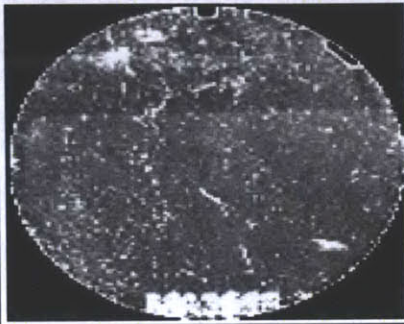
Shot 64999

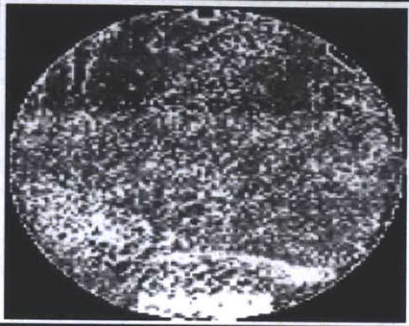
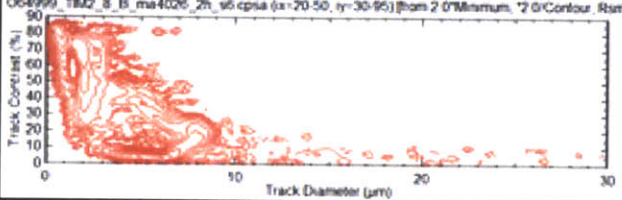
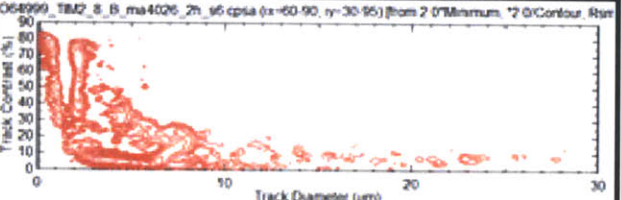
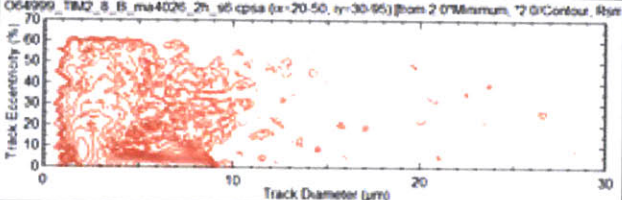
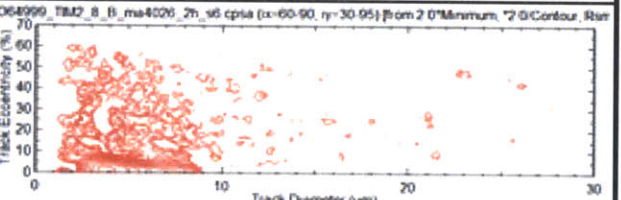
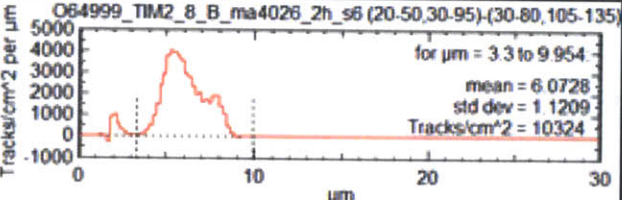
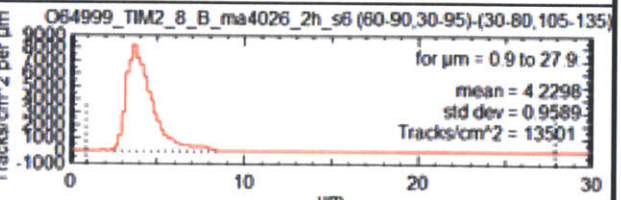
Tim 1, 4:00					
Shot	64999	Piece	ma3982	Type	Bert
Etch Time (hours)	6	Distance (cm)	150	Magnification	40x
<b>Step (um):</b>	50		<b>Step (um):</b>	25	
<b>Limit c (%)</b>	0 ≤ c ≤ 70		<b>Limit c (%)</b>	0 ≤ c ≤ 60	
<b>Limit e (%)</b>	0 ≤ e ≤ 12		<b>Limit e (%)</b>	0 ≤ e ≤ 8	
<b>Limit Area</b>	20 ≤ x ≤ 50 30 ≤ y ≤ 95		<b>Limit Area</b>	20 ≤ x ≤ 50 30 ≤ y ≤ 95	
<b>Background</b>	30 ≤ x ≤ 80 105 ≤ y ≤ 135		<b>Background</b>	30 ≤ x ≤ 80 105 ≤ y ≤ 135	
<b>N(d,c)</b>		<b>N(d,c)</b>			
					
<b>N(d)</b>		<b>N(d)</b>			
					
<b>N(d,e)</b>		<b>N(d,e)</b>			
					
<b>Average d (um)</b>	19.925	<b>Average d (um)</b>	16.62		
<b>Fluence (tracks/cm^2)</b>	1.00E+04	<b>Fluence (tracks/cm^2)</b>	1.58E+04		
<b>Yield</b>	2.83E+09	<b>Yield</b>	4.46E+09		

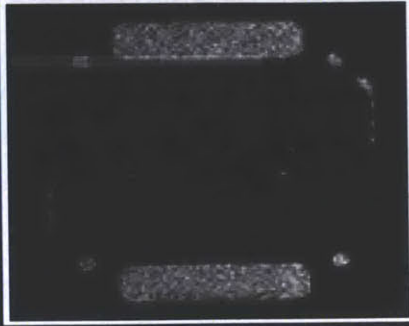
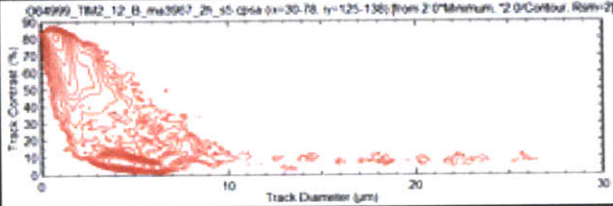
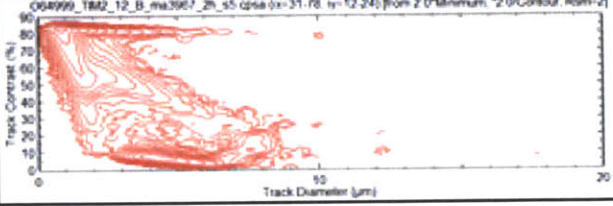
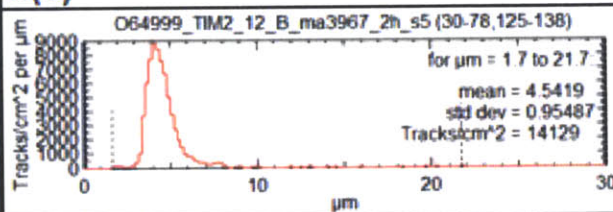
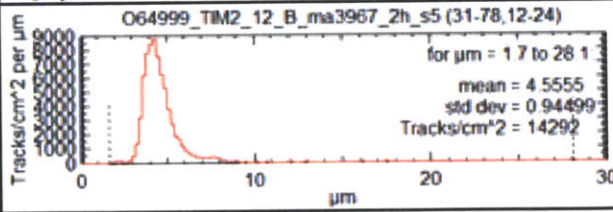
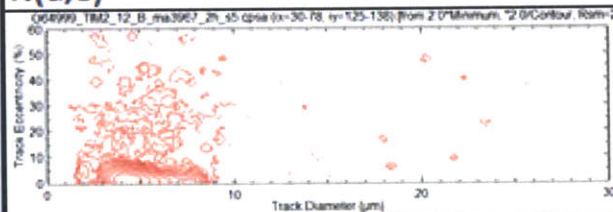
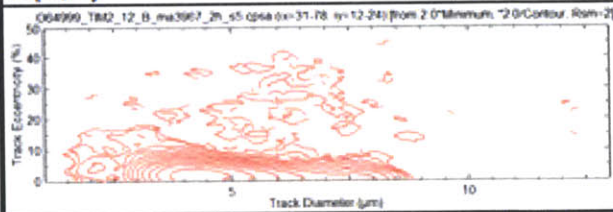
Tim 1, 8:00					
Shot	64999	Piece	ma3984	Type	Bert
Etch Time (hours)	2	Distance (cm)	150	Magnification	40x
<b>Step (um):</b>	50		<b>Step (um):</b>	25	
<b>Limit c (%)</b>	$0 \leq c \leq 50$		<b>Limit c (%)</b>	$0 \leq c \leq 26$	
<b>Limit e (%)</b>	$0 \leq e \leq 14$		<b>Limit e (%)</b>	$0 \leq e \leq 10$	
<b>Limit Area</b>	$20 \leq x \leq 50$ $30 \leq y \leq 95$		<b>Limit Area</b>	$20 \leq x \leq 50$ $30 \leq y \leq 95$	
<b>Background</b>	$30 \leq x \leq 80$ $105 \leq y \leq 135$		<b>Background</b>	$30 \leq x \leq 80$ $105 \leq y \leq 135$	
<b>N(d,c)</b>			<b>N(d,c)</b>		
					
<b>N(d)</b>		<b>N(d)</b>			
					
<b>N(d,e)</b>		<b>N(d,e)</b>			
					
<b>Average d (um)</b>	6.0554	<b>Average d (um)</b>	4.1347		
<b>Fluence (tracks/cm^2)</b>	9.94E+03	<b>Fluence (tracks/cm^2)</b>	1.64E+04		
<b>Yield</b>	2.81E+09	<b>Yield</b>	4.65E+09		

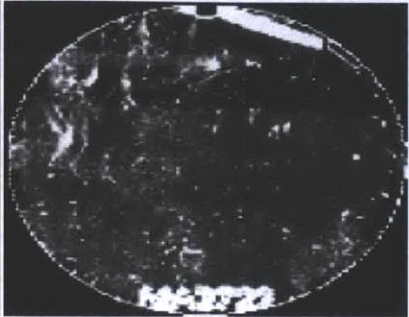
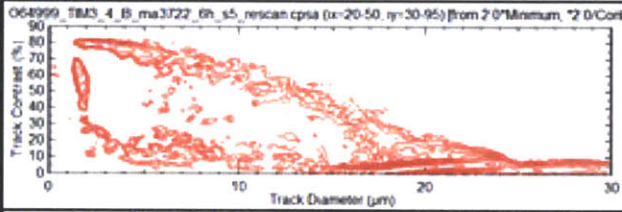
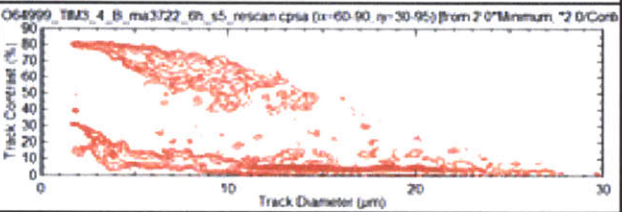
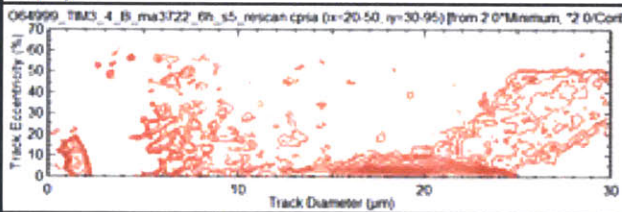
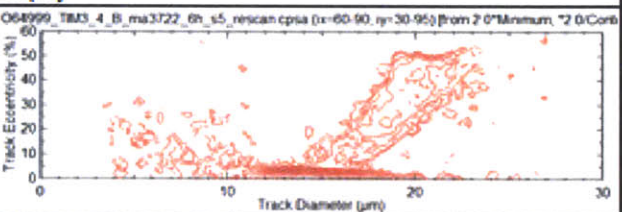
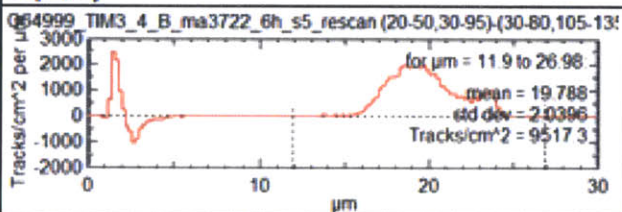
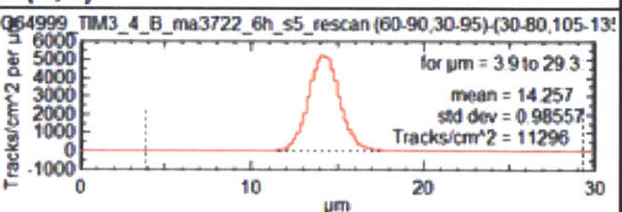


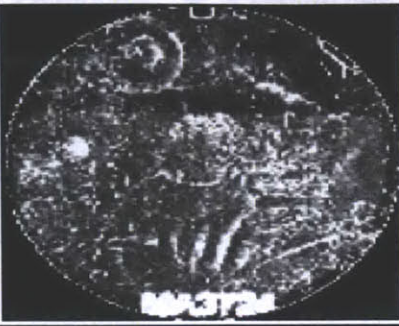
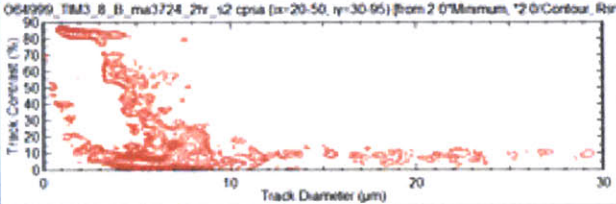
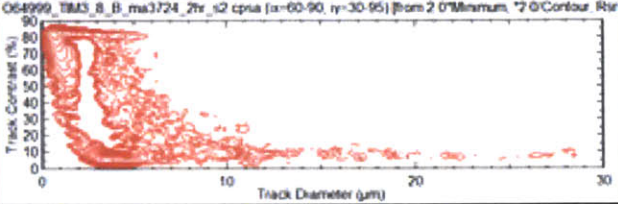
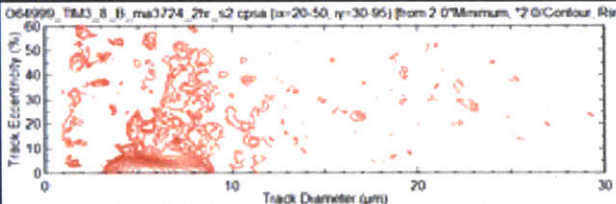
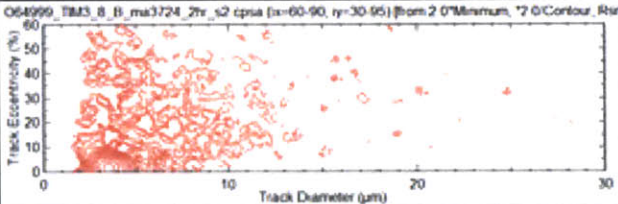
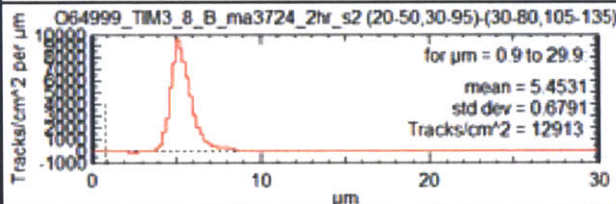
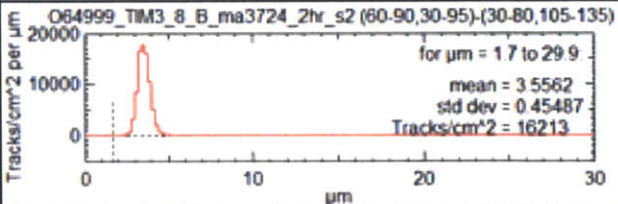
Tim 1, 12:00					
Shot	64999	Piece		Type	WRF
Etch Time (hours)	2	Distance (cm)	150	Magnification	40x
D v. E Parameter (c)				Energy	
Limit c (%)	$0 \leq c \leq 17$			Sigma	
Limit e (%)	$0 \leq e \leq 12$				
Limit Area	$30 \leq x \leq 78$				
Top	$125 \leq y \leq 138$				
Limit Area	$30 \leq x \leq 78$				
Bottom	$12 \leq y \leq 25$				
<b>N(d,c)</b>		<b>N(d,c)</b>			
					
<b>N(d)</b>		<b>N(d)</b>			
					
<b>N(d,e)</b>		<b>N(d,e)</b>			
					
Average d (um)		4.6667	Average d (um)		4.5172
Fluence (tracks/cm^2)		1.11E+04	Fluence (tracks/cm^2)		1.50E+04
Yield		3.13E+09	Yield		4.24E+09

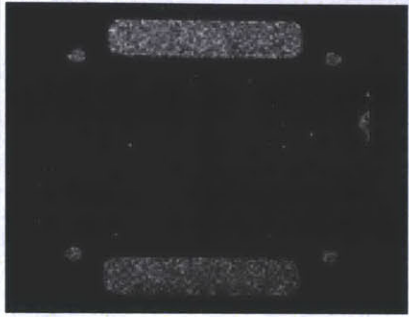
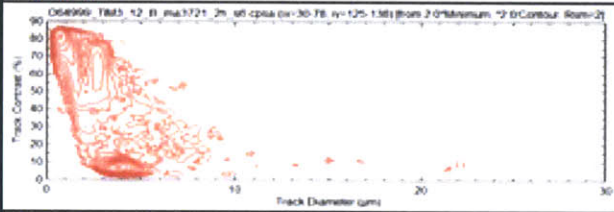
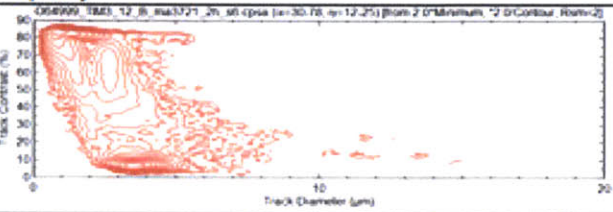
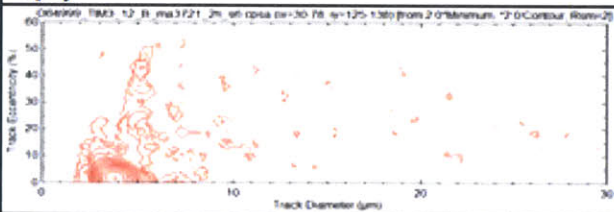
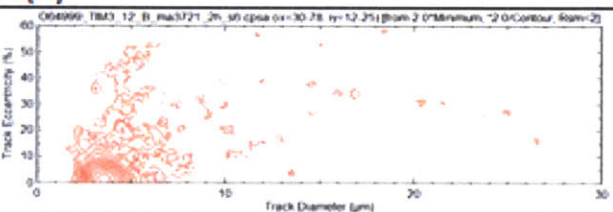
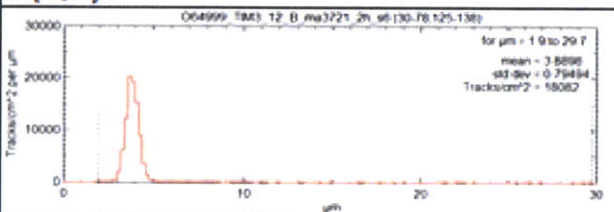
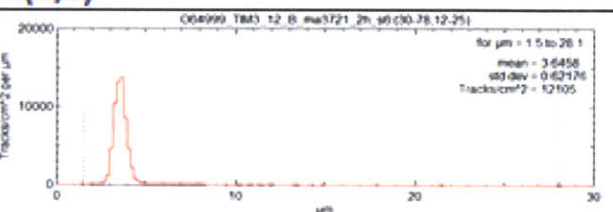
Tim 2, 4:00					
Shot	64999	Piece	ma3968	Type	Bert
Etch Time (hours)	6	Distance (cm)	150	Magnification	40x
<b>Step (um):</b>	50		<b>Step (um):</b>	25	
<b>Limit c (%)</b>	$0 \leq c \leq 72$		<b>Limit c (%)</b>	$0 \leq c \leq 70$	
<b>Limit e (%)</b>	$0 \leq e \leq 10$		<b>Limit e (%)</b>	$0 \leq e \leq 8$	
<b>Limit Area</b>	$20 \leq x \leq 50$ $30 \leq y \leq 95$		<b>Limit Area</b>	$20 \leq x \leq 50$ $30 \leq y \leq 95$	
<b>Background</b>	$30 \leq x \leq 80$ $105 \leq y \leq 135$		<b>Background</b>	$30 \leq x \leq 80$ $105 \leq y \leq 135$	
<b>N(d,c)</b>			<b>N(d,c)</b>		
<b>N(d)</b>		<b>N(d)</b>			
<b>N(d,e)</b>		<b>N(d,e)</b>			
<b>Average d (um)</b>		20.228	<b>Average d (um)</b>		16.659
<b>Fluence (tracks/cm^2)</b>		9.72E+03	<b>Fluence (tracks/cm^2)</b>		1.62E+04
<b>Yield</b>		2.75E+09	<b>Yield</b>		4.57E+09

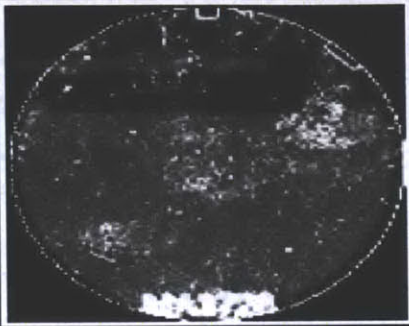
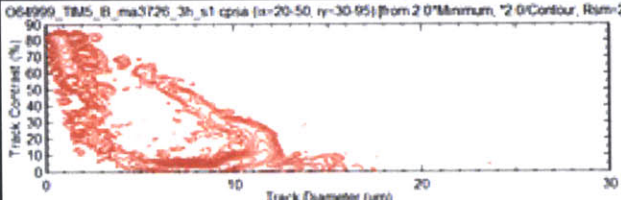
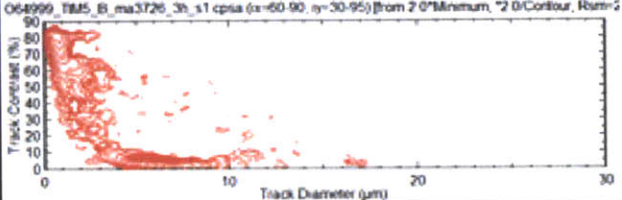
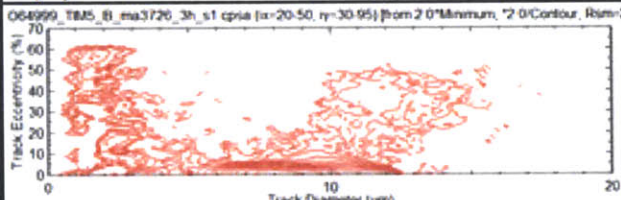
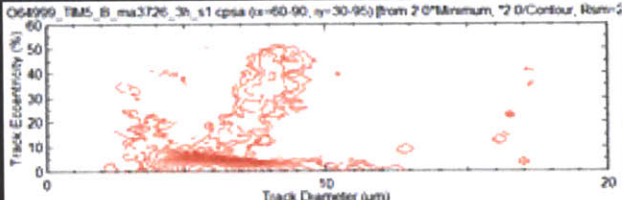
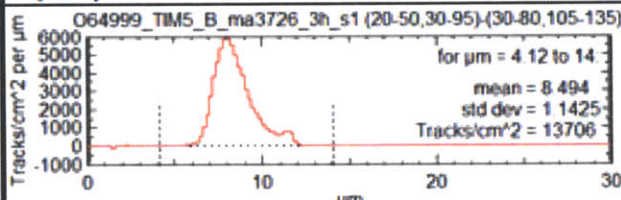
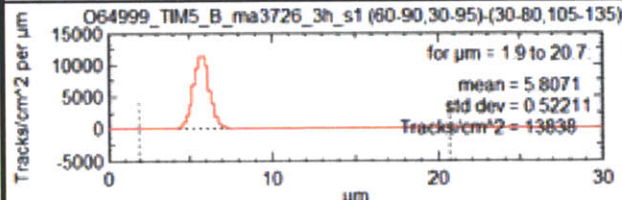
Tim 2, 8:00					
Shot	64999	Piece	ma4026	Type	Bert
Etch Time (hours)	2	Distance (cm)	150	Magnification	40x
Step (um):	50		Step (um):	25	
Limit c (%)	$0 \leq c \leq 45$		Limit c (%)	$0 \leq c \leq 30$	
Limit e (%)	$0 \leq e \leq 12$		Limit e (%)	$0 \leq e \leq 10$	
Limit Area	$20 \leq x \leq 50$ $30 \leq y \leq 95$		Limit Area	$20 \leq x \leq 50$ $30 \leq y \leq 95$	
Background	$30 \leq x \leq 80$ $105 \leq y \leq 135$		Background	$30 \leq x \leq 80$ $105 \leq y \leq 135$	
<b>N(d,c)</b>			<b>N(d,c)</b>		
					
<b>N(d)</b>		<b>N(d)</b>			
					
<b>N(d,e)</b>		<b>N(d,e)</b>			
					
Average d (um)	6.0728	Average d (um)	4.2298		
Fluence (tracks/cm^2)	1.03E+04	Fluence (tracks/cm^2)	1.35E+04		
Yield	2.92E+09	Yield	3.82E+09		

Tim 2, 12:00					
Shot	64999	Piece	ma3967	Type	WRF
Etch Time (hours)	2	Distance (cm)	150	Magnification	40x
D v. E Parameter (c)				Energy	
Limit c (%)	$0 \leq c \leq 24$			Sigma	
Limit e (%)	$0 \leq e \leq 12$				
Limit Area	$30 \leq x \leq 78$				
Top	$125 \leq y \leq 138$				
Limit Area	$30 \leq x \leq 78$				
Bottom	$12 \leq y \leq 25$				
N(d,c)		N(d,c)			
					
N(d)		N(d)			
					
N(d,e)		N(d,e)			
					
Average d (um)		4.5419	Average d (um)		4.5555
Fluence (tracks/cm^2)		1.41E+04	Fluence (tracks/cm^2)		1.43E+04
Yield		3.99E+09	Yield		4.04E+09

Tim 3, 4:00					
Shot	64999	Piece	ma3722	Type	Bert
Etch Time (hours)	6	Distance (cm)	150	Magnification	40x
Step (um):	50		Step (um):	25	
Limit c (%)	$0 \leq c \leq 70$		Limit c (%)	$0 \leq c \leq 9$	
Limit e (%)	$0 \leq e \leq 11$		Limit e (%)	$0 \leq e \leq 7$	
Limit Area	$20 \leq x \leq 50$ $30 \leq y \leq 95$		Limit Area	$20 \leq x \leq 50$ $30 \leq y \leq 95$	
Background	$30 \leq x \leq 80$ $105 \leq y \leq 135$		Background	$30 \leq x \leq 80$ $105 \leq y \leq 135$	
<b>N(d,c)</b>			<b>N(d,c)</b>		
					
<b>N(d)</b>		<b>N(d)</b>			
					
<b>N(d,e)</b>		<b>N(d,e)</b>			
					
Average d (um)	19.788	Average d (um)	14.257		
Fluence (tracks/cm^2)	9.52E+03	Fluence (tracks/cm^2)	1.13E+04		
Yield	2.69E+09	Yield	3.19E+09		

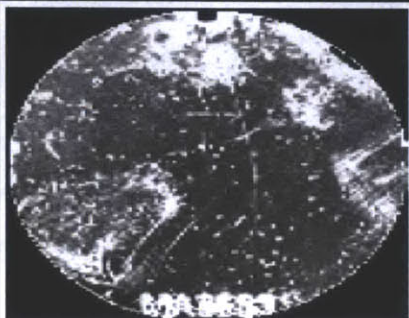
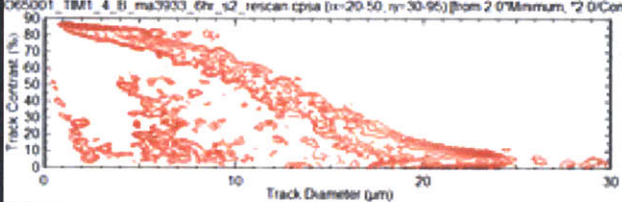
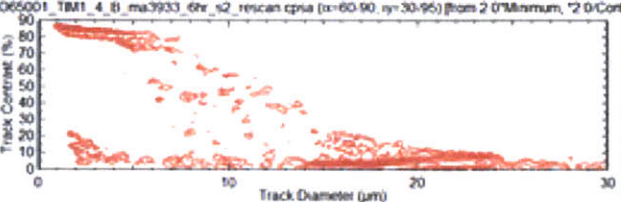
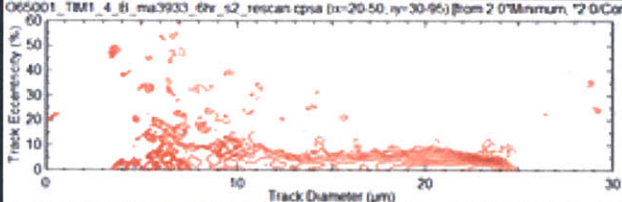
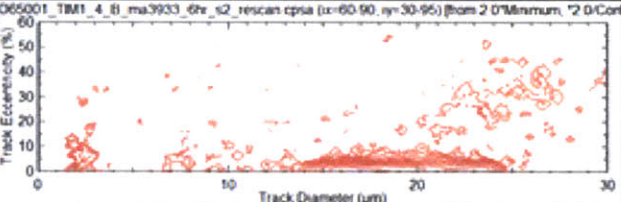
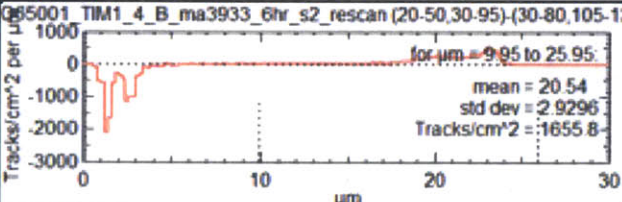
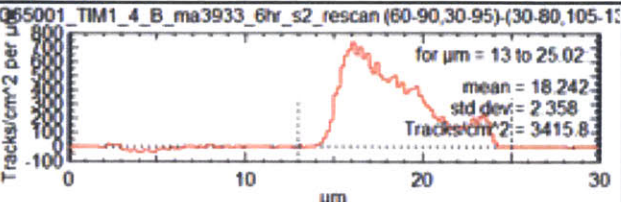
Tim 3, 8:00					
Shot	64999	Piece	ma3724	Type	Bert
Etch Time (hours)	2	Distance (cm)	150	Magnification	40x
<b>Step (um):</b>	50		<b>Step (um):</b>	25	
Limit c (%)	$0 \leq c \leq 37$		Limit c (%)	$0 \leq c \leq 18$	
Limit e (%)	$0 \leq e \leq 9$		Limit e (%)	$0 \leq e \leq 11$	
Limit Area	$20 \leq x \leq 50$ $30 \leq y \leq 95$		Limit Area	$20 \leq x \leq 50$ $30 \leq y \leq 95$	
Background	$30 \leq x \leq 80$ $105 \leq y \leq 135$		Background	$30 \leq x \leq 80$ $105 \leq y \leq 135$	
<b>N(d,c)</b>					
<b>N(d)</b>					
<b>N(d,e)</b>					
<b>Average d (um)</b>	5.4531		<b>Average d (um)</b>		3.5562
<b>Fluence (tracks/cm^2)</b>	1.29E+04		<b>Fluence (tracks/cm^2)</b>		1.62E+04
<b>Yield</b>	3.65E+09		<b>Yield</b>		4.58E+09

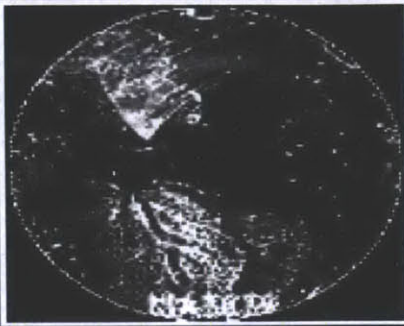
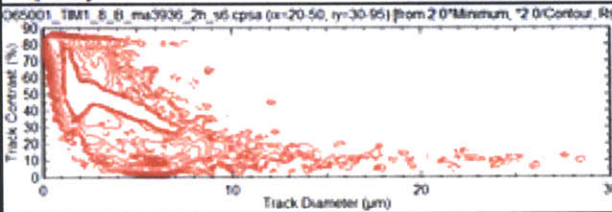
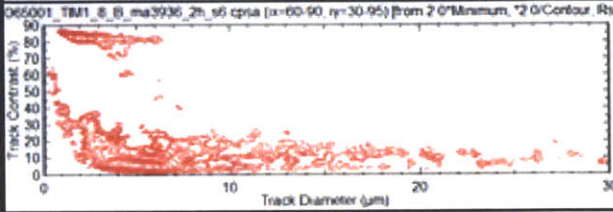
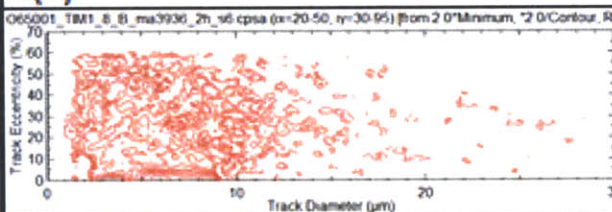
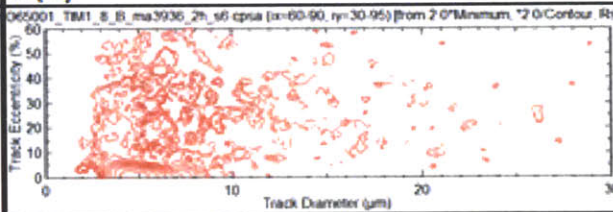
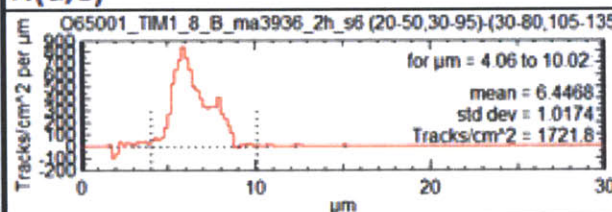
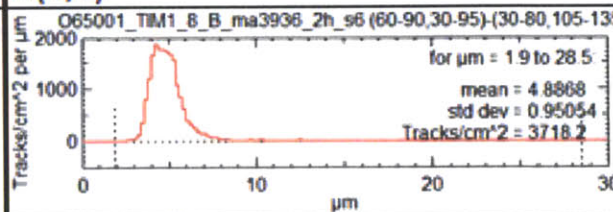
Tim 3, 12:00						
Shot	64999	Piece		Type	WRF	
Etch Time (hours)	2	Distance (cm)	150	Magnification	40x	
D v. E Parameter (c)				Energy		
Limit c (%)				$0 \leq c \leq 17$	Sigma	
Limit e (%)				$0 \leq e \leq 14$		
Limit Area				$30 \leq x \leq 78$		
Top				$125 \leq y \leq 138$		
Limit Area				$30 \leq x \leq 78$		
Bottom	$12 \leq y \leq 25$					
N(d,c)			N(d,c)			
						
N(d)			N(d)			
						
N(d,e)			N(d,e)			
						
Average d (um)	3.8898	Average d (um)	3.6458			
Fluence (tracks/cm^2)	1.81E+04	Fluence (tracks/cm^2)	1.21E+04			
Yield	5.11E+09	Yield	3.42E+09			

TIM 5					
Shot	64999	Piece	ma3726	Type	Bert
Etch Time (hours)	3	Distance (cm)	150	Magnification	40x
Step (um):	50		Step (um):	25	
Limit c (%)	$0 \leq c \leq 60$		Limit c (%)	$0 \leq c \leq 13$	
Limit e (%)	$0 \leq e \leq 10$		Limit e (%)	$0 \leq e \leq 10$	
Limit Area	$20 \leq x \leq 50$ $30 \leq y \leq 95$		Limit Area	$60 \leq x \leq 90$ $30 \leq y \leq 95$	
Background	$30 \leq x \leq 80$ $105 \leq y \leq 135$		Background	$30 \leq x \leq 80$ $105 \leq y \leq 135$	
N(d,c)		N(d,c)			
					
N(d)		N(d)			
					
N(d,e)		N(d,e)			
					
Average d (um)	8.494	Average d (um)	5.8071		
Fluence (tracks/cm^2)	1.37E+04	Fluence (tracks/cm^2)	1.38E+04		
Yield	3.88E+09	Yield	3.91E+09		

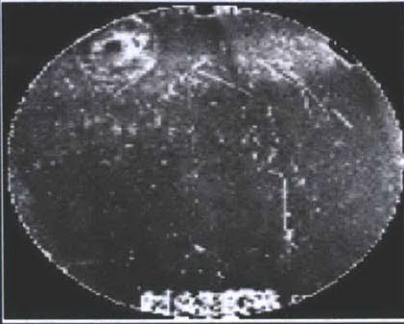


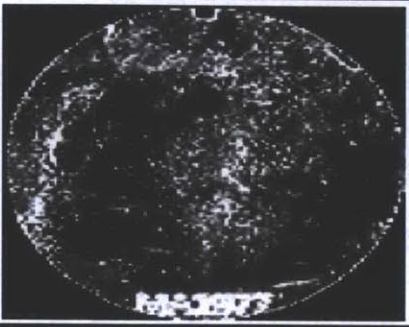
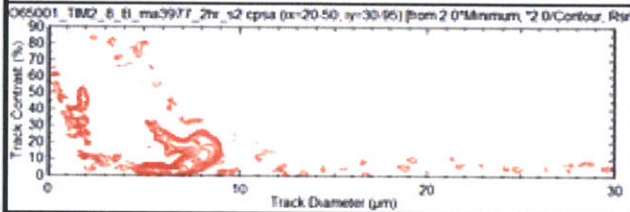
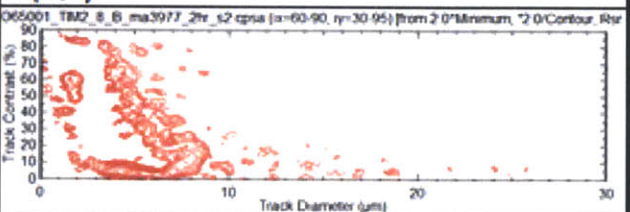
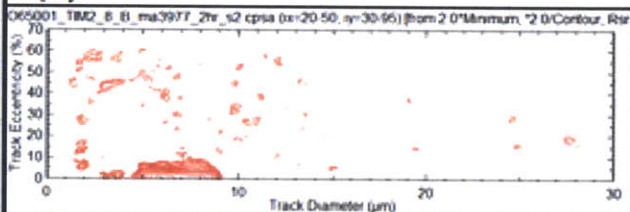
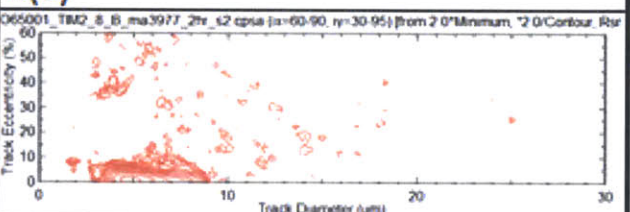
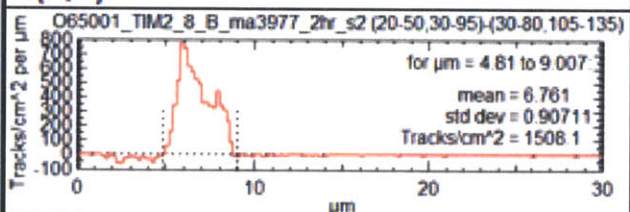
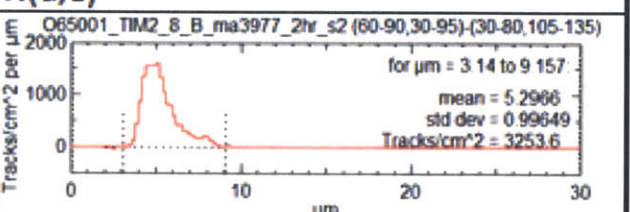
Shot 65001


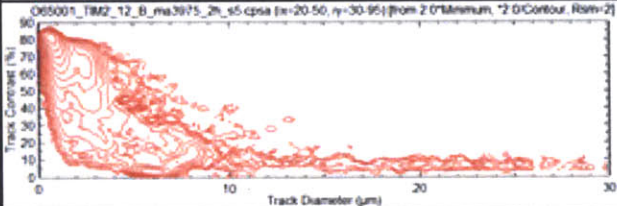
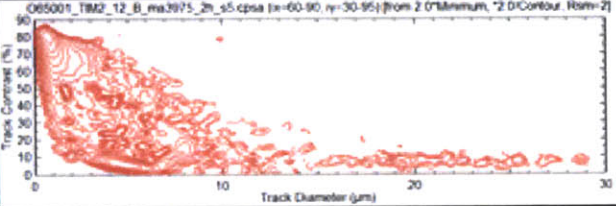
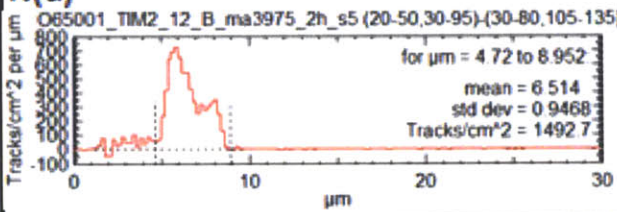
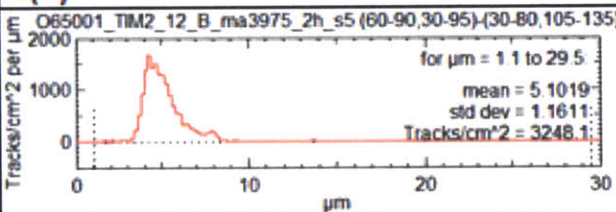
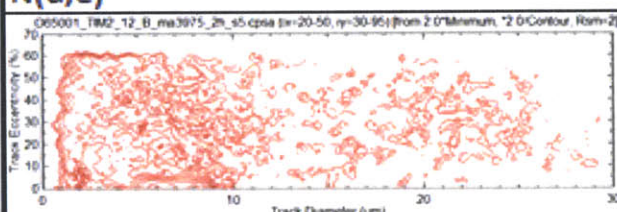
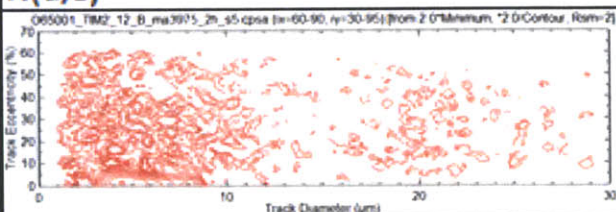
Tim 1, 4:00						
Shot	65001	Piece	ma3933	Type	Bert	
Etch Time (hours)	6	Distance (cm)	150	Magnification	40x	
<i>Step (um):</i>	50		<i>Step (um):</i>	25		
Limit c (%)	0 ≤ c ≤ 70		Limit c (%)	0 ≤ c ≤ 23		
Limit e (%)	0 ≤ e ≤ 10		Limit e (%)	0 ≤ e ≤ 10		
Limit Area	20 ≤ x ≤ 50 30 ≤ y ≤ 95		Limit Area	20 ≤ x ≤ 50 30 ≤ y ≤ 95		
Background	30 ≤ x ≤ 80 105 ≤ y ≤ 135		Background	30 ≤ x ≤ 80 105 ≤ y ≤ 135		
<b>N(d,c)</b>			<b>N(d,c)</b>			
<b>N(d)</b>			<b>N(d)</b>			
<b>N(d,e)</b>			<b>N(d,e)</b>			
<b>Average d (um)</b>	20354		<b>Average d (um)</b>	18.242		
<b>Fluence (tracks/cm^2)</b>	1.66E+03		<b>Fluence (tracks/cm^2)</b>	3.42E+03		
<b>Yield</b>	4.68E+08		<b>Yield</b>	9.66E+08		

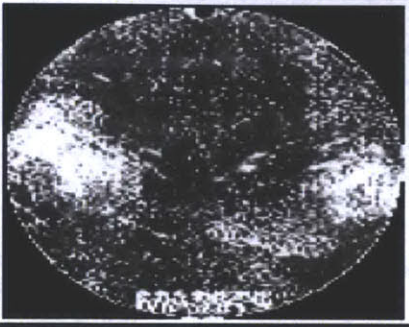
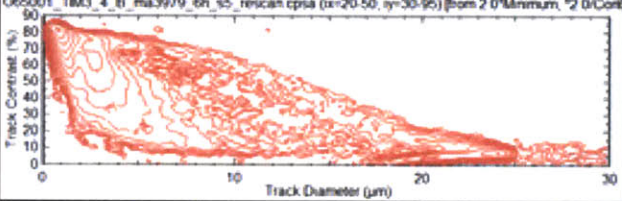
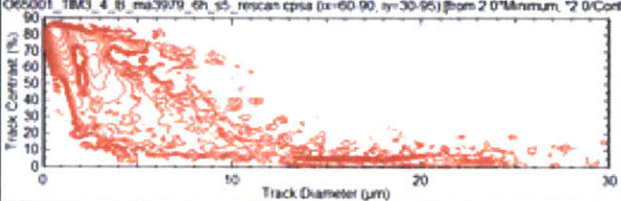
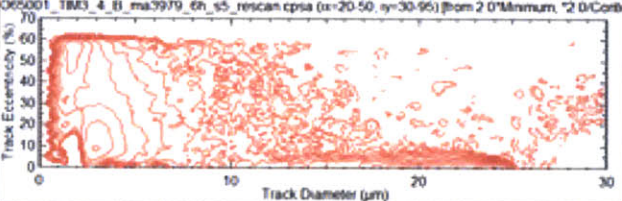
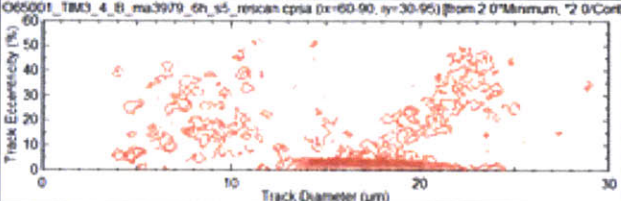
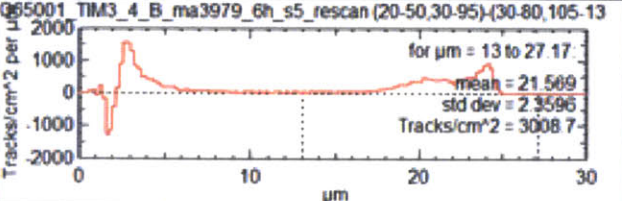
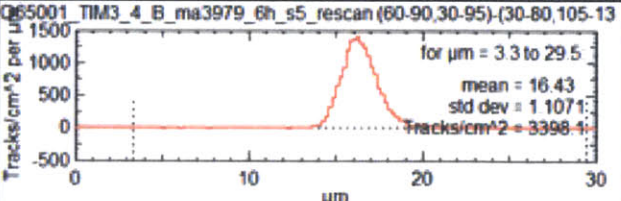
Tim 1, 8:00					
Shot	65001	Piece		Type	Bert
Etch Time (hours)	2	Distance (cm)	150	Magnification	40x
<i>Step (um):</i>	50		<i>Step (um):</i>	25	
Limit c (%)	$0 \leq c \leq 30$		Limit c (%)	$0 \leq c \leq 16$	
Limit e (%)	$0 \leq e \leq 8$		Limit e (%)	$0 \leq e \leq 9$	
Limit Area	$20 \leq x \leq 50$ $30 \leq y \leq 95$		Limit Area	$20 \leq x \leq 50$ $30 \leq y \leq 95$	
Background	$30 \leq x \leq 80$ $105 \leq y \leq 135$		Background	$30 \leq x \leq 80$ $105 \leq y \leq 135$	
<b>N(d,c)</b>			<b>N(d,c)</b>		
					
<b>N(d)</b>		<b>N(d)</b>			
					
<b>N(d,e)</b>		<b>N(d,e)</b>			
					
Average d (um)	6.4468	Average d (um)	4.8868		
Fluence (tracks/cm^2)	1.72E+03	Fluence (tracks/cm^2)	3.72E+03		
Yield	4.87E+08	Yield	1.05E+09		

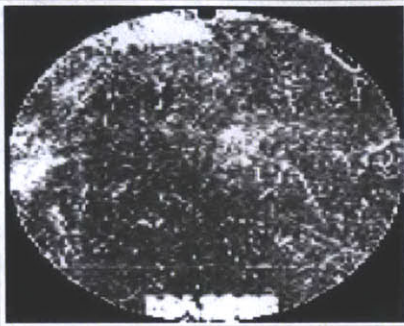
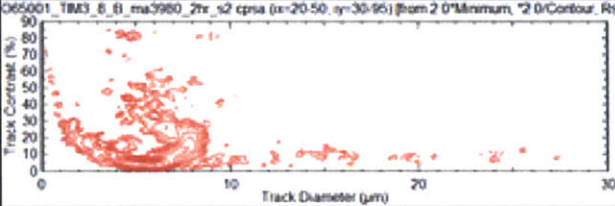
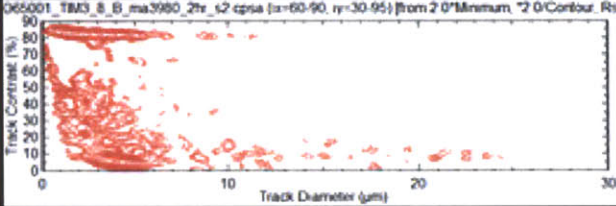
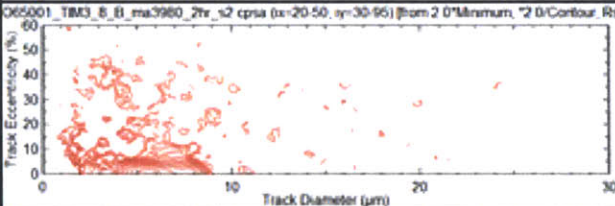
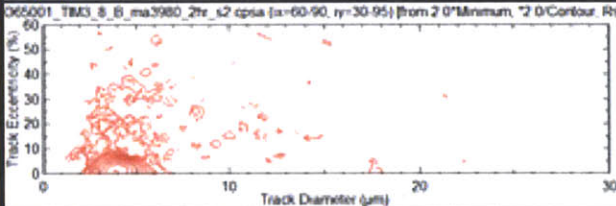
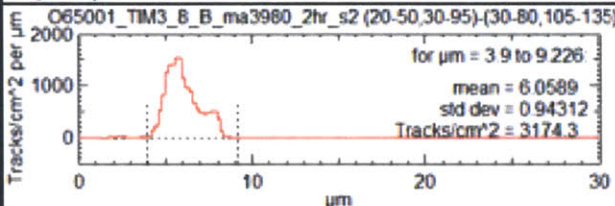
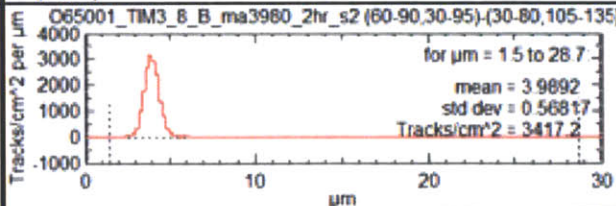
Tim 1, 12:00						
Shot	65001	Piece	ma3935	Type	Bert	
Etch Time (hours)	2	Distance (cm)	150	Magnification	40x	
<b>Step (um):</b>	50			<b>Step (um):</b>	25	
Limit c (%)	0 ≤ c ≤ 32			Limit c (%)	0 ≤ c ≤ 26	
Limit e (%)	0 ≤ e ≤ 9			Limit e (%)	0 ≤ e ≤ 9	
Limit Area	20 ≤ x ≤ 50 30 ≤ y ≤ 95			Limit Area	20 ≤ x ≤ 50 30 ≤ y ≤ 95	
Background	30 ≤ x ≤ 80 105 ≤ y ≤ 135			Background	30 ≤ x ≤ 80 105 ≤ y ≤ 135	
<b>N(d,c)</b>				<b>N(d,c)</b>		
<b>N(d)</b>			<b>N(d)</b>			
<b>N(d,e)</b>			<b>N(d,e)</b>			
<b>Average d (um)</b>	6.4054		<b>Average d (um)</b>		4.7295	
<b>Fluence (tracks/cm^2)</b>	1.56E+03		<b>Fluence (tracks/cm^2)</b>		3.44E+03	
<b>Yield</b>	4.40E+08		<b>Yield</b>		9.71E+08	

Tim 2, 4:00					
Shot	65001	Piece	ma3976	Type	Bert
Etch Time (hours)	6	Distance (cm)	150	Magnification	40x
<i>Step (um):</i>	50		<i>Step (um):</i>	25	
Limit c (%)	$0 \leq c \leq 70$		Limit c (%)	$0 \leq c \leq 50$	
Limit e (%)	$0 \leq e \leq 9$		Limit e (%)	$0 \leq e \leq 9$	
Limit Area	$20 \leq x \leq 50$		Limit Area	$20 \leq x \leq 50$	
	$30 \leq y \leq 95$			$30 \leq y \leq 95$	
Background	$30 \leq x \leq 80$		Background	$30 \leq x \leq 80$	
	$105 \leq y \leq 135$	$105 \leq y \leq 135$			
<b>N(d,c)</b>			<b>N(d,c)</b>		
<b>N(d)</b>			<b>N(d)</b>		
<b>N(d,e)</b>			<b>N(d,e)</b>		
<b>Average d (um)</b>		21.883	<b>Average d (um)</b>		18.679
<b>Fluence (tracks/cm^2)</b>		1.15E+03	<b>Fluence (tracks/cm^2)</b>		2.97E+03
<b>Yield</b>		3.26E+08	<b>Yield</b>		8.40E+08

Tim 2, 8:00					
Shot	65001	Piece	ma3977	Type	Bert
Etch Time (hours)	2	Distance (cm)	150	Magnification	40x
Step (um):	50		Step (um):	25	
Limit c (%)	$0 \leq c \leq 30$		Limit c (%)	$0 \leq c \leq 25$	
Limit e (%)	$0 \leq e \leq 10$		Limit e (%)	$0 \leq e \leq 10$	
Limit Area	$20 \leq x \leq 50$ $30 \leq y \leq 95$		Limit Area	$20 \leq x \leq 50$ $30 \leq y \leq 95$	
Background	$30 \leq x \leq 80$ $105 \leq y \leq 135$		Background	$30 \leq x \leq 80$ $105 \leq y \leq 135$	
N(d,c)			N(d,c)		
					
N(d)		N(d)			
					
N(d,e)		N(d,e)			
 for $\mu\text{m} = 4.81$ to $9.007$ mean = 6.761 std dev = 0.90711 Tracks/cm <sup>2</sup> = 1508.1		 for $\mu\text{m} = 3.14$ to $9.157$ mean = 5.2966 std dev = 0.99649 Tracks/cm <sup>2</sup> = 3253.6			
Average d (um)	6.761	Average d (um)	5.2966		
Fluence (tracks/cm <sup>2</sup> )	1.51E+03	Fluence (tracks/cm <sup>2</sup> )	3.25E+03		
Yield	4.26E+08	Yield	9.20E+08		

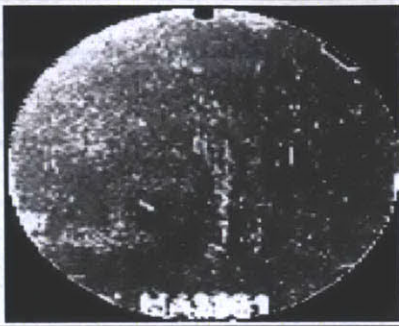
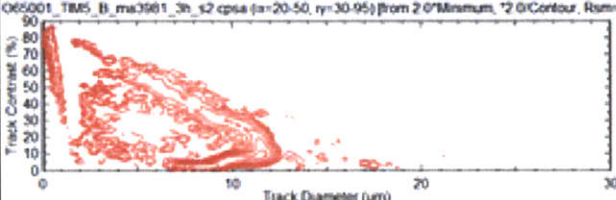
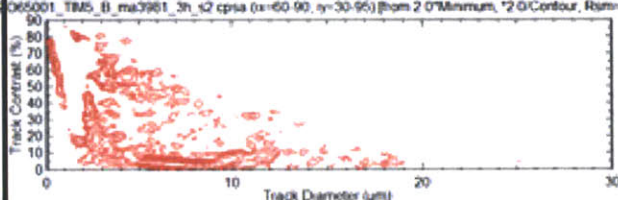
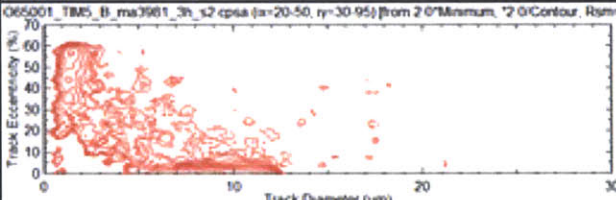
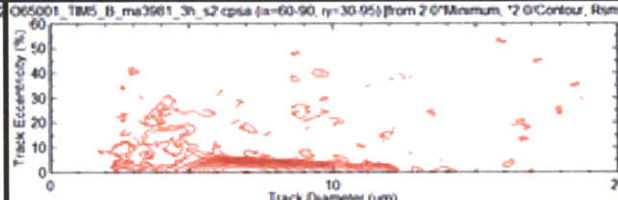
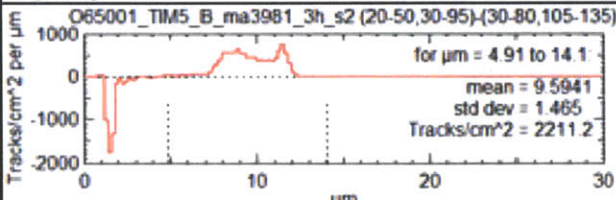
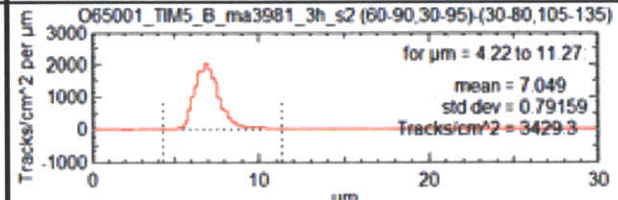
Tim 2, 12:00					
Shot	65001	Piece	ma3975	Type	Bert
Etch Time (hours)	2	Distance (cm)	150	Magnification	40x
Step (um):	50		Step (um):	25	
Limit c (%)	$0 \leq c \leq 32$		Limit c (%)	$0 \leq c \leq 23$	
Limit e (%)	$0 \leq e \leq 8$		Limit e (%)	$0 \leq e \leq 9$	
Limit Area	$20 \leq x \leq 50$ $30 \leq y \leq 95$		Limit Area	$20 \leq x \leq 50$ $30 \leq y \leq 95$	
Background	$30 \leq x \leq 80$ $105 \leq y \leq 135$		Background	$30 \leq x \leq 80$ $105 \leq y \leq 135$	
N(d,c)			N(d,c)		
					
N(d)		N(d)			
 <p>for <math>\mu\text{m} = 4.72</math> to <math>8.952</math> mean = 6.514 std dev = 0.9468 Tracks/cm<sup>2</sup> = 1492.7</p>		 <p>for <math>\mu\text{m} = 1.1</math> to <math>29.5</math> mean = 5.1019 std dev = 1.1611 Tracks/cm<sup>2</sup> = 3248.1</p>			
N(d,e)		N(d,e)			
					
Average d (um)	6.514	Average d (um)	5.1019		
Fluence (tracks/cm^2)	1.49E+03	Fluence (tracks/cm^2)	3.25E+03		
Yield	4.22E+08	Yield	9.18E+08		

Tim 3, 4:00					
Shot	65001	Piece	ma3979	Type	Bert
Etch Time (hours)	6	Distance (cm)	150	Magnification	40x
Step (um):	50		Step (um):	25	
Limit c (%)	$0 \leq c \leq 65$		Limit c (%)	$0 \leq c \leq 10$	
Limit e (%)	$0 \leq e \leq 10$		Limit e (%)	$0 \leq e \leq 7$	
Limit Area	$20 \leq x \leq 50$ $30 \leq y \leq 95$		Limit Area	$20 \leq x \leq 50$ $30 \leq y \leq 95$	
Background	$30 \leq x \leq 80$ $105 \leq y \leq 135$		Background	$30 \leq x \leq 80$ $105 \leq y \leq 135$	
<b>N(d,c)</b>			<b>N(d,c)</b>		
					
<b>N(d)</b>		<b>N(d)</b>			
					
<b>N(d,e)</b>		<b>N(d,e)</b>			
					
Average d (um)	21.569	Average d (um)	16.43		
Fluence (tracks/cm^2)	3.01E+03	Fluence (tracks/cm^2)	3.40E+03		
Yield	8.51E+08	Yield	9.61E+08		

Tim 3, 8:00					
Shot	65001	Piece	ma3980	Type	Bert
Etch Time (hours)	2	Distance (cm)	150	Magnification	40x
<i>Step (um):</i>	50		<i>Step (um):</i>	25	
Limit c (%)	$0 \leq c \leq 35$		Limit c (%)	$0 \leq c \leq 15$	
Limit e (%)	$0 \leq e \leq 10$		Limit e (%)	$0 \leq e \leq 10$	
Limit Area	$20 \leq x \leq 50$ $30 \leq y \leq 95$		Limit Area	$20 \leq x \leq 50$ $30 \leq y \leq 95$	
Background	$30 \leq x \leq 80$ $105 \leq y \leq 135$		Background	$30 \leq x \leq 80$ $105 \leq y \leq 135$	
<b>N(d,c)</b>			<b>N(d,c)</b>		
					
<b>N(d)</b>		<b>N(d)</b>			
					
<b>N(d,e)</b>		<b>N(d,e)</b>			
					
Average d (um)		6.0589	Average d (um)		3.9892
Fluence (tracks/cm^2)		3.17E+03	Fluence (tracks/cm^2)		3.42E+03
Yield		8.98E+08	Yield		9.66E+08



Tim 3, 12:00					
Shot	65001	Piece	ma3978	Type	Bert
Etch Time (hours)	2	Distance (cm)	150	Magnification	40x
Step (um):	50			Step (um):	25
Limit c (%)	$0 \leq c \leq 30$			Limit c (%)	$0 \leq c \leq 14$
Limit e (%)	$0 \leq e \leq 10$			Limit e (%)	$0 \leq e \leq 10$
Limit Area	$20 \leq x \leq 50$ $30 \leq y \leq 95$			Limit Area	$20 \leq x \leq 50$ $30 \leq y \leq 95$
Background	$30 \leq x \leq 80$ $105 \leq y \leq 135$			Background	$30 \leq x \leq 80$ $105 \leq y \leq 135$
N(d,c)			N(d,c)		
N(d)			N(d)		
N(d,e)			N(d,e)		
Average d (um)		6.3858	Average d (um)		4.1266
Fluence (tracks/cm^2)		3.05E+03	Fluence (tracks/cm^2)		3.52E+03
Yield		8.63E+08	Yield		9.96E+08

TIM 5					
Shot	65001	Piece	ma3981	Type	Bert
Etch Time (hours)	3	Distance (cm)	150	Magnification	40x
<i>Step (um):</i>	50		<i>Step (um):</i>	25	
Limit c (%)	$0 \leq c \leq 60$		Limit c (%)	$0 \leq c \leq 13$	
Limit e (%)	$0 \leq e \leq 9$		Limit e (%)	$0 \leq e \leq 8$	
Limit Area	$20 \leq x \leq 50$ $30 \leq y \leq 95$		Limit Area	$20 \leq x \leq 50$ $30 \leq y \leq 95$	
Background	$30 \leq x \leq 80$ $105 \leq y \leq 135$		Background	$30 \leq x \leq 80$ $105 \leq y \leq 135$	
<b>N(d,c)</b>			<b>N(d,c)</b>		
					
<b>N(d)</b>		<b>N(d)</b>			
					
<b>N(d,e)</b>		<b>N(d,e)</b>			
					
<b>Average d (um)</b>	9.5941	<b>Average d (um)</b>	7.049		
<b>Fluence (tracks/cm^2)</b>	2.21E+03	<b>Fluence (tracks/cm^2)</b>	3.43E+03		
<b>Yield</b>	6.25E+08	<b>Yield</b>	9.70E+08		